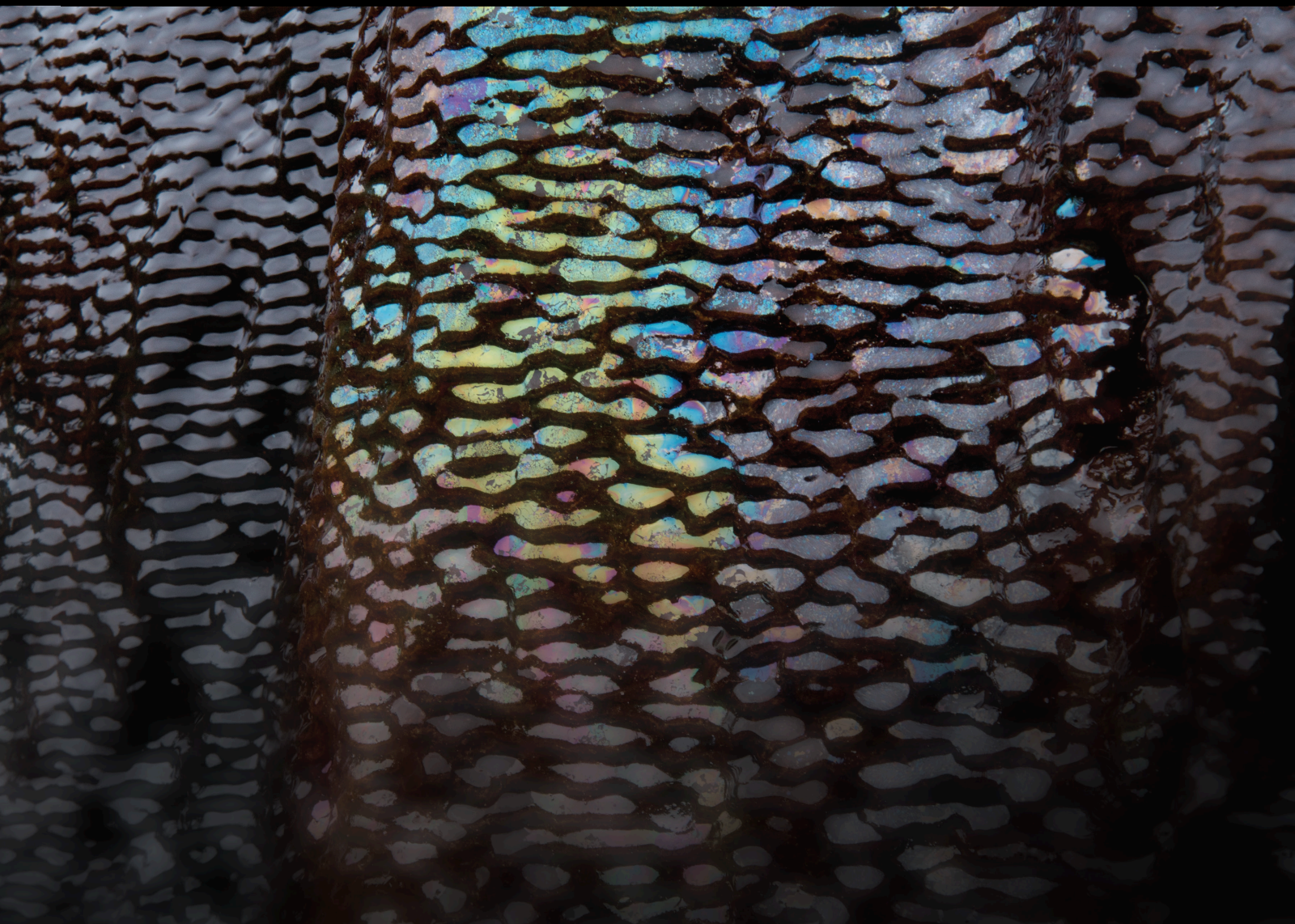# Advances in Shallow Landslide Hydrology and Triggering Mechanisms: A Multidisciplinary Approach

Lead Guest Editor: Claudia Meisina
Guest Editors: Marco Bittelli, Roberto Valentino, Massimiliano Bordoni, and Roberto Tomás-Jover

Advances in Shallow Landslide Hydrology and Triggering Mechanisms: A Multidisciplinary Approach

Advances in Shallow Landslide Hydrology and Triggering Mechanisms: A Multidisciplinary Approach

Lead Guest Editor: Claudia Meisina
Guest Editors: Marco Bittelli, Roberto Valentino, Massimiliano Bordoni, and Roberto Tomás-Jover

Editorial Board

Contents

WILEY | Hindawi

Editorial
Advances in Shallow Landslide Hydrology and Triggering Mechanisms: A Multidisciplinary Approach

Claudia Meisina [ID],[1] **Marco Bittelli,**[2] **Roberto Valentino,**[3] **Massimiliano Bordoni,**[1] **and Roberto Tomás-Jover**[4]

[1]*Department of Earth and Environmental Sciences, University of Pavia, Via Ferrata 1, 27100 Pavia, Italy*
[2]*Department of Agricultural Sciences, University of Bologna, Viale Fanin 44, 40127 Bologna, Italy*
[3]*Department of Chemistry, Life Sciences and Environmental Sustainability, University of Parma, Parco Area delle Scienze, 157/a, 43124 Parma, Italy*
[4]*Departamento de Ingeniería Civil, Universidad de Alicante, Apartado de Correos 99, 03080 Alicante, Spain*

Correspondence should be addressed to Claudia Meisina; claudia.meisina@unipv.it

The vadose zone of steep slopes is often affected by rainfall-induced shallow landslides, which can cause widespread direct and indirect damage to the terrain and infrastructures, as well as urban and rural developments. These phenomena are determined by hydrological or subsurface flow processes and also mechanical (stress equilibrium) processes. Some models attempt to link dynamics of hydrologic behavior with the mechanical state of a hillslope and the onset of failure. However, the hydrological dynamics leading to shallow landslide initiation, the hydraulic properties at the slope scale, and the role of hysteretic effects as well as the soil nonequilibrium processes in slope stability assessment are still not completely understood and require further investigation. Furthermore, these open questions are generally treated separately by geologists, hydrologists, agronomists, and geotechnical engineers, whereas a multidisciplinary approach is a key factor in the study of these phenomena occurring in the vadose zone.

Starting from these issues, the main focus of this special issue is on presenting the advances in shallow landslide hydrology from both the earth sciences and soil mechanics perspectives and their influence on behavior and triggering of shallow landslides.

This special issue collects papers representing some of the most recent developments in this field, with a special emphasis given to recent results obtained by both small-scale experiments and analysis of specific case histories. The main topics of the papers included in the special issue regarded the following:

(i) Analysis and modeling of landslide hydrology at different scales

(ii) Hydrological modeling of the materials forming deposits of past landslides

(iii) Field hydrological monitoring of slopes

(iv) Seasonal, yearly, and interyearly hydrological dynamics of a slope

(v) Models of hydromechanical triggering of shallow landslides

(vi) Antecedent and initial hydrological conditions that predispose to landslide triggering

(vii) Porous media dynamics in landslide systems

(viii) Landslide water balance models

Ten papers were submitted for this special issue. Our distinguished reviewers from respective research fields

narrowed the field to six papers which were finally accepted. The following is a short summary of the findings of each of these papers.

C. Zhang et al. performed physical tank experiments to investigate the ways of generation of pore water pressure in a slope affected by a landslide. The results of this experimental approach stress that pore water pressure values and changes in time, related to the different positions of the groundwater table along the hillslope, are significantly affected by infiltration time from the surface to different layers in depth, by surface runoff amount, and by lateral flows.

L. Schilirò et al. investigated the impact of the initial soil hydrological conditions on the triggering of rainfall-induced shallow landslides, proposing an innovative experimental setup which integrated laboratory simulations by means of a sloping flume and physically based numerical modeling. Initial hydrological conditions have a fundamental role on determining the type of the triggering mechanism and the soil types that could be affected by shallow failures.

H. Cai et al. analyzed the hydromechanical behavior of the materials forming the accumulation zone of a past earthquake-induced landslide, which was affected by erosions and shallow failures. Monitoring of water content and pore water pressure trends and of the flow directions in a laboratory small-scale physical model of the real landslide allowed recognizing preferential flows and seepage-induced internal erosion in the deposit that could lead to the triggering of shallow instabilities.

A. Wayllace et al. analyzed the hydrological behavior of an active landslide in Colorado (USA) and its effects on the stability of the slope. Field observation of displacements and groundwater variations are used to determine a conceptual model that takes into account also site morphology and stratigraphy, atmospheric conditions, and the main physical mechanisms in the hillslope. A series of 2D finite element numerical simulations, which are based on the conceptual model and calibrated with field data, are then used to assess slope stability.

J. Iqbal et al. analyzed the effect of reservoir fluctuations on an active landslide in the Xiangjiaba Reservoir area, Southwest China. On the basis of field investigations and laboratory tests, the authors carried out a slope stability analysis using FLAC 3D software. Numerical results shed light on the fact that the minimum safety requirements under the working condition of reservoir level fluctuation are not reached and then surface monitoring should be carried out in order to set up early warning prior to failure.

Y.-S. Yang and H.-F. Yeh evaluated the probability of failure by means of a fuzzy point estimate method in order to consider the inherent uncertainties associated with soil properties (i.e., cohesion and friction angle). To this aim, a hydromechanical coupling model on HYDRUS 2D and the Slope Cube Module were used. The results reveal that fuzzy theory effectively evaluates the variability of the factor of safety as well as the reliability index.

Conflicts of Interest

I confirm that the Lead Guest Editor and the other Guest Editors have no conflict of interest.

Claudia Meisina
Marco Bittelli
Roberto Valentino
Massimiliano Bordoni
Roberto Tomás-Jover

WILEY | Hindawi

Research Article

An Experimental Study on the Hydromechanical Behaviours of the Evolution of Postearthquake Landslide Deposits

Huan Cai,[1,2] **Zong-Ji Yang** ![ORCID],[1] **Li-Yong Wang,**[1,2] **Xiao-Qin Lei,**[1] **Xiao-Long Fu,**[1,2] **Shi-Hao Liu,**[1,2] **and Jian-Ping Qiao**[1]

[1]*Institute of Mountain Hazards and Environment, CAS, Chengdu 610041, China*
[2]*University of Chinese Academy of Sciences, Beijing 100049, China*

Correspondence should be addressed to Zong-Ji Yang; yzj@imde.ac.cn

In this study, a series of experiments of the full-scale physical model was employed to investigate the hydromechanical behaviours of the postearthquake landslide evolution, in forms of rill erosion and shallow headward failure on the rill bank slopes under unsaturated conditions. Soil-water characteristic curves (SWCC) were established using the Brooks-Corey (BC) and van Genuchten (VG) models. The stability of the shallow failure was then analyzed via a one-dimensional and unsaturated stability analysis model of the infinite slope. This measurement revealed that the preferential flow and the matrix flow coexisted when infiltration occurred and the VG model performs better in fitting the SWCC than the BC model. Consistent feedback between stability calculations and experimental observations enables the analysis of mechanisms of rill erosion and slope failure of postseismic landslide under the impact of preferential flow. Furthermore, the seepage-induced internal erosion phenomenon was observed in the experiment. This work thus provides a new perspective on the triggering mechanisms of debris flow during the postseismic period.

1. Introduction

The Wenchuan earthquake in 2008 undermined the geologic stability and thoroughly changed the microgeomorphic conditions in the Longmenshan region of Sichuan province, southwestern China [1–3]. Numerous earthquake-induced landslide deposits have undergone remarkable mass remobilization under heavy precipitation during the postseismic period [4–7]. These deposits are unstable, and the surface runoff caused by heavy precipitation strongly influences the accumulation of landslide deposits in the debris flow source region, where rills gradually cut deep trenches that provide effective free surfaces for both banks of the channel [7, 8]. In such a condition, shallow headward failures have occurred on both sides of the extensional rills and gullies in these landslide deposits. Mass remobilization provided a considerable amount of source materials for the initiation of debris flows, thereby directly causing postseismic debris flow outbreaks in the earthquake-stricken area [9–11] and seriously

threatening local reconstruction and safety. Investigations of abrupt topographic transformations, rapid erosional processes, and changes in material source conditions have become new priorities for prevention and management of postseismic debris flow. However, the mechanisms underlying these phenomena remain untested.

Understanding the evolution mechanism of shallow headward failure and rill erosion of earthquake-induced landslide deposits in the headwater valleys caused by heavy rainfall is key to developing an early warning system of postseismic debris flow disasters [12, 13]. The study of rainfall-induced landslides is a fairly complex topic involving a multidisciplinary technology [14]. So far, a laboratory model test is still the most reliable method for studying the rainfall-triggered landslide since the soil properties and boundary conditions can be controlled and the pore water pressures and stresses inside the slopes can be monitored [15]. Many scholars have conducted model tests to study the processes and mechanisms of landslide evolution

[11, 14, 16–22], and they have made important contributions to our understanding of the mechanisms behind rainfall-triggered landslides. Besides, the earthquake-induced landslide deposit is composed of coarse-textured gravelly soil whose structure is characterized by fracture development, high permeability, and an extremely low fraction of fine particle [23]. Thus, the rapid preferential flow infiltration becomes the most important hydraulic characteristic of earthquake-induced landslide deposits under unsaturated conditions [24, 25]. Consequently, the soil-water characteristic curve (SWCC) and coupled hydromechanical processes of preferential flow are distinctive. However, due to rainfall-induced shallow failure as well as sediment delivery on postearthquake landslide deposits, the hydromechanical behaviour of shallow headward failures triggered by preferential flow in response to rainfall under partially saturated conditions is poorly understood. To date, tests on infiltration flows and hydromechanical behaviours of unsaturated soils have mainly focused on fine-textured soils (e.g., clays and silts) with relatively small particle sizes and pore diameters [26, 27]. There have been relatively less studies on the coupled hydromechanical behaviours of coarse-textured gravelly soils. Moreover, no experimental study of the shallow headward failure of earthquake-induced landslide deposits under rainfall conditions has been reported.

With the development of soil mechanics theories, greater attention has been paid to unsaturated soil materials and their failure mechanisms are inconsistent with the principles and concepts of classical, saturated soil mechanics. Unlike the simpler saturated sands, silts, and clays, these materials puzzled scientists for decades [28]. Because the shear strength of saturated soils could be estimated more conservatively than that of unsaturated soils, the traditional soil mechanics theories have been used for engineering assessments as an orthodox method. Yet, the discrepancy between theoretical assumptions and the actual physical states of soils, together with such factors as rising construction cost, has motivated us to rethink these problems [29]. For example, to assess the stability of slopes with seepage flow more accurately, slope stability analyses have been expanded to include coupled hydromechanical processes under variably saturated conditions [30–35]. These analyses incorporate the variation of saturation, leading to more accurate assessments of the stability of slopes under infiltration conditions and demonstrating that a better physical representation of water flow and stress can be attained in unsaturated soils [35] The main objective of this work is to integrate the hydromechanical behaviours and failure mechanism of unsaturated landslide material during artificial rainfall model tests.

Based on the patterns of postearthquake mass transportation attributable to the shallow failure mode of the landslide deposits in the region affected by the Wenchuan earthquake, a series of full-scale physical model tests were conducted using the natural, coarse-textured soils from earthquake-induced landslide deposits. With the aid of an unsaturated infinite slope stability analysis model, changes in the one-dimensional unsaturated factor of safety (FS) of the experimental slope with artificial rainfall were computed at first. The experimental and calculation results were then compared and analyzed. By providing experimental data for predicting the infiltration characteristics and stability of landslide deposits composed of coarse-textured gravelly soils with rill erosion and shallow headward failure under unsaturated conditions, this study is aimed at providing new insights into the failure modes and mechanisms of rainfall-induced landslides and debris flows during the postseismic period.

2. Methods

2.1. Model Test

2.1.1. Case Study. The study focuses on the shallow failure mechanisms of the Yindongzi landslide in the Baisha River Basin. This landslide occurred in the Yindongzi Trench, Lianhe Village, Hongkou Township, Dujiangyan county, Chengdu City, Sichuan province, China, which is the meizoseismal area of the Wenchuan earthquake, and it is filled with typical earthquake-induced landslide deposits [13]. The Yindongzi landslide deposit is on the right side of the junction between the initiation zone and the transportation zone of the main gully (Figure 1(a)). The crown elevation of the landslide is 1520 m, the toe elevation is 1352 m, and the relief between the crown and the toe is 168 m. The horizontal projection area is 7.6×10^4 m^2, and the slope surface area is 10×10^4 m^2. The principal sliding direction is 182°, and the landslide is generally fan shaped. The landslide deposit accumulated in the gully along a slope of 35-42° and with a volume of approximately 31×10^4 m^3. The postseismic Yindongzi landslide exhibits a shallow failure mode along the banks of the gully under heavy rainfall. The rill erosion banks of the landslide deposit were chosen for model testing (Figure 1(b)). Soils on the bank surfaces have undergone shallow failure over a long period of rainfall and have continuously expanded on both sides, providing source materials for debris flow initiation in the Yindongzi gully. These materials have become the main source of subsequent debris flows, threatening the safety and property of 260 people in 56 households at the settlement site at the trench mouth (Figure 1(d)).

2.1.2. Test Design. In order to reproduce the rainfall-induced failure process of natural rill banks as realistically as possible, a full-scale (1 : 1) model was built according to the observed rill banks (Figure 1(b)). The height and length of natural rill banks in the Yindongzi landslide deposits were almost 1~3 m, and the slope gradient was dominantly 60°. The physical model was built in strict accordance with the actual shape of the slope, with a height of 1.2 m, a length of 3.0 m, and a slope angle of 60° (Figure 2). Thus, this model meets the requirements of geometric similarity. There were two measurement lines in the physical model. Two sets of pore water pressure and soil volumetric water content sensors were buried along each measurement line at the heights of 25 cm, 50 cm, 75 cm, and 100 cm from the ground within the 120 cm thick longitudinal section. Land surface tilt meters were deployed on the bank surface at the same height as sensors. A schematic diagram of the layout of the sensors is

(a)

(b)

(c)

(d)
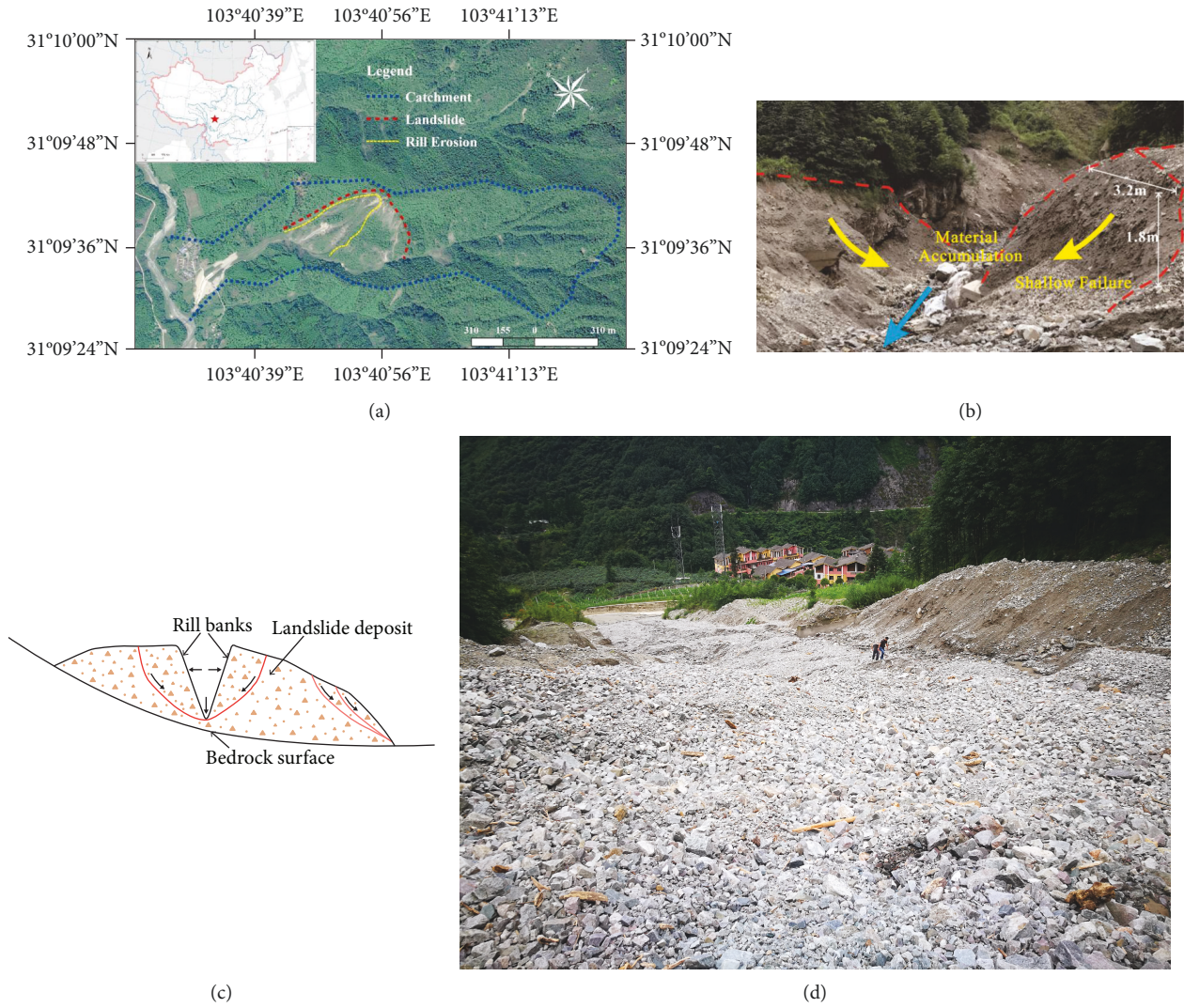
FIGURE 1: (a) Location and scale of Yindongzi landslide. (b) Free surfaces of rill banks on the landslide deposit. (c) A schematic diagram of shallow headward failure in rill erosion in the landslide deposit. (d) An outbreak of debris flows in Yindongzi gully.

(a)

(b)
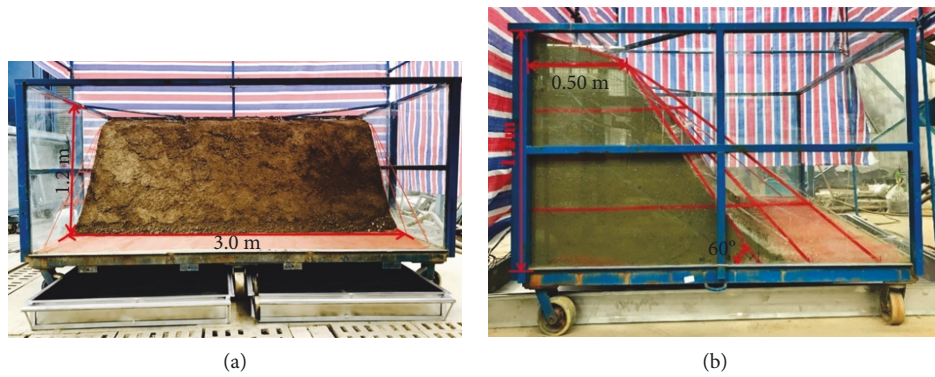
FIGURE 2: Pictures of the physical model: (a) front view and (b) side view.

shown in Figure 3. The volumetric water content sensors were numbered from VWC-1 to VWC-8, the pore water pressure sensors were numbered from PWP-1 to PWP-8, and the surface tilt meters were numbered from TS1 to TS8. The experiments were conducted under three rainfall intensity conditions with 170 mm/h, 140 mm/h, and 110 mm/h of
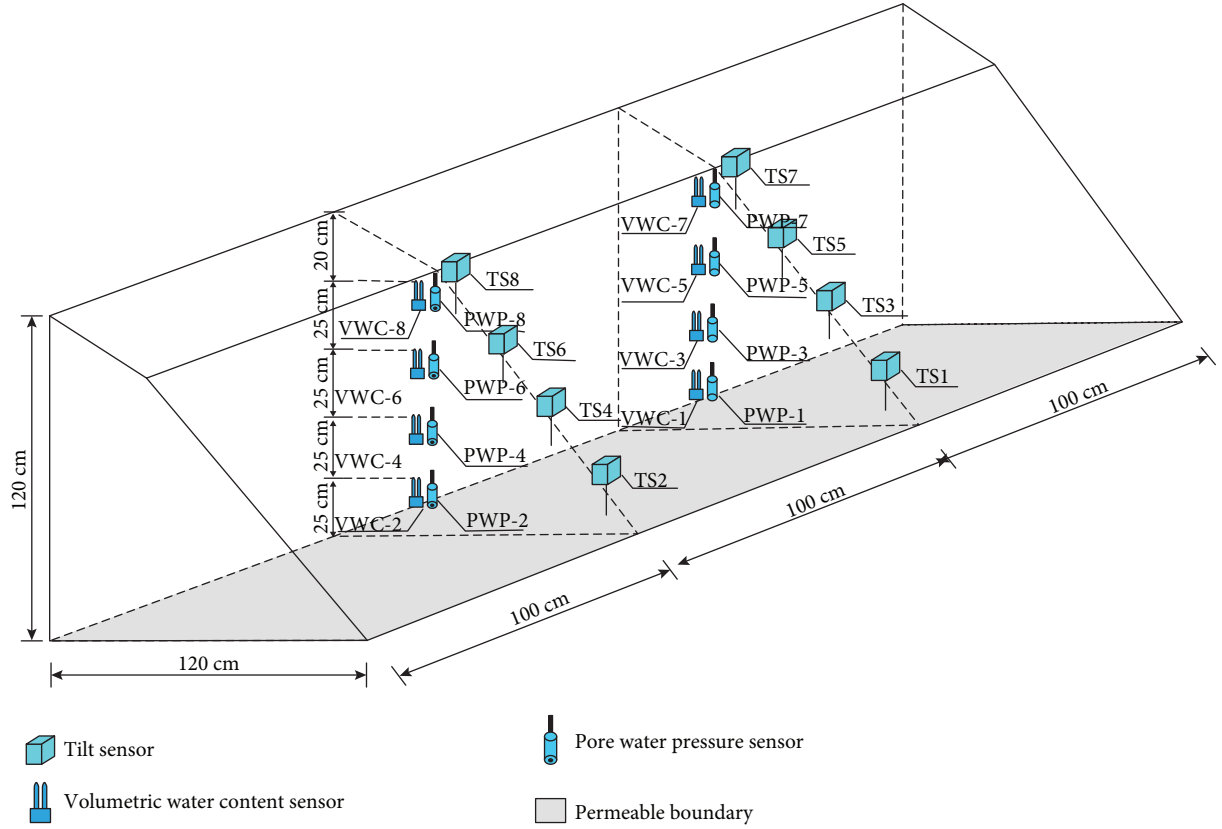
Figure 3: Schematic diagram of embedded sensors.

Table 1: Experimental strategies.

Series	Rainfall intensity (mm/h)	Slope angle (°)
Test 1	170	60
Test 2	140	60
Test 3	110	60

rainfall. Three sets of tests were conducted as shown in Table 1.

The model tests were conducted on an indoor landslide simulation platform (Figure 4), which is mainly composed of a rainfall system, a landslide model tank, and a measurement system. The artificial rainfall simulator has 36 sprinklers, by which rainfall intensity could be adjusted from 30 mm/h to 180 mm/h. To evaluate the sprinkle uniformity of the artificial rainfall, the coefficient of rainfall homogeneity was introduced. It was originally proposed by Christiansen [36], and the calculation formula is

$$C_u = 100 \left(1.0 - \frac{\sum X}{mn} \right), \qquad (1)$$

where X is the difference between the observed spray intensity and the average intensity value m at each point; n is the total number of observation points; C_u is the sprinkle homogeneity (%). To ensure that water can be sprinkled evenly, C_u

Figure 4: Rainfall-induced landslide simulation platform.

is required to be over 80% [37] and this value is larger than 85% in this test. The length, width, and height of the model tank were 3.0 m, 2.0 m, and 1.2 m, respectively. The framework was made of structural steel, and the base was a flat steel plate. Tank walls were made of transparent, toughened glass, except for the front wall, which was left open for allowing large displacement of landslides and debris flow.

The shallow failure occurred mainly at the depth of 0.5 m, where the gravelly soil exhibited high permeability.

(a)

(b)

(c)

(d)
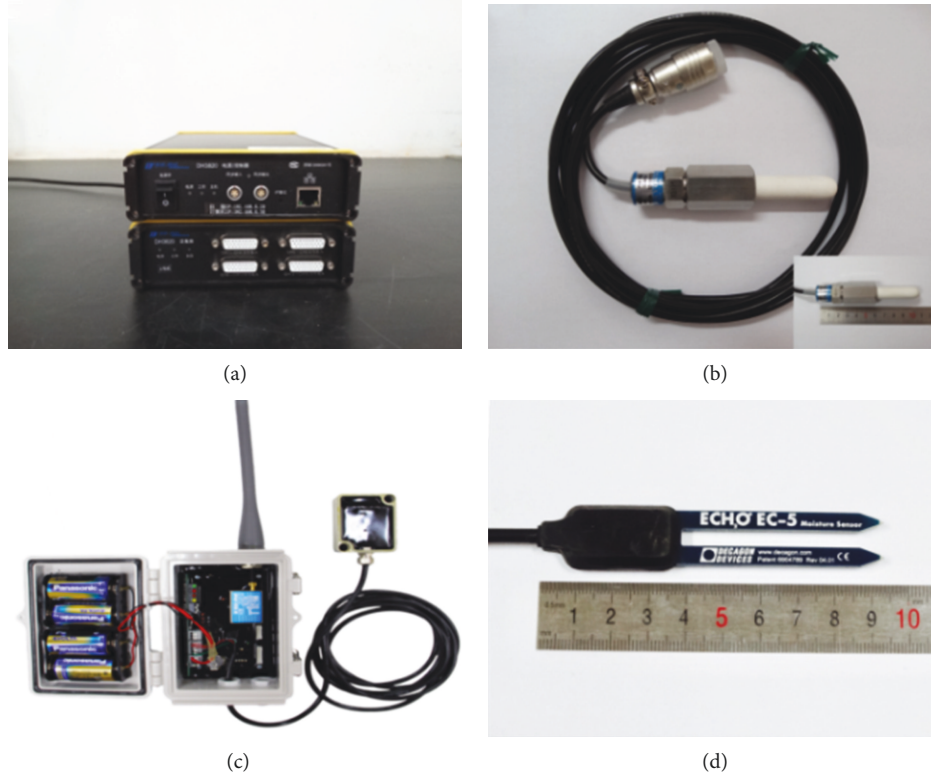
FIGURE 5: Pictures of the measuring system for the model test: (a) data logger; (b) pore water pressure sensor; (c) the wireless tiltmeter; (d) soil moisture sensor.

Therefore, the seepage observed in the natural rill banks was vertical infiltration with no groundwater rising and failure occurred in an unsaturated condition instead of failure with lateral saturated seepage. Permeable boundary conditions are typical for shallow failure with unsaturated infiltration. To simulate the permeable boundary, 13 rows ∗ 20 columns totalling 260 round holes with a diameter of 10 mm were evenly distributed at the bottom of the model tank so that the infiltrating rainwater could freely flow out. Before the experiment, a nylon gauze with a mesh diameter of 1 mm was laid to prevent large particles from leaking. Finally, two shallow troughs of equal size were placed beneath the model tank to collect the mud generated by seepage in the soil. The front view and side view of the physical model are shown in Figure 2.

The measurement system included a data acquisition system (Figure 5(a)) and the following three sensors: pressure sensor (Figure 5(b)), ground surface tiltmeter (Figure 5(c)), and soil moisture sensor (Figure 5(d)). The data acquisition system was a Jiangsu Donghua DH3820 high-speed static strain test analysis system, which was used for collecting and analyzing the voltage signal output of each sensor. The type of pore water pressure sensors was PGM-1KG low-pressure transducer by KYOWA, Japan, which can measure the pore water pressure and soil suction with the installation of a customized porcelain component. The wireless surface tiltmeters were developed by the Chuo Kaihatsu Corporation, Japan, and were compatible with the SCA100T-D01

series 2-axis MEMS tiltmeter module made by Murata [12, 38], Japan, with an accuracy of 0.0025°. The type of soil moisture sensors was EC-5 by Decagon, USA; the measurement accuracy of this sensor for the gravelly soil used in this test is ±3%, and its resolution is 0.25%.

2.1.3. Test Materials. After the Wenchuan earthquake in 2008, years of heavy rainfall caused landslide deposits to become unconsolidated, develop high water permeability, and lose fine particles. To reproduce the preearthquake gradation characteristics of the soil in this region by inferring the grading curves of the analogous landslide deposits from the earthquake-stricken area [7, 11], the material for tests was gravelly soil obtained from the overlying deposit layer of the Yindongzi landslide with a particle size of less than 6 cm, mixed with 5% fine material with a particle size less than 1 mm. A series of geotechnical tests of model materials have been done, including a particle analysis test (for particle size distribution), a triaxial test (for soil cohesion c and friction angle φ), a direct shear test (for soil cohesion c and friction angle φ), infiltration test (for saturated hydraulic conductivity k_s), and a routine soil test (specific gravity G_s and dry density ρ_d). The coefficient of uniformity (C_u) of the model gravelly soil is 25.79, and the coefficient of curvature (C_c) is 1.63, indicating a well and continuous particle grading. Although some boulders were removed to improve particle grading, the soil still maintained the same characteristic well grading as the original state, which allowed a

TABLE 2: Basic parameters for original and model soils.

Soil types	Soil unit weight (kN·m⁻³)	Maximum dry density (g·cm⁻³)	Saturated hydraulic conductivity (cm·s⁻¹)	Poisson ratio (-)	Effective cohesion (kPa)	Effective friction angle (°)	Initial moisture (-)	Porosity (-)
Original	18.9	1.90	2.78×10^{-3}	0.26	19-25	35-40	0.113-0.133	0.23
Model	17.0-20.0	2.20	1.67×10^{-3}	0.28	28.6	30-35	0.095-0.125	0.27
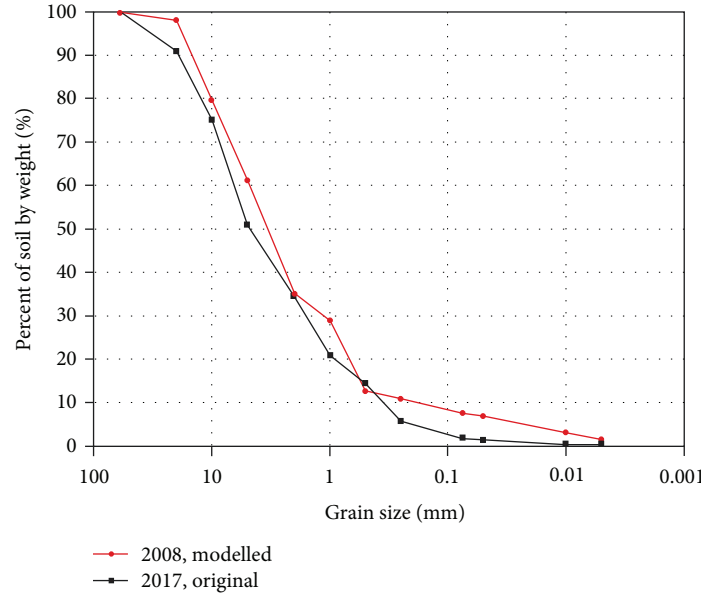
FIGURE 6: Particle grading curves of original and model soils.

realistic simulation of the soil structure as well as physical and mechanical properties of unconsolidated landslide deposits. The basic soil parameters are listed in Table 2, and particle gradation of the natural landslide deposit soil, as well as the experimental deposit soil, is shown in Figure 6.

2.1.4. Soil Porosity and Evidence for Preferential Flow. The coarse-textured gravelly soil gathered from the landslide site has a loose porous structure, which enables preferential flow to run through certain pathways [39]. In order to prove the occurrence of preferential flow in the soil, the relationship between soil density and porosity was verified via a special device (Figure 7(a)). By controlling the weight of soil in a limited volume, the soil density (ρ) could be set as the goal. When water flows through the pipe into the gravelly soil, the mass would sink and the porosity could be calculated by measuring the added weight of water. The calculation equation and details of this device can be found in an article written by Zhao et al. [40]. The result is shown in Figure 7(b) that the soil porosity is nearly linear with the density under the same water content. The density of model slopes was controlled at a range of 1.6-1.8 g/cm³, and porosity ranged from 36.9% to 26.6% correspondingly. Such a high porosity in gravelly soil indicates the possibility for the generation of preferential flow. Furthermore, dye infiltration experiences

have been done to show the flow path in this soil column with densities of 1.6 g/cm³, 1.7 g/cm³, and 1.8 g/cm³ (Figure 8). The height of the soil column was 35 cm, and methylene blue solution was used as a dye tracer so that the flow path could be observed clearly. It can be seen in Figure 8 that preferential flow occurred in all conditions. With the increasing soil density, the depth of initiation for preferential flow increases significantly from 3 cm to 13 cm, indicating more resistance for water flow in denser soil.

2.2. Theoretical Analysis

2.2.1. Soil-Water Characteristic Curve. In this study, the two most commonly used models, the Brooks-Corey (BC) and van Genuchten (VG) models, were utilized to describe the soil-water characteristic curve (SWCC) of the experimental soil. The SWCC can be fitted by the measured matric suction and the corresponding volumetric water content. A relatively simple equation of the soil-water characteristic curve was proposed by Brooks [41] as follows:

$$S_e(Z,t) = \frac{\theta(Z,t) - \theta_r}{\theta_s - \theta_r} = \begin{cases} |\alpha\psi(Z,t)|^{-n}, & \alpha\psi < -1, \\ 1, & \alpha\psi > -1. \end{cases} \tag{2}$$

(a)

(b)
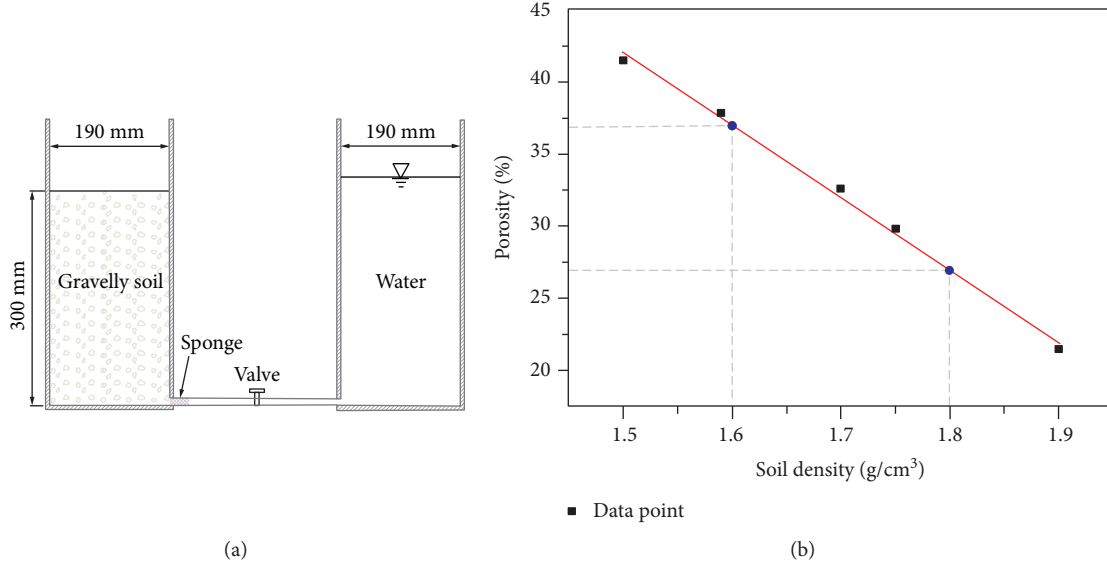
FIGURE 7: (a) Diagram of the soil porosity measurement device and (b) relationship between soil porosity and density.

Genuchten [42] proposed a smooth, closed, three-parameter soil-water characteristic curve model with the following expression:

$$S_e(Z, t) = \begin{cases} [1 + |\alpha\psi(Z, t)|^n]^{-m}, \psi < 0, \\ 1, \psi \geq 0, \end{cases} \quad (3)$$

where θ_r is the residual water content, θ_s is the saturated water content, α, m, and n are the fitting parameters, where $m = 1 - 1/n$, α approximately is equal to the reciprocal of the air entry pressure value and its unit is kPa^{-1}, and S_e is the effective saturation, ψ is the matric suction, and Z is the soil depth.

2.2.2. Infinite Slope Stability Analysis Model. The stability of rainfall-induced shallow landslides is usually evaluated with the one-dimensional limit equilibrium model named as "infinite slope stability model" [16, 27, 43]. The classical slope stability model used to assume saturated conditions in practice ; later, Baum et al. [43] and Lu et al. [34] extended this model to unsaturated conditions through coupling suction stress.

The suction stress of the VG model is

$$\psi(Z, t) = \frac{\left(S_e(Z, t)^{-(1/m)} - 1\right)^{1/n}}{\alpha}$$

$$= \frac{\left[((\theta(Z, t) - \theta_r)/(\theta_s - \theta_r))^{-(1/m)} - 1\right]^{1/n}}{\alpha}, \quad (4)$$

$$\sigma^s(Z, t) = S_e \psi(Z, t)$$

$$= \frac{\theta(Z, t) - \theta_r}{\theta_s - \theta_r} \frac{\left[((\theta(Z, t) - \theta_r)/(\theta_s - \theta_r))^{-(1/m)} - 1\right]^{1/n}}{\alpha}. \quad (5)$$

The unsaturated infinite slope stability analysis model is

$$Fs(Z, t) = \frac{\tan \phi'}{\tan \beta} + \frac{c' - \sigma^s(Z, t) \tan \phi'}{(\gamma_d + \gamma_w \cdot \theta(Z, t))Z \sin \beta \cos \beta}. \quad (6)$$

Equation (5) is then substituted into equation (6) to obtain a coupled analysis model for unsaturated infinite slope stability by the VG model. In equation (6), σ^s is the suction stress defined by Lu and Likos [29] and ψ is the matric suction; γ_d is the dry weight of soil, γ_w is the volumetric weight of water, c' and ϕ' are the effective cohesion and effective internal friction angle of soil, respectively, β is the angle of the slope, and Z is the soil depth.

3. Test Results

3.1. Slope Shallow Failure Mode and Process Analysis. Experimental observations reveal the shallow failure mode of the slope with a gradient of 60°. The typical failure process of the slope is test series 3 shown in Figure 9, which can be generally described as the following steps. Before rainfall started, the slope is stable (Figure 9(a)). With rainwater infiltrating into the slope, part of the slope changes from an unsaturated state to a saturated state at first. After 7 min 58 s of rainfall, the first local failure occurred at the upper right part of the slope (Figure 9(b)). The soil structure began to change accompanied by the water content and pore water pressure variation. Cracks occurred on the upper left part of the slope and fine particles migrated a lot at the surface (Figure 9(c)). Then, cracks extended and the first general failure occurred, leaving a scrape in the back edge of the failure (Figures 9(d) and 9(e)). After 18 min 57 s of rainfall, the second general failure occurred in the middle of the slope and the total area of failure enlarged (Figure 9(f)). Rainwater accumulated in gullies on the slope surface, and the runoff brought particles away (Figure 9(g)). The failure area continued to enlarge
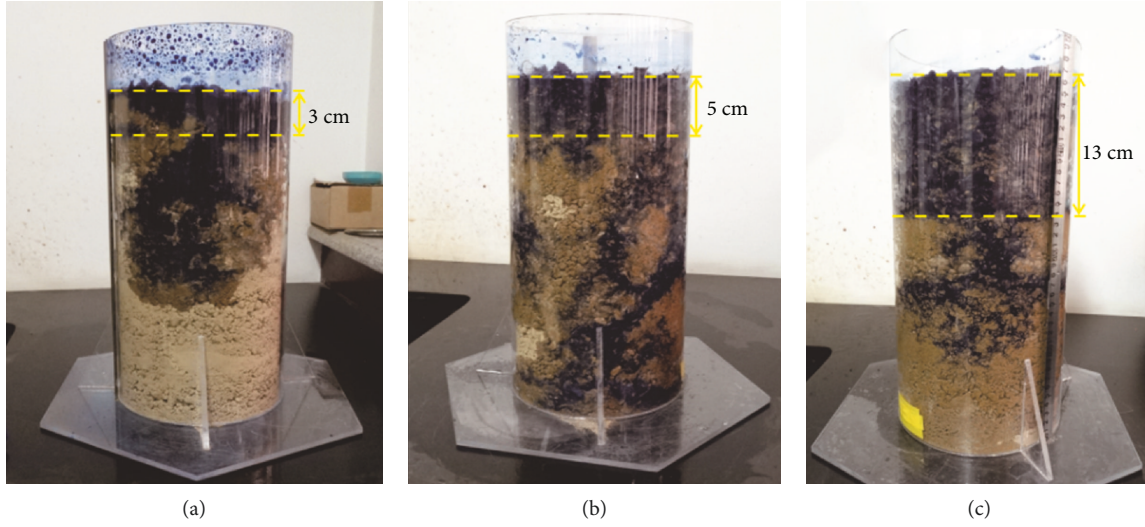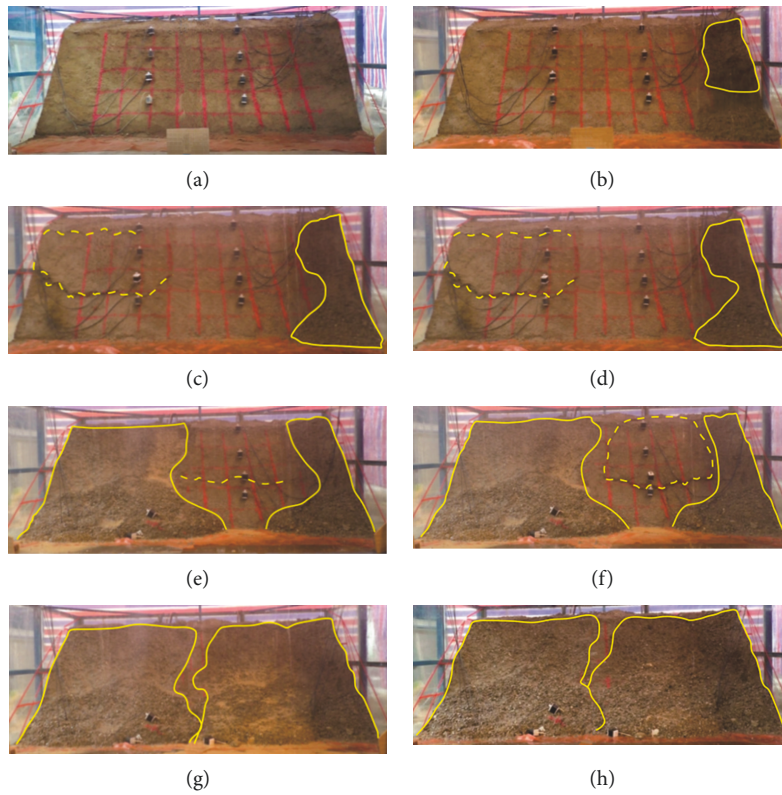
FIGURE 9: Slope failure process and phenomenon at time stages. Failure regions and cracks are outlined by yellow solid lines and dashed lines, respectively. (a) $t = 0$; (b) $t = 7$ min 58 s; (c) $t = 12$ min 45 s; (d) $t = 13$ min 05 s; (e) $t = 18$ min 19 s; (f) $t = 18$ min 57 s; (g) $t = 21$ min 25 s; (h) $t = 53$ min 00 s.

until fine particles were washed away. Finally, the slope tended to be stable and the failure area no longer enlarged (Figure 9(h)). The typical failure model of the slope with a gradient of 60°can be summarized as local failure expansion causes large-scale overall collapse.

3.2. Soil Moisture and Matric Suction Changes. The variations of matric suction and volumetric water content in test series 1-3 under rainfall intensities of 170 mm/h, 140 mm/h, and 110 mm/h are shown in Figure 10. The responses of volumetric water content and matric suction are used in this study to
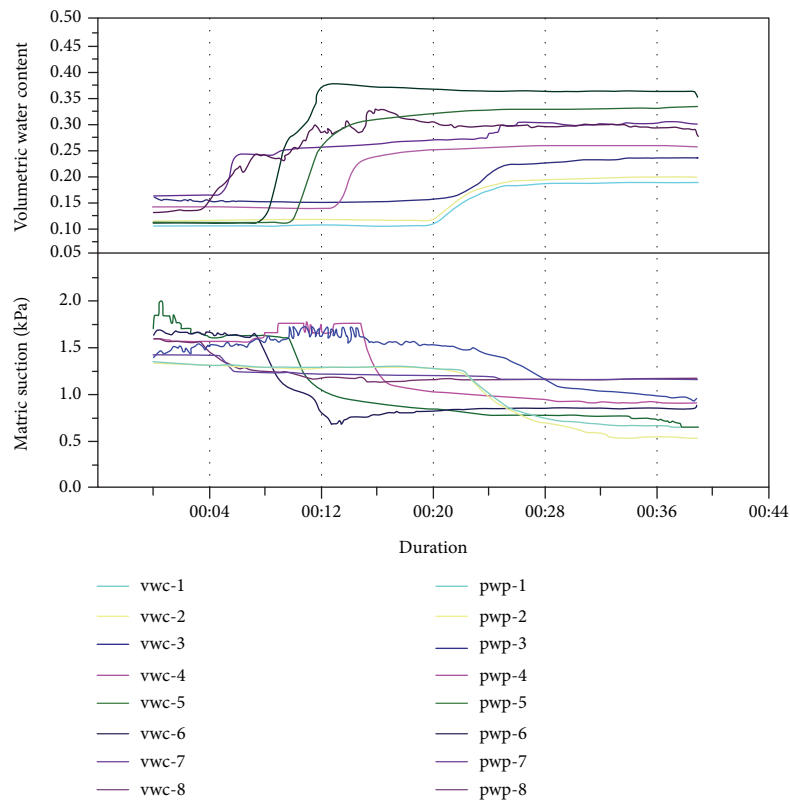
(a)
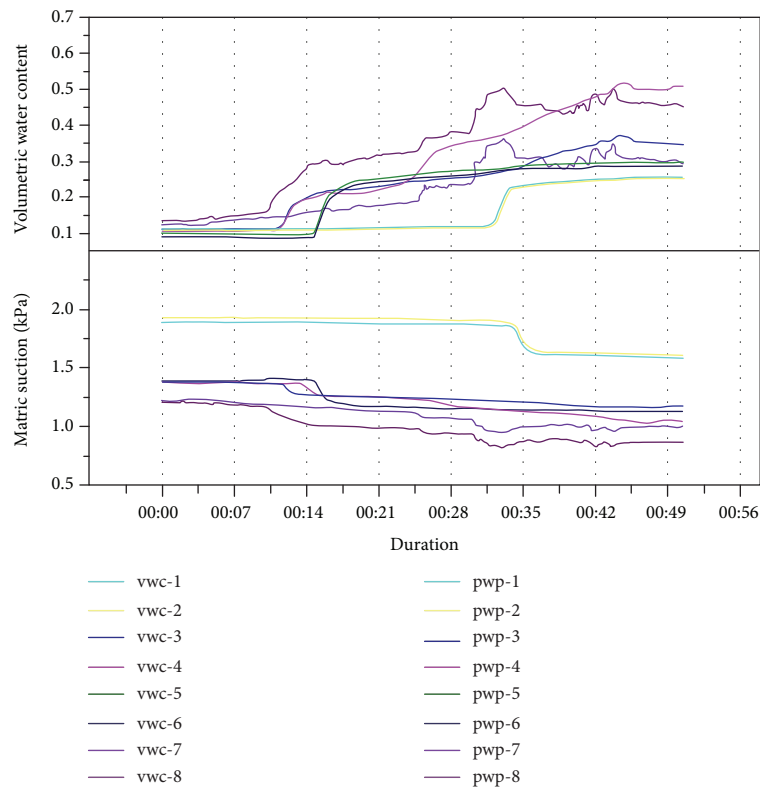
(b)

Figure 10: Continued.

(c)
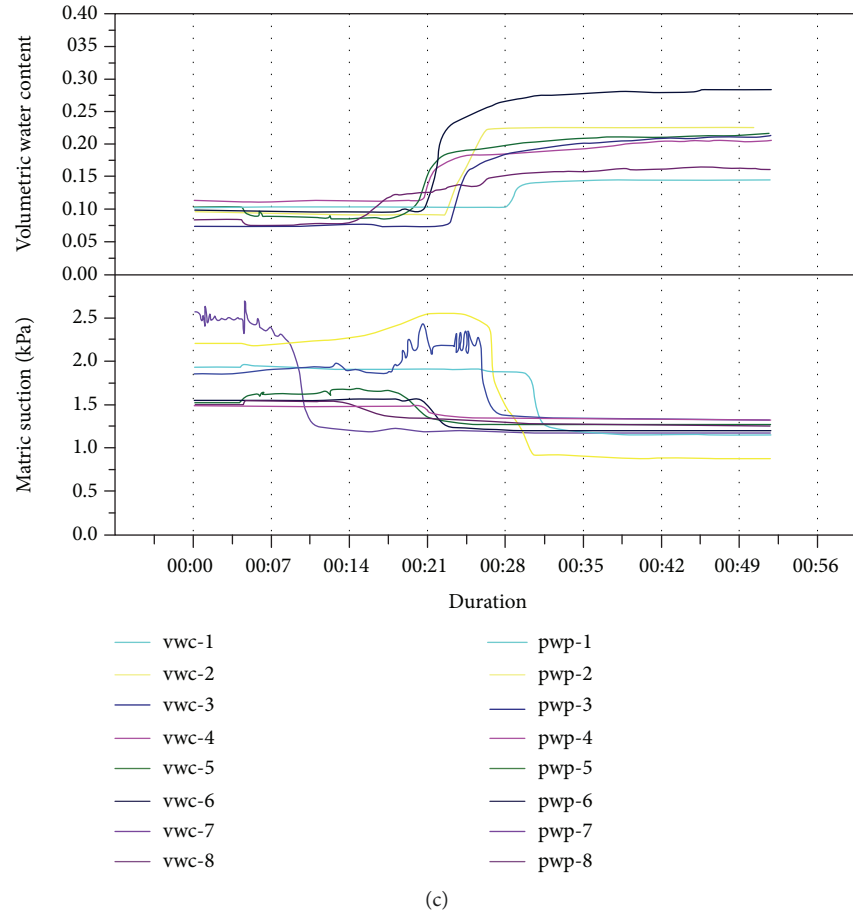
FIGURE 10: Matric suction and volumetric water content changes under different rainfall conditions: (a) test 1, $I = 170$ mm/h; (b) test 2, $I = 140$ mm/h; (c) test 3, $I = 110$ mm/h.

represent the roles of preferential flows and matrix flows. Due to the appearance of preferential flows, the volumetric water content rapidly increases and the soil moisture redistributes while the matric suction has not responded yet and therefore exhibits delay. The role of matrix flows is reflected in the reduction of matric suction caused by water infiltration in the soil matrix (capillary) and is observed as a delayed response of the matric suction compared to that of soil-water content. As shown in Figures 9(a)–9(c), the volumetric water content of the soil kept nearly constant at the beginning of rainfall in all tests. After 4-34 minutes of rainfall, the volumetric water content at each measuring point in the slope increased sharply by the sequence of soil layers. During this period, the rainwater infiltrated through large pores and fissures in longitudinal sections and it finally remained at 19.7%-48.4% and the matric suction decreased almost simultaneously after the volumetric water content increased. It is worth noting that the delay of matrix flow did not occur at soil depths of 25 cm and 50 cm, which indicated that both preferential flow and matrix flow formed almost simultaneously in shallow soil layers. Therefore, tests revealed that the seepage characteristics and processes of headward failure of the landslide deposits resulted from the interaction of a double-seepage field of coexisted preferential flow and matrix flow.

3.3. Soil-Water Characteristic Curve. Under heavy rainfall conditions, the preferential flow can rapidly flow through fractures and macropores causing rapid increases of water content and pore water pressure, thus affecting the infiltration process and the stability of the bank slope. To understand the influence of preferential flow on the stability of landslide deposits under different rainfall intensities, it is necessary to first establish the soil-water characteristic curve representing the impact of preferential flow. The soil-water characteristic curves described with the BC model and the VG model can be fitted with the measured matric suction and volumetric water content at different depths during the wetting process. Curve fitting is done in Origin software with its analysis and fitting module, in which user-defined functions can be created (e.g., BC model and VG model) and the fitting curve can be accomplished automatically according to the fitting data and the input expression. The fitting algorithm of Origin is based on a nonlinear least squares method, and fitting results and graphs can be exported when the fitting process is over. As shown in Figure 11, the VG model has higher goodness of fitting than the BC model and its correlation coefficient R^2 is larger than 0.9. In contrast, the BC model is less accurate in fitting SWCC ($R^2 < 0.75$). Therefore, the VG model can better fit the soil-water characteristic curve of coarse-textured gravelly soils

(a)

(b)

(c)

(d)
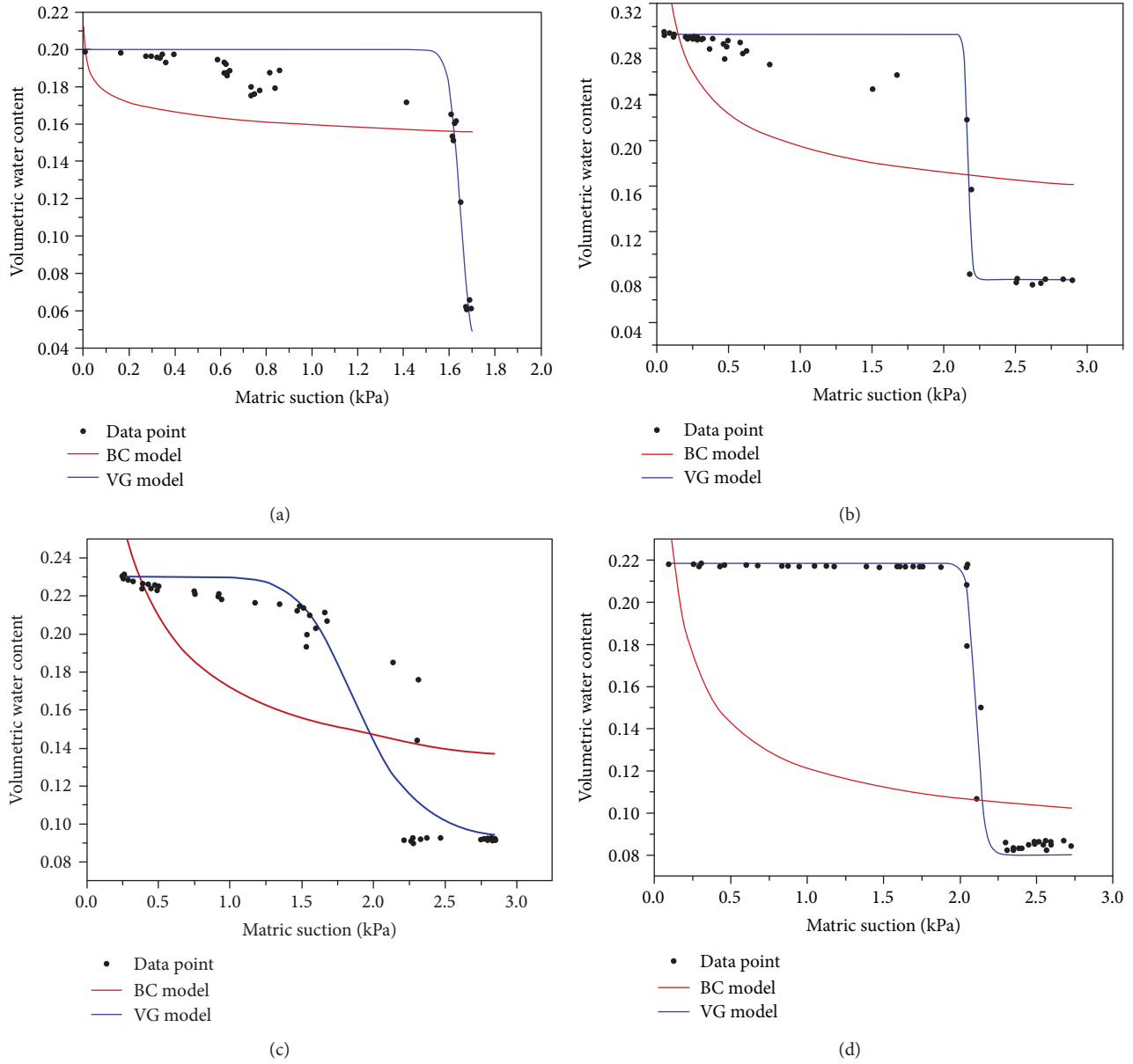
FIGURE 11: SWCC at different depths in test series 3: (a) $d = 25$ cm; (b) $d = 50$ cm; (c) $d = 75$ cm; (d) $d = 100$ cm.

TABLE 3: Fitting parameters for wetting process at different depths in test series 3.

Fitting model	Depth (cm)	α_{vg} (kPa^{-1})	n_{vg}	R^2
	25	0.6067	68.6838	0.9947
	50	0.4609	175.0497	0.9639
Van Genuchten	75	0.5369	9.2780	0.9261
	100	0.4749	77.3908	0.9765
	Depth (cm)	α_{bc} (kPa^{-1})	n_{bc}	R^2
Brooks-Corey	25	0.0081	0.0706	0.1766
	50	0.1326	0.3233	0.5256
	75	0.3656	0.5348	0.5291
	100	0.1314	0.5786	0.7244

under the impact of preferential flow. Fitting parameters are shown in Table 3. Because of model limitations, the fitting goodness of the BC model is low when moisture reaches a relatively high content and the advantage of the BC model is that it requires fewer parameters with a clear physical meaning. However, because the fitting curve of the BC model does not have inflection points, the result is a discontinuous fitting. As a consequence, the curve is less representative in fitting the high-water-content state (near saturation) or the quick response of preferential flow. Moreover, compared with silt and clay, it can be seen that coarse-textured gravelly soil has a lower matric suction [29, 44]. The air entry pressure under the VG model ranges from 1.4 to 2.2 kPa, which is relatively low. Due to the scarcity of fine particles and the large percentage of coarse particles (e.g., sand and gravel), a low air entry value was observed, which is similar to the results of a recent study by Yang et al. [11] on the soil-water characteristic curve of coarse-textured, gravelly soil of landslides in the Wenchuan earthquake area. In this study, the volumetric water content at which matric suction is near zero in the VG model was defined as the "relative saturated water content."

3.4. Stability Analysis. Stability of bank slopes is related to the gravity and the matric suction of the unsaturated soil. Under unsaturated conditions, the changes in water content caused by rainfall infiltration result in changes in the moisture and matric suction of the soil and thus greatly influence slope stability. Because rainfall-induced landslides occur under the influence of water infiltration, the wetting process is usually more important in describing the physical processes of slope failure. Meanwhile, the camera recorded the behaviour and timing of deformation during experiments and the surface tiltmeter was able to accurately capture the tilt angle changes of the soil at measuring points. By comparing the slope failure processes under different rainfall intensities with the rainfall duration, it was found that the surface inclination variations match with the failure stages observed.

The relationship between the surface inclination and the factor of safety (FS) calculated by the VG model during the infiltration process in all tests is shown in Figure 12. The FS calculated in tests is between 1.04 and 0.97, and a value below 1.0 indicates bank instability. In the case of rainfall intensities of 170 mm/h, 140 mm/h, and 110 mm/h, after 5 min 30 s, 11 min 51 s, and 13 min 51 s of rainfall, the first general failures occurred in test series 1, 2, and 3, respectively. The moment when the FS begins to drop coincides with that of the failure initiation, and they completely fail when FS drops to less than 1.0 at different depths except for TS1-FS-1, TS2-FS2, and TS4-FS4 in the test. The reason for the discrepancies between FS and inclination of TS1, TS2, and TS4 is that the embedded sensors at the same level may not detect the water content and matric suction changes because the wetting front in the slope has not yet reached the depth while shallow failure occurred on the surface. Meanwhile, the upper shallow slide on the slope also pushes the lower tilt sensors and causes its fall. The negative tilt angle means that the tipping direction of the sensor was the opposite of the defined positive direction.

Therefore, a change of the tilt angle from a negative value to a positive value shows that tilt meters tumbled during rapid sliding. After the deformation was complete, the tilt angle stabilized and remained unchanged thereafter. For example, under a rainfall intensity of 140 mm/h (Figure 12(b)), the tilt angles of the x-axis of TS1 and TS5 tilt meters began to change suddenly after 10 min 53 s of rainfall, corresponding to the first local failure on the right side of the model. Immediately following this, the x-axis tilt angles of TS4 and TS8 tilt meters change abruptly. The second general failure occurred on the left side of the slope at 11 min 15 s, and the tilt angles of the x-axis and y-axis stabilized after 13 minutes of rainfall. At this time, the tiltmeter was completely overturned and the tilt sensors were buried in the soil and no longer moving. Inclination changes recorded by the surface tilt meter indicate bank failure at the corresponding positions, which can be utilized as an early warning index and needs further study.

Combining Figures 10 and 12, it can be seen that the variation of the FS at different depths is related to the performance of matric suction and soil moisture. FS tends to be stable below 1.0 when matric suction bottoms out and the soil moisture reaches the highest point. Although the influence of matric suction on the factor of safety is very limited (maximum decrease of 0.07), this also implies that the matric suction, as a meaningful component of the effective stress of unsaturated soils, contributes to the stability of shallow rill banks to a certain extent. The soil mechanics parameters for the FS calculation are shown in Table 4.

3.5. Change in Particle Size Distribution. The seepage erosion causes changes in the soil pore structure, seepage field, and stress field and is one of the failure mechanisms in rainfall-induced landslides [45]. To study particle migration caused by rainfall infiltration, soil samples were taken at equal intervals and equal penetration depths (30 cm) at different locations along the same cross-section at 0 cm, 30 cm, and 60 cm (upper, middle, and lower sections, respectively) from the top surface of the bank after the experiment shown in Figure 13. Three samples were collected per section, and there were nine soil samples in total. In order to assess the average changes of particle migration in depth, samples from the same soil layer were mixed for particle analysis. The characteristic particle size changes of each soil layer under the rainfall intensity of 140 mm/h are shown in Figure 14. The effective diameter d_{10} of the upper, middle, and lower soil samples increased from 0.17 mm to 0.23 mm, 0.18 mm, and 0.19 mm, respectively. The continuous particle size d_{30} increased from 1.10 mm to 1.80 mm, 1.65 mm, and 1.45 mm, respectively. The limiting particle diameter d_{60} increased from 4.40 mm to 6.10 mm, 6.40 mm, and 6.00 mm, respectively. The increase in particle size of the upper, middle, and lower sections verifies the occurrence of fine-grained soil particle migration in the landslide deposits during rainfall infiltration (i.e., the occurrence of seepage erosion). Changes in the characteristic particle size can reflect the vertical migration of fine particles from top to bottom during rainfall infiltration. The d_{30} and d_{60} of the lower section are smaller than those of the middle and upper sections, indicating that the loss of fine particles in the lower section is less pronounced
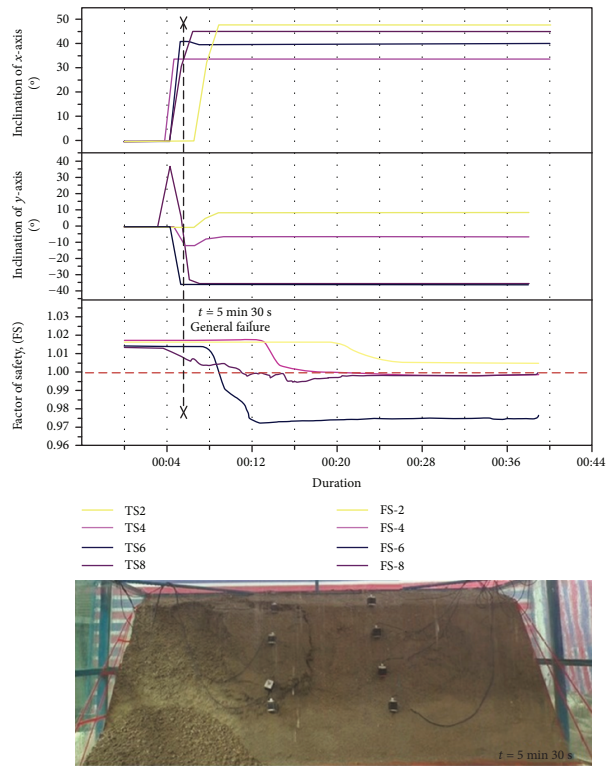
(a)
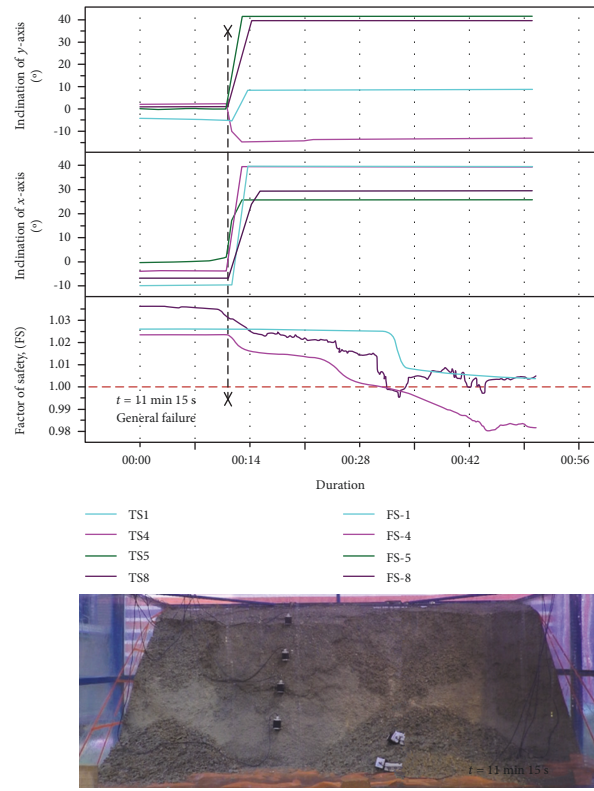
(b)

Figure 12: Continued.

(c)
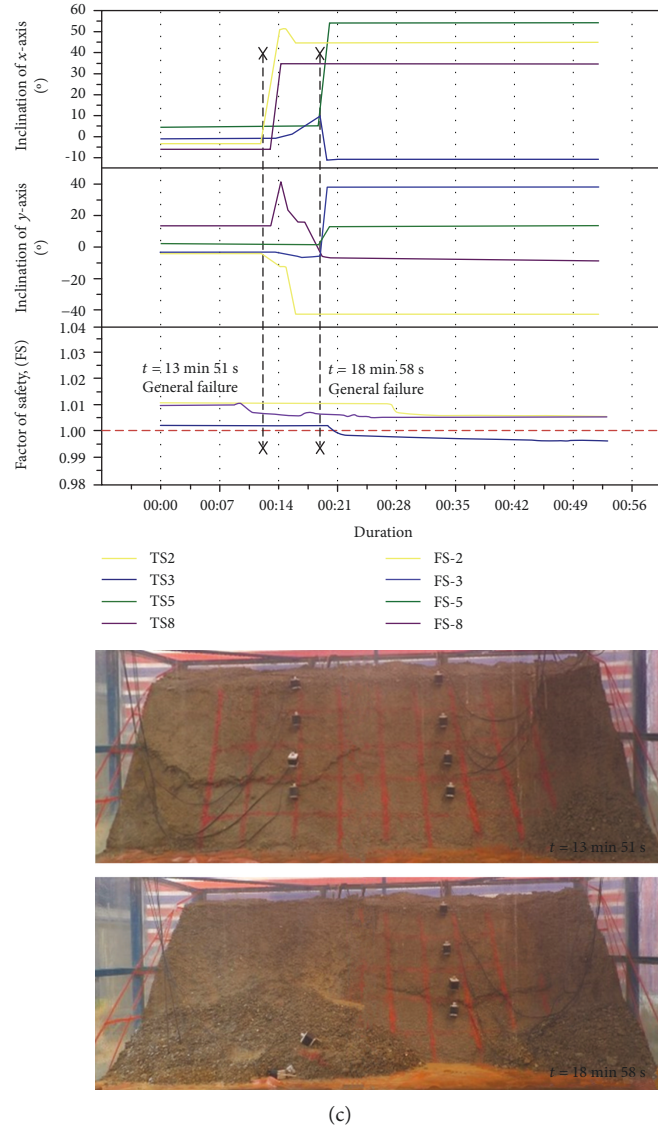
FIGURE 12: Relations between inclinations and the factor of safety during the wetting path in different tests and the video shots of general failure: (a) test series 1, $I = 170$ mm/h; (b) test series 2, $I = 140$ mm/h; (c) test series 3, $I = 110$ mm/h.

TABLE 4: Soil parameters for slope stability analysis.

Depth Z (cm)	Effective cohesion c' (kPa)	Effective friction angle ϕ' (°)	Natural unit weight γ_s (kN·m^{-3})	Slope angle β (°)
25	1.5	30	18	60
50	2.5	30	18	60
75	3.0	33	18	60
100	5.0	33	18	60

than that in the upper and middle sections. The particle gradation curves of the original soil sample and the soil sample from each layer are given in Figure 15. The cumulative percentage of particles by mass with a diameter of less than 1.0 mm in the upper, middle, and lower sections of the deposits decreased from 29.1% in the original soil sample to 25.7%, 26.6%, and 27.6%, respectively. The cumulative fraction of particles by mass with a diameter of less than 1.0 mm in the

lower soil sample is 1.9% and 1.0% greater than those in the upper and middle sections, respectively. This directly reflects the loss of fine particles in each layer of soil, where the proportion of coarse particles increases as the fine particles migrate.

Figure 16 demonstrates real-time rainfall intensity and cumulative rainfall in all tests. It can be seen that the amount of the cumulative rainfall in test series 1-3 are 101 mm, 118.2 mm, and 76 mm with the rainfall duration of 38

FIGURE 13: Sampling sites for particle migration analysis.
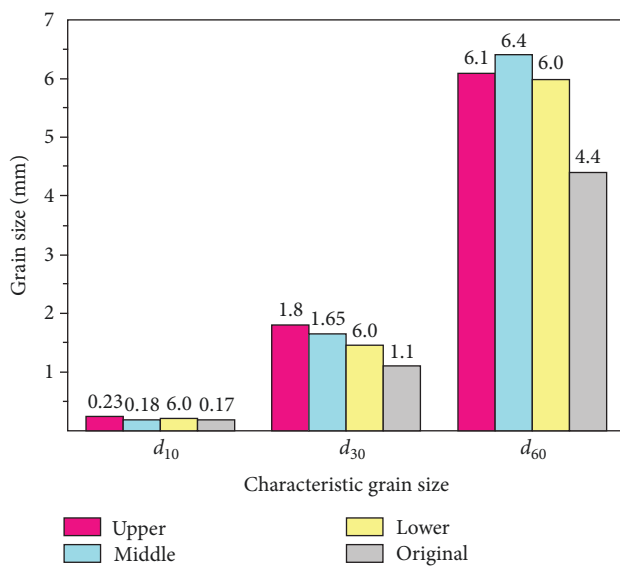
FIGURE 14: Characteristic particle size of soil samples at different depths in test series 2.

FIGURE 15: Grading curves for soil samples at different depths.

minutes, 50 minutes, and 53 minutes, respectively. After test series 2, a total dry weight of particles with a diameter being less than 1.0 mm of 4.579 kg was gained from the collected slurry. Under rainfall intensities of 170 mm/h and 110 mm/h, the final particles collected with a diameter being less than 1.0 mm had dry weights of 4.659 kg and 3.997 kg, respectively. Therefore, although the rainfall intensity decreases in test series 2 compared with test series 1, there is a considerable increase in the rainfall duration and this greater abundance of accumulated rainwater causes the fine particle to migrate more efficiently, suggesting that fine particle migration is positively correlated with both rainfall duration and cumulative rainfall.

4. Discussion

The variations of rainfall intensities in the experiment were not significant for all the tests except for the first 10 minutes of test 3; consequently, the cumulative rainfall showed approximately linear increases with time (Figure 16). With

the rainfall intensities of 170 mm/h, 140 mm/h, and 110 mm/h, the critical cumulative rainfall amounts at which the tilt meter detected an abrupt change were 15.82 mm, 25.63 mm, and 14.31 mm, respectively. The rainfall thresholds in test 3 did not rise with smaller rainfall intensity or longer rainfall duration compared with those in test 1, which can be explained by the slope infiltration theory proposed by Horton [46]. For an initially dry and well-drained soil layer, the infiltration capacity is relatively high at the beginning of rainfall, with vertical infiltration at a steady rate. Over time, the infiltration rate decreases by orders of magnitude and eventually converges upon a constant. On a sloped surface such as a rill bank, if the rainfall rate is greater than the water uptake capacity of the soil, the remaining water will flow along the ground surface (i.e., "excessive rainfall" results in surface runoff) [46]. The rainfall infiltration rate is usually much slower than that of the surface runoff. When rainfall exceeds soil absorption capacity, the runoff will form simultaneously along all banks of the basin or drainage basin. In test 1, the actual rainfall intensity is 162.6 mm/h (4.52×10^{-3} cm/s), which is about twice as large as that in test 3 (2.44×10^{-3} cm/s). However, the hydraulic conductivity of the soil in model tests is only 1.67×10^{-3} cm/s (shown in Table 2). Under the high-intensity rainfall of test 1, rainwater cannot infiltrate completely in time because rainfall intensity far exceeds the soil infiltration capacity, resulting in the runoff, which causes erosion on the slope surface and reduces the strength of the slope. Conversely, under the low-intensity rainfall of test 3, it approaches the infiltration capacity of the soil and the soil weight rapidly increases after the rainwater infiltration, resulting in the shallow failure.

The phenomenon of grain coarsening due to vertical migration of the fine particles was observed in the tests, which also has been mentioned in other pieces of research [8, 47–49]. In these researches, the displacement or mobility of soil with different gradings was modeled and observed. Results showed that the mobility of soil tended to be lowered with the decreasing of fine particles, suggesting that grain

(a)

(b)

(c)
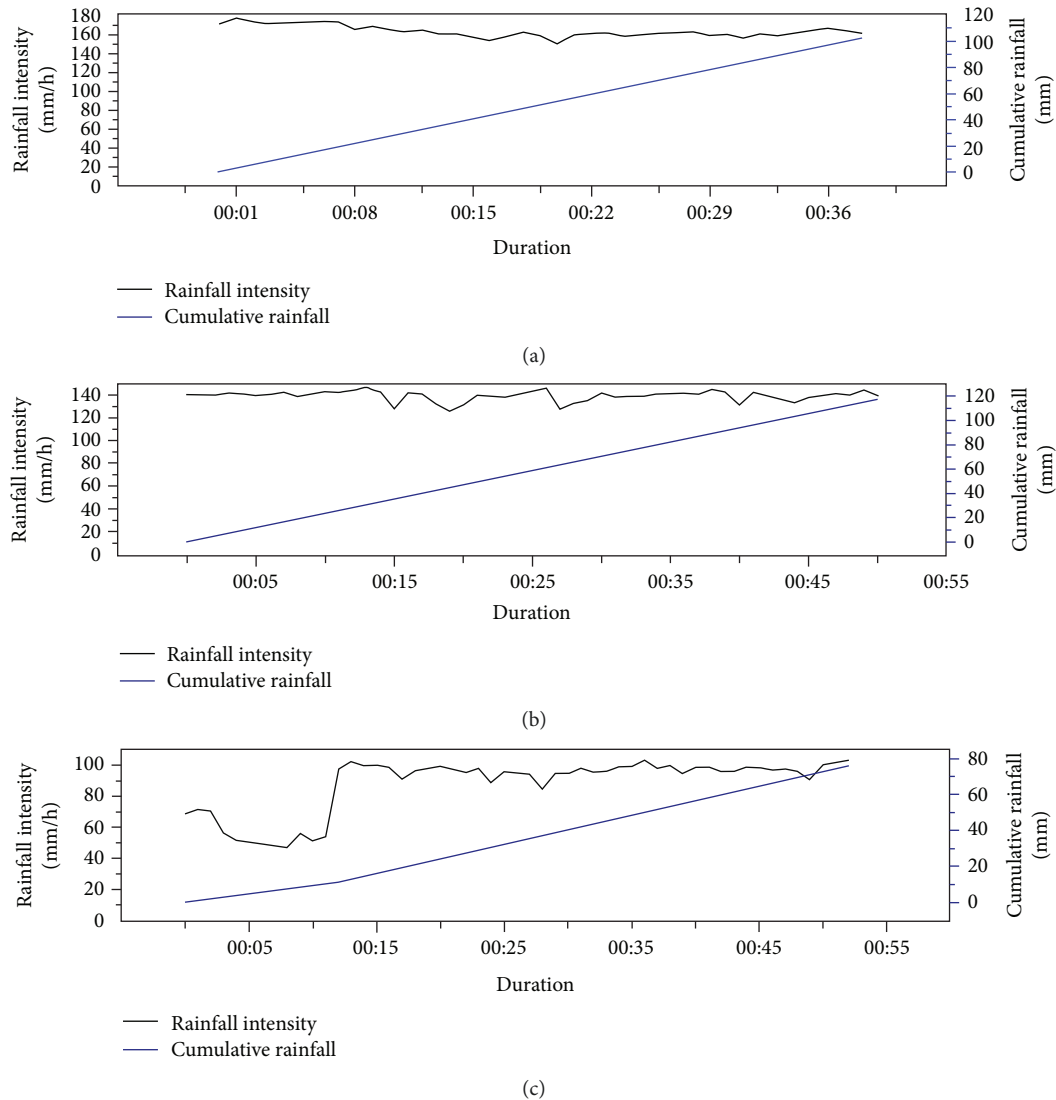
FIGURE 16: Real-time rainfall intensities and cumulative rainfall in (a) test series 1, (b) test series 2, and (c) test series 3.

coarsening improved the resistance of mass remobilization. Lei et al. [45, 50] pointed out that the relatively impermeable layer caused by fines blockage leads to the generation of positive excess pore pressure and initiates the slope failure. However, the pure erosion (i.e., absolute fines migration) generally increases the soil porosity and facilitates the rainfall infiltration, which advances the grain coarsening degree in soil. To some extent, the grain coarsening linked with pure erosion in soil is beneficial for slope stability and this phenomenon may be one of the reasons for explaining the geohazard mitigation and posteffect in earthquake regions.

5. Conclusions

This paper focuses on the phenomena in which earthquake-induced landslide deposits in the debris flow source region undergo rill erosion and failure under heavy rainfall conditions and are transformed into material sources for future debris flows after major earthquakes. The Yindongzi landslide in the Baisha River Basin, a typical meizoseismal area in the mountainous area of Sichuan province, southwestern China, was used as an example. A model test of shallow failures of rill banks was conducted indoors on a full-scale slope with a steep gradient under heavy rainfall conditions, using natural soils from the earthquake-induced landslide deposits. Rainfall infiltration characteristics were integrated with the hydromechanical coupling mechanism to investigate the evolution, outbreak, and propagation of rill bank failure under heavy rainfall. The conclusions are as follows:

(1) Through experimental observations, the typical failure model of the unsaturated gravelly soil slope with a gradient of 60° can be summarized as local failure expansion causes large-scale overall collapse. With rainwater infiltrating into the slope, part of the slope changes from an unsaturated state to a saturated state at first. Secondly, the soil structure begins to change. The soil moisture and pore water pressure vary

continuously and fine particles migrate both in the slope and at the surface. Then, soil strength reduces and failure initiates. The localized failure begins to occur and expands to large-scale, general slope failure later on, forming scarps at the back edge of the failure. Finally, the slope tends to be stable and the failure area no longer enlarges.

(2) The seepage characteristics of rainfall-induced slope failure in tests are the result of the interaction between preferential flow and matrix flow. The matrix flow is affected by matric suction, which shows a significant delay compared with the occurrence of preferential flow in soil layers of 75 cm and 100 cm in depth. The VG model provides a better fit to the soil-water characteristic curve, which reflects the dominance of preferential flow in coarse-textured gravelly soils ($R^2 \geq 0.9$). Tests reveal that coarse-textured gravelly soils have lower matric suction and air entry pressure values. Such soils exhibit unique properties because of their structural characteristics, namely, lower fine particle content, larger pore size, and wider particle size gradation when compared with clay and silt.

(3) Calculation results in FS show that the matric suction can contribute to the stability of shallow rill banks under unsaturated conditions. Sudden changes of the inclination captured by tiltmeters are well correlated with a reduction in the FS. Therefore, the inclination can be utilized as an index for early warning.

(4) The experiments verified the vertical migration of fine particles caused by rainfall infiltration. Statistics reveal that a significant increase in either rainfall duration or cumulative rainfall amount enables fine particle to migrate fully.

This study presents a new perspective on the formation mechanisms and the source transformation conditions of debris flows induced by rainfall after earthquakes. Further, it provides a framework for the development of early warnings for rainfall-induced landslides and debris flows during the postseismic period.

Data Availability

The data used to support the findings of this study are available from the corresponding author upon request.

Conflicts of Interest

The authors declare no conflict of interest.

Acknowledgments

References

[1] R. Huang and W. Li, "Post-earthquake landsliding and long-term impacts in the Wenchuan earthquake area, China," *Engineering Geology*, vol. 182, Part B, pp. 111–120, 2014.

[2] W. Yang, W. Qi, M. Wang, J. Zhang, and Y. Zhang, "Spatial and temporal analyses of post-seismic landslide changes near the epicentre of the Wenchuan earthquake," *Geomorphology*, vol. 276, pp. 8–15, 2017.

[3] C. Li, M. Wang, K. Liu, and J. Xie, "Topographic changes and their driving factors after 2008 Wenchuan earthquake," *Geomorphology*, vol. 311, pp. 27–36, 2018.

[4] C. Ma, Y. Wang, K. Hu, C. Du, and W. Yang, "Rainfall intensity–duration threshold and erosion competence of debris flows in four areas affected by the 2008 Wenchuan earthquake," *Geomorphology*, vol. 282, pp. 85–95, 2017.

[5] C. Tang, C. J. Van Westen, H. Tanyas, and V. G. Jetten, "Analysing post-earthquake landslide activity using multi-temporal landslide inventories near the epicentral area of the 2008 Wenchuan earthquake," *Natural Hazards and Earth System Sciences*, vol. 16, no. 12, pp. 2641–2655, 2016.

[6] S. Zhang, L. Zhang, S. Lacasse, and F. Nadim, "Evolution of mass movements near epicentre of Wenchuan earthquake, the first eight years," *Scientific Reports*, vol. 6, no. 1, article 36154, 2016.

[7] R. L. Fan, L. M. Zhang, H. J. Wang, and X. M. Fan, "Evolution of debris flow activities in Gaojiagou Ravine during 2008–2016 after the Wenchuan earthquake," *Engineering Geology*, vol. 235, pp. 1–10, 2018.

[8] S. Zhang and L. M. Zhang, "Impact of the 2008 Wenchuan earthquake in China on subsequent long-term debris flow activities in the epicentral area," *Geomorphology*, vol. 276, pp. 86–103, 2017.

[9] L. Wang, M. Chang, X. Dou, G. Ma, and C. Yang, "Analysis of river blocking induced by a debris flow," *Geofluids*, vol. 2017, Article ID 1268135, 8 pages, 2017.

[10] G. W. Lin, H. Chen, Y. H. Chen, and M. J. Horng, "Influence of typhoons and earthquakes on rainfall-induced landslides and suspended sediments discharge," *Engineering Geology*, vol. 97, no. 1-2, pp. 32–41, 2008.

[11] Z. Yang, J. Qiao, T. Uchimura, L. Wang, X. Lei, and D. Huang, "Unsaturated hydro-mechanical behaviour of rainfall-induced mass remobilization in post-earthquake landslides," *Engineering Geology*, vol. 222, pp. 102–110, 2017.

[12] Z. Yang, W. Shao, J. Qiao et al., "A multi-source early warning system of MEMs based wireless monitoring for rainfall-induced landslides," *Applied Sciences*, vol. 7, no. 12, article 1234, 2017.

[13] Z. Yang, H. Cai, W. Shao et al., "Clarifying the hydrological mechanisms and thresholds for rainfall-induced landslide: in situ monitoring of big data to unsaturated slope stability analysis," *Bulletin of Engineering Geology and the Environment*, vol. 78, no. 4, pp. 2139–2150, 2019.

[14] G. Wang and K. Sassa, "Factors affecting rainfall-induced flowslides in laboratory flume tests," *Géotechnique*, vol. 51, no. 7, pp. 587–599, 2001.

[15] L. Z. Wu, R. Q. Huang, Q. Xu, L. M. Zhang, and H. L. Li, "Analysis of physical testing of rainfall-induced soil slope failures," *Environmental Earth Sciences*, vol. 73, no. 12, pp. 8519–8531, 2015.

[16] R. M. Iverson, M. E. Reid, and R. G. LaHusen, "Debris-flow mobilization from landslides," *Annual Review of Earth and Planetary Sciences*, vol. 25, no. 1, pp. 85–138, 1997.

[17] Y. Okura, H. Kitahara, H. Ochiai, T. Sammori, and A. Kawanami, "Landslide fluidization process by flume experiments," *Engineering Geology*, vol. 66, no. 1-2, pp. 65–78, 2002.

[18] R. P. Orense, S. Shimoma, K. Maeda, and I. Towhata, "Instrumented model slope failure due to water seepage," *Journal of Natural Disaster Science*, vol. 26, no. 1, pp. 15–26, 2004.

[19] W. A. Take, M. D. Bolton, P. C. P. Wong, and F. J. Yeung, "Evaluation of landslide triggering mechanisms in model fill slopes," *Landslides*, vol. 1, no. 3, pp. 173–184, 2004.

[20] S. D. N. Lourenço, K. Sassa, and H. Fukuoka, "Failure process and hydrologic response of a two layer physical model: implications for rainfall-induced landslides," *Geomorphology*, vol. 73, no. 1-2, pp. 115–130, 2006.

[21] C. C. Huang, C. L. Lo, J. S. Jang, and L. K. Hwu, "Internal soil moisture response to rainfall-induced slope failures and debris discharge," *Engineering Geology*, vol. 101, no. 3-4, pp. 134–145, 2008.

[22] Y. S. Lee, C. Y. Cheuk, and M. D. Bolton, "Instability caused by a seepage impediment in layered fill slopes," *Canadian Geotechnical Journal*, vol. 45, no. 10, pp. 1410–1425, 2008.

[23] P. Cui, C. X. Guo, J. W. Zhou, M. H. Hao, and F. G. Xu, "The mechanisms behind shallow failures in slopes comprised of landslide deposits," *Engineering Geology*, vol. 180, pp. 34–44, 2014.

[24] W. Shao, Z. Yang, J. Ni, Y. Su, W. Nie, and X. Ma, "Comparison of single- and dual-permeability models in simulating the unsaturated hydro-mechanical behavior in a rainfall-triggered landslide," *Landslides*, vol. 15, no. 12, pp. 2449–2464, 2018.

[25] W. Shao, T. Bogaard, M. Bakker, and M. Berti, "The influence of preferential flow on pressure propagation and landslide triggering of the rocca pitigliana landslide," *Journal of Hydrology*, vol. 543, pp. 360–372, 2016.

[26] D. G. Fredlund, D. Sheng, and J. Zhao, "Estimation of soil suction from the soil-water characteristic curve," *Canadian Geotechnical Journal*, vol. 48, no. 2, pp. 186–198, 2011.

[27] N. Lu and J. W. Godt, *Hillslope Hydrology and Stability*, Cambridge University Press, New York, USA, 2013.

[28] D. G. Fredlund and H. Rahardjo, *Soil Mechanics for Unsaturated Soils*, John Wiley & Sons, Inc., Toronto, Canada, 1993.

[29] N. Lu and W. J. Likos, *Unsaturated Soil Mechanics*, John Wiley & Sons, Inc., New York, USA, 2004.

[30] D. V. Griffiths and N. Lu, "Unsaturated slope stability analysis with steady infiltration or evaporation using elasto-plastic finite elements," *International Journal for Numerical and Analytical Methods in Geomechanics*, vol. 29, no. 3, pp. 249–267, 2005.

[31] N. Lu and J. Godt, "Infinite slope stability under steady unsaturated seepage conditions," *Water Resources Research*, vol. 44, no. 11, 2008.

[32] R. I. Borja and J. A. White, "Continuum deformation and stability analyses of a steep hillside slope under rainfall infiltration," *Acta Geotechnica*, vol. 5, no. 1, pp. 1–14, 2010.

[33] G. Buscarnera and A. J. Whittle, "Constitutive modelling approach for evaluating the triggering of flow slides," *Canadian Geotechnical Journal*, vol. 49, no. 5, pp. 499–511, 2012.

[34] N. Lu, A. Wayllace, and S. Oh, "Infiltration-induced seasonally reactivated instability of a highway embankment near the Eisenhower Tunnel, Colorado, USA," *Engineering Geology*, vol. 162, pp. 22–32, 2013.

[35] S. Oh and N. Lu, "Slope stability analysis under unsaturated conditions: case studies of rainfall-induced failure of cut slopes," *Engineering Geology*, vol. 184, pp. 96–103, 2015.

[36] J. E. Christiansen, "Irrigation by sprinkler," *Agriculture Experimental Station Bulletin*, vol. 37, pp. 1–124, 1942.

[37] Ministry of Housing and Urban-Rural Development of the People's Republic of China, *GB/T 50085-2007 Technical Code for Sprinkler Engineering*, China Planning Press, Beijing, China, 2007.

[38] T. Uchimura, I. Towhata, T. T. Lan Anh et al., "Simple monitoring method for precaution of landslides watching tilting and water contents on slopes surface," *Landslides*, vol. 7, no. 3, pp. 351–357, 2010.

[39] W. Shao, Y. Su, Z. Yang, X. Ma, and J. Langhammer, "Quantify the pore water velocity distribution by a celerity function," *Geofluids*, vol. 2018, Article ID 1054730, 19 pages, 2018.

[40] G. W. Zhao, Y. J. Jiang, J. P. Qiao, H. J. Meng, and Z. J. Yang, "Experimental investigation of overtopping failure of landslide dams with different cmpactness conditions," *Chinese Journal of Rock Mechanics and Engineering*, vol. 37, no. 6, pp. 1496–1505, 2018.

[41] R. H. Brooks, *Hydraulic Properties of Porous Media*, McGill-Queen's University Press, 1964.

[42] M. T. van Genuchten, "A closed-form equation for predicting the hydraulic conductivity of unsaturated soils," *Soil Science Society of America Journal*, vol. 44, no. 5, pp. 892–898, 1980.

[43] R. L. Baum and J. W. Godt, "Correction to "estimating the timing and location of shallow rainfall-induced landslides using a model for transient, unsaturated infiltration"," *Journal of Geophysical Research: Earth Surface*, vol. 118, no. 3, pp. 1999–1999, 2013.

[44] E. C. Leong and H. Rahardjo, "Review of soil-water characteristic curve equations," *Journal of Geotechnical & Geoenvironmental Engineering*, vol. 123, no. 12, pp. 1106–1117, 1997.

[45] X. Lei, Z. Yang, S. He, E. Liu, H. Wong, and X. Li, "Numerical investigation of rainfall-induced fines migration and its influences on slope stability," *Acta Geotechnica*, vol. 12, no. 6, pp. 1431–1446, 2017.

[46] R. E. Horton, "The rôle of infiltration in the hydrologic cycle," *Transactions, American Geophysical Union*, vol. 14, no. 1, pp. 446–460, 1933.

[47] X. Fan, C. H. Juang, J. Wasowski et al., "What we have learned from the 2008 Wenchuan earthquake and its aftermath: a decade of research and challenges," *Engineering Geology*, vol. 241, pp. 25–32, 2018.

[48] W. Hu, G. Scaringi, Q. Xu, Z. Pei, T. W. J. Van Asch, and P. Y. Hicher, "Sensitivity of the initiation and runout of flowslides in loose granular deposits to the content of small particles: an insight from flume tests," *Engineering Geology*, vol. 231, pp. 34–44, 2017.

[49] G. Wang and K. Sassa, "Pore-pressure generation and movement of rainfall-induced landslides: effects of grain size and fine-particle content," *Engineering Geology*, vol. 69, no. 1-2, pp. 109–125, 2003.

[50] X. Q. Lei, Z. J. Yang, S. M. He, E. L. Liu, H. Wong, and X. P. Li, "Hydro-mechanical analysis of rainfall-induced fines migration process within unsaturated soils," *Journal of Mountain Science*, vol. 14, no. 12, pp. 2603–2619, 2017.

WILEY | Hindawi

Research Article

Hydrological Behavior of an Infiltration-Induced Landslide in Colorado, USA

Alexandra Wayllace [iD],[1] **Barbara Thunder,**[2] **Ning Lu,**[1] **Aziz Khan,**[3] **and Jonathan W. Godt** [iD][4]

[1]*Department of Civil and Environmental Engineering, Colorado School of Mines, Golden, CO 80401, USA*
[2]*Hart Crowser Inc., Seattle, WA 98121, USA*
[3]*Colorado Department of Transportation Research Branch, Denver, CO 80222, USA*
[4]*Landslide Hazards Program, U.S. Geological Survey, Denver, CO 80225, USA*

Correspondence should be addressed to Alexandra Wayllace; awayllac@mines.edu

Infiltration-induced landslides are common in mountainous and hilly areas of the world. When they occur near transportation corridors, they can impact public safety, impede transport of goods and people, and damage transportation infrastructure. This work presents a study of the hydrological behavior and its effects on the stability of an active landslide located on an embankment along Interstate-70 west of the Eisenhower Tunnel in central Colorado, USA. Groundwater dynamics were monitored for three years; two piezometers were installed near the head of the slide and one piezometer was placed near the toe. The hydrological observations at this site are unusual in that water table positions beneath the westbound shoulder of the highway (upslope) varied twice as much as water table positions beneath the eastbound shoulder (downslope), only 30 m distant horizontally. To better understand the factors controlling these observed differences, observations of the stratigraphy and the geomorphology of the watershed beyond the landslide body were incorporated into a conceptual model tested using numerical simulations of two-dimensional, variably saturated groundwater flow. Results from the numerical simulations calibrated against field measurements and a seasonally varying stability analysis of the site show that the large observed differences in the water table positions over the short horizontal distance are likely due to a combination of (1) the large size of the watershed that allows a significant amount of infiltration of snowmelt into the hillslope, (2) the contrast of hydrological properties of soils in the watershed, and (3) the changes in steepness of the dip of the bedrock below the slide. These three factors control the direction, speed, and amount of groundwater flow traveling through the slope. It is also shown that the seasonal hydrology of the site is a key factor in the stability of the slope, where most of the observed displacement occurs during the early summer season. Variations in the water table level within a year resulting from low snow years compared to variations from high snow years can be as much as 100%. Finally, it is important to consider the large contributing area of the watershed when evaluating the hillslope hydrologic conditions and remediation options.

1. Introduction

Infiltration-induced landslides are geological hazards that affect millions of people each year through property damage, remediation costs, and fatalities. Traditional slope stability analyses focus mostly on the mechanical behavior of the slope materials and typically use limiting equilibrium methods to calculate factors of safety. A number of studies have examined infiltration-induced landslides by combining analyses of the hydrological behavior of hillslopes with assessments of slope stability over large areas (e.g., [1–5]); although most of these studies recognize the critical importance of changing water movement and pressure transmission through unsaturated soil, they neglect the effect of the variably saturated hydrological behavior on effective stress and therefore on the soil strength. When water infiltrates into hillslopes, the water content in the hillslope and the water table (or phreatic surface) level vary accordingly. As

a consequence, matric suction, suction stress, total unit weight, and effective stress change throughout the hillslope, and thus, the stability of the slope is affected. Recently, several studies have combined hydromechanical process models with slope stability analyses to examine these consequences (e.g., [6–10]). However, accurate forewarning of landslide initiation remains a challenge and more information on specific case studies is valuable.

We describe a case study of an active landslide in Summit County, Colorado, along Interstate 70 (I-70) west of the Eisenhower/Johnson Memorial Tunnels (Figure 1). This section of highway is located near the continental divide surrounded by very steep terrain and is heavily traveled with an average daily traffic greater than 20,000 vehicles per day. Access to the landslide site with heavy equipment is limited, and the cost to permanently remedy the landslide situation is estimated to exceed $10 million; such a remedial fix would also require closing the highway for an extended period, which is not practical. Paving records indicate that the road surface has been displaced by more than 0.6 m in the previous two decades and repaired with as many as five pavement overlays a year to maintain a level road surface. Because of the importance of this part of I-70 to commercial and other travel, several efforts to obtain more site information and reduce pavement settlement have been undertaken over the years [9, 11]. In 2010, a systematic effort was initiated to obtain information on the landslide and assess the factors controlling its stability using a conceptual model of seasonally variably hydrology and hydromechanical framework of analysis [9]. As part of this effort, three piezometers and two inclinometers were installed to monitor groundwater fluctuations and deformation, respectively. The observations obtained from these instruments identified highly variable seasonal groundwater table fluctuations on the downstream side of the highway (9 to 12 m) whereas 30 m across the highway the groundwater table fluctuates seasonally only 4 to 5 m. Because changes in slope stability over seasonal timescales are driven by hydrologic variations, development of cost-effective mitigation strategies requires understanding hydrological behavior over a range of infiltration conditions. This work provides a conceptual model based on the morphology and stratigraphy of the site, the atmospheric conditions, and the main physical mechanisms in the hillslope, supported by field observations of displacement and groundwater variations. A series of numerical simulations based on the conceptual model and calibrated with field data are then used to assess slope stability.

2. Site Description and Instrumentation

The landslide is located on I-70 between mileposts 212.0 and 212.1, on the southern facing slope of the Williams Fork Mountains at 3,255 m above sea level in Summit County, Colorado (Figure 1). The slide area is approximately 175 m wide and 120 m long and mostly located south of I-70 where the highway embankment slopes about 31°. The underlying bedrock is predominantly composed of Proterozoic-age metasedimentary gneiss, schist, and pegmatite with intrusive granite bands; morainal deposits can be found on the surface

[12]. The bedrock is weathered up to 12 m thick in a saprolite layer, which is typically covered by 1 to 4 m thick colluvial deposits along valley walls. Presently, much of the area is forested although the bedrock is exposed at the surface in the steepest slope sections and along the cut slopes just north of I-70.

The stratigraphy of the site is a result of disturbance related to the construction of I-70 and the boring of the Eisenhower/Johnson Memorial Tunnels in the late 1960s. Sections of colluvium and layers of highly fractured rock were excavated, and tunnel cuttings were used as fill to construct the embankment for the road surface [13]. During the excavation process, multiple landslides were triggered on the slopes immediately north of I-70. The first slope movement at the study site was observed in 1973; since then, movements have been recorded nearly every year.

A series of subsurface investigations have been performed to assess groundwater and stability conditions at the site. In 1996, six boreholes were advanced and three inclinometers were installed by Kumar Associates; four additional boreholes were advanced in 2011 and 2015. During these later investigations, undisturbed material specimens were obtained and tested in the laboratory for hydrological and mechanical properties [14]. These investigations informed the development of a stratigraphic profile of the landslide site and the contributing watershed (Figure 2). On the slope north of I-70, very thin colluvial deposits less than 0.9 m thick at the surface are followed by a highly fractured rock layer extending to 12.2 m depth, below which more competent gneiss bedrock is present. The highly fractured layer consists of pebble to small boulder size black gneiss and some granite with chaotic fracturing in all directions. Most fractures are clean, but traces of yellowish clay are present on some fracture surfaces. In the highway portion, asphalt pavement is 0.076 m thick along the westbound shoulder but up to 0.76 m thick in the eastbound shoulder. Under the pavement, the highway embankment fill extends down to depths of 8.5 m and 9.8 m below ground surface (bgs) in the westbound and eastbound shoulders, respectively. This layer is composed mostly of tunnel cuttings and is a mix of gravel and scattered boulders in a brown, clayey sand matrix, with the presence of some organic material. Prior reports on the area refer to this layer as "tunnel muck." The highway embankment fill is underlain by a 0.9 to 1.5 m thick layer of highly decomposed black and grey gneiss cobbles 0.1 to 0.15 m in size with slickensided, clay-filled joints. Clay deposits 0.3 to 0.6 m thick are present in this layer beneath the eastbound shoulder, while much thinner clay layers are observed beneath the westbound shoulder. Below the decomposed gneiss, the bedrock is present at 12.2 m to 14.3 m bgs on the westbound shoulder and 23.7 m to 25.3 m bgs on the eastbound shoulder. We note that the dip of the bedrock surface is less steep beneath I-70 than it is upslope; the change in dip may be a natural bench in the bedrock slope or may have been excavated or blasted to accommodate the roadway. Near the toe of the slide, there are native colluvial and alluvial soils at the surface up to 4 m deep underlain by 0.9 to 1.2 m of moderately weathered black gneiss bedrock. Competent gneiss bedrock is encountered at 5.2 m bgs.
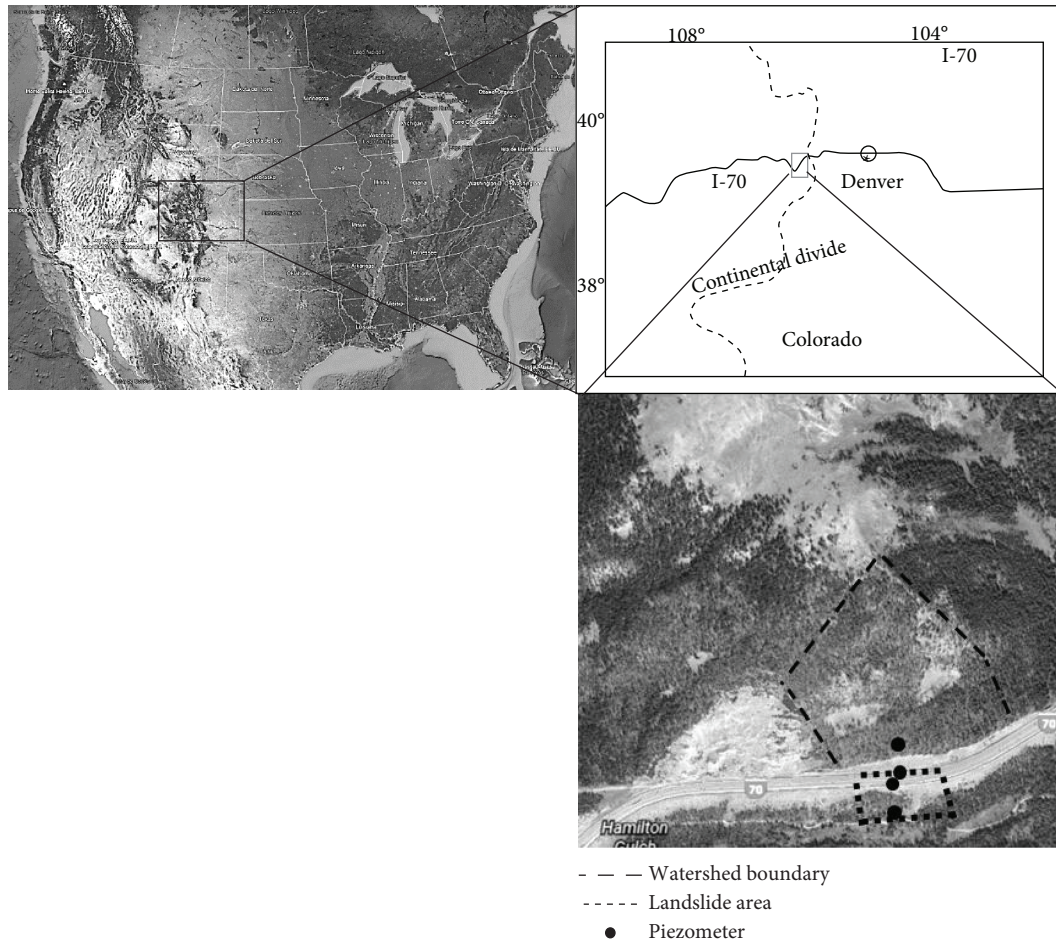
FIGURE 1: Site location with plan view of estimated watershed area, landslide area, and location of piezometers. Images obtained from Google Earth.

Undisturbed samples obtained from the boreholes advanced in 2011 and 2015 were tested to obtain hydrological and strength soil properties. The soil water retention curve (SWRC) and the hydraulic conductivity function (HCF) of two samples of the colluvium and the tunnel fill were measured in the laboratory using the Transient Water Retention and Imbibition Method [15] and modeled with the van Genuchten [16] and Mualem [17] models to obtain the residual moisture content θ_r, the saturated moisture content θ_s, and the van Genuchten parameters α and n. Direct shear tests of two samples at in situ moisture content were performed to obtain the effective cohesion and friction angle c' and ϕ' of the colluvium and the fill. In addition, three tension infiltrometer tests using a minidisk device from Meter Group (Any use of trade or firm names is for informational purposes only and does not imply endorsement by the U.S. Government.) were performed on the colluvium near the toe of the landslide to establish a range of in situ hydraulic conductivity while a slug test in the borehole north of I-70 provided an estimate of the saturated hydraulic conductivity (k_s) of the highly fractured gneiss. These values are reported in Table 1.

In 2009 and 2011, inclinometers were installed in the westbound shoulder, in the eastbound shoulder, and near the toe of the slide. From the inclinometer readings and field observation, the upslope part of the failure surface of the landslide likely daylights near the westbound shoulder of I-70 and runs along the contact between the decomposed gneiss and more competent bedrock [9]. Figure 3 is an example of inclinometer readings on the westbound and eastbound shoulders taken since 2012; the failure surface on the eastbound is at about 28 m bgs. Little horizontal displacement is measured at the westbound shoulder at the inclinometer location, indicating that the borehole does not intersect the failure surface. Inclinometer readings taken in 2008-2009 and displacement measured versus elapsed time are reported in Lu et al. [9].

In 2011 and 2012, three Geokon 4500S[1] vibrating-wire piezometers were installed to record groundwater table variations every 30 minutes. These sensors are located in the westbound shoulder at 17.37 m bgs (P1), in the eastbound shoulder at 33.53 m bgs (P3), and near the toe of the slide at 9.02 m bgs (P2) (Figure 2). All three piezometers were calibrated in the laboratory according to the manufacturer's instructions and installed in the field using bentonite as local hydraulic seal. The piezometer data obtained from 2011 to 2015 along with precipitation data is provided in Figure 4 and shows the seasonal variation of the water table positions
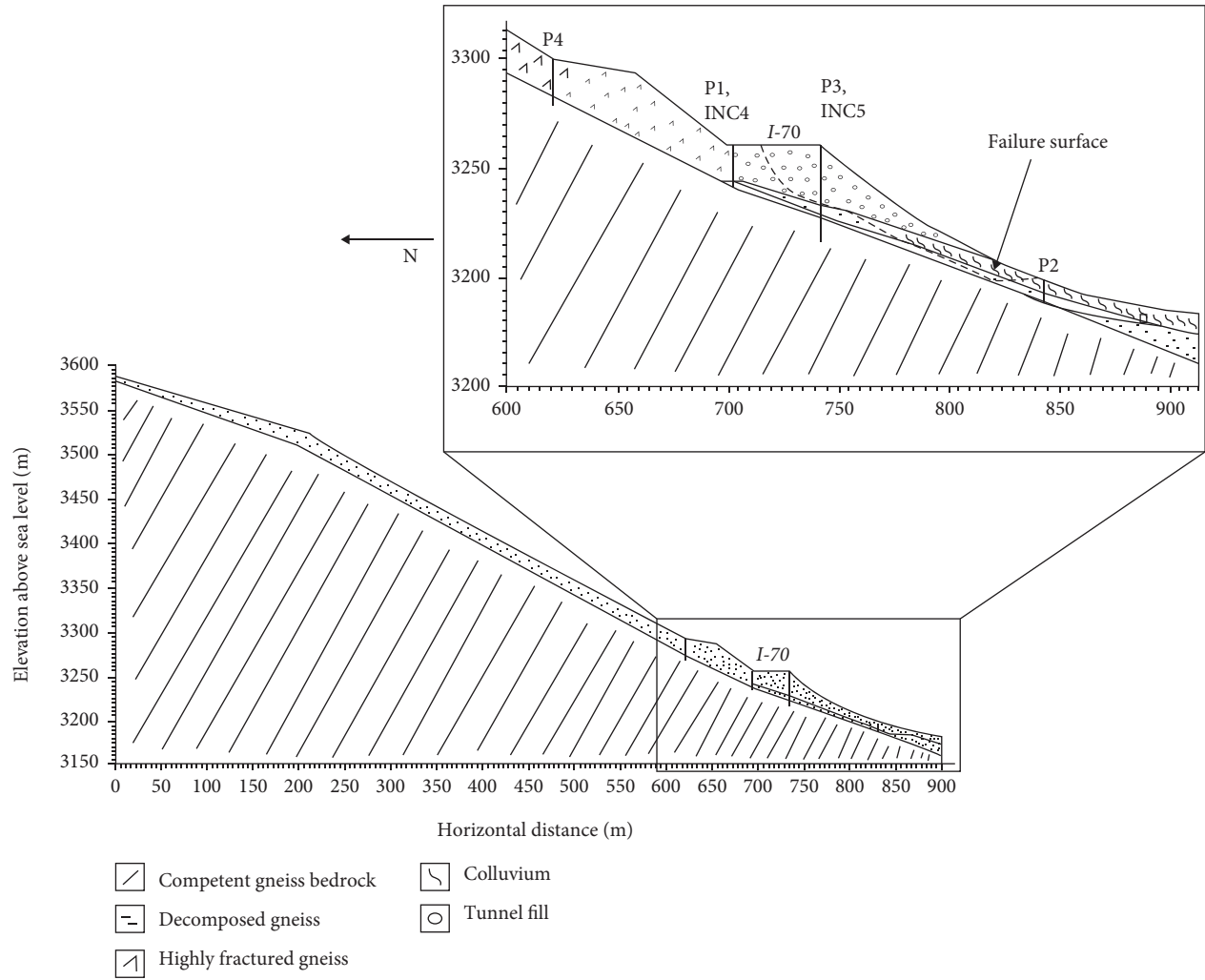
Figure 2: Geologic cross section of the study site.

Table 1: Material properties of soil layers.

Material	Hydrological properties					Strength properties		
	Residual moist. cont. θ_r	Saturated moist. cont. θ_s	Van Genuchten parameters α (m^{-1})	n	Sat. Hyd. conductivity k_s (m/day)	Effective cohesion c' (kPa)	Effective friction angle ϕ' (deg)	Unit weight γ (kN/m^3)
Pavement						0	32	25
Bedrock	0.06*	0.34*	1.374*	1.72*	0.001	95	34	23
Decomposed gneiss	0.065*	0.41*	7.5*	1.89*	1.06*	1	23	21
Highly fract. gneiss	0.06*	0.34	1.374*	1.72*	40	1	35	22
Colluvium	0.08	0.33	2.35	2.12	6	0	34	20
Tunnel fill	0.08	0.33	2.35	2.12	0.5	0	30	21

*Parameter obtained through numerical model calibration.

at the three locations. Depth to water table below ground surface was calculated by subtracting the measured pressure heads from the location of the sensor. Piezometer P1 located on the westbound shoulder shows a large and rapid response

to infiltration each spring when the water table rises 9 to 12 m in a period of 3 to 4 weeks; however, only 30 m across the highway, P3 located on the eastbound shoulder shows water table changes of only 4 to 5 m. These observations prompted
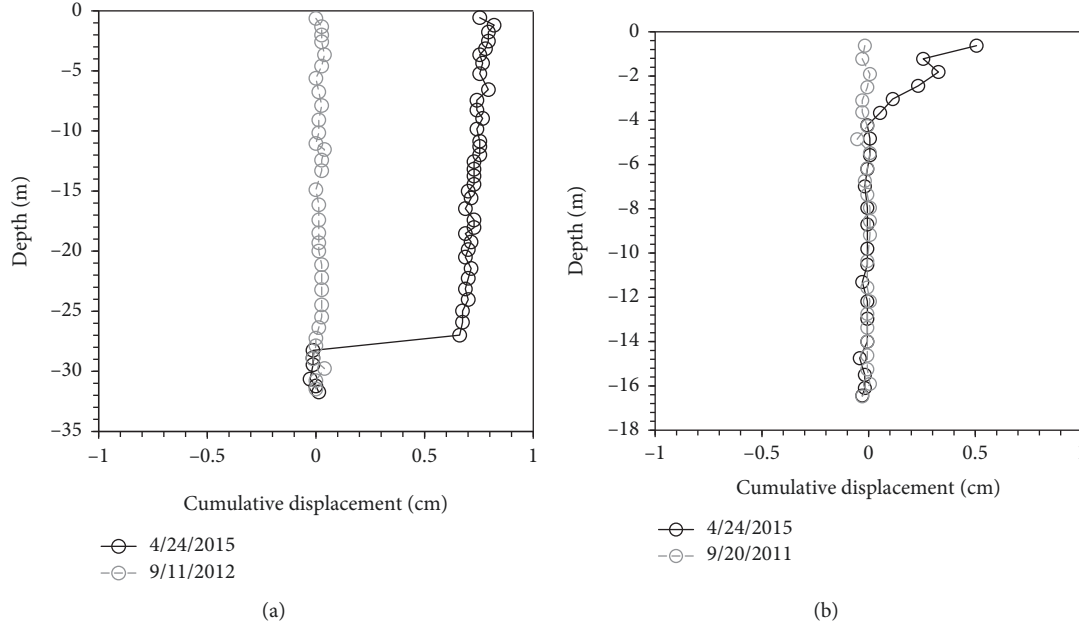
FIGURE 3: Example of inclinometer data from 2011-2015: (a) INC4 along the westbound shoulder and (b) INC5 along the eastbound shoulder (CDOT, 2015).

the consideration of the larger watershed in the hydrological analysis. Piezometer P2 is located near Straight Creek at the base of the valley, which controls the water table response to some degree and reduces the magnitude of response (1 to 2 m) in this location.

Precipitation data are obtained from a National Resources Conservation Service (NRCS) SNOTEL station at Grizzly Peak, located approximately 14 km southwest of the landslide site. Snowpack information is reported in terms of snow water equivalents (SWE), which represents the total height of a water column the snowpack would be reduced to if melted. Precipitation data include both snowfall and rainfall in the area. Because no long-term measurement of snowpack and rainfall is available for the watershed above the landslide, we instead rely on the Grizzly Peak SNOTEL data for daily atmospheric conditions. The Grizzly Peak station is located about 100 m higher in elevation in similar terrain on the same side of the continental divide with respect to the landslide site. However, the Grizzly Peak station is in a more heavily forested location. Less tree-cover and the highway corridor lead to greater solar and wind exposure at the landslide site, which presumably leads to an earlier and more rapid melting of the snowpack at the landslide site compared to Grizzly Peak.

3. Conceptual Hydromechanical Model

The following conceptual model is proposed based on the field characterization, measured groundwater table variations, and anecdotal reports of slide movement from personnel from the Colorado Department of Transportation (CDOT). It was evident that accurate analysis of the slope stability conditions required accounting for the larger watershed that contributes to the landslide site (Figure 1).

The material variations in the complex disturbed stratigraphy beneath the highway would also need to be considered in any conceptual model. The seasonal variation in infiltration and water table fluctuations can be described by four stages that generally coincide with the annual seasons. Schematic diagrams of the site profile at these four stages are provided in Figure 5 and an example of groundwater table variations at the piezometer locations is given in Figure 6.

Stage I. Winter: in December through the end of February, the water table is at its deepest position below the ground surface with minimal fluctuations. In general, the water table closely follows the contact between the competent bedrock and the weathered gneiss and is below the failure surface of the landslide. Typically, during this period, temperatures are below freezing, snow accumulates in the watershed, and there is negligible infiltration or evaporation. Depending on the year, snow depth can vary from 0.8 m to as much as 2.9 m with snow water equivalent values of 0.3 m to 0.8 m. Throughout this season and as a part of road maintenance, the Colorado Department of Transportation plows snow and packs it onto the westbound shoulder. The embankment is at its most stable condition and minimum displacements occur (Figure 5(a)).

Stage II. Early spring: with the warming temperatures in the early spring, the snowpack starts to melt. Due to the low moisture content of the soils near the surface, the hydraulic conductivity is relatively low, and meltwater enters the hillslope perpendicular to the slope surface [9]. In general, very little change in the groundwater level occurs during this stage, indicating that most of the infiltration does not yet reach the saturated zone. However, a small rise in the water

(a)

(b)

(c)
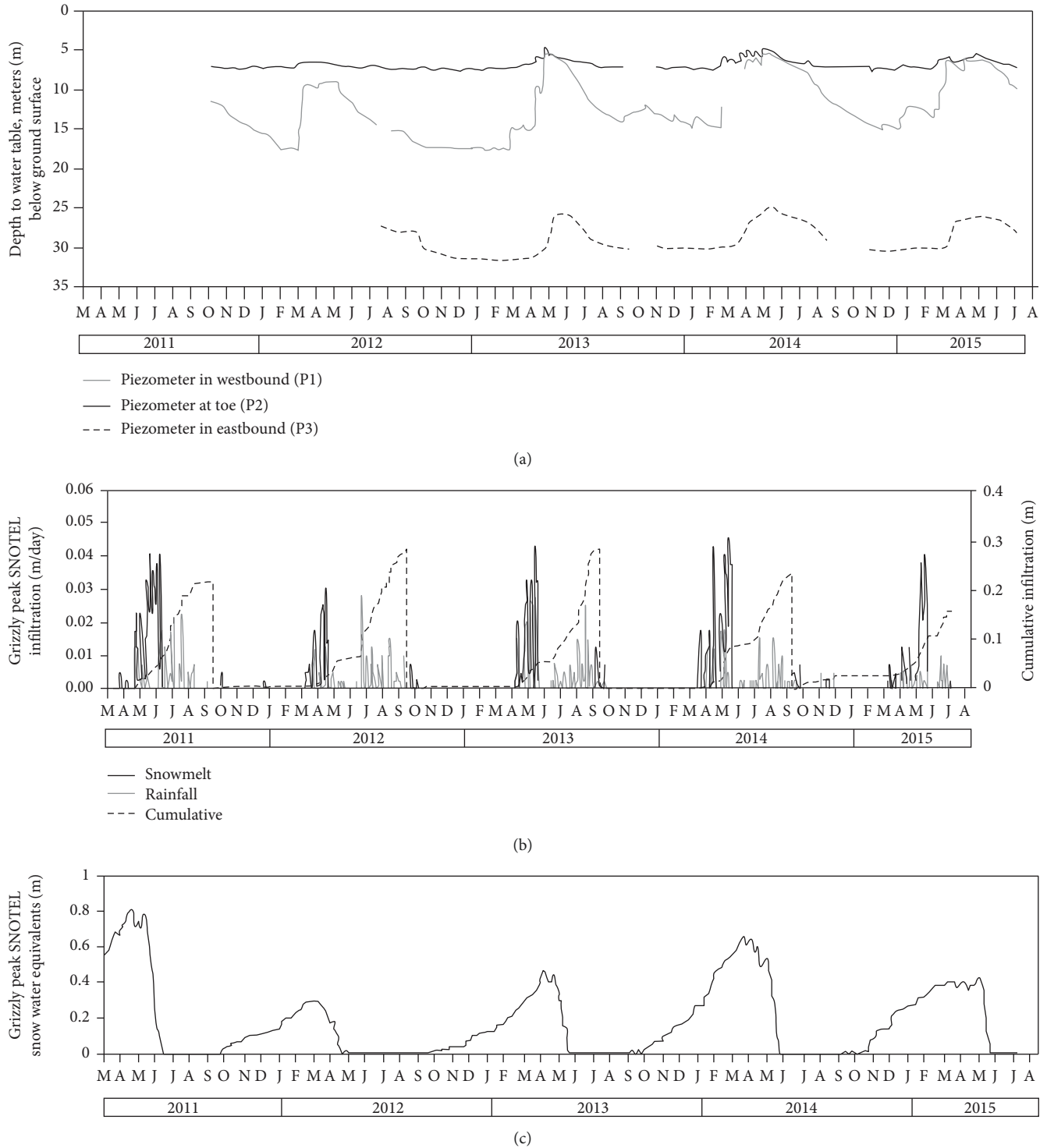
Figure 4: (a) Piezometer data, (b) infiltration data from Grizzly Peak, and (c) snow water equivalent data from Grizzly Peak.

table below the westbound shoulder occurs, likely due to the packed plowed snow melting along the shoulder. No water infiltrates through the highway surface because the snowfall is plowed off the road and the asphalt pavement is relatively impermeable. Since the water table stays mostly below the failure surface, minimum displacements occur (Figure 5(b)).

Stage III. Late spring and early summer: in April and May, snowmelt and occasional rainfall continue to infiltrate into the hillslope, now flowing faster through soils with greater moisture contents and therefore higher hydraulic conductivities. When the wetting front reaches the saturated zone near the bedrock boundary, the large contrast between the hydraulic conductivities of the highly fractured gneiss and
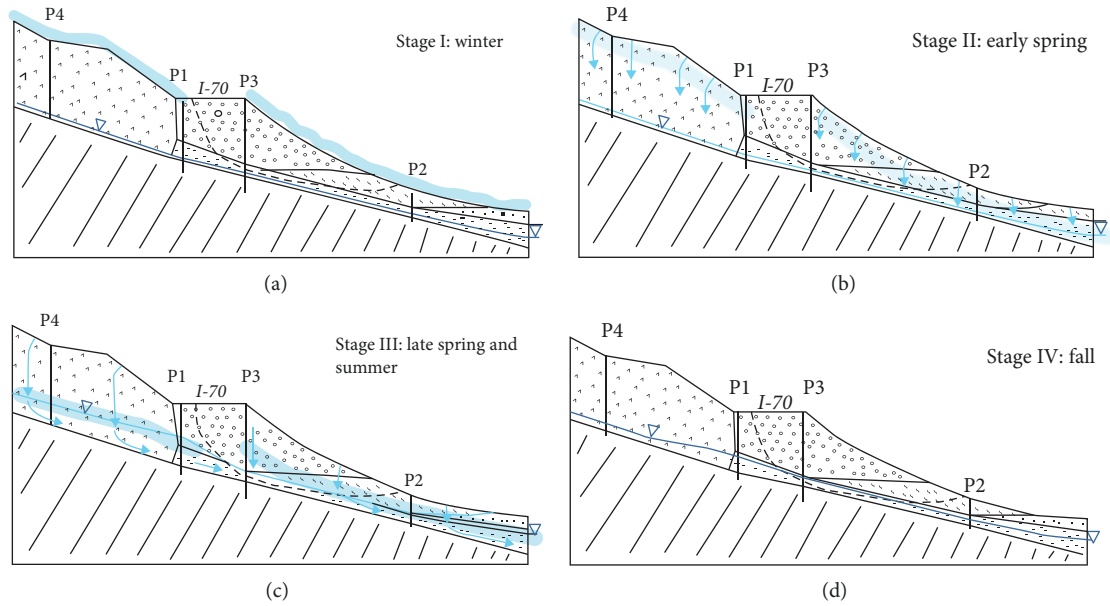
Figure 5: Conceptual model diagram. (a) Stage I (winter): snow accumulates, water table at its deepest position. (b) Stage II (early spring): snow starts melting, water table only rises slightly near westbound shoulder. (c) Stage III (late spring and summer): snow melts, water table level rises, and the landslide is active. (d) Stage IV (fall): water table drains.
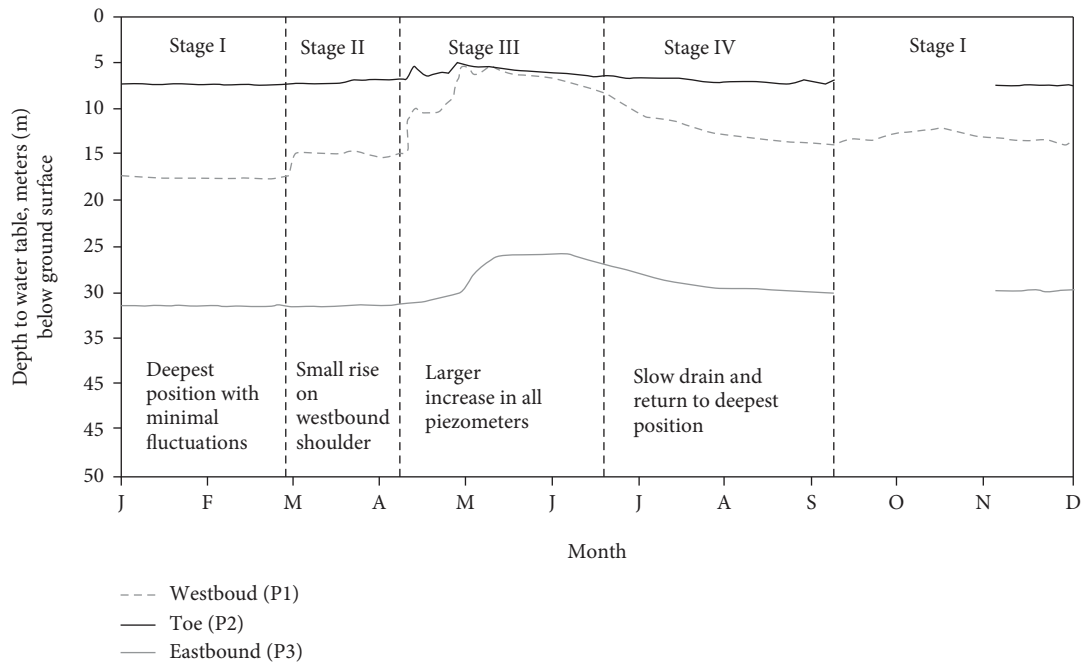
Figure 6: Water table variation for months in 2014 (January through December) showing four stages in conceptual model. Data was lost for P2 and P3 during the months of September and October.

the competent bedrock results in flow parallel to the bedrock interface [9]. In the northern part of the slope, the bedrock is steeply inclined, so large volumes of groundwater travel downslope swiftly. Once the fast-moving groundwater reaches the highway portion, two changes in the stratigraphy cause a backup of the groundwater flow: (1) the lower hydraulic conductivities of the fill and decomposed gneiss

and (2) the shallower bedrock dip. Consequently, a significant rise in water table elevation occurs along the westbound shoulder while 30 m across the highway the water level increases by only half as much. Additionally, the response in the eastbound shoulder is delayed by as much as 30 days from the initial response in the westbound. Further downslope, near the toe, groundwater flow encounters native
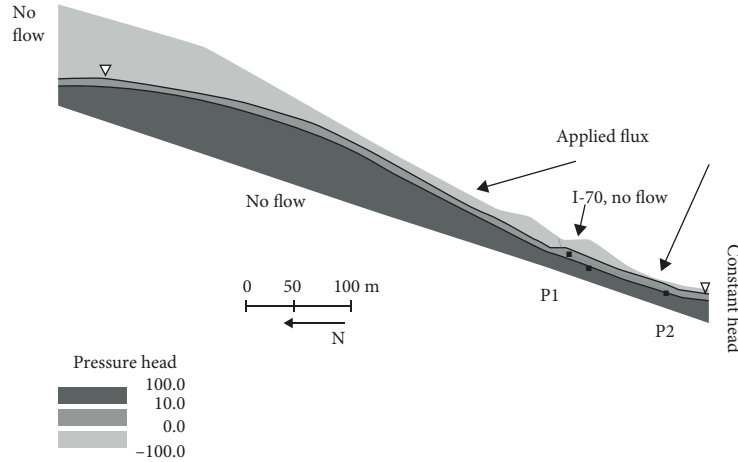
FIGURE 7: Numerical model domain: boundary conditions, initial conditions, and observation nodes.

colluvial and alluvial soils with higher hydraulic conductivities. The higher hydraulic conductivities, combined with the fact that the Straight Creek is about 90 m away, result in minimum fluctuations of the water table near the toe (Figure 5(c)).

Depending on the snow depth and temperature conditions, annual cumulative infiltration can range from 0.4 m to 1.2 m; during most years, snowmelt contributes about 80% of the infiltration. Due to the large infiltration, the water table rises above the failure surface which results in the reduction of effective stress and shear strength of the soils. At this point, the embankment is likely at its least stable condition and the landslide is reactivated.

Stage IV. Fall: during late summer and fall, rainfall is the only contributor to infiltration and is minimal compared to the snowmelt in earlier months. The groundwater drains downslope generally at a slower rate than its previous rise; eventually, the water table reaches a steady state condition at a position below the failure surface. In drier years, this steady state condition can be reached in 3 months whereas it may take more than five months in wetter years (Figure 5(d)). Since pore water pressures decrease, effective stresses and shear strength increase and minimum displacements are expected.

Expected changes in slope stability in this conceptual model roughly coincide with inclinometer readings taken in 2008-2009 by the Colorado Department of Transportation [9] and with multiple anecdotal reports from CDOT personnel about paving that stretch of the highway.

4. Numerical Model of the Site's Hydrological Behavior

4.1. Setup of Numerical Model. The conceptual model indicates that the hydrological behavior of the site has a decisive effect on the stability of the slope. With the change in water content and pore water pressures, suction stress changes; consequently, effective stresses are affected, and therefore, the stability of the slope varies. In order to quantify these

effects, a two-dimensional finite element numerical model that simulates the hydrology of the Straight Creek landslide was used based on the conceptual model to simulate the hydrological conditions of the site. The governing equation used for the transient unsaturated flow in the hillslope is Richards' equation [18]:

$$\nabla \cdot K(h)\nabla H + W = \frac{\partial \theta(h)}{\partial t}, \qquad (1)$$

where $K(h)$ is the hydraulic conductivity function (HFC), H is the total head, W is flux from a source or to a sink, and $\theta(h)$ is the soil water retention curve.

The numerical model was set up using the water flow module of the commercial software Hydrus-2D. Six hydrogeologic units comprise the domain which mimics the stratigraphy obtained during the field investigations and covers the area identified as the watershed contributing to the site (Figure 7). Hydrological and strength properties are reported in Table 1 and were obtained from laboratory testing, field measurements, and previous reports on the site. The numbers marked with a star were obtained as a part of the calibration of the numerical model. Initial conditions were reached by applying a constant infiltration of 0.001 m/day for several years so that a steady state was attained. The magnitude of the infiltration applied was chosen so that the resulting initial pressure head profile reflects the water table position observed in the field during the winter months (at its lowest position). A "no flow" boundary condition is applied on the north end to represent the extent of the watershed as no groundwater will enter or exit the system from this area; likewise, a "no flow" condition is also applied to the lower boundary of the domain, far enough into the bedrock to prohibit vertical seepage through the bedrock layer; a constant head boundary condition downslope (south side) so that the water table is held at 8 m bgs, representing the effects of Straight Creek about 90 m away from the toe of the slide; finally, variable flux is applied along the land surface with the exception of the highway portion which has a no flow boundary (Figure 7).

Applied fluxes for the land surface boundary condition (Figure 7) are based on atmospheric and precipitation data from the Grizzly Peak SNOTEL station. SWE data from 2011 to 2015 are provided in Figure 4(c); snow accumulates during the winter months; in the beginning of the spring, there are some days when the temperature is warmer than freezing producing a decrease in the snowpack and therefore some infiltration into the slope. Precipitation in the model includes both snowfall and rainfall and is presented in Figure 4(b); any negative change in SWE is interpreted as snowpack melting and assumed to directly infiltrate, any increase in cumulative precipitation when SWE is zero and temperatures are above freezing is assumed to also directly infiltrate. Finally, observation nodes P1, P2, and P3 were placed at locations coinciding with the piezometers in the field.

The model was calibrated using the piezometer data from year 2013. The variables in Table 1 marked with a star were used as adjusting parameters to obtain the smallest difference between measured and modeled groundwater table elevations. Additionally, the qualitative behavior of annual changes in groundwater elevation for the locations at the three piezometers was taken into account. This process was iterative; initial estimates for the inverse modeled variables were obtained from the Hydrus-2D soils bank and hydrologic parameters of only one soil material at a time were inverse modeled. Even though hydraulic conductivity values had been measured in situ for the colluvium and highly fractured gneiss, these variables were also inverse modeled within a narrow range because hydraulic conductivity is very sensitive to effects of scale and disturbance. Once the model was calibrated, data from years 2014 and 2015 were used to validate it.

A comparison of the observed and simulated groundwater table fluctuations is presented in Figure 8(a). Solid lines represent the data measured in the field while the dotted lines plot the data obtained with the numerical model. There are two main differences between simulated and observed water levels: (1) a lag in time between the measured and simulated increase in water table level; this may be the result of the fact that the location of the Grizzly Peak station is more forested than the landslide site, causing the later to experience faster and earlier infiltration, and (2) in the beginning of the spring, the field data show an increase of about 2 m in the water level measured by the westbound shoulder before the other sensors detect a change. This may be due to the fact that snow on that stretch of the highway is plowed into the westbound shoulder, so that at the end of the winter there is a tall compacted ice/snow block. When the temperature warms up, more water infiltrates close to the westbound shoulder than in the rest of the slope.

It is evident that infiltration occurs earlier in the study site than in Grizzly Peak; for example, in 2015, the monitored groundwater table increases before any SWE negative changes were measured in Grizzly Peak. Adjusting the timing of the infiltration by applying it three weeks earlier leads to a better comparison between the observed and simulated groundwater responses (Figure 8(b)). The observed seasonal changes in water table position are reflected in the numerical simulation with a large rise in the westbound shoulder location (P1), followed by a smaller rise in the eastbound shoulder location (P3) and minimal change near the toe of the slope (P2). Simulated results mirror the observed ratio between the rise of the water table in westbound (P1) and eastbound (P3) locations each year, which is roughly 2 : 1. For example, in 2015, the water table increased about 9 m beneath the westbound shoulder while it only changed 4.3 m beneath the eastbound shoulder.

4.2. Numerical Model Results. Once calibrated, the numerical model was used to (1) investigate in more detail the infiltration process in the site using particle tracking and looking at pressure head profiles, (2) perform a parametric analysis to predict groundwater table location for a dry year (precipitation is lower than average) and for a wet year (precipitation is higher than average), and (3) perform a slope stability analysis for the 4 stages in the conceptual model for a year with average precipitation.

Flow pathways created by particle tracking at five locations on the surface north of the highway confirm the contribution of the watershed to the groundwater in the site (Figure 9). On the north side of the highway, water infiltrates into the slope through the highly fractured gneiss; subsequently, most of the water flows downslope parallel to the interface with the competent bedrock eventually discharging at the creek. Water that infiltrates at points located further than 300 m in horizontal distance from the highway flows into the competent bedrock layer, which has a significantly lower hydraulic conductivity. Additionally, when the soils near the surface have low initial moisture content, their hydraulic conductivity could be as low as 0.01 m/day slowing down the initial water infiltration.

Pressure head transects in the study area provide an insight on the groundwater table location with respect to the failure surface. As an example, pressure head distributions of the slide area for the year 2015 are provided in Figure 10. The modeled groundwater table is marked as the interface between the dark grey and the medium dark grey contours. For comparison, the measured water table locations are plotted with a thick red dotted line. In addition, a white dotted line illustrates the position of the slide's failure surface. During the winter season (Stage I), the simulated water table rests along the competent bedrock boundary, below the failure surface; thus, the soil above the water table has negative pressure heads that mostly range between -5 m and 0 m although close to the surface there are areas with even lower pore water pressures. When the spring season begins (Stage II), water starts infiltrating into the hillslope and simulated pressure heads and moisture contents increase. The simulated water table underneath the westbound shoulder increases ~0.9 m in elevation, which is smaller than the ~2.5 m measured with the piezometer; this difference may be due to a combination of snow plowed into the westbound shoulder of the highway and working with precipitation data from Grizzly Peak which experiences later snowmelt infiltration than our site. In this stage, most of the

(a)

(b)
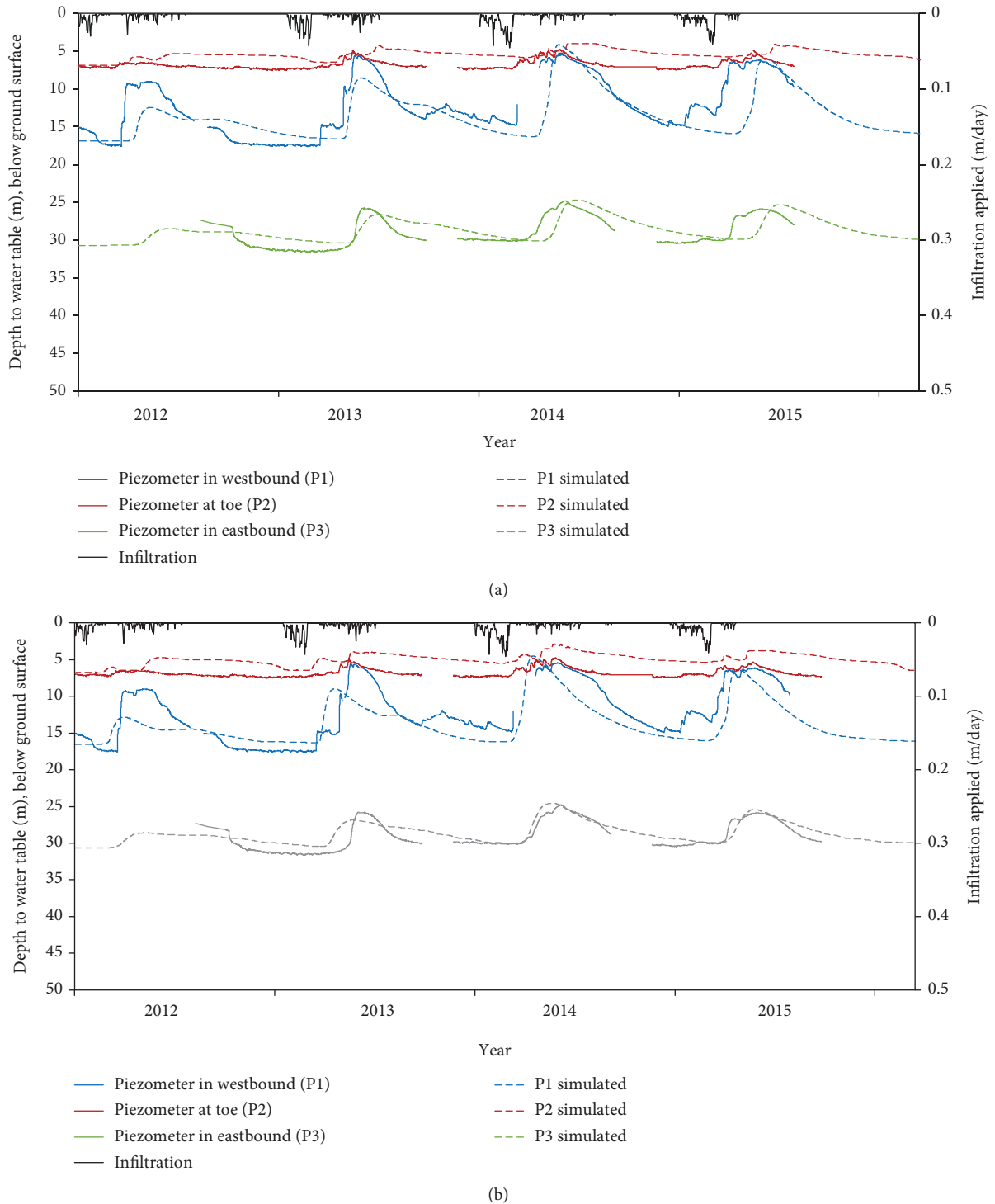
FIGURE 8: Comparison of groundwater table levels monitored in the field and simulated with numerical model: (a) with infiltration applied as reported at Grizzly Peak and (b) with infiltration applied three weeks earlier.

water infiltrating into the slope does not yet reach the water table, so aside from the area near the westbound shoulder, there are only small changes in the water table location. In the early summer (Stage III), the infiltration reaches the saturated zone and the simulated water table rises throughout the watershed. Both simulated results and measured data

indicate a 9 m rise in the groundwater table underneath the westbound shoulder. Likewise, about 30 m across the highway, a 4.6 m rise is both modeled and measured underneath the eastbound shoulder. In the fall (Stage IV), infiltration rates decline and the simulation shows a decrease in pressure head and moisture content near the surface and a
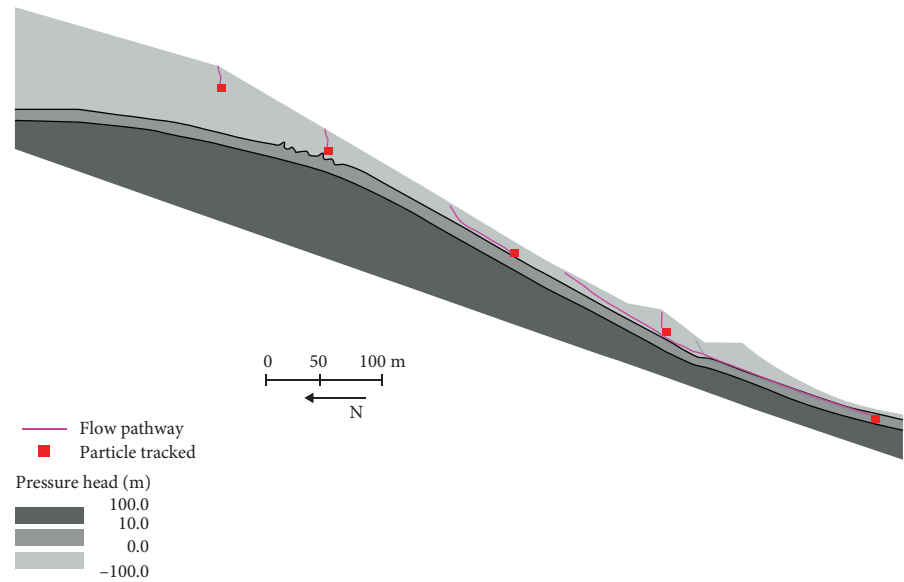
FIGURE 9: Flow pathways of one year created by particle tracking of five points in the slope north of I-70.
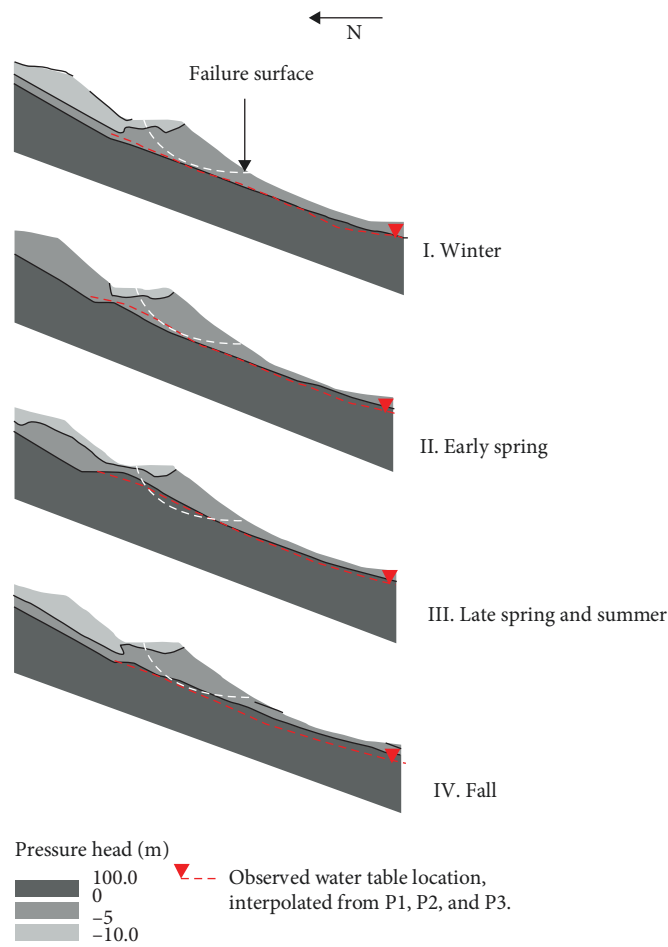
FIGURE 10: Simulated snapshots of pressure head transects near I-70 compared with measured water table during each conceptual model stage over the course of one average year. Winter transect taken at the lowest water table position, late spring and summer transect taken at peak values for water table position, and early spring and summer transect taken at average water table position values within the stage.

lowering of the water table throughout the watershed. The simulated water table drains earlier in the westbound location than the water table recession observed in the field, whereas a slight delay in draining is seen in the simulation near the eastbound location. Once again, we attribute this delay between observed and simulated changes in water table level to assuming atmospheric conditions that are similar to the study site, but not always exact. The numerical model qualitatively describes the behavior of the water table near the toe, but the simulated results show an overall water table about 2 m shallower than the field observations. This difference may be due to having a constant head boundary for the southern extent of the modeled watershed instead of a changing head with time; however, not enough information for meaningful time varying boundary conditions is available.

We evaluated groundwater conditions for two scenarios: (1) a "dry year" with a cumulative infiltration of 0.49 m, which is similar to 2002 and lower than the annual average of 0.58 m, and (2) a "wet year" with cumulative infiltration of 1.10 m, which is similar to 2011 and much larger than average. Both scenarios start with the same initial conditions. The changes in groundwater level at the locations of piezometers P1, P2, and P3 are provided in Figure 11; the thick lines plot data during a wet year while the thin dashed lines show variations during a dry year. In the winter season, the groundwater table is similar in both cases because no infiltration occurs during that time; however, the difference between annual minimum and maximum water table elevations between the wet and dry years is more than 100%. Beneath the westbound shoulder (P1), the water table changes by as much as 10.7 m in the wet year while the change is only 4.7 m in the dry year. In both scenarios, the variation of the water table underneath the eastbound shoulder is about half as much as in the westbound, with 5.2 m in the wet year and 1.84 m in the dry year. Near the toe, the water table changes 1.4 m in the wet year and 0.47 m in the dry year.

5. Slope Stability Analysis

The stability of the site was analyzed using an extended Bishop's method of slices, accounting for the effect of suction stress in the soil. Using water contents and pore water pressures obtained from the numerical model results, suction stresses can be calculated using the closed-form equations proposed by Lu and Likos [19, 20]:

$$\sigma^S = -(u_a - u_w), \quad u_a - u_w \leq 0,$$
$$\sigma^S = -(u_a - u_w)S_e, \quad u_a - u_w \geq 0,$$

(2)

where σ^S is the suction stress that is a characteristic function of saturation or matric suction, $(u_a - u_w)$ is the matric suction, and S_e is the equivalent degree of saturation. Effective stress for variably saturated porous materials is defined as [19]

$$\sigma' = \sigma - (u_a + \sigma^S)I,$$

(3)
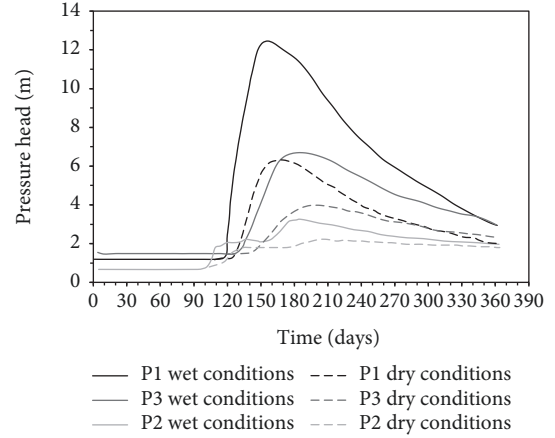
Figure 11: Pressure head variation at P1, P2, and P3 for a dry year (cumulative infiltration of 0.49 m) and a wet year (cumulative infiltration of 1.10 m). Initial conditions taken at January 1.

where σ is the total stress tensor, I is the second-order identity tensor, and u_a is the pore air pressure. The factor of safety using extended Bishop's method of slices was calculated using Lu and Godt [21] proposed equation:

$$FS_S = \sum_{n=1}^{m} \frac{\left(c' b_n + W_n \tan \Phi' - \sigma_n^S b_n \tan \Phi'\right)/\left(I\left(a_n, \Phi', FS_S\right)\right)}{\sum_{n=1}^{m} W_n \sin \alpha_n},$$
$$I = \cos \alpha_n + \frac{\tan \Phi'}{FS_S} \sin \alpha_n,$$

(4)

where c' and ϕ' are the effective cohesion and friction angle of the soil at the base of the slice, b_n is the width of the slice, W_n is the weight of the slice, and α_n is the angle of the slice with respect to the horizontal. A cross-sectional area with the sliding surface, material distribution, and slice discretization is provided in Figure 12. Four stability analyses corresponding to the groundwater table conditions in the four identified stages were performed. The results are consistent with the conceptual model; the factor of safety is larger in winter, when the water table is below the failure surface and suction stresses in the hillslope materials improve the stability of the embankment. As groundwater table rises, pore water pressures along the failure surface become positive and factor of safety decreases. During the beginning of summer, when the water table is at its peak, the factor of safety is smaller than 1, which signifies failure. During the rest of the year, the factor of safety ranges from 1.02 to 1.05, and therefore, little or no displacement is expected.

6. Summary and Conclusions

Infiltration-induced landslides are common geological hazards in the world, and their occurrence results in costly damages that sometimes claim lives; many of these landslides are triggered by a change in the hydrological conditions. This

Stage	Season	Factor of safety
I	Winter	1.05
II	Early spring	1.02
III	Spring and early summer	0.94
IV	Fall	1.03

Competent bedrock Decomposed bedrock
Highly fractured bedrock Alluvium
Tunnel fill Slices analyzed

FIGURE 12: Stability analysis using modified Bishop's method that accounts for suction stress. Center and radius of failure circle displayed.

paper presents a study of the hydrological behavior and its effects on slope stability of a seasonally active landslide on an embankment on Interstate-70 west of the Eisenhower Tunnel. Records indicate that more than 0.6 m of vertical displacement were measured in the past four decades. In addition, previous studies on the site identified the main physical mechanisms in the slope and quantified the importance of understanding the hydrological behavior in the site. Thus, three piezometers were installed near the crest and the toe of the landslide and groundwater table was monitored every 30 minutes for three years. The difference between annual minimum and maximum water table levels beneath the westbound shoulder is twice as much as the annual difference beneath the eastbound shoul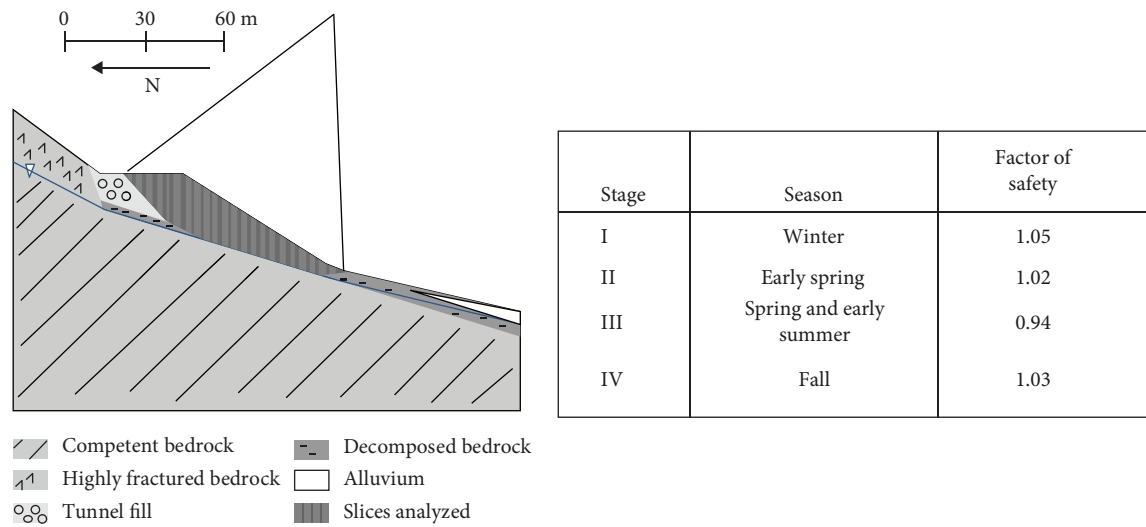der, only 30 m apart. During an average year, the water table beneath the westbound shoulder can rise about 9 m whereas it can rise 30 m across the highway, the water table underneath the eastbound shoulder rises half as much (about 4.6 m). The changes in water table level near the toe are smaller than 2 m. The objective of this work is to characterize this hydrological setting by developing (1) a sound conceptual model that captures the principal mechanisms in the site and (2) a numerical model that can produce results similar to the field measurements. Once calibrated, the hydrological numerical model is used to investigate in more detail the infiltration process in the site, to perform a parametric analysis to predict groundwater table locations for precipitations lower and higher than average conditions, and to perform a seasonally varying stability analysis on the site. The following conclusions can be drawn from these analyses.

(1) Detailed characterization of the subsurface soil layers, stratigraphy, and atmospheric conditions is needed to accurately simulate transient changes in hydrological responses that drive seasonal variations in slope instability. These factors must be defined throughout the entire watershed, not only the immediate landslide area but also the upslope area where

groundwater recharge takes place, to fully understand the hydrological conditions of the immediate landslide site

(2) The large difference in water table position cross a relatively small distance is due to a combination of three factors: (a) the large size of the watershed that allows a significant amount of infiltration into the uphill slope area, (b) the contrast of hydrological properties of soils in the watershed, especially saturated hydraulic conductivities around the area immediately beneath the highway, and (c) the changes in the steepness of the competent bedrock as it transitions from the northern slopes to the area underneath the highway. These factors control the direction, flux, and amount of excess groundwater flow traveling through the slope

(3) The numerical modeling results indicate that the difference between minimum and peak water table levels in the site can vary by more than a 100% depending on the seasonal hydrologic conditions. In both, a wet and a dry year, the larger changes occur underneath the westbound shoulder; in a dry year, the water table varies by ~4.7 m whereas in a wet year it can rise up to 10.7 m

(4) Pore water pressures near the failure surface change from negative in winter to positive in the beginning of the summer; consequently, suction stresses and therefore the factor of safety vary throughout the year. Using extended Bishop's method of slices for variably saturated soil, the factor of safety varies from 1.02 to 1.05 in winter, early spring, and fall but reduces to 0.939 (which indicates failure) in the beginning of the summer

(5) The numerical modeling results indicate that future remediation options should focus on minimizing the large water table rise north of I-70

Data Availability

The data used to support the findings of this study are included within the article.

Disclosure

The field characterization portion of this study was presented in the Eighth International Conference on Case Histories in Geotechnical Engineering Congress, Philadelphia, PA.

Conflicts of Interest

The authors declare that they have no conflicts of interest.

Acknowledgments

References

[1] N. Casagli, S. Dapporto, M. Ibsen, V. Tofani, and P. Vannocci, "Analysis of the landslide triggering mechanism during the storm of 20th–21st November 2000, in Northern Tuscany," *Landslides*, vol. 3, no. 1, pp. 13–21, 2005.

[2] G. B. Crosta and P. Frattini, "Distributed modelling of shallow landslides triggered by intense rainfall," *Natural Hazards and Earth System Sciences*, vol. 3, no. 1-2, pp. 81–93, 2003.

[3] R. M. Iverson, "Landslide triggering by rain infiltration," *Water Resources Research*, vol. 36, no. 7, pp. 1897–1910, 2000.

[4] H. Rahardjo, X. W. Li, D. G. Toll, and E. C. Leong, "The effect of antecedent rainfall on slope stability," *Geotechnical & Geological Engineering*, vol. 19, no. 3-4, pp. 371–399, 2001.

[5] T. Tsai, H. Chen, and J. Yang, "Numerical modeling of rainstorm-induced shallow landslides in saturated and unsaturated soils," *Environmental Geology*, vol. 55, no. 6, pp. 1269–1277, 2008.

[6] R. I. Borja and J. A. White, "Continuum deformation and stability analyses of a steep hillside slope under rainfall infiltration," *Acta Geotechnica*, vol. 5, no. 1, pp. 1–14, 2010.

[7] D. V. Griffiths and N. Lu, "Unsaturated slope stability analysis with steady infiltration or evaporation using elasto-plastic finite elements," *International Journal for Numerical and Analytical Methods in Geomechanics*, vol. 29, no. 3, pp. 249–267, 2005.

[8] N. Lu and J. W. Godt, "Infinite slope stability under unsaturated seepage conditions," *Water Resources Research*, vol. 44, article W11404, 2008.

[9] N. Lu, A. Wayllace, and S. Oh, "Infiltration-induced seasonally reactivated instability of a highway embankment near the Eisenhower Tunnel, Colorado, USA," *Engineering Geology*, vol. 162, pp. 22–32, 2013.

[10] F. Vahedifard, D. Leshchinsky, K. Mortezaei, and N. Lu, "Effective stress-based limit-equilibrium analysis for homogeneous unsaturated slopes," *International Journal of Geomechanics*, vol. 16, no. 6, article D4016003, 2016.

[11] A. Wayllace, N. Lu, S. Oh, and D. Thomas, "Perennial infiltration-induced instability of Interstate 70 embankment west of the Eisenhower/Johnson Memorial Tunnels," in *Geo-Congress 2012: State of the Art and Practice in Geotechnical Engineering*, pp. 497–506, Oakland, CA, USA, March 2012.

[12] T. S. Lovering, *Geology and Ore Deposits of the Montezuma Quadrangle*, vol. 178, US Govt. Print. Off, Colorado, 1935.

[13] Robinson & Associates, *The Geologic Investigation of the Straight Creek Landslides*, Colorado Department of Highways, Denver, CO, USA, 1971.

[14] B. Thunder, *The Hydromechanical Analysis of an Infiltration-Induced Landslide Along I-70 in Summit County, CO, [M.S. Thesis]*, Colorado School of Mines, Golden, CO, USA, 2016.

[15] A. Wayllace and N. Lu, "A transient water release and imbibitions method for rapidly measuring wetting and drying soil water retention and hydraulic conductivity functions," *Geotechnical Testing Journal*, vol. 35, no. 1, pp. 103–117, 2012.

[16] M. T. van Genuchten, "A closed form equation for predicting the hydraulic conductivity of unsaturated soils," *Soil Science Society of American Journal*, vol. 44, no. 5, pp. 892–898, 1980.

[17] Y. Mualem, "A new model for predicting the hydraulic conductivity of unsaturated porous media," *Water Resources Research*, vol. 12, no. 3, pp. 513–522, 1976.

[18] L. A. Richards, "Capillary conduction of liquids through porous mediums," *Journal of Applied Physics*, vol. 1, no. 5, pp. 318–333, 1931.

[19] N. Lu and W. J. Likos, *Unsaturated Soil Mechanics*, John Wiley and Sons, New York, NY, USA, 2004.

[20] N. Lu and W. J. Likos, "Suction stress characteristic curve for unsaturated soil," *Journal of Geotechnical and Geoenvironmental Engineering*, vol. 132, no. 2, pp. 131–142, 2006.

[21] N. Lu and J. Godt, *Hillslope Hydrology and Stability*, John Wiley and Sons, New York, NY, USA, 2012.

WILEY | Hindawi

Research Article

The Role of Initial Soil Conditions in Shallow Landslide Triggering: Insights from Physically Based Approaches

L. Schilirò [iD], G. Poueme Djueyep, C. Esposito, and G. Scarascia Mugnozza

Department of Earth Sciences and Research Center for the Geological Risks (CERI), "Sapienza" University of Rome, Piazzale Aldo Moro 5, 00185 Rome, Italy

Correspondence should be addressed to L. Schilirò; luca.schiliro@uniroma1.it

In the last years, the shallow landslide phenomenon has increasingly been investigated through physically based models, which try to extend over large-area simplified slope stability analyses using physical and mechanical parameters of the involved material. However, the parameterization of such models is usually challenging even at the slope scale, due to the numerous parameters involved in the failure mechanism. In particular, considering the scale of the phenomenon, the role of transient hydrology is essential. For this reason, in this work we present the outcome of different experimental tests conducted on a soil slope model with a sloping flume. The tested material was sampled on Monte Mario Hill (Rome, Central Italy), an area which has been frequently affected by rainfall-induced landslide events in the past. In this respect, we also performed a physically based numerical analysis at the field conditions, in order to evaluate the response of the terrain to a recent extreme rainfall event. The results of the flume tests show that, for the same material, two different triggering mechanisms (i.e., uprise of a temporary water table and advance of the wetting front) occur by varying the initial water content only. At the same time, the results of the numerical simulations indicate that clayey sand and lean clay are the soil types mostly influenced by the abovementioned rainfall event, since the initial moisture conditions enhance the formation of a wide wetting front within the soil profile.

1. Introduction

Many of the rainfall-induced landslides occurring all over the world are shallow-type; namely, the sliding surface is located at a depth from a few decimeters to some meters. They generally occur in response to prolonged intense rainfall events and involve either residual weathered soils or transported colluvial deposits. This type of landslides represents a widespread hazard that frequently results in considerable damage to infrastructure and human losses in many mountainous regions of the world, especially in areas characterized by the widespread presence of natural (e.g., [1–3]) and/or human-reworked soil cover (e.g., [4–6]). For this reason, in recent years great efforts are being made to improve the assessment of the temporal and spatial occurrence of rainfall-induced shallow landslides, especially through physically based models (e.g., [7–10]). However, the fundamental controls leading to slope failure driven by rainfall are still not well quantified [11], and thus the improvement of current models

is still an important research topic [12]. In fact, despite the small size, it is not straightforward to define the complex interaction between hydrological and mechanical processes that develops before and during the triggering process [13]. In principle, the infiltrating water flow may cause both the development of a temporary perched water table, usually at the contact between the soil cover and the less permeable bedrock [14], and a decrease of the resisting effect (apparent cohesion) induced by increasing positive water pressure values in the unsaturated portion [15, 16]. In this respect, it has been well recognized that matric suction can play a crucial role in the stability of unsaturated soil slopes [17]. Additionally, rainfall-induced slope failures heavily depend on the relationship between suction and water content which, in turn, are related with unsaturated conductivity functions as well as the rainfall intensity [18]. Considering the complexity of this research topic, a considerable amount of experiments has been conducted on understanding the behavior of water-induced shallow landslides under controlled laboratory
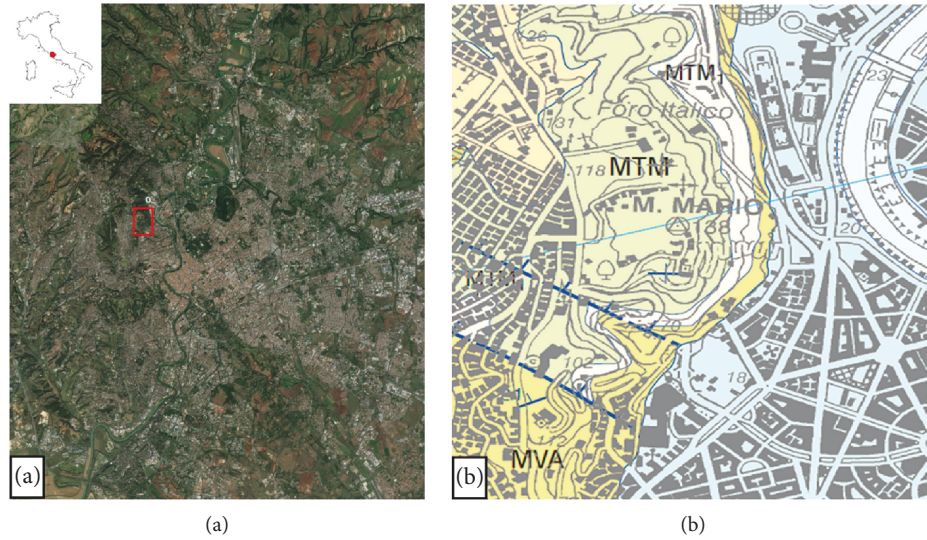
FIGURE 1: (a) Satellite image of the Rome urban area, with the location of Monte Mario Hill; (b) geological sketch of the Monte Mario area (from [36]).

conditions using sloping flumes (e.g., [19–23]). Several authors [24–26] also reproduced via numerical modelling the performed experimental tests, assuming a triggering mechanism that commonly occurs when the wetting bands progress into the soil, resulting in loss of suction and in effective stress reduction [27, 28]. Although these studies significantly contributed to better understanding the conditions leading to water-induced shallow landslides, there have been relatively few investigations for linking such experimental evidences with real widespread landslide events [29], evaluating in detail the triggering mechanisms [30]. In this sense, physically based models aimed at predicting the occurrence of shallow landslides over large areas (e.g., [31–34]) can be viewed as reliable tools, unless the uncertainties concerning the input parameter values be reduced as much as possible.

For this reason, in this work we analyze the triggering mechanisms of shallow landslides evaluating the effect of the initial soil conditions through laboratory flume experiments. Specifically, different tests have been performed on a soil sampled on Monte Mario Hill (Rome, Central Italy). This area has been affected by recurring rainfall-induced landslide events in the past, including the one that occurred between January 31 and February 2, 2014. In this sense, the outcome of the experiments has been also analyzed in relation to the results provided by HYDRUS-1D [35], a USDA (United States Department of Agriculture) Salinity Laboratory software package which can simulate the water flow into unsaturated porous media resulting from a rainfall event. Specifically, the insights resulting from the laboratory tests and the numerical simulations have been used to better understand the potential failure conditions for the shallow landslides occurred during the 2014 event.

2. General Features of the Study Area and the 2014 Event

The Monte Mario Hill, which is located in the northwestern sector of the city of Rome, on the right bank of Tiber River

(Figure 1(a)), represents the highest relief of the city (144 m a.s.l.). From a geological point of view (Figure 1(b)), it is composed at the bottom by a silty-clay succession of lower-upper Pliocene age (Monte Vaticano Formation (MVA)). This formation has a discordant contact with the upper Monte Mario Formation (MTM), a lower Pleistocene succession composed of silty sands [37]. At the base of this formation, it is also possible to identify a portion of reduced thickness (15 m) constituted by clayey silts (Farneto Member MTM_1). From a morphological point of view, Monte Mario is characterized by a relatively high slope gradient, especially along the eastern sector, which represents the result of both natural and anthropogenic factors, like fluvial erosion and manmade cuts. Such a slope gradient also enhances the triggering of rainfall-induced landslides, which generally involve a thin (0.5–2 m) layer of eluvial-colluvial superficial deposits overlaying the majority of the slopes. In this respect, between January 31 and February 2, 2014, 68 landslides have been recorded all around the city (Figure 2(a)), of which 12 occurred along slopes of Monte Mario only [38]. According to the data recorded by the Roma Monte Mario station, which is located within the study area, such landslides have been triggered by approximately 250 mm of rainfall cumulated in three days. However, in this time interval, two main subevents may be distinguished. The first (and most severe in terms of rainfall amounts) started in the early hours of January 31st and ended after about 24 hours, with a total cumulated rainfall of about 190 mm. This subevent was characterized by extremely high rainfall intensity peaks, such as the one that occurred between 4:00 and 5:00 a.m. (46 mm). Very high values continued to be recorded throughout the morning, with 3-hour and 6-hour rainfall equal to 87.6 and 140 mm, respectively. On the contrary, the second subevent, which took place in the afternoon of February 2nd from about 1:00 to 6:00 p.m., was of shorter duration and characterized by less intensity peaks, resulting in a total average cumulated rainfall of approximately 40 mm. Most of the triggered landslides involved relatively shallow (less than 1 m) portions of

(a)

(b)
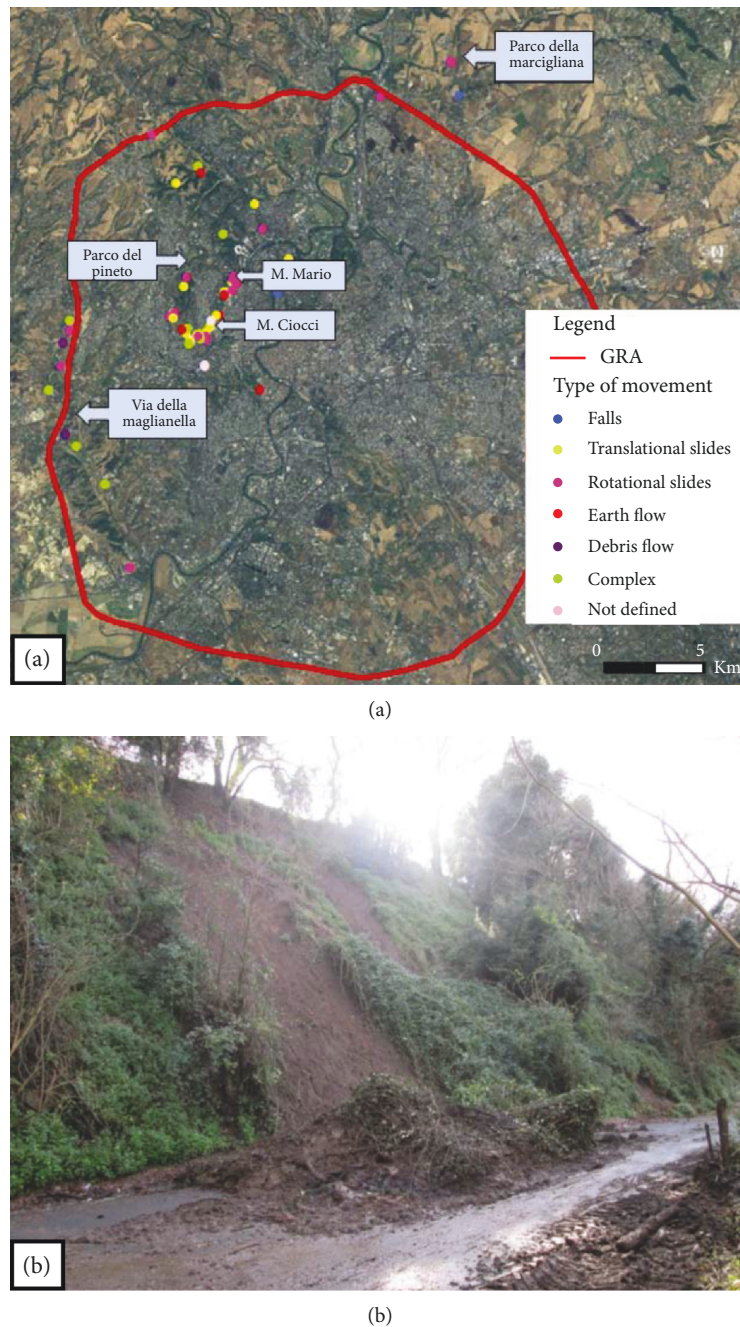
Figure 2: (a) Location of landslides inventoried in the Rome urban area after the exceptional rainfall of January 31-February 2, 2014 (from [38]); (b) an example of landslide triggered on Monte Mario Hill during the 2014 event.

weathered soil (Figure 2(b)) and can be classified as translational and rotational slides, earth flows, and debris flows [38]. Despite their limited thickness, such landslides caused the disruption of the road network, with consequent vehicle traffic bans and inconveniences for citizens as well as substantial damages to other infrastructures.

3. Materials and Methods

3.1. Physical and Mechanical Characterization of the Soil Cover. A series of field and laboratory activities have been

carried out in order to outline the main features of the soil cover affected by the slope failures that occurred in 2014. After removing the most surficial soil layer (approximately 20 cm), twenty-one undisturbed samples have been collected on site by driving into the soil a core cutter having a diameter of 100 mm (Figures 3(a) and 3(b)). The material is generally characterized by a medium plasticity and a high content of sand and clay, while the gravel and silt amount seldom exceeds 20-30% (Table 1). Specifically, the sampled material can be identified in four different USCS classes, which are consistent with eluvial and colluvial deposits resulting from

(a)

(b)

(c)

(d)

FIGURE 3: (a) Locations of the 21 samples collected on Monte Mario; (b) the sampling stage; (c) borehole for the evaluation of the soil cover thickness. The location of the three boreholes is marked in green in Figure (a); (d) test for density and unit weight of soil in place by the sand cone method.

TABLE 1: Physical properties and corresponding USCS-USDA class for the 21 samples collected on Monte Mario Hill.

Sample code	Soil thickness (m)	Gravel (%)	Sand (%)	Silt (%)	Clay (%)	W_L (%)	IP (%)	USCS class	USDA class
S1		22.3	33.9	16.7	27.1	29	5.7	SC	Loam
S2		4.2	12.7	34.5	48.6	39.6	11.6	CL	Silty clay loam
S3		19.6	52	13	15.4	—	—	SC	Sandy loam
S4		25.3	50.8	12.8	11.1	—	—	SM	Sandy loam
S5		5.5	66.4	8.6	19.5	25.9	4.8	SC	Sandy loam
S6	1.3	4	51	17.1	27.9	36.2	10.7	SC	Sandy clay loam
S7		8.4	77.5	0.9	13.2	—	—	SC	Loamy sand
S8		6.5	87.5	3	3	—	—	SM	Sand
S9		2.8	9.6	36.5	51.1	35.1	11.3	CL	Clay loam
S10		9.1	19	30.2	41.7	34	9.8	CL	Clay loam
S11		6.4	63.8	11.4	18.4	—	—	SC	Sandy loam
S12		13.3	68.3	11.5	6.9	—	—	SM	Loamy sand
S13	1.1	0	3.8	38.5	57.7	50.3	16	MH	Silty clay
S14		7	35.6	29.5	27.9	25.2	6.1	CL	Loam
S15		5.4	25.3	29.8	39.5	37.9	14.6	CL	Clay loam
S16		16.1	30.7	24	29.2	29.8	8.5	CL	Loam
S17		1.1	13.6	35	50.3	45.4	10.8	CL	Silty clay loam
S18		0	3.5	50.2	46.3	32.9	5.7	CL	Silty clay loam
S19		1	7	27.5	64.5	48.6	15.3	CL	Silty clay
S20	0.75	5.7	30.3	21.3	42.7	41.9	16.8	CL	Clay loam
S21		10.7	48.6	13.9	26.8	34.2	11.5	SC	Sand

the weathering of medium to fine-grained rocks, such as those outcropping on Monte Mario Hill. In this respect, the sandy samples have been mainly collected where the Monte Mario Formation outcrops (i.e., medium-upper part of the slope), while the material characterized by a higher amount of clay was generally sampled in the lower part of the slope, in correspondence of the Monte Vaticano Formation.

In correspondence of sampling site S21, further material (approximately 500 kg) has been collected for performing the flume tests described in Section 3.2. In this sense, it is important to specify that the soil unit weight has been determined in this specific site by the sand cone method (Figure 3(d)), and the resulting value (14.9 kN/m^3, which corresponds to a porosity of 48%, given a unit weight of soil solids of 26.4 kN/m^3 and a field water content of 11.5%) has been properly reproduced within the flume during the experimental tests.

3.2. Experimental Set-Up. The experimental equipment (Figure 4(a)) comprises a rectangular sloping flume 100 cm long, 60 cm wide, and 20 cm high, whose sides were made in plexiglass in order to allow the visual observation of the wetting and triggering processes. To assure the same friction between the soil particles and the base of the flume as of that of particles inside the flume, a rough plastic panel was applied to the surface of the flume base. A stiff permeable barrier was fixed in front of the soil to contain it after the failure, whereas a video camera was used to monitor failure initiation time and location. Two properly placed spray nozzles above the flume guarantee an artificial rainfall having a raindrop size

distribution and impact energy consistent with the experiment scale (Figure 4(b)). For assuring the correct functioning of the system, the supplied water pressure has been kept constant at 3.2 bar, resulting in a steady rainfall input of approximately 1/mm/min. During each test, the water content and pore water pressure within the soil were measured using, respectively, 4 EC-5 soil moisture sensors and 4 UMS-T5 mini-tensiometers (Figure 4(c)). These sensors are connected to a data logger which acquires data each two seconds.

Three different flume inclinations have been used during the experiments (i.e., 27°, 32°, and 35°) which represent, respectively, the minimum, average, and maximum slope values within the 2014 landslide source areas. The soil initial water content ranges between 11.9% and 19.2%, and it was obtained, before placing the soil into the flume, by wetting a specific quantity of oven-dried soil with the amount of water needed to reach the desired water content value. After the soil was set into the flume, the water content was checked by sampling the soil in different points. The initial porosity was attained overlaying four compacted soil layers parallel to the flume base (Figure 5(a)). Given the fixed geometry and volume of a 4 cm thick layer, the soil weight required to fill that volume was calculated considering also the fixed initial water content. During the soil placement within the flume, the 8 sensors have been placed at different depths (Figure 5(b)), with the aim of observing the infiltration process throughout the soil slope model. Finally, in order to achieve the least possible disturbance of slope conditions, a wedge-shaped slope was created in the termination of the material (Figure 5(c)). The inclination of the wedge-shaped

(a)

Rainfall system

(b)

Soil moisture
sensor EC-5

Mini-tensiometer
UMS-T5

(c)
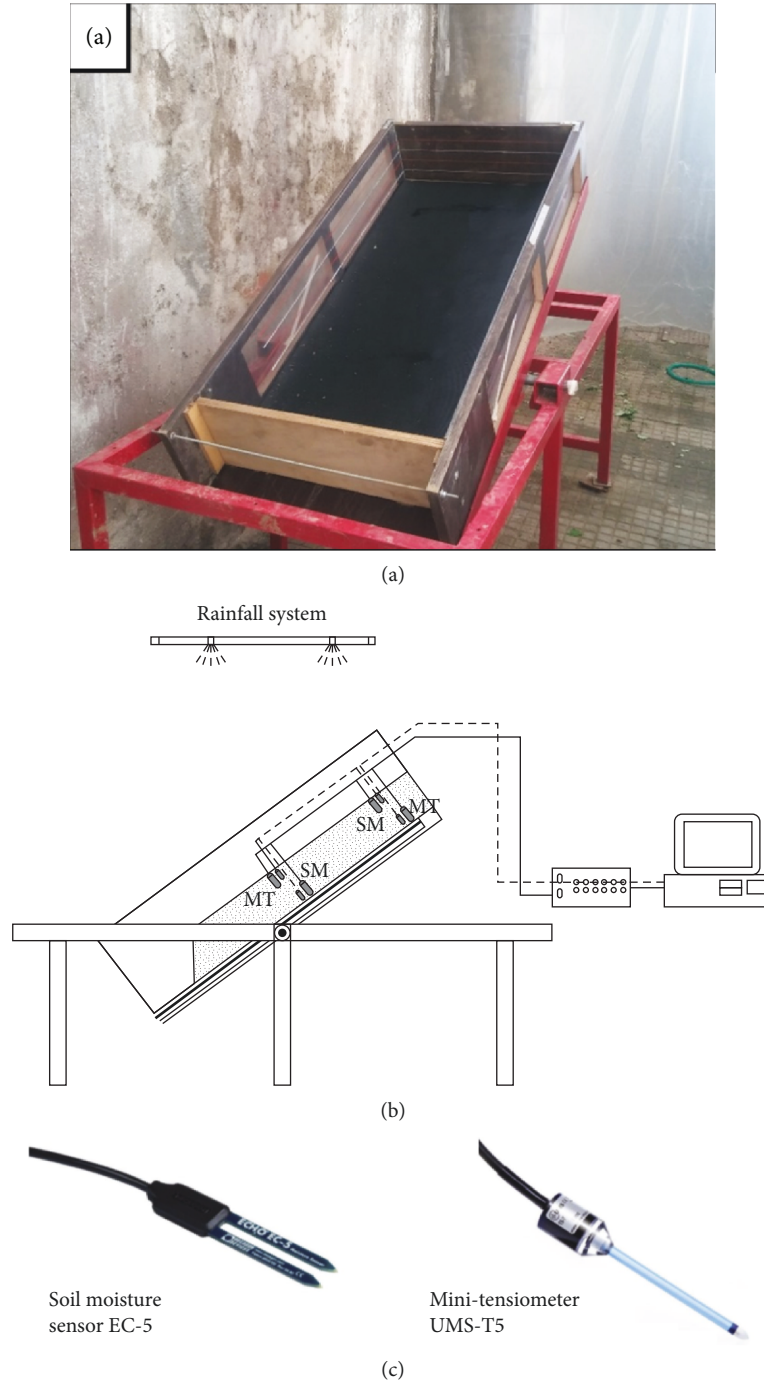
FIGURE 4: (a) The experimental flume; (b) scheme of the experimental apparatus (SM: soil moisture sensor; MT: mini-tensiometer); (c) sensors used for the monitoring of soil water content and pore water pressure during the tests.

slope was set to 30° (lower than the friction angle) to ensure that failure occurred within the soil volume and not affecting this terminal slope only. This geometry was considered suitable for the experimental purposes, and then, it has been kept constant in each test.

4. Results

Ten flume tests have been performed by varying the initial water content (w) and the flume slope angle (α) (Table 2).

According to the obtained results, different observations can be made: (1) as the initial water content or slope increases, the failure time decreases (Figure 6); (2) by changing the initial water content, the failure time variation is higher in tests with a slope angle (α) of 35° than in those with 32° (Figure 6); (3) in tests with $\alpha = 27°$, no failure occurred, but only a gradual erosion of the superficial layers, even with the wettest initial soil conditions (i.e., $w = 16.4\%$); (4) tests n.9 and n.10 have been performed for replicating tests n.6 and n.3, respectively. The aim was to evaluate the

(a)

(b)

(c)

FIGURE 5: (a) Placement of a 4 cm soil layer within the flume; (b) position and installation depth of the 8 sensors according to a schematic upper view of the soil slope model; (c) the soil slope model just before the beginning of a test. The lateral view allows to notice the wedge-shaped slope at the termination of soil volume.

TABLE 2: Initial soil conditions and time of failure for each performed flume test.

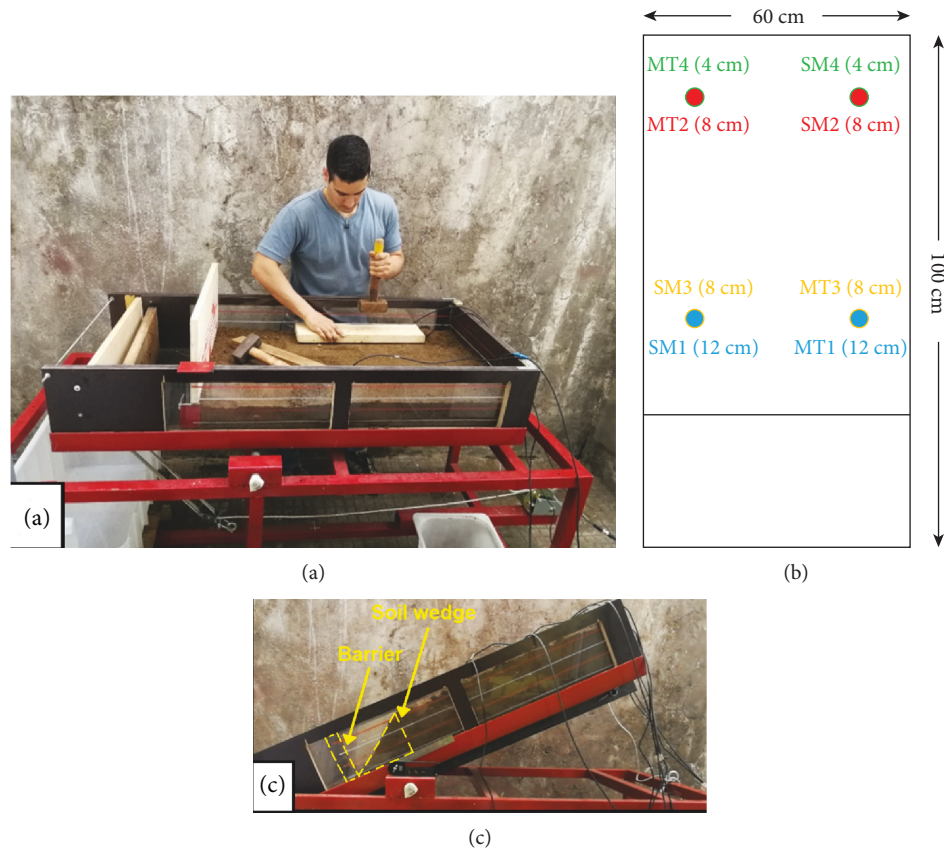| Test	Date	Slope angle (°)	Initial water content (%)	Degree of saturation (%)	Time of failure (min)
1	24/04/2018	27	12.4	36.1	No failure
2	29/04/2018	27	16.4	47.8	No failure
3	09/05/2018	32	11.9	34.7	1 h 21 min 05 sec.
4	15/05/2018	32	14.7	42.8	1 h 13 min 50 sec.
5	25/05/2018	32	19.2	56.0	0 h 45 min 00 sec.
6	04/06/2018	35	11.9	34.7	0 h 42 min 08 sec.
7	11/06/2018	35	14.4	42.0	0 h 37 min 30 sec.
8	14/06/2018	35	16	46.6	0 h 24 min 37 sec.
9	05/07/2018	35	12.1	35.3	0 h 45 min 47 sec.
10	18/07/2018	32	12.0	35.0	1 h 25 min 45 sec.

reproducibility of the assumed boundary conditions and, in turn, the reliability of the obtained results: in both tests, the failure time difference with the corresponding tests is lower than five minutes.

As regards the failure mode, it was generally extremely rapid, with evidences of incipient instability only a few seconds before the failure (Figure 7). The detachment generally involved a soil thickness between 7 and 12 cm; thus, considering that the total soil thickness is 16 cm, the failure surface always developed within the soil profile and not at the contact

between soil and the flume base. Furthermore, it is worth noting that, if the initial water content is relatively low, failure typically induces the mobilization of greater soil volumes, and vice versa.

Other interesting observations can be made by analyzing the records from the eight sensors placed within the soil during the tests. In this respect, if we compare data from test n.3 ($\alpha = 32°$, $w = 11.9\%$) and test n.5 ($\alpha = 32°$, $w = 19.2\%$), a different soil behavior in response to the rainfall input can be recognized. Specifically, in both tests
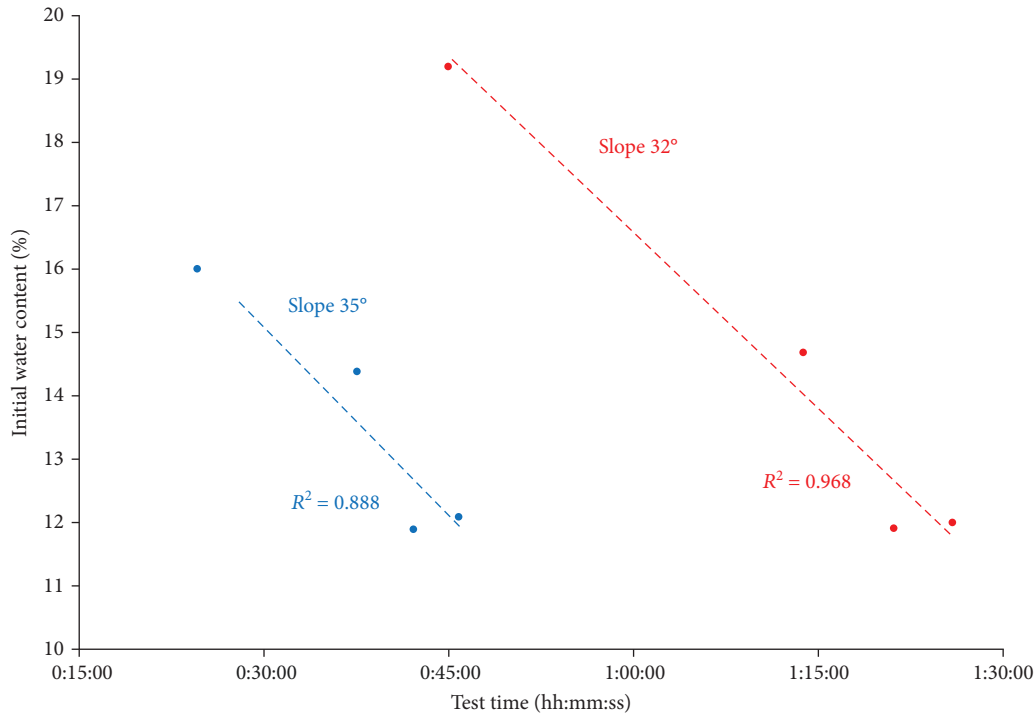
FIGURE 6: Failure time vs. initial water content for different flume slopes.

starting from initial negative values of pore water pressure induced by partial soil saturation, soil undergoes progressive reduction of the matric suction, until the development of positive pore water pressures. However, in test n.3 such development occurs first for the deepest mini-tensiometers (MT1 and MT2) and then for the shallowest ones (MT3 and MT4) (Figure 8(a)). On the contrary, in test n.5, the sensors that first record a drastic reduction of matric suction are those located in the most surficial portion of soil (Figure 8(b)). Actually, in this specific test also MT2 recorded positive pore water pressures almost simultaneously to MT3; however, this point can be explained with a not sufficient soil compaction in the area above the sensor, which caused an excessive water percolation in that specific point.

As regards the water content, even if in test n.3 the first sensor that records an increase in water content is the shallowest one (SM4), at the end of the test the highest values are still recorded by the deepest sensors (SM1 and SM2) (Figure 8(c)). Conversely, in test n.5, SM3 and SM4 first recorded an increase in water content, reaching the highest values during the whole test (Figure 8(d)).

The same behavior, in terms of infiltration, can be observed also in tests with $\alpha = 35°$ (Figure 9). In such a case, the greater slope angle induces most sudden variations of water content and pore water pressure, also enhancing an earlier response of sensors located closer to the soil wedge (i.e., MT1-MT3, and SM1-SM3). In this respect, it is worth noticing that in test n.6 ($w = 11.9\%$) failure occurs while the sensors farthest from the soil wedge (MT4 and MT2) still recorded negative pore water pressure values (Figure 9(a)).

5. Discussions

On the basis of the observations deriving from the outcomes of the performed tests, different insights can be inferred. Firstly, a strong sensitivity of the tested material to changing the flume slope angle can be noticed. In fact, if no failure was observed for $\alpha = 27°$ regardless of the rainfall duration, for tests with $\alpha = 32°$, failure occurred in about one hour, and the time of failure strongly reduces, increasing by just three degrees the flume slope. Afterwards, a different response of the soil, in terms of infiltration, was observed by varying the initial water content, while keeping constant both slope and porosity, as well as the rainfall input. Specifically, for tests with lower initial water content, the sensors that first recorded variations induced by the infiltrating water flux are those located in the deepest part of the soil. On the contrary, for tests with higher initial water content, the first variations were detected by the shallowest sensors. This point suggests two different triggering mechanisms for the soil slope model. In the first case, it is possible to hypothesize the formation of a temporary water table at the base of the flume, which progressively rises until failure occurs, involving a relatively high amount of material (Figure 10(a)). In the second case, failure is likely induced by the advance of the wetting front, which mobilizes a lower soil thickness with respect to the preceding instance (Figure 10(b)). Therefore, the most interesting insight deriving from the flume tests is that the triggering mechanism may change only considering variation of the initial water content. In preceding works, several authors (e.g., [39–41]) highlight how antecedent soil moisture greatly affects the rate and depth of advance of the wetting front during intense rainfall, but not the type of

01:20:58   01:21:03   01:21:05

(a)   (b)   (c)
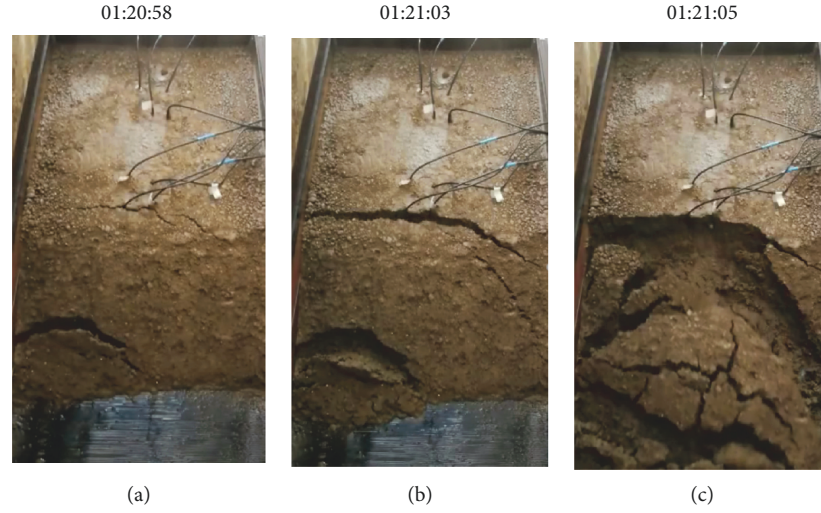
FIGURE 7: Temporal evolution of failure during test n.3.

(a)

(b)

(c)

(d)
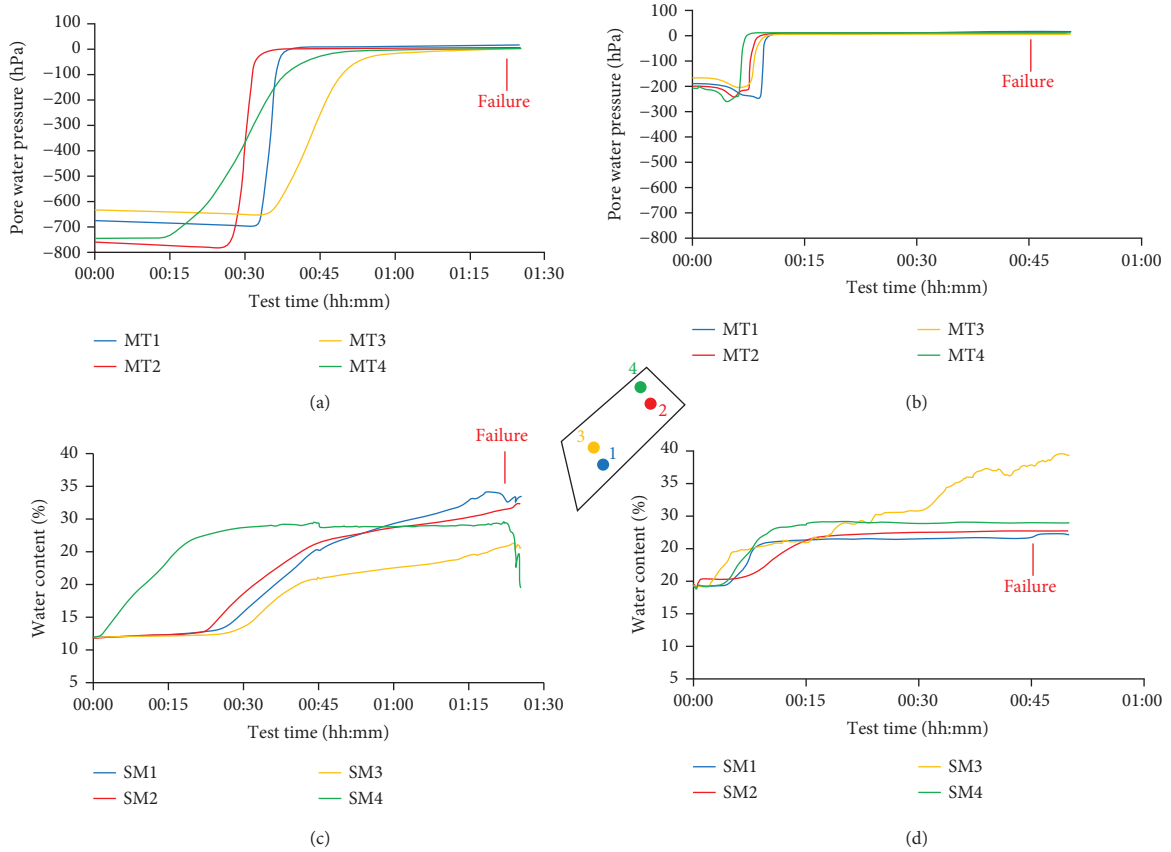
FIGURE 8: Pore water pressure (a and b) and soil moisture data (c and d) recorded during test n.3 ($\alpha = 32°$, $w = 11.9\%$) and test n.5 ($\alpha = 32°$, $w = 19.2\%$), respectively.

triggering mechanism that, instead, is generally associated with the rainfall intensity [28, 42] and grain-size soil characteristics. In this sense, [43] assert that shallow landslides affecting fine-grained soils are induced by the reduction in matric suction near the ground surface due to rainfall infiltration, while a significant triggering factor for coarse-grained soils of high permeability like sands is a rise in the water table.

Therefore, the role of initial soil moisture in relation to the triggering mechanism should be examined more in detail for evaluating the potential shallow landslide triggering conditions, especially when physically based numerical models are employed. In this respect, it is considered that one of the main drawbacks of such models relies on the complexity in correctly evaluating the input parameters, especially over large areas. In this respect, different authors (e.g., [44–46])

(a)

(b)

(c)

(d)
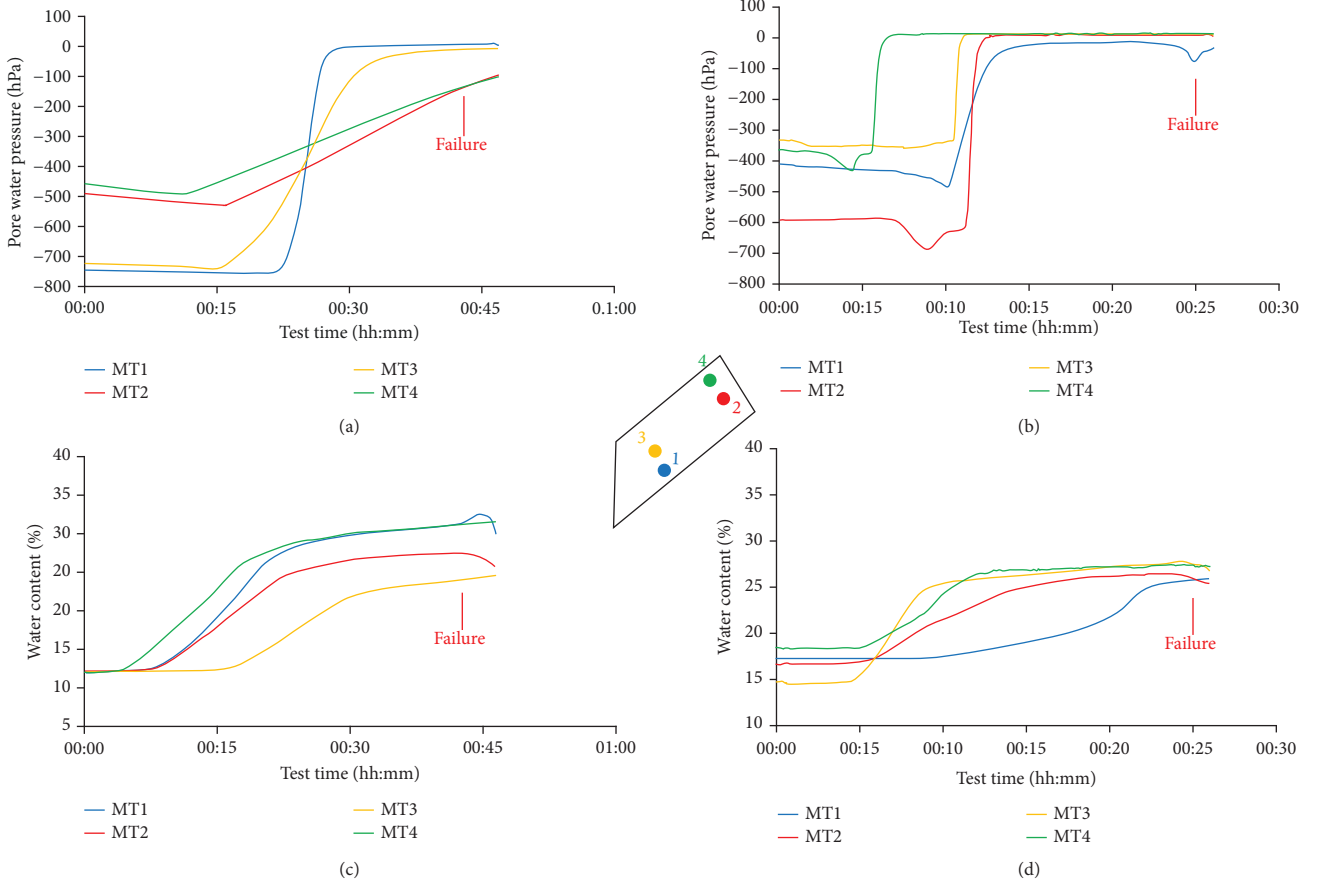
FIGURE 9: Pore water pressure (a and b) and soil moisture data (c and d) recorded during test n.6 ($\alpha = 35°$, $w = 11.9\%$) and test n.8 ($\alpha = 35°$, $w = 16\%$), respectively.

(a)

(b)
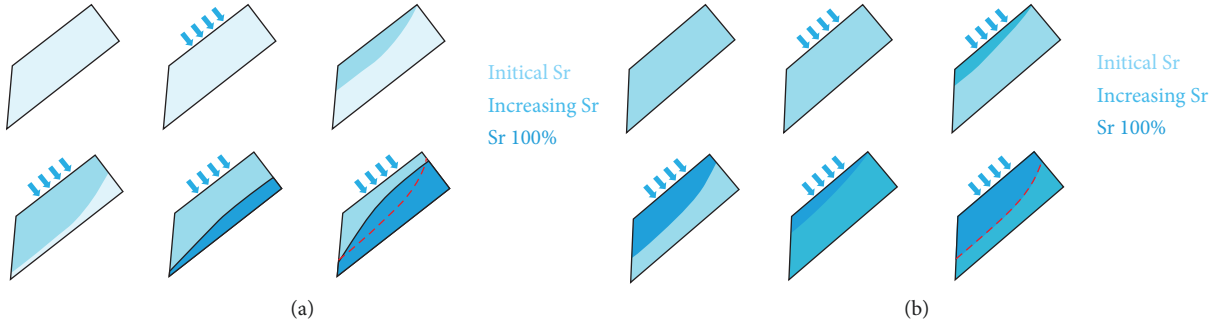
FIGURE 10: The triggering mechanisms hypothesized according to the experimental evidences: (a) failure induced by an uprise of a temporary perched water table (for soils with relatively low initial water content); (b) failure induced by the advance of the wetting front (for soils with relatively high initial water content).

have observed that soil cohesion, friction angle, and soil thickness represent the major sources of error for this type of analyses. With regard to the mechanical parameters, the problem is mainly related to the limited sampling [47, 48] and the difficulty to properly evaluate the vegetation effect in terms of root cohesion [49, 50]. As regards the soil thickness, several authors proposed linear correlations with elevation and slope gradient [51], semi-empirical geomorphology-based approaches [52], and multivariate statistical analyses of terrain parameters [53]. However, the results of the experimental tests demonstrate that a reliable analysis of the

TABLE 3: Hydrodynamic parameters for the four soil types of Monte Mario (θ_r: residual water content; θ_s: saturated water content; K_s: hydraulic conductivity).

Soil type	θ_r (-)	θ_s (-)	K_s (m s^{-1})
SC	0.06	0.39	$3.84E - 06$
CL	0.07	0.37	$3.41E - 07$
MH	0.08	0.36	$1.14E - 07$
SM	0.04	0.35	$1.53E - 05$

FIGURE 11: Water content trend vs. depth resulting from the HYDRUS-1D simulation of the January 31-February 1, 2014, rainfall event that occurred in Rome. Each graph refers to one of the soil types outcropping on Monte Mario Hill: (a) clayey sand (SC); (b) lean clay (CL); (c) silt (MH); (d) silty sand (SM). Legend: W_{res}: residual water content; W_{in}: initial water content; W_{sat}: saturated water content.

shallow landslide triggering conditions requires not only the proper evaluation of the input parameters but also the use of an infiltration model that must be coherent with the real expected events.
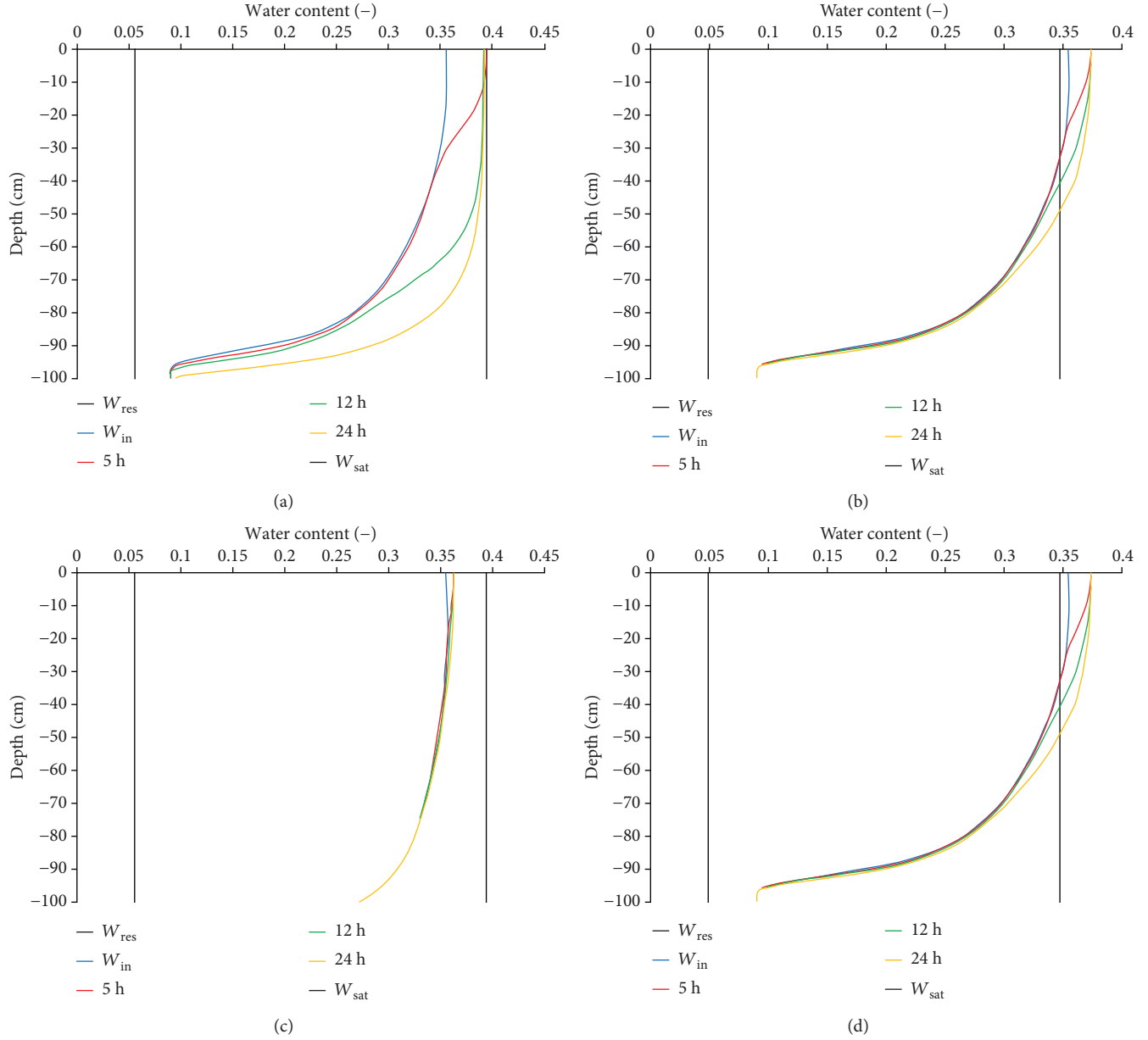
For this reason, we decided to evaluate the hydraulic effects induced by the rainfall event that occurred in Rome in 2014 to four different soil types outcropping on Monte Mario. To do this, we used HYDRUS-1D, a numerical model which can describe the water flow within an unsaturated porous medium, such as a superficial deposit, on the basis of a modified version of Richards' equation. Different numerical simulations have been first performed for the period August 1, 2013, January 30, 2014, in order to quantify the effect of the antecedent rainfall on soil moisture conditions.

Afterwards, the simulations have been extended to include the main rainfall event causing the triggering of the majority of landslides (specifically, between 1 a.m. of January 31st and 1 a.m. of February 1st). The van Genuchten–Mualem model [54] was chosen as a hydraulic model to simulate water flow, whereas the hydrodynamic parameters θ_s, θ_r, and K_s (Table 3) are predicted from soil grain size distribution using the ROSETTA Lite module [55]. Daily rainfall data (source: *Centro Funzionale della Protezione Civile della Regione Lazio*—Functional Civil Protection Centre of the Latium Region) have been used as input for the model, whereas evapotranspiration is accounted for by inserting the maximum and minimum temperature values (source: *Servizio Idrografico e Mareografico Nazionale*—National

Hydrographic and Marine Services) recorded during the investigated period into the Hargreaves equation [56]. With regard to the thickness of the model, we decided to use the average value of the three measurements deriving from the boreholes (1 m), while the soil column inclination has been set in order to obtain a superficial slope equal to 32°.

According to the simulations, it results that SC and CL are the soil types mostly influenced by the rainfall event (Figures 11(a) and 11(b)). In detail, both soils start from relatively high initial (W_{in}) moisture conditions (between 25% and 35% in the first 90 cm of soil). Afterwards, a clear wetting front forms, in particular after the 5 h rainfall and advances, causing the saturation of the first 20-30 cm. It is worth noting how such advance is greater in the case of SC as a consequence of the higher hydraulic conductivity. In the case of MH soil (Figure 11(c)), although W_{in} is similar to that of the preceding soils, the rainfall effect is substantially irrelevant, at least in the short term, probably due to the lower hydraulic conductivity that enhances the run-off. The rainfall impact is small also for SM (Figure 11(d)): in this specific case, W_{in} is quite low and homogenous, which coupled with the high hydraulic conductivity of the material, inducing significant water content changes. However, these variations are not still sufficient to form either a wetting front (excluding the very first cm of soil) or a perched water table at the base of the column.

6. Conclusions

In this study, different flume tests have been performed to analyze the triggering process of rainfall-induced shallow landslides, with a specific focus on the role of the initial hydraulic conditions by changing the slope. In detail, it was observed that the increase in the initial water content anticipates the triggering time, particularly in the case of slope = 35°. This point, together with the lack of failure for tests with $\alpha = 27°$, also suggests the marked sensitivity of the tested material to even small slope variations. With regard to the failure mode, the data deriving from the soil moisture and pore water pressure sensors indicate two potential triggering mechanisms to variations of the initial water content, i.e., failure induced by uprise of a temporary perched water table and by the advance of the wetting front in the case of relatively low and relatively high initial soil moisture, respectively. At this point, for analyzing such process at the field conditions, we performed a numerical analysis with HYDRUS-1D, a physically based model which simulates the water flow into unsaturated porous media. On the basis of the data collected on site (i.e., Monte Mario Hill, Rome), we simulated numerically the rainfall event occurring between January 31 and February 1, 2014, which triggered 68 landslides along slopes of Monte Mario and the surrounding areas. According to the simulations, it results that SC and CL soil types are those mostly influenced by the 2014 rainfall event, since the higher initial moisture conditions enhance the formation of a wide wetting front within the soil profile.

In conclusion, the evidence that the triggering mechanism may change only due to variations of the initial water content should be considered also for future research activities regarding the physically based modelling of shallow landslides. Specifically, future improvements may concern a better evaluation of the role of other parameters (such as soil thickness and slope) in the triggering process. With respect to the case study described in this paper, starting from field evidences, further experimental tests should be performed, also considering the other soil types outcropping on Monte Mario. In this way, it will also be possible to verify if the current inferences may be extended to the entire area. In this fashion, physical laboratory modelling can also be viewed as a supporting tool for numerical models aimed at temporal and spatial prediction of shallow landslides occurrence over large areas. In fact, the rationale is to define the relation between rainfall, soil moisture, and triggering mechanisms for known laboratory boundary conditions and then to extend this relation at the investigated site through monitoring data collected in the field.

Data Availability

The data used to support the findings of this study are included within the article.

Conflicts of Interest

The authors declare that they have no conflicts of interest.

Acknowledgments

References

[1] F. C. Dai, C. F. Lee, and Y. Y. Ngai, "Landslide risk assessment and management: an overview," *Engineering Geology*, vol. 64, no. 1, pp. 65–87, 2002.

[2] C. W. Lin, S. H. Liu, S. Y. Lee, and C. C. Liu, "Impacts of the Chi-Chi earthquake on subsequent rainfall-induced landslides in central Taiwan," *Engineering Geology*, vol. 86, no. 2-3, pp. 87–101, 2006.

[3] M. Schwarz, F. Preti, F. Giadrossich, P. Lehmann, and D. Or, "Quantifying the role of vegetation in slope stability: a case study in Tuscany (Italy)," *Ecological Engineering*, vol. 36, no. 3, pp. 285–291, 2010.

[4] C. Camera, T. Apuani, and M. Masetti, "Modeling the stability of terraced slopes: an approach from Valtellina (Northern Italy)," *Environmental Earth Sciences*, vol. 74, no. 1, pp. 855–868, 2015.

[5] G. B. Crosta, P. Dal Negro, and P. Frattini, "Soil slips and debris flows on terraced slopes," *Natural Hazards and Earth System Sciences*, vol. 3, no. 1/2, pp. 31–42, 2003.

[6] M. G. Persichillo, M. Bordoni, M. Cavalli, S. Crema, and C. Meisina, "The role of human activities on sediment connectivity of shallow landslides," *Catena*, vol. 160, pp. 261–274, 2018.

[7] G. Formetta, V. Rago, G. Capparelli, R. Rigon, F. Muto, and P. Versace, "Integrated physically based system for modeling landslide susceptibility," *Procedia Earth and Planetary Science*, vol. 9, pp. 74–82, 2014.

[8] J. Y. Ho and K. T. Lee, "Performance evaluation of a physically based model for shallow landslide prediction," *Landslides*, vol. 14, no. 3, pp. 961–980, 2017.

[9] Z. Liao, Y. Hong, D. Kirschbaum, and C. Liu, "Assessment of shallow landslides from Hurricane Mitch in central America using a physically based model," *Environmental Earth Sciences*, vol. 66, no. 6, pp. 1697–1705, 2012.

[10] Y. Thiery, R. Vandromme, O. Maquaire, and S. Bernardie, "Landslide susceptibility assessment by EPBM (Expert Physically Based Model): strategy of calibration in complex environment," in *Advancing Culture of Living with Landslides*, M. Mikoš, Ž. Arbanas, Y. Yin, and K. Sassa, Eds., vol. 2017, Springer, Cham, 2017.

[11] R. I. Borja, X. Liu, and J. A. White, "Multiphysics hillslope processes triggering landslides," *Acta Geotechnica*, vol. 7, no. 4, pp. 261–269, 2012.

[12] K.-t. Chang, S.-. H. Chiang, and F. Lei, "Analysing the relationship between typhoon-triggered landslides and critical rainfall conditions," *Earth Surface Processes and Landforms*, vol. 33, no. 8, pp. 1261–1271, 2008.

[13] G. Sorbino and M. V. Nicotera, "Unsaturated soil mechanics in rainfall-induced flow landslides," *Engineering Geology*, vol. 165, pp. 105–132, 2013.

[14] R. L. Baum, J. W. Godt, and W. Z. Savage, "Estimating the timing and location of shallow rainfall-induced landslides using a model for transient, unsaturated infiltration," *Journal of Geophysical Research*, vol. 115, no. F3, 2010.

[15] A. W. Bishop, "The principle of effective stress," *Tek Ukebl*, vol. 106, pp. 859–863, 1959.

[16] J. W. Godt, R. L. Baum, and N. Lu, "Landsliding in partially saturated materials," *Geophysical Research Letters*, vol. 36, no. 2, 2009.

[17] D. G. Fredlund and H. Rahardjo, *Soil Mechanics for Unsaturated Soils*, John Wiley & Sons, Inc, New York, 1993.

[18] D. H. Kim, S. K. Kim, and I. Gratchev, "Unsaturated seepage behavior study using soil column test," *Proceedings of the 18th Southeast Asian Geotechnical Conference*, 2013, Singapore, 29-31 May, 2013, 2013.

[19] S. D. N. Lourenço, K. Sassa, and H. Fukuoka, "Failure process and hydrologic response of a two layer physical model: implications for rainfall-induced landslides," *Geomorphology*, vol. 73, no. 1-2, pp. 115–130, 2006.

[20] L. Montrasio and L. Schilirò, "Inferences on modeling rainfall-induced shallow landslides from experimental observations on stratified soils," *Italian Journal of Engineering Geology and Environment*, vol. 18, no. 2, pp. 77–85, 2018.

[21] L. Olivares and E. Damiano, "Post-failure mechanics of landslides: laboratory investigation of flowslides in pyroclastic soils," *Journal of Geotechnical and Geoenvironmental Engineering*, vol. 133, no. 1, pp. 51–62, 2007.

[22] G. Wang and K. Sassa, "Factors affecting rainfall-induced flowslides in laboratory flume tests," *Géotechnique*, vol. 51, no. 7, pp. 587–599, 2001.

[23] G. Wang and K. Sassa, "Pore-pressure generation and movement of rainfall-induced landslides: effects of grain size and fine-particle content," *Engineering Geology*, vol. 69, no. 1-2, pp. 109–125, 2003.

[24] L. Montrasio and R. Valentino, "Experimental analysis and modelling of shallow landslides," *Landslides*, vol. 4, no. 3, pp. 291–296, 2007.

[25] R. K. Regmi, K. Jung, H. Nakagawa, X. K. Do, and B. K. Mishra, "Numerical analysis of multiple slope failure due to rainfall: based on laboratory experiments," *Catena*, vol. 150, pp. 173–191, 2017.

[26] D. Tsutsumi and M. Fujita, "Relative importance of slope material properties and timing of rainfall for the occurrence of landslides," *International Journal of Erosion Control Engineering*, vol. 1, no. 2, pp. 79–89, 2008.

[27] N. Lu and W. J. Likos, *Unsaturated Soil Mechanics*, John Wiley & Sons, New York, NY, USA, 2004.

[28] N. Lu and J. Godt, "Infinite slope stability under steady unsaturated seepage conditions," *Water Resources Research*, vol. 44, no. 11, 2008.

[29] L. Montrasio, L. Schilirò, and A. Terrone, "Physical and numerical modelling of shallow landslides," *Landslides*, vol. 13, no. 5, pp. 873–883, 2016.

[30] T. van Asch, B. Yu, and W. Hu, "The development of a 1-D integrated hydro-mechanical model based on flume tests to unravel different hydrological triggering processes of debris flows," *Water*, vol. 10, no. 7, p. 950, 2018.

[31] H. An, T. T. Viet, G. Lee et al., "Development of time-variant landslide-prediction software considering three-dimensional subsurface unsaturated flow," *Environmental Modelling and Software*, vol. 85, pp. 172–183, 2016.

[32] M. Alvioli and R. L. Baum, "Parallelization of the TRIGRS model for rainfall-induced landslides using the message passing interface," *Environmental Modelling and Software*, vol. 81, pp. 122–135, 2016.

[33] R. L. Baum, W. Z. Savage, and J. W. Godt, "TRIGRS-A Fortran program for transient rainfall infiltration and grid-based regional slope stability analysis, version 2.0," in *U.S. Geological Survey Open-File Report, 2008–1159*, p. 75, Denver Publishing Service Center, Denver, CO, USA, 2008.

[34] R. Rigon, G. Bertoldi, and T. M. Over, "GEOtop: a distributed hydrological model with coupled water and energy budgets," *Journal of Hydrometeorology*, vol. 7, no. 3, pp. 371–388, 2006.

[35] J. Šimůnek, M. Huang, M. Šejna, and M. T. van Genuchten, *The HYDRUS-1D Software Package for Simulating the One-Dimensional Movement of Water, Heat, and Multiple Solutes in Variably-Saturated Media. Version 1*, International Ground Water Modeling Center, Colorado School of Mines, Golden, Colorado, 1998.

[36] R. Funiciello, G. Giordano, and M. Mattei, *Memorie Descrittive della Carta Geologica d'Italia*, vol. 80, Carta geologica di Roma, Roma, 2008.

[37] F. Bozzano, S. Martino, and M. Priori, "Natural and man-induced stress evolution of slopes: the Monte Mario hill in Rome," *Environmental Geology*, vol. 50, no. 4, pp. 505–524, 2006.

[38] D. Alessi, F. Bozzano, A. Di Lisa et al., "Geological risks in large cities: the landslides triggered in the city of Rome (Italy) by the rainfall of 31 January-2 February 2014. Italian Journal of Engineering Geology and," *Environment*, vol. 1, pp. 15–34, 2014.

[39] R. L. Baum, J. P. McKenna, J. W. Godt, E. L. Harp, and S. R. McMullen, "Hydrologic monitoring of landslide-prone coastal bluffs near Edmonds and Everett, Washington, 2001-2004," in *U.S. Geological Survey Open-File Report, 2005–1063*, p. 42, U.S. Geological Survey Publications Warehouse, 2005.

[40] M. Bordoni, C. Meisina, R. Valentino, N. Lu, M. Bittelli, and S. Chersich, "Hydrological factors affecting rainfall-induced shallow landslides: from the field monitoring to a simplified slope stability analysis," *Engineering Geology*, vol. 193, pp. 19–37, 2015.

[41] M. Bordoni, R. Valentino, C. Meisina, M. Bittelli, and S. Chersich, "A simplified approach to assess the soil saturation degree and stability of a representative slope affected by shallow landslides in Oltrepò Pavese (Italy)," *Geosciences*, vol. 8, no. 12, p. 472, 2018.

[42] P. D'Odorico, S. Fagherazzi, and R. Rigon, "Potential for landsliding: dependence on hyetograph characteristics," *Journal of Geophysical Research*, vol. 110, no. F1, article F01007, 2005.

[43] R. Schnellmann, M. Busslinger, H. R. Schneider, and H. Rahardjo, "Effect of rising water table in an unsaturated slope," *Engineering Geology*, vol. 114, no. 1-2, pp. 71–83, 2010.

[44] L. Claessens, G. B. M. Heuvelink, J. M. Schoorl, and A. Veldkamp, "DEM resolution effects on shallow landslide hazard and soil redistribution modelling," *Earth Surface Processes and Landforms*, vol. 30, no. 4, pp. 461–477, 2005.

[45] K. J. Shou and Y. L. Chen, "Spatial risk analysis of Li-shan landslide in Taiwan," *Engineering Geology*, vol. 80, no. 3-4, pp. 199–213, 2005.

[46] T. Uchida, K. Tamur, and K. Akiyama, "The role of grid cell size, flow routing algorithm and spatial variability of soil depth on shallow landslide prediction," in *5th International Conference on Debris-Flow Hazards Mitigation: Mechanics, Prediction and Assessment*, R. Genevois, D. L. Hamilton, and A. Prestininzi, Eds., vol. 2011, pp. 149–157, Casa Editrice Università La Sapienza, Rome, Italy, 2011.

[47] D. V. Griffiths, J. Huang, and G. A. Fenton, "Probabilistic infinite slope analysis," *Computers and Geotechnics*, vol. 38, no. 4, pp. 577–584, 2011.

[48] J.-C. Huang, S.-J. Kao, M.-L. Hsu, and J.-C. Lin, "Stochastic procedure to extract and to integrate landslide susceptibility maps: an example of mountainous watershed in Taiwan," *Natural Hazards and Earth System Sciences*, vol. 6, no. 5, pp. 803–815, 2006.

[49] J. Y. Ho, K. T. Lee, T. C. Chang, Z. Y. Wang, and Y. H. Liao, "Influences of spatial distribution of soil thickness on shallow landslide prediction," *Engineering Geology*, vol. 124, pp. 38–46, 2012.

[50] T. S. Nguyen, S. Likitlersuang, and A. Jotisankasa, "Influence of the spatial variability of the root cohesion on a slope-scale stability model: a case study of residual soil slope in Thailand," *Bulletin of Engineering Geology and the Environment*, pp. 1–15, 2018.

[51] G.-M. Saulnier, K. Beven, and C. Obled, "Including spatially variable effective soil depths in TOPMODEL," *Journal of Hydrology*, vol. 202, no. 1-4, pp. 158–172, 1997.

[52] F. Catani, S. Segoni, and G. Falorni, "An empirical geomorphology-based approach to the spatial prediction of soil thickness at catchment scale," *Water Resources Research*, vol. 46, no. 5, 2010.

[53] T. K. Tesfa, D. G. Tarboton, D. G. Chandler, and J. P. McNamara, "Modeling soil depth from topographic and land cover attributes," *Water Resources Research*, vol. 45, no. 10, 2009.

[54] M. T. van Genuchten, "A closed-form equation for predicting the hydraulic conductivity of unsaturated soils1," *Soil Science Society of America Journal*, vol. 44, no. 5, pp. 892–898, 1980.

[55] M. G. Schaap, F. J. Leij, and M. T. van Genuchten, "ROSETTA: a computer program for estimating soil hydraulic parameters with hierarchical pedotransfer functions," *Journal of Hydrology*, vol. 251, no. 3-4, pp. 163–176, 2001.

[56] D. T. Jensen, G. H. Hargreaves, B. Temesgen, and R. G. Allen, "Computation of ETo under nonideal conditions," *Journal of Irrigation and Drainage Engineering*, vol. 123, no. 5, pp. 394–400, 1997.

WILEY | Hindawi

Research Article

Physical Tank Experiment Investigation on Rainfall Producing Groundwater Level in Homogeneous Material Slopes

Chao Zhang [1], **Wei Shao,**[2,3] **Fucai Yue,**[2] **Pooya Saffari,**[2] **and Wen Nie** [2]

[1]*State Key Laboratory of Geomechanics and Geotechnical Engineering, Institute of Rock and Soil Mechanics, Chinese Academy of Sciences, Wuhan 430071, China*
[2]*Quanzhou Institute of Equipment Manufacturing, Haixi Institutes, Chinese Academy of Sciences, Quanzhou, Fujian 362000, China*
[3]*School of Hydrology and Water Resources, Nanjing University of Information Science and Technology, Nanjing, 210044 Jiangsu, China*

Correspondence should be addressed to Wen Nie; wen.nie@fjirsm.ac.cn

It has been recognized that pore water pressure (PWP) changes in response to precipitation play a critical role in rainfall-triggered landslides. Tank models as a kind of undetermined model are widely applied for estimating groundwater levels in slopes. Most of these applications treat the tank models as a theoretical model. Therefore, in this study, physical tank experiments are reported, indicating an evaluation of three typical conceptual tank models (i.e., simple tank model, surface runoff tank model, and lateral water flow supply tank model). To reduce the slope structure controlling affection, the study takes homogenous soil material as the simulation of the slope mass. The experimental results demonstrated how the groundwater tables producing pore water pressure were affected by infiltration time lags, surface runoff, and lateral flow.

1. Introduction

Landslides are important and widespread natural hazards within alpine regions and can have significant impacts on human lives and infrastructures. Pore water pressure plays an important role in determining the stability of rainfall-triggered landslides. The increase of pore water pressure may reach positive values that are highly undesirable for slope stability, while, for unsaturated soil slopes, the change of pore water pressure caused by rainfall infiltration is an important triggering factor of landslides. A series of small-scale slope experiments highlight that the presence of coarse-textured unsaturated pumiceous layers, interbedded between finer ashy layers, can delay the wetting front advancement, thus initially confining the infiltration process within the finer uppermost layer [1]. Soil water content is the result of multifactor interactions, and proper soil water retention curves and hydraulic conductivity functions are necessary for a correct analysis of groundwater flow in unsaturated slopes [2]; however, measurement of soil water

content is time consuming and costly. In addition, there is no mathematical relationship between pore water pressure and the related parameters [3]. Therefore, it is required to establish hydrological models to estimate the pore water pressure in slopes. The hydrological models can be deterministic or based on an optimized method. The deterministic hydrological model commonly uses Darcy-Richards or Boussinesq equations to simulate the groundwater flow in slopes [4]. Or some models can describe the interaction between the soil and atmosphere in pyroclastic soils with a view to understanding whether and to what extent the prediction of the hydraulic (and mechanical) behavior of geotechnical problems regulated by rainfall-induced fluctuations of matric suction is influenced by evaporation phenomena [5]. However, the method is usually computationally intensive, and the application needs a detailed investigation of the geometries and hydraulic properties of the soil material [6]. In contrast with the deterministic model, the model based on the optimized method does not normally require detailed information on hydraulic properties of the slope

material such as permeability and infiltration. In the model, the historical data are used for estimating the parameters of the defined model structure [7, 8]. The pore water pressure and the groundwater level can be determined from these parameters. The method is applicable to a wide range of slopes. A tank model is a nonlinear theorized calculation optimized model used to describe the behaviors of water hydraulic properties [9]. The simple tank model [9], surface runoff tank model [10], and lateral water flow supply tank model [11, 12] are the three typical types of this model. The widely used simple tank model is a complex linear theorized calculation [9]. It is based on the water balance theory that tracks water into and out of a particular area of interest. The model can be used for calculation of pore water pressure in porous media. The 1D simple tank model usually can simulate the groundwater level of one point in a shallow slope without considering the lateral water flow supply [9]. In order to consider the lateral groundwater flow, infiltration time lag, and surface runoff, a multistorage tank model (such as the surface runoff tank model and lateral water flow supply tank model) is needed. The multistorage tank model can estimate the groundwater fluctuations of landslides caused by heavy rainfall [10–12]. The distinct properties of the three tank models are as shown in Table 1.

The simple tank model is easy to implement with high computational efficiency. However, its applications were limited to a low slope angle (one point for the pore water pressure (PWP) represents the entire water table level) and high porosity and permeability soil materials without considering surface runoff. The surface runoff tank models can overcome the limitations from surface infiltration rates and enable a simulation of the surface runoff generated by the excess infiltration rainwater [13]. The lateral water supply tank model can be applied for any slope angle, but its complicated structure produces a higher systematically cumulative error. The highlight of the application of the tank model is using a simple model structure with as-little-as-possible model parameters to describe the water balance including water content and groundwater level [14, 15]. Unfortunately, most applications of the tank model are still a theoretic model and require many parameters for calibration. As a "grey model," there are few direct physical experiments about the investigation of the tank model hydraulic parameters. The tank model based on the optimized method should always seek less, not more, model parameters. Thus, this research aims to investigate the simple hydraulic phenomena under different rainfall events based on physical tank experiments. These investigations would help to construct the tank model with less or limited parameters and a simple structure. In this study, physical tank experiments are employed to investigate the relationships between rainfall events and groundwater pressure ignoring the infiltration process in the homogenous soil materials as the simulation of slope mass during the rainfall events [14] (Figure 1), and only a few parameters (rainfall and groundwater pressure) were used to constrain the tank model for the estimation of pore water pressure.

TABLE 1: Characters of the three typical tank models.

Type	Characters of applications
Simple tank model [9]	Simple model; assumed low slope angle; no surface runoff; negligible lateral water flow supply
Surface runoff tank model [10]	Considering surface runoff; requires maximum infiltration rate test; less lateral water flow supply
Lateral water flow supply tank model [11, 12]	Increasing model complex; relatively high error; any slope angle

2. Methods

2.1. Test Setup and Testing Materials

2.1.1. Physical Tank Models. A series of physical tank model systems made of plexiglass was conducted, and the hydrological behavior of a slope mass, representing a homogenous hillslope, was investigated (Figure 1). In order to shape the slope mass, the soil was filled inside the tank in layers of 5 cm height. A plate squeezed the soil mass by applying 120 N force to each soil layer (Figure 2).

2.1.2. Rainfall Simulator. For the purpose of rainfall simulations, the rainfall intensity test and uniform degree test of rainfall are necessary before the experiments. A water pump was installed to increase water pressure and supply artificial rainfall through nozzles (uniformity coefficient was ~0.87). The pump can adjust the water pressure between the water input and output by a pressure-increasing valve. The spray nozzles can produce the uniform misty rainfall. A flowmeter between the pump and nozzles steadily controlled the rainfall intensity (10–250 ml/min) by a flow adjustment. A water storage tank was used for the water supply. The level of water inside the tank was measured with a ruler which was placed on the edge of the tank. The rainfall simulator is shown in Figure 3.

2.1.3. Rainfall Intensity Test. A simple tank with dimensions of $300 \times 300 \times 300$ mm was used in order to test the rainfall intensity. The collected simulation rainfall in unit time is compared to the calculated rainfall depending on the flowmeter. The flow rates of the flowmeter were 15 to 120 ml/min and the increment value was 15 ml/min. Each test lasted 0.5 hr. The test results are shown in Figure 4.

2.1.4. Uniform Degree Test of Simulation Rainfall. Generally, the uniformity coefficient of a stable rainfall simulation should be greater than 0.8 [16]. The uniform degree of rainfall can be calculated as follows:

$$k = 1 - \sum_{i=1}^{n} \frac{|x_i - x|}{nx}, \tag{1}$$

where k is the uniformity coefficient, x_i is the rainfall at the measurement positions, x is the average rainfall at the measurement positions, and n is the number of measurement positions.
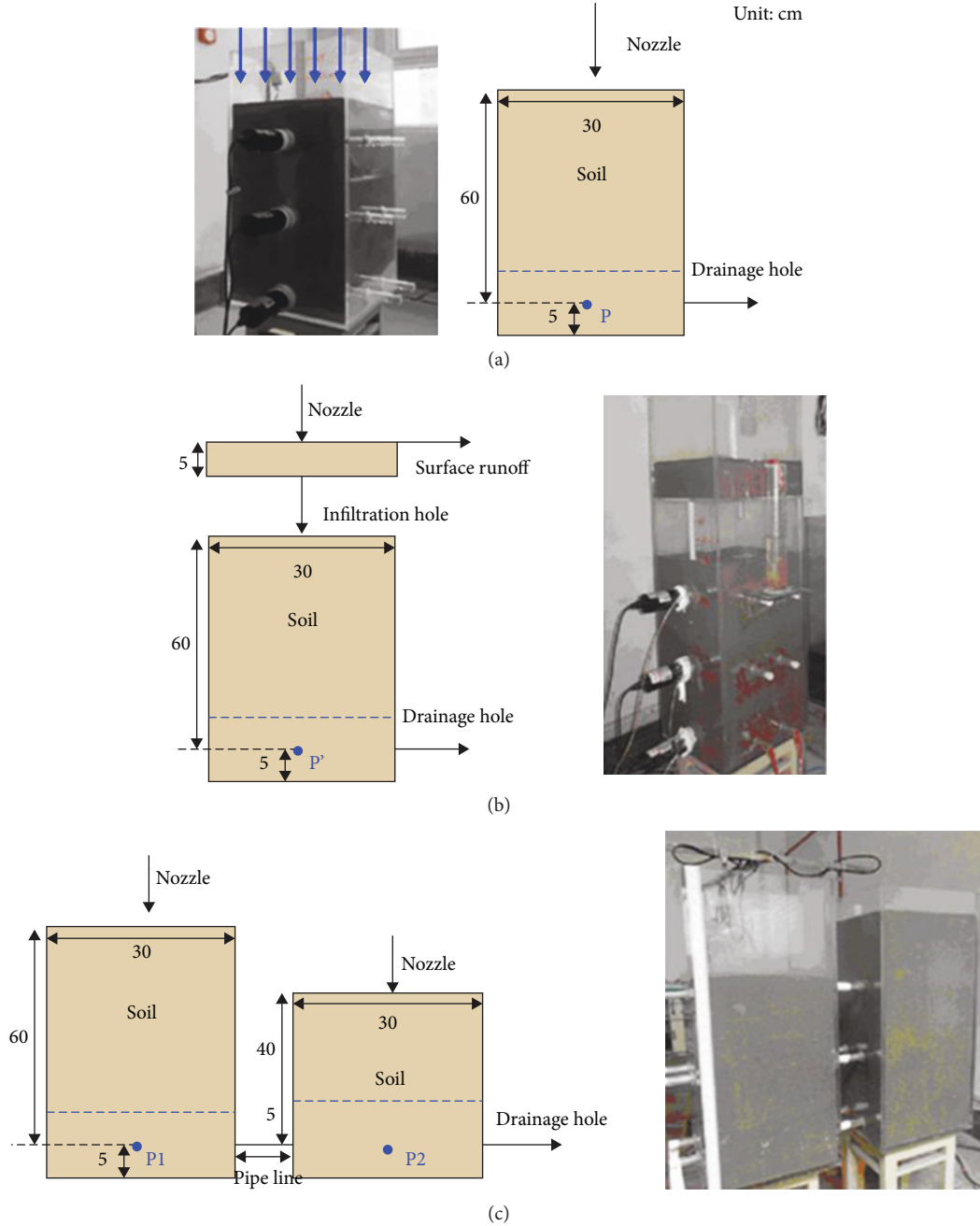
(a)

(b)

(c)

Figure 1: Physical tank model experiments (P, P', P1, and P2 are pore water pressure sensors): (a) simple tank model; (b) surface runoff tank model; (c) lateral water flow supply tank model.

In this test, four measuring glasses were randomly placed in the rainfall zone. The applied three rainfall events had rainfall intensities of 25, 45, and 65 mm/hr lasting for 30 min. The uniformity coefficients were calculated as 0.84, 0.88, and 0.90, respectively.

2.1.5. Pore Water Pressure and Drainage Records. To record the pore water pressure, PWP, two pore water pressure transducers (model number CYY2, Xi'an Weizheng Technology Corp. Ltd., Xi'an, China) have been used. Each transducer had a diameter of 3 cm, a height of 1.6 cm, and a measuring range of +10 kPa, with a deviation of 0.2%. A drainage line

on the right bottom of the physical tank model was prepared to calculate the drained water. The water was collected using measuring glasses. A video camera recorded the level of water inside the measuring glasses during the test (Figure 5).

Calibration of pore water pressure transducers is necessary before the experiments. A tank ($300 \times 300 \times 700$ mm) was employed for the calibration of the pore water pressure transducers. The transducers were placed in the bottom of the tank. Every time a 3 cm height of the water table was added at the top of the tank, the monitoring value of the transducers was recorded (the output of the transducers is electric current). The graph of applied pore water pressure

Figure 2: Soil being filled into the tank model. Every 5 cm depth soil layer is pressed by the flat.

values against the current values recorded by the PWP transducers is shown in Figure 6.

2.1.6. Data Collection and Software. We used a data acquisition system (Figure 7) (CK01L0R-C20 type) that adopts the RS485 communication interface, which supports long-distance data transmission transferring the recorded data by transducers to a computer. The system uses a MODBUS-RTU protocol and has high data transmission stability, versatility of the multichannel analog input, and 14-bit ADC precision. The collected data is an electric current (0-20 mA) which comes from the transducers.

A software designed by VC++ displayed real-time data and dynamic curves. The interface of the software is divided into three main parts (Figure 8). The left top box represents the real-time value of the water pressure, the top right part produces the monitor data graphs, and in the lower part, the original signals are displayed. The software functions include defining the units, producing the monitor data graph, recording data, and adjusting the monitoring time interval.

2.1.7. Testing Material. The soil material used in the experiments was collected from the toe of Ming Mountain, near the Yangtze River Bank, Chongqing, China (Figure 9). Ming Mountain is located at the Three Gorges Reservoir Area, where the average annual rainfall is 1074.6 mm and 70% of the annual rainfall occurs between May and September. The soil was relatively homogenous and consisted of quaternary alluvial materials.

~500 kg of soil materials was collected for conducting experiments. The materials were sieved through a no. 4 (4.75 mm) size sieve for removing the gallets. The soil's particle-size distribution curve is shown in Figure 10. The soil is classified as silty clay in which 90% of particle-size concentrates are in a range of 0.1-0.4 mm. The initial density of

materials was determined as 1.82-1.85 g/cm^3, while the saturated density was calculated as 2.04-2.07 g/cm^3.

2.2. Experiment Procedures. In this study, three types of conceptual tank models for three typical slopes were considered (Figure 1). Every test was conducted under similar initial conditions, such as geometry (cuboid), material (silty clay), moisture content, and initial groundwater level (PWP) (0.6-0.75 kPa, deviation +3%). In each test, the PWP sensor at the bottom of the tank recorded the changes of PWP during the rainfall events. The measuring glass collected the drainage.

2.2.1. Simple Tank Experiment. A total of 7 tests were conducted applying the simple tank model. The experiments included fixed and variable rainfall intensity-duration inputs for the hydrology calculations which are given in Table 2. For example, test 1 simulated a 25 mm/hr (36 min) rainfall event, while test 4 simulated the rainfall events of 25 mm/hr (12 min), 65 mm/hr (12 min), and 25 mm/hr (12 min). The arrangements are aimed at testing the pore pressure under different (variable) rainfall durations and intensities and reconcile the theory with the experimental results.

2.2.2. Surface Runoff Tank Experiment. Surface runoff tank experiments were conducted to investigate how the maximum infiltration rate controls the PWP production in the slope mass by reducing rainfall infiltration. A total of 3 tests were conducted at different rainfall intensities of 25, 45, and 65 mm/hr, and each rain event last for 24 min as shown in Table 3.

2.2.3. Lateral Water Flow Supply Tank Experiment. In addition, two tests were conducted using the lateral water flow supply tank experiment to investigate how lateral flow affects the PWP in both tanks (Table 4). Test 1 simulated a 45 mm/hr (24 min) rainfall event, while test 2 simulated the rainfall event of 65 mm/hr (36 min).

3. Results and Analysis

3.1. Simple Tank Experiment. The pore pressure is proportional to the groundwater level, and the simple tank experiment modal can be written as

$$H_{i+1} - H_i = r_i - d_i, \tag{2}$$

$$d_i = a \cdot H_i, \tag{3}$$

where H_{i+1} and H_i are the groundwater levels at time $i + 1$ and i, respectively; r_i and d_i are the rainfall and drainage at time i, respectively; and a is the parameter. Equations (2) and (3) show the process of rainfall-triggered groundwater pressure. For the model construction, understanding the relation between two parameters of rainfall and drainage can predict the changes of pore pressure. It is unnecessary to know the process parameter clearly like water flow velocity and suction. Figure 11 shows the PWP and drainage during tests 1-7 (Table 2). The PWP in the whole processes can be divided into three stages: (1) the initial stage without an
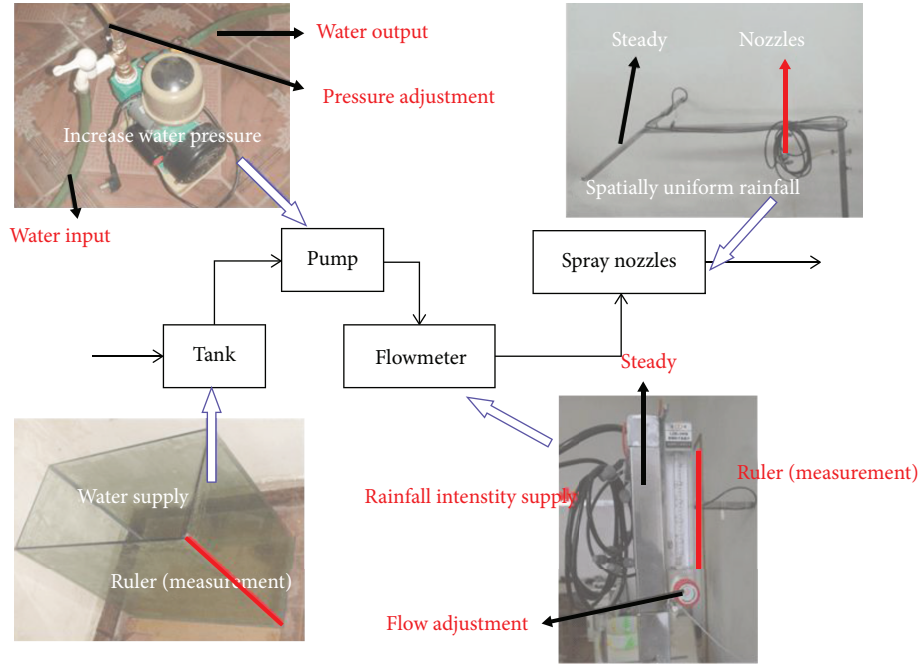
FIGURE 3: Rainfall simulator systems. They include a water supply (tank with ruler), a water output (pump), a rainfall intensity adjustment (flowmeter), and a rainfall output (spray nozzles).
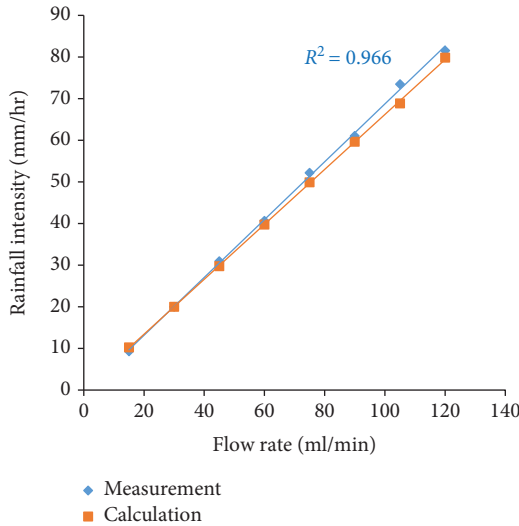

FIGURE 4: Rainfall intensity simulation test (measured rainfall intensity vs. applied rainfall intensity under different flow rate inputs).

obvious increase in PWP, (2) the second stage with a significant increase in PWP due to the impact of infiltration, and (3) the third stage with a decrease in PWP due to drainage. Figure 11(a) represents the variation of PWP during the experiment for tests 1 to 4. It can be observed that the peak values of PWP varied from 0.7 to 1.6 kPa, while the peak times of PWP varied from 36 to 40 min. Figure 11(b) indicates the variation of PWP during the experiment for tests 5 to 7. In these tests, the peak values of PWP changed from 0.9 to 1.3 kPa while peak times of PWP changed from

30 to 40 min. On the other hand, Figures 11(c) and 11(d) show the variation of drainage. The peak values of drainage rates for tests 1 to 4 were determined from 10 to 50 ml/min at the peak times from 30 to 50 min (Figure 11(c)), while the peak values of drainage rates for tests 5 to 7 were determined from 5 to 30 ml/min (Figure 11(d)) at the peak times from 24 to 40 min. It is found that the amount of rainfall affects the value and time of the PWP peak. Simply, a high rainfall value means a short time lag and a high value of the PWP peak.

Figure 12(a) investigates the relation between PWP and cumulative rainfall of test 3. In the initial stage, the value of PWP due to cumulative rainfall was increased constantly with a very small rate while at the second stage (increase stage), a significant rise in PWP was observed. The PWP decreased at the third stage (decrease stage) where the stage involves the power or exponent function. Degrees of correlations between PWP and cumulative rainfall in the initial, increase, and decrease stages were 0.93, 0.96, and 0.92, respectively. The relationship between drainage rate and PWP in test 3 is given in Figure 12(b). The figure demonstrates a linear relationship between PWP and the drainage rate with the correlation degree of 0.987. It can be observed that a higher PWP caused a faster drainage than a lower PWP.

From equation (2), H_{i+1} and H_i calculated by r_i and d_i are not accurate due to the rainfall time lag in the soil mass, while, in the original conceptual model, the tank model is empty without materials. Thus, equation (2) has no consideration of the time lag. The suggestion is adding a parameter between pore pressures and rainfall drainage to reduce the error. For shallow landslides, the time lag error may not be as obvious as deep-seated landslides. For the drainage, due
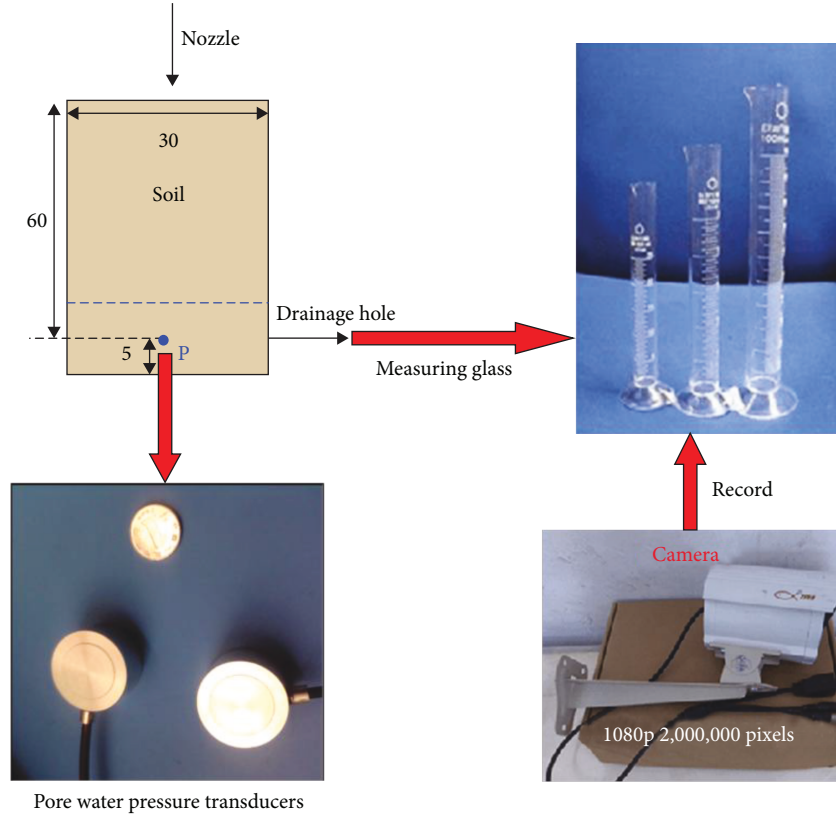
FIGURE 5: Pore water pressure and drainage records.

(a)

(b)
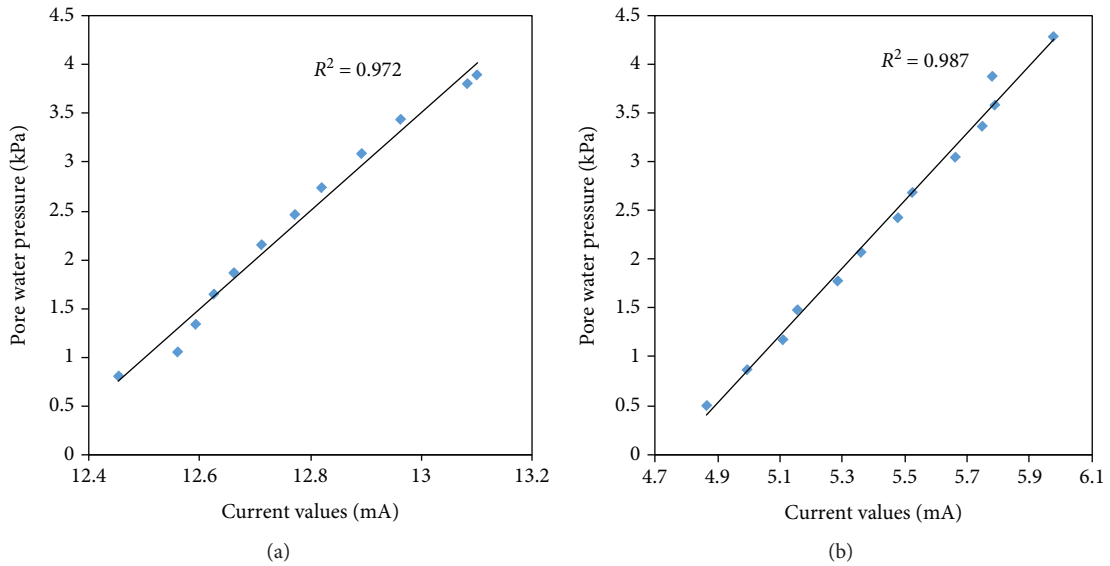
FIGURE 6: Pore water pressure sensor calibration.

to the less time lag effect of groundwater level reduction in the soil mass, equation (3) can basically describe the process accurately. Thus, the improvement of the model based on the pore pressure parameter can be written as

$$P_{i+1} - P_i = a1 \cdot (r_i - d_i), \quad d_i = a2 \cdot P_i, \qquad (4)$$

where P_{i+1} and P_i are the pore pressures at times $i+1$ and i, respectively; r_i and d_i are the rainfall and drainage at time i, respectively; and $a1$ and $a2$ are the parameters.

3.2. Surface Runoff Tank Experiment. For the surface runoff tank experiment, equation (5) would be added to

FIGURE 7: Data acquisition system. It includes an analog input interface, a 24 VDC power interface, and a USB-485converter.

FIGURE 8: Software for displaying monitoring data.

FIGURE 9: Soil sample location. They were collected from the toe of Ming Mountain, near the Yangtze River Bank, Chongqing, China.

Figure 10: Particle-size distribution curves of the used soil.

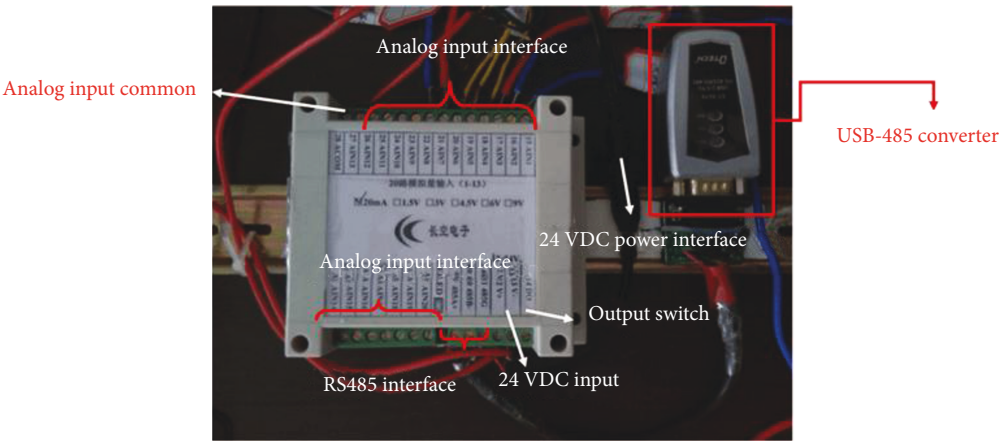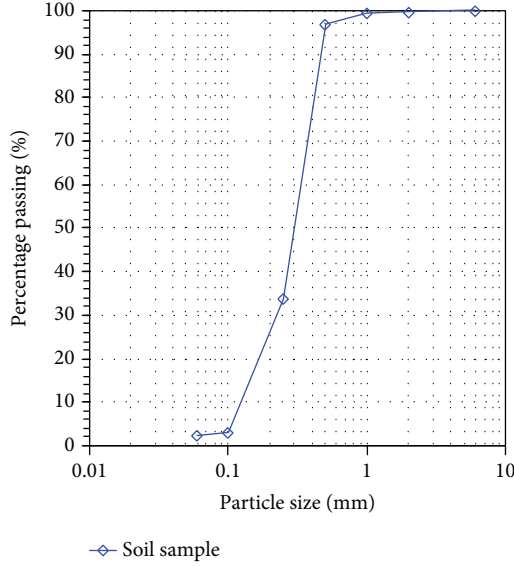Table 2: Experiment arrangements of the simple tank model.

No.	Rainfall input intensity (duration)	Output objects
1	25 mm/hr (36 min)	P; drainage
2	45 mm/hr (36 min)	P; drainage
3	65 mm/hr (36 min)	P; drainage
4	25 mm/hr (12 min), 65 mm/hr (12 min), 25 mm/hr (12 min)	P; drainage
5	25 mm/hr (24 min)	P; drainage
6	45 mm/hr (24 min)	P; drainage
7	65 mm/hr (24 min)	P; drainage

Table 3: Experiments of surface runoff tank model.

No.	Rainfall input-intensity (duration)	Output objects
1	25 mm/hr (24 min)	P'; drainage; surface runoff
2	45 mm/hr (24 min)	P'; drainage; surface runoff
3	65 mm/hr (24 min)	P'; drainage; surface runoff

Table 4: Experiments of the surface runoff tank model.

No.	Rainfall input intensity (duration)	Output objects
1	45 mm/hr (24 min)	P1; P2; drainage
2	65 mm/hr (24 min)	P1; P2; drainage

describe the maximum infiltration rate limitation (infiltration capacity):

$$H'_{i+1} - H'_i = i_i - d_i, \tag{5}$$

$$i_i = r_i - b \cdot s_i, \tag{6}$$

$$d_i = c \cdot H'_i, \tag{7}$$

where H'_{i+1} and H'_i are the groundwater tables at times $i + 1$ and i, respectively; r_i and d_i are the rainfall and drainage at time i, respectively; b and c are the learning parameters; and i_i means the infiltration at time i. s_i is the surface water runoff at time i. For the model construction, compared to the simple tank model, we just need to consider the infiltration capacity which is mainly decided by the soil hydraulic property. It is unnecessary to know the process parameter clearly like water flow velocity and soil hydraulic property like permeability. Thus, the distinct point between the simple and surface runoff tank experiment is the infiltration capacity. The upper tank has a limited infiltration ability realized by a downward infiltration hole. In other words, if there is heavy rainfall, the upper tank could drain some of the excess rain water as surface runoff. Figure 13(a) shows the variation of PWP vs. time for test numbers 1 to 3. It can be observed that peak values of PWP were from 0.85 to 0.95 kPa at the peak times of 45, 75, and 80 min for 65, 45, and 25 mm/hr rainfall events, respectively. As shown in Figure 13(a), the PWP under the 45 mm/hr and 65 mm/hr rainfall events were lower than the PWP under the same rainfall events during simple tank experiments (Figure 11(a)). The surface runoff in Figure 13(b) shows that infiltration thresholds controlled the rainfall surface runoff. During the rainfall periods, the drainage rates were 60, 25, and 7 ml/min for 65, 45, and 25 mm/hr rainfall events, respectively. For the bottom drainage (Figure 13(c)), the results were similar to the simple tank model, except that the maximum

infiltration reduced the amount of drainage. Peak values of drainage rates were 2, 5, and 5 ml/min for the 25, 45, and 65 mm/hr rainfall events, respectively, and peak times of drainage rates were 40, 60, and 63 min for 65, 45, and 25 mm/hr rainfall events, respectively. Figure 13(d) shows the rate of infiltration vs. time. Two types of surface runoff are distinguished: Hortonian overland flow occurs when precipitation exceeds the infiltration rate. Saturated overland flow occurs when the soil has reached complete saturation. It takes 3, 5, and 9 min to make the surface soil become saturated for 25, 45, and 65 mm/hr rainfall events, respectively. Then, the saturated overland flow occurs; thus, all the three rainfall infiltrations are limited around 38 ml/min. It can be seen that the maximum infiltration rate was about 38 ml/min for the 25, 45, and 65 mm/hr rainfall events and this indicates that the maximum hydraulic conductivity could be around 38 ml/min at the soil surface (the thin soil layer in the upper tank).

From equation (5), H_{i+1} and H_i calculated by i_i and d_i are still not accurate due to the rainfall time lag in the soil mass. Using i_i not r_i is necessary to reduce the error including the infiltration rate and time lag, while, in the original conceptual model, the tank model is empty without materials. Thus, equation (5) did not include the time
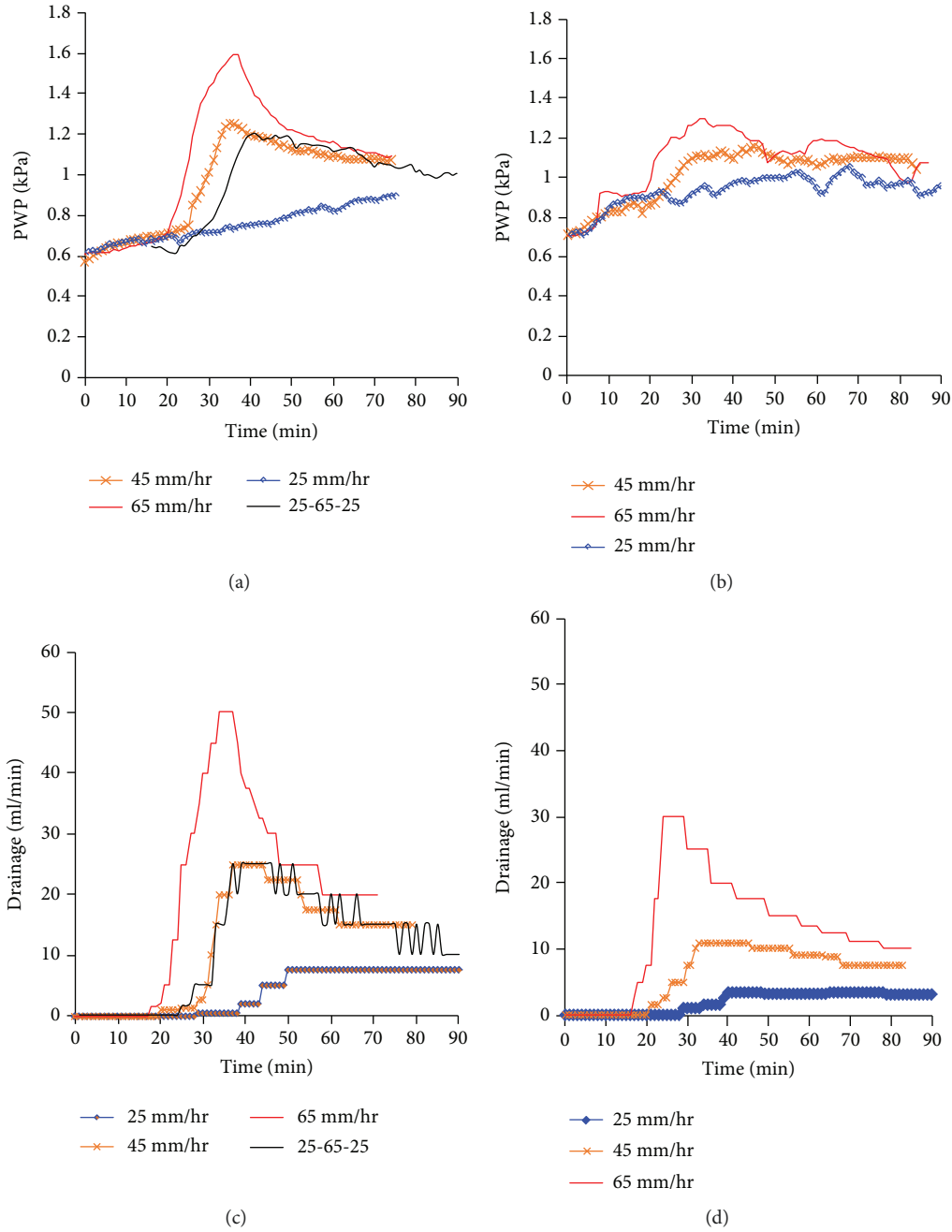
(a)

(b)

(c)

(d)

Figure 11: PWP and drainage rate in the simple tank experiments: (a) PWP vs. time for tests 1-4; (b) PWP vs. time for tests 5-7; (c) drainage vs. time for tests 1-4; (d) drainage vs. time for tests 5-7.

lag. The suggestion is adding a parameter between pore pressures and infiltration to reduce the error. A parameter, b, between rainfall and surface runoff is used to adjust the water balance between infiltration and rainfall in equation (6). For the drainage, due to the less time lag effect of the groundwater level reduction in the soil mass, equation (7) can describe the process accurately. Considering the surface runoff, only two parameters a' and b need to be determined by observing the rainfall, drainage, and pore pressure. Thus, it is a straightforward method. The improvement

of the model based on the pore pressure parameter can be written as

$$P'_{i+1} - P'_i = b1 \cdot (i_i - d_i), \quad d_i = b2 \cdot P'_i, \quad (8)$$

where P'_{i+1} and P'_i are the pore pressures at times $i+1$ and i, respectively; d_i is the rainfall and drainage at time i; $b1$ and $b2$ are the learning parameters; and i_i means the infiltration at time i.
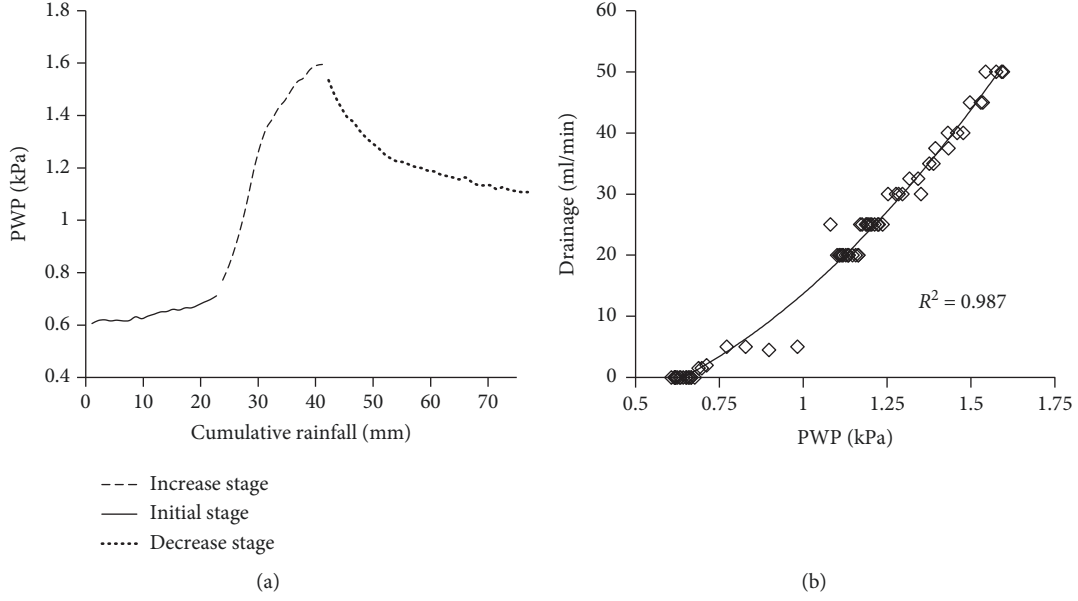
FIGURE 12: (a) PWP vs. cumulative rainfall (test 3); (b) PWP vs. drainage (test 3).

3.3. Lateral Water Flow Supply Tank Experiment. If the lateral water flow supply is considered, two tank models are necessary for calculation. The conceptual tank model could be

$$H_{1(i+1)} - H_{1i} = r_i - (H_{1i} - H_{2i}), \tag{9}$$

$$H_{2(i+1)} - H_{2i} = r_i - (H_{1i} - H_{2i}), \tag{10}$$

$$d_i = d \cdot H_{2i}, \tag{11}$$

where $H_{1(i+1)}$ and H_{1i} are the groundwater tables of the left tank at times $i + 1$ and i, respectively; $H_{2(i+1)}$ and H_{2i} are the groundwater tables of the right tank at times $i + 1$ and i, respectively; r_i and d_i are the rainfall and drainage at time i, respectively; and d is the learning parameter. For the model construction, compared to the simple tank model, the lateral water flow balance needs to be considered which is mainly dictated by the difference of the pore pressures of both sides. It is unnecessary to know the process parameter clearly like water flow velocity and soil property like permeability. Lateral water flow supply complicates the calculation of the groundwater table especially due to the coupling of the infiltration time lags. Figure 14 illustrates the monitoring data from the PWP sensors and the drainage hole in the lateral water flow supply tank model. From Figure 14(a), it can be observed that the PWP of the right (higher) tank model (P1) increased from -0.1 to 1 and from -0.5 to 2 kPa for the 45 and 65 mm/hr rainfall events, respectively. However, PWP for the right (lower) tank model (P2) was increased from 0.5 to 1.25 and from 0.5 to 2 kPa for the 45 and 65 mm/hr rainfall events, respectively. The maximum values of PWP for both P1 and P2 occurred after 40 to 50 min of the test. The figure shows that the PWP of the right (lower) tank model (P2) firstly begin to increase due to the water supply from the left (higher) tank model. The left tank model as

the water supplier mostly affects the right one, although in the beginning, the right one could offer some water to the left one conversely (as shown in Figure 1(c), the right tank's short vertical infiltration path could produce a higher groundwater table than that of the left tank in the beginning). The recorded drainage rates during the test are presented in Figure 14(b). The peak values of the drainage rates are 13 and 45 ml/min for the 45 and 65 mm/hr rainfall events, respectively, which occurred at 35 min after the beginning of the test for both rainfall events.

From equation (9), $H_{1(i+1)}$ and H_{1i} can be calculated by r_i and the lateral water flow supply which is mainly decided by the difference of the pore pressures in both tanks. From equation (10), $H_{2(i+1)}$ and H_{2i} can be calculated by r_i and the lateral water flow supply which is also mainly decided by the difference of the pore pressures in both tanks. As the lateral water flow is under the saturation state, the time lag effect is not obvious, while, in original conceptual model, the tank model is empty without materials. Thus, equations (9) and (10) are suggested to add two parameters ($c1$ and $c2$) between the groundwater pore pressures and lateral water flow pore pressures (Equations (12) and (13)). Considering the surface runoff, only two parameters a' and b need to be determined by observing the rainfall, drainage, and pore pressure. Thus, it is a straightforward method. The improvement of the model based on the pore pressure parameter can be written as

$$P_{1(i+1)} - P_{1i} = r_i - c1 \cdot (P_{1i} - P_{2i}), \tag{12}$$

$$P_{2(i+1)} - P_{2i} = r_i - c2 \cdot (P_{1i} - P_{2i}), \tag{13}$$

$$d_i = c3 \cdot P_{2i}, \tag{14}$$

where $P_{1(i+1)}$ and P_{1i} are the pore pressures of the left tank at times $i + 1$ and i, respectively; $P_{2(i+1)}$ and P_{2i} are
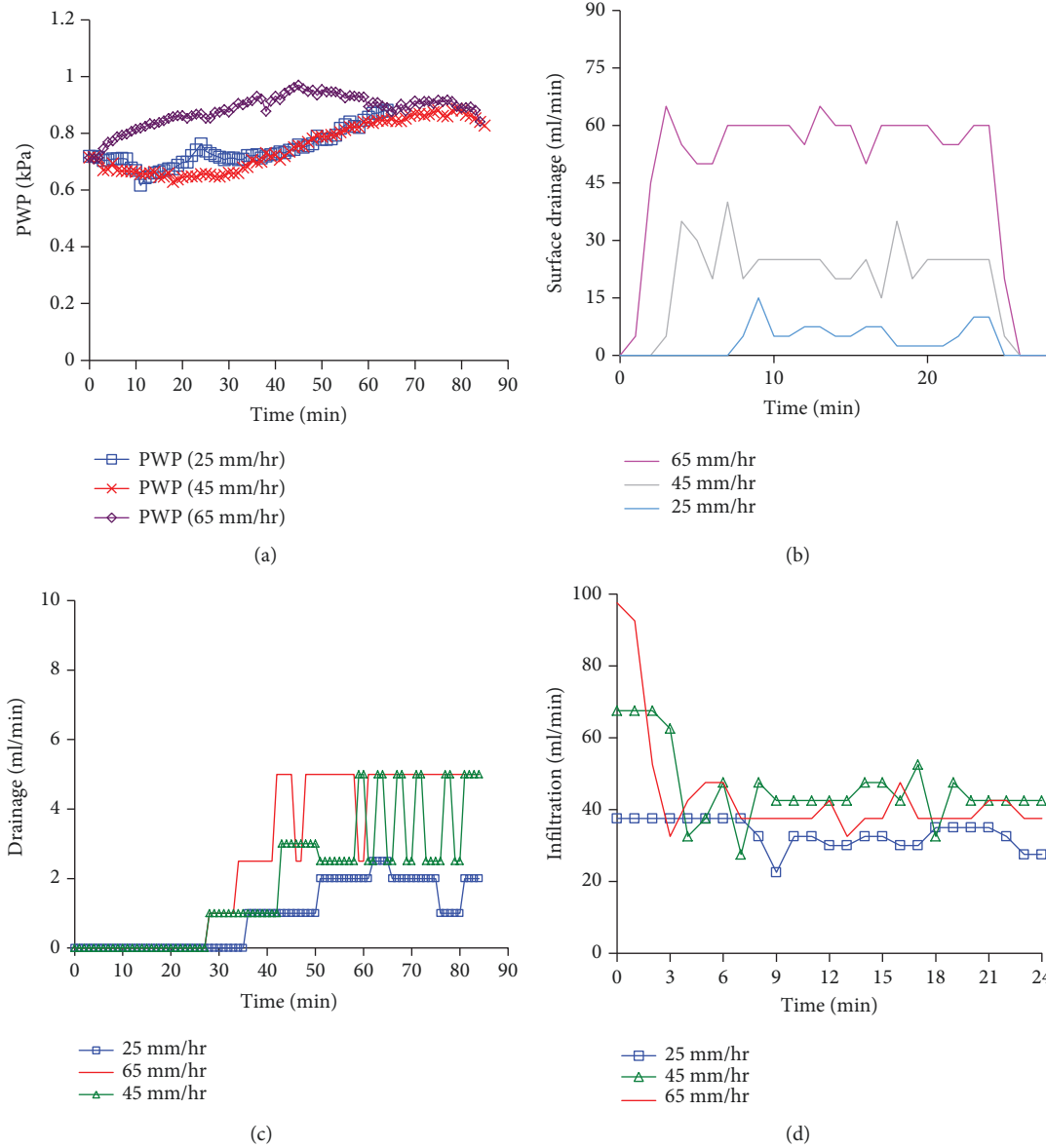
FIGURE 13: Monitoring data from P', surface runoff, and drainage hole (surface runoff tank model): (a) PWP (P') vs. time; (b) surface runoff drainage vs. time; (c) drainage rate vs. time; (d) infiltration rate vs. time.

the pore pressures of the right tank at times $i+1$ and i, respectively; r_i and d_i are the rainfall and drainage at time i, respectively; and $c1$, $c2$, and $c3$ are the parameters.

4. Conclusions

Changes of PWP are controlled by the balancing among the rainfall infiltration, water flow supply, and the drainage. The relationships between PWP on the bottom of the tank, drainage, and rainfall based on three kinds of physical models (the simple tank model, surface runoff tank model, and water flow supply tank model) were investigated. Drainage processes under different rainfall

events were also deciphered. Some conclusions are as follows:

(1) The amount of rainfall affects the value and time of PWP peak. Simply, a high rainfall value means a short time lag and a high value of the PWP peak. PWP decreases the effective stress and changes the stress state in the soil that eventually leads to slope failure. In addition, rainfall infiltration replaces the air in the void spaces with water. Since water is heavier than air, this will increase the soil weight. Greater weight means higher stress and being prone to be dragged down by gravity, leading to slope instability. As a result, the increase in the peak PWP will increase the damage to the slope engineering
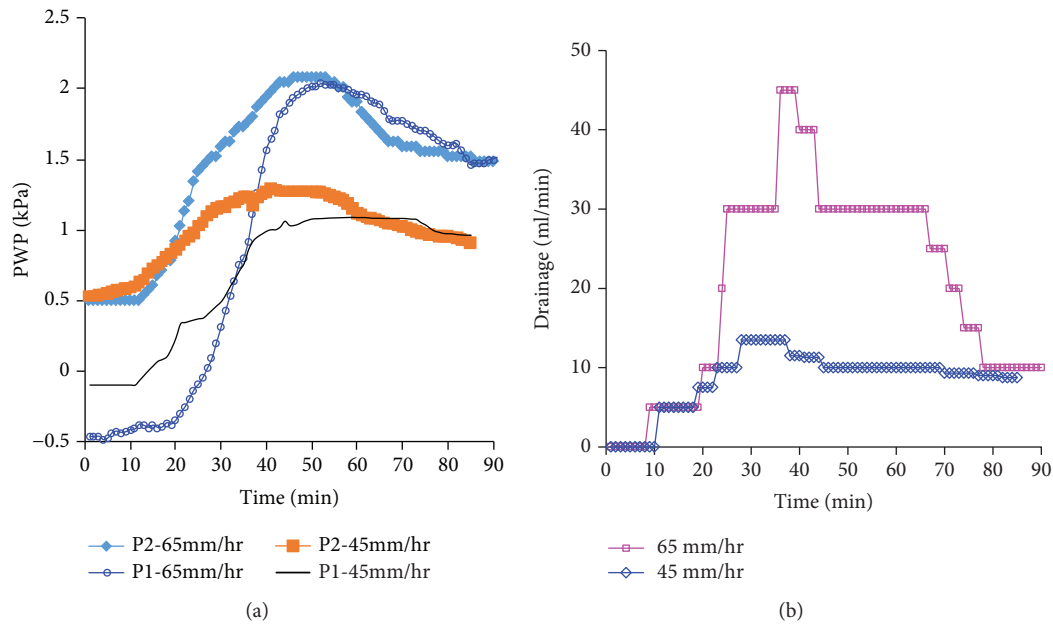
(a)

(b)

Figure 14: Monitoring data from the PWP sensors and drainage hole (water flow supply tank model): (a) PWP (P1 and P2) vs. time; (b) drainage vs. time.

(2) Infiltration capacity of the surface soil controls the rainfall surface runoff and infiltration capacity. With the decrease of the infiltration threshold, the soil infiltration capacity is reduced and the surface runoff is gradually increased. For the law of rainfall infiltration in the slope mass, understanding the threshold of infiltration of the surface soil is very important

(3) Lateral water flow from a higher part to a lower part of a slope system can fast improve the PWP of the lower part which is mainly dictated by the differences of pore pressure in both sides

(4) The tank model based on the optimized method does not consider the water flow process but needs parameter training. The parameter advance is necessary for setting up the direct links between the pore pressure and rainfall drainage as well as improving the accuracy of the model

Data Availability

Please contact the corresponding author.

Conflicts of Interest

The authors declare that they have no conflicts of interest.

Acknowledgments

References

[1] E. Damiano, R. Greco, A. Guida, L. Olivares, and L. Picarelli, "Investigation on rainwater infiltration into layered shallow covers in pyroclastic soils and its effect on slope stability," *Engineering Geology*, vol. 220, pp. 208–218, 2017.

[2] M. Pirone, R. Papa, M. V. Nicotera, and G. Urciuoli, "Hydraulic behaviour of unsaturated pyroclastic soil observed at different scales," *Procedia Engineering*, vol. 158, pp. 182–187, 2016.

[3] M. Mustafa, M. H. Isa, R. B. Rezaur, and H. Rahardjo, "Data-driven modelling for pore water pressure variation responses to rainfall," in *WIT Transactions on The Built Environment*, vol. 1, pp. 447–455, WIT Press, 2015.

[4] S. K. Kampf and S. J. Burges, "A framework for classifying and comparing distributed hillslope and catchment hydrologic models," *Water Resources Research*, vol. 43, no. 5, 2007.

[5] G. Rianna, L. Pagano, and G. Urciuoli, "Investigation of soil-atmosphere interaction in pyroclastic soils," *Journal of Hydrology*, vol. 510, pp. 480–492, 2014.

[6] W. Shao, T. Bogaard, M. Bakker, and M. Berti, "The influence of preferential flow on pressure propagation and landslide triggering of the Rocca Pitigliana landslide," *Journal of Hydrology*, vol. 543, pp. 360–372, 2016.

[7] N. A. Abebe, F. L. Ogden, and N. R. Pradhan, "Sensitivity and uncertainty analysis of the conceptual HBV rainfall–runoff model: implications for parameter estimation," *Journal of Hydrology*, vol. 389, no. 3-4, pp. 301–310, 2010.

[8] F. Faris and F. Fathani, "A coupled hydrology/slope kinematics model for developing early warning criteria in the Kalitlaga landslide, Banjarnegara, Indonesia," in *Progress of Geo-Disaster Mitigation Technology in Asia*, Environmental Science and Engineering (Environmental Engineering), F. Wang, M. Miyajima, T. Li, W. Shan, and T. Fathani, Eds., pp. 453–467, Springer, Berlin, Heidelberg, 2013.

[9] Y. Ishihara and S. Kobatake, "Runoff model for flood forecasting," *Bulletin of the Disaster Prevention Research Institute*, vol. 29, no. 1, pp. 27–43, 1979.

[10] H. Ohtsu, S. Janrungautai, and K. Takahashi, "A study on the slope risk evaluation due to rainfall using the simplified storage tank model," in *Proceeding of the 2nd Southeast Asia Workshop on Rock Engineering*, pp. 67–72, Bangkok, Thailand, 2003.

[11] K. Takahashi, Y. Ohnish, J. Xiong, and T. Koyama, "Tank model and its application to groundwater table prediction of slope," *Chinese Journal of Rock Mechanics and Engineering*, vol. 27, no. 12, pp. 2501–2508, 2008.

[12] J. Xiong, K. T. Ohnish, and T. Koyama, "Parameter determination of multi-tank model with dynamically dimensioned search," in *Process Symposium Rock Mechanics*, pp. 19–24, Japan, Kyoto, 2009.

[13] W. Bodhinayake, B. C. Si, and K. Noborio, "Determination of hydraulic properties in sloping landscapes from tension and double-ring infiltrometers," *Vadose Zone Journal*, vol. 3, no. 3, pp. 964–970, 2004.

[14] W. Nie, *Estimating and predicting pore-pressure influence on deep-seated landslides, [M.S. thesis]*, Technische Universität München, 2017.

[15] W. Nie, M. Krautblatter, K. Leith, K. Thuro, and J. Festl, "A modified tank model including snowmelt and infiltration time lags for deep-seated landslides in alpine environments (Aggenalm, Germany)," *Natural Hazards and Earth System Sciences*, vol. 17, no. 9, pp. 1595–1610, 2017.

[16] W. Nie, Y. C. Liang, L. Chen, and W. Shao, "Modelling of river-groundwater interactions under rainfall events based on a modified tank model," *Geofluids*, vol. 2017, Article ID 5192473, 11 pages, 2017.

Research Article

Evaluate the Probability of Failure in Rainfall-Induced Landslides Using a Fuzzy Point Estimate Method

Ya-Sin Yang and **Hsin-Fu Yeh**

Department of Resources Engineering, National Cheng Kung University, No. 1 University Road, Tainan City, Taiwan

Correspondence should be addressed to Hsin-Fu Yeh; hfyeh22@gmail.com

Traditional slope stability analysis mostly adopts the limit equilibrium method, which predetermines the slope failure surface and assumes that failure occurs simultaneously at all points of the failure surface. The method is based on the balance of forces and torques. The slope stability is represented by the factor of safety. The lowest factor of safety obtained after repeated analysis indicates the most failure-prone slope surface. However, the factor of safety for only one slope failure surface is obtained when applying this method. The distribution and changes of factor of safety in the interior of the slope are not identified. In addition, the analysis of factor of safety is influenced by the uncertainty in soil mechanical parameters, whereas uncertainty is not quantified in the traditional deterministic analysis. Therefore, a probabilistic approach, which uses the probability distribution function to explain the randomness of parameters, is proposed for quantifying the uncertainty. Nonetheless, when the observation data are not sufficient for determining the probability distribution function, the fuzzy theory can be an alternative method for the analysis. The fuzzy theory is based on fuzzy sets. It expresses the ambiguity of incomplete sets of information using a membership function. Moreover, a correct judgment can be made without verbose iterations. Hence, the aim of this study is to examine the uncertainty in soil mechanical parameters. The membership functions between soil mechanical parameters, i.e., cohesion and angle of internal friction, were constructed based on the fuzzy theory. The fuzzy point estimation was used in combination with the hydrologic and mechanical coupling model on HYDRUS 2D and the Slope Cube Module. The local factor of safety at different depths of the slope was determined using the local factor of safety theory. The probability of failure at different depths was calculated through reliability analysis, which could serve as an early warning for subsequent slope failures.

1. Introduction

Slope stability is affected by intrinsic and triggering factors. The intrinsic factors include soil, groundwater, vegetation, slope gradient, and lithology. The triggering factors include volcanic eruptions, earthquakes, and rainfall. A common trigger for natural slopes is rainfall [1–8]. Rainfall-induced slope failures are usually shallow, with a depth of failure not exceeding three meters, and they likely occur on slopes with a gradient of 30° to 40° [9]. Lu and Godt [10] suggested that the failure mechanism for rainfall-induced shallow failures is that, as the rainfall infiltrates into the soil, the soil matric suction declines and the pore pressure rises positively. As the soil matric suction decreases, there would be a

nonlinear drop in soil shear strength. Hence, when the soil is nearly saturated, the matric suction approaches zero, resulting in slope instability and further inducing disasters such as landslides and debris flow.

Studies related to rainfall-induced slope failure can be divided into three types according to their theoretical basis: statistical-model-based [4, 11–19], contributing factor [20–24], and physical-model-based analyses [5, 25–31]. Among them, the physical-model-based analysis coupled with hydromechanical mechanism models has overcome the excessive dependence of statistical models on rainfall data. The method can describe the hydromechanical changes caused by transient rainfall in the interior of the slope, as well as the associated failure mechanism. With its higher

predictive power and capability of quantifying the effect of each parameter on slope stability [32], the method is now widely used. Nevertheless, the analytical process is limited by uncertainty caused by measurement error, spatial variability, and limited information [33]. The result of slope stability analysis may deviate from reality owing to the uncertainty in model parameters [34].

Therefore, probabilistic analysis is used to quantify the uncertainty [7, 35–39]. Nawari and Liang [40] and Giasi et al. [41] suggested that an adequate number of reliable observation values are required for probabilistic analysis. Precise mean values and standard deviations are derived from the observation values to construct a reasonable probability density function [42]. In addition, Juang (in 1998) and Nawari and Liang [40] proposed that the uncertainty in parameters may be nonstochastic. Previous studies have shown that, when the data available are not sufficient for defining the probability density function, the uncertainty in rock mass parameters can be expressed effectively with the use of a fuzzy set [43, 44]. This method has been applied to some of the cases for slope stability analysis [30, 41, 45–48].

Traditional slope stability analysis adopts the limit equilibrium analysis, which discretizes the potential sliding soil mass into smaller vertical slices without considering soil deformation. It assumes that failure occurs simultaneously at all points of the failure surface. This method is based on the balance of forces and torques. The slope stability is represented by the factor of safety. Various analytical methods have been developed based on different assumptions on the balance of forces [49–52]. In recent years, the finite element method has been widely applied to slope stability analysis in order to calculate the factor of safety in slopes with high complexity (complex geometries, boundaries, and loading conditions) and to investigate the stress–strain relationship in soil [53–58]. Liu and Shao [59] introduced the finite element limit equilibrium analysis, which combines the limit equilibrium analysis and finite element analysis. It is used to examine the slope stability and evaluate the breaking load of a rigid foundation and retaining wall.

The above analytical methods based on the balance of forces or on the stress field usually seek a single general slope stability index. Hence, it is almost impossible to identify the changes in pore water pressure and effective stress owing to rainfall infiltration, or the actual slope failure surface and its geometry. Therefore, Lu et al. [60] proposed the theory of local factor of safety (LFS), which can calculate the factor of safety at discrete points in the soil mass and describe the geometry and position of the potential failure surface. Previous studies have revealed that the factor of safety (probability of failure) is highly dependent on the coefficient of correlation between cohesion and angle of internal friction [61–63]. It has been shown that the two parameters are not independent of each other and that the correlation between them is mostly negative [64–67]. Jiang et al. [63] noted that, when analyzing the probability of failure, a significant deviation may occur if we assume an independent relationship between cohesion and angle of internal

friction (i.e., no correlation). Aladejare and Wang [68] also pointed out that neglecting the coefficient of correlation between cohesion and angle of internal friction may result in an order-of-magnitude difference in the result of the analysis. Moreover, the factor of safety does not necessarily reflect the actual safety level. With the use of reliability analysis, considering the variability of variables and calculating the probability of failure and reliability index will provide a more valid representation of the reliability of slope stability.

Hence, the aim of this study is to examine the uncertainty in soil mechanical parameters. The membership functions for the soil mechanical parameters, i.e., cohesion and angle of internal friction, were constructed based on the fuzzy theory. The fuzzy point estimation was used in combination with the hydromechanical coupling model on HYDRUS 2D and the Slope Cube Module. The local factor of safety at different depths of the slope was determined. The probability of failure at different depths was calculated through reliability analysis, which could serve as an early warning for subsequent slope failures.

2. Materials and Methods

2.1. Seepage Analysis. In this study, the analytic solution of transient seepage in an unsaturated layer developed by Šimůnek et al. [69] based on the Richards equation was used as the governing equation of the two-dimensional seepage as follows:

$$\frac{\partial \theta(h_m)}{\partial t} = \nabla \cdot K(h_m) \nabla H + W, \tag{1}$$

where θ is the volumetric water content (-), t is the time (T), h_m is the pore water pressure or hydraulic head (L), H is the total head (L), W is the source or sink ($L^3 T^{-1}$), $K(h_m)$ is the hydraulic conductivity function (HCF) that varies with the pore water pressure (LT^{-1}), and $\theta(h_m)$ is the volumetric water content that varies with the pore pressure in the soil-water retention curve (SWRC) ($-$).

The soil water content and HCF of an unsaturated zone vary with the hydraulic head and are highly nonlinear. In this study, the relationship between soil water content and matric suction was predicted using the closed-form analytic solution proposed by van Genuchten [70] (see equation (2)). It is also referred to as the SWRC. Based on the SWRC, Mualem [71] introduced the HCF for unsaturated layers (see equation (3)).

$$\theta(h) = \theta_r + \frac{\theta_s - \theta_r}{\left[1 + (\alpha h)^n\right]^m}, \tag{2}$$

$$K = K_s S_e^l \left[1 - \left(1 - S_e^{1/m}\right)^m\right]^2, \tag{3}$$

where θ_s is the saturated soil water content ($-$), θ_r is the residual soil water content ($-$), h is the matric suction ($ML^{-1}T^{-2}$), α is the reciprocal correlation of the air-entry value ($M^{-1}LT^2$), n is related to the SWRC gradient

$(-)$, K_s is the hydraulic conductivity in saturated soil (LT^{-1}), $m = 1 - 1/n$, l is the coefficient of correlation of soil porosity $(-)$, and S_e is the equivalent degree of saturation $(-)$, shown as

$$S_e = \frac{\theta - \theta_r}{\theta_s - \theta_r}. \tag{4}$$

2.2. Principle of Effective Stress in Unsaturated Soil.

We adopted the principle of effective stress proposed by Lu and Likos [72], which unified the possible physical and chemical interparticle mechanisms in soil and proposed the concept of suction stress. The effective stress based on the concept of suction stress is shown as follows [73]:

$$\sigma' = \sigma - u_a - \sigma^s, \tag{5}$$

$$\sigma^s = -\sigma_c = -\sigma_{cap} - \sigma_{pc} - S(u_a - u_w), \tag{6}$$

where σ^s is the suction stress $(ML^{-1}T^{-2})$, σ_c is the Born repulsive force $(ML^{-1}T^{-2})$, σ_{cap} is the capillary force $(ML^{-1}T^{-2})$, σ_{pc} is the combined van der Waals attractive force and electric double-layer force $(ML^{-1}T^{-2})$, S is the degree of saturation in the soil $(-)$, and $(u_a - u_w)$ is also the matric suction $(ML^{-1}T^{-2})$. The matric suction, capillary force, van der Waals attractive force, and electric double-layer force balance the Born repulsive force in the soil. However, as the grain size of the soil increases, the effect of the van der Waals attractive force and electric double-layer force becomes negligible.

As each of the stress components in soil can be expressed as a function of matric suction $(u_a - u_w)$, degree of saturation S, and water content θ, and as the suction stress in soil is mainly controlled by the soil water content, Lu et al. [74] derived the suction stress characteristic curve (SSCC) from the soil-water characteristic curve, based on the principle of thermodynamics and by considering suction stress as the energy stored in the pedon. The following analytical solution is shown:

$$\sigma^s = -S_e(u_a - u_w) = -\frac{S - S_r}{1 - S_r}(u_a - u_w) = -\frac{\theta - \theta_r}{\theta_s - \theta_r}(u_a - u_w), \tag{7}$$

where S_e is the equivalent degree of saturation (-), S_r is the residual saturation (-), θ is the soil water content (-), θ_s is the saturated soil water content (-), and θ_r is the residual soil water content (-). Moreover, van Genuchten [70] calculated the equivalent degree of saturation using the following closed-form equation:

$$S_e = -\frac{S - S_r}{1 - S_r} = \left\{ \frac{1}{1 + [\alpha(u_a - u_w)]^n} \right\}^{1 - 1/n}, \tag{8}$$

where α and n are fitting parameters correlated to the air-entry value of SWRC and the gradient, respectively. Therefore, the suction stress can be expressed in the following
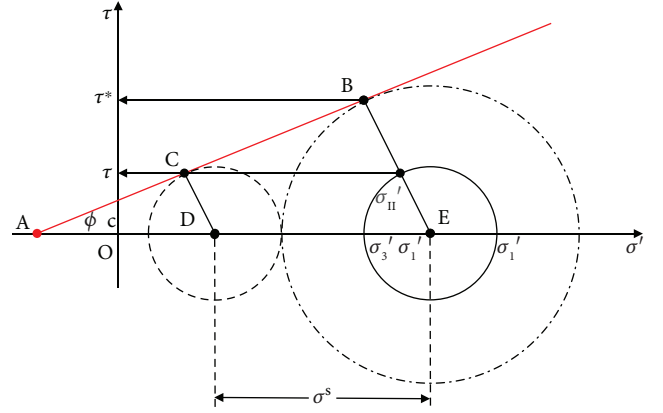

FIGURE 1: Conceptual illustration of the local factor of safety [60].

forms. The change in soil suction stress with water content can be illustrated by estimating the SSCC:

$$\sigma^s = -\frac{(u_a - u_w)}{\left\{1 + [\alpha(u_a - u_w)]^n\right\}^{(n-1)/n}},$$
$$\sigma^s = -\frac{S_e}{\alpha}\left(S_e^{n/1-n} - 1\right)^{1/n}. \tag{9}$$

2.3. Theory of Local Factor of Safety.

The local factor of safety is based on the Mohr–Coulomb failure criterion, and is defined by the ratio between the potential Coulomb stress and the current Coulomb stress as follows:

$$\text{LFS} = \frac{\tau*}{\tau}, \tag{10}$$

where $\tau*$ is the potential Coulomb stress and τ is the current Coulomb stress. The theory is illustrated in Figure 1, in which the current state of stress in the soil is represented by the realization of Mohr's circle. The shear stress τ acting on the soil when a failure occurs is obtained by translating Mohr's circle to the Mohr–Coulomb failure envelope. When the effective stress of the soil decreases owing to the increase in water content, Mohr's circle is translated leftward, during which its size is almost unchanged. By extending the Coulomb stress, the potential Coulomb stress $\tau*$ at the intersection point of Mohr's circle and the Mohr–Coulomb failure envelope (point B) is determined. The local factor of safety is obtained by the calculation of similar triangles as follows:

$$\text{LFS} = \frac{\tau*}{\tau} = \frac{\text{BE}}{\text{CD}} = \frac{\text{AE}}{\text{AD}}, \tag{11}$$

$$\text{BE} = \text{AE} \sin \varphi = \left(\frac{c'}{\tan \varphi} + \frac{\sigma_1' + \sigma_3'}{2} \right) \times \sin \varphi$$
$$= \left[2c' + \left(\sigma_1' + \sigma_3' \right) \tan \varphi \right] \times \frac{\cos \varphi'}{2}, \tag{12}$$
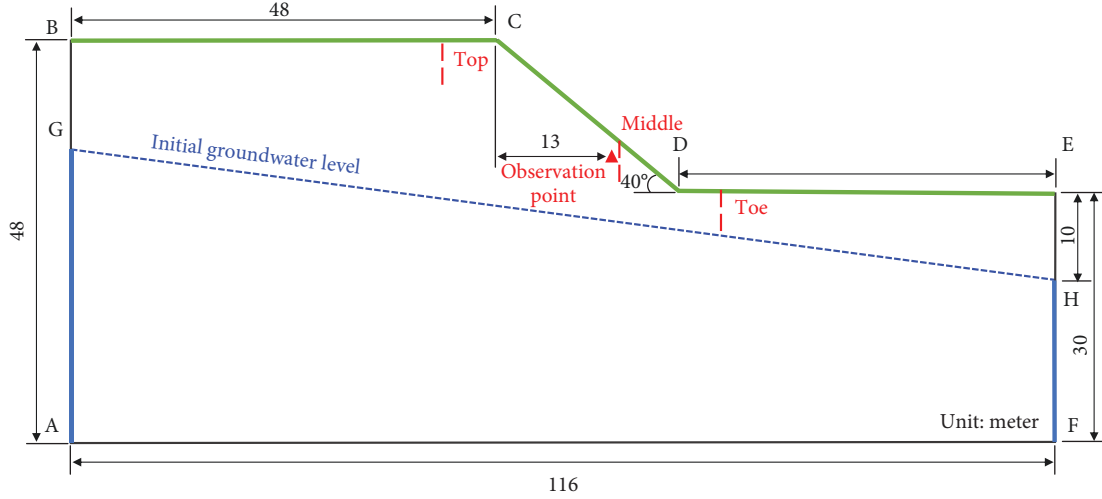
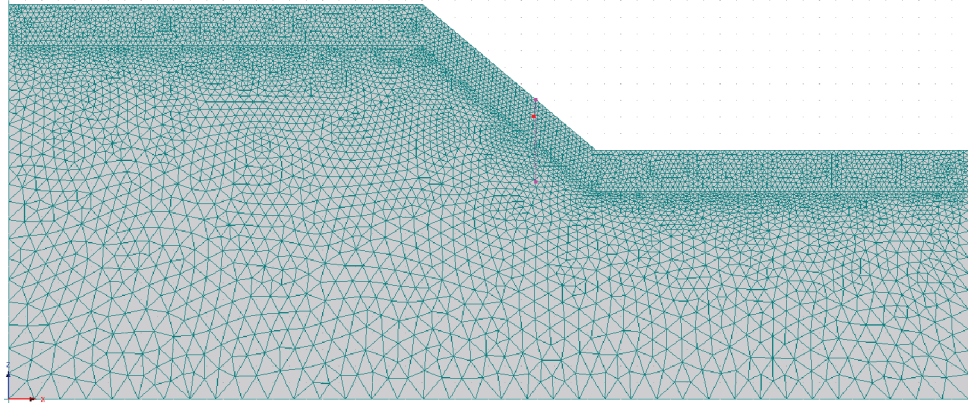FIGURE 2: Illustration of the slope conceptual model.

FIGURE 3: Illustration of the slope model grid.

where c' is the effective cohesion of the soil, φ' is the effective angle of friction of the soil, and σ'_1 and σ'_3 are the maximum and minimum effective stresses of the soil, respectively.

The following expression of LFS can be derived from equations (11) and (12):

$$\text{LFS} = \frac{\tau *}{\tau} = \frac{\cos \varphi}{\sigma'_1 - \sigma'_3} \left[2c' + \left(\sigma'_1 + \sigma'_3 \right) \tan \varphi' \right]. \quad (13)$$

Substituting equation (5) into equation (13) gives

$$\text{LFS} = \frac{\tau *}{\tau} = \frac{\cos \varphi'}{\sigma_1 - \sigma_3} \left[2c' + (\sigma_1 + \sigma_3 - 2\sigma_s) \tan \varphi' \right]. \quad (14)$$

Using modeling and finite element analysis, we can analyze the effect of changes in water content or suction stress on the stability of soil units at different locations or depths of the slope.

2.4. Fuzzy Theory. The fuzzy theory is also called the fuzzy set theory. The fuzzy number is a special case in a fuzzy set. If no assumption is specified (when limited data are available), the fuzzy number is assumed to be triangular and comprises maximum (a), minimum (b), and modal or peak (m) values. The maximum and minimum values of a fuzzy number can be expressed as

$$\begin{aligned} x_a &= m - k\sigma_x, \\ x_b &= m + k\sigma_x. \end{aligned} \quad (15)$$

The k-value is determined by the actual engineering situation of the slope and ranges between 0.5 and 3 [45]. The larger the k-value, the larger is the scope of distribution of the mechanical parameter, and hence, the lower is the reliability of the selected parameter, and vice versa. In this study, the k-value was considered to be 2.

Fuzzy point estimation combines the vertex method and the point estimate method. The vertex method was proposed by Dong and Shah [75]. The method is based on α-cut and interval analysis. It computes combinations of vertices of the variables, which replace the membership functions as an input variable. Therefore, given N membership functions of the input variables, there would be 2^N combinations of vertices. The point estimate method developed by

Rosenblueth [76] evaluates the uncertainty parameters of a performance function. The mean value and standard deviation of a performance function are assessed using a two-point estimate. The upper limits of variables obtained from the α-cut sets are $(c_{-}^{\alpha_i}, c_{+}^{\alpha_i})$ and $(\varphi_{-}^{\alpha_i}, \varphi_{+}^{\alpha_i})$. Four sets of vertex combinations are derived through modeling to yield four sets of output values $(\mathrm{FS}_{--}, \mathrm{FS}_{-+}, \mathrm{FS}_{+-}, \mathrm{FS}_{++})$. The contributions of each α-cut set value to the result are compared. In this study, we adopted the concept of fuzzy weighted average. The mean value and standard deviation of the factor of safety are illustrated below:

$$E[\mathrm{FS}] = \frac{\sum_{i=1}^{M} \alpha_i \mathrm{FS}_{\alpha_i}}{\sum_{i=1}^{M} \alpha_i},$$

$$\sigma^2[\mathrm{FS}] = \frac{\sum_{i=1}^{M} \sum_{j=1}^{2^n} \alpha_i \mathrm{FS}_{\alpha_i}^2}{\sum_{i=1}^{M} \alpha_i} - E[\mathrm{FS}], \quad (16)$$

where M is the number of α-cut sets. Nine α-cut sets ranging from 0.1 to 0.9 were considered in this study.

The probability of failure was calculated from the reliability index [77] assuming a normally distributed factor of safety. Therefore, the reliability index is normally distributed. The reliability index β and the probability of failure (P_f) can be represented as follows:

$$\beta = \frac{E[\mathrm{FS}] - 1}{\sigma_{\mathrm{FS}}},$$

$$P_f = 1 - \Phi(\beta) = \Phi(-\beta). \quad (17)$$

3. Results and Discussion

In this study, a two-dimensional numerical model was developed using HYDRUS 2D. We performed a transient seepage analysis based on the seepage theory proposed by Richards (1931). The Slope Cube Module was used to examine the stress change experienced by the soil. Slope stability analysis was performed using the local factor of safety theory. The probability of failure at different depths of the slope was calculated through reliability analysis. The slope is 18 m high, with a slope angle of 40°. Figure 2 illustrates the conceptual model of the slope. BCDE is the boundary of rainfall infiltration, AG and HF define the hydraulic head boundaries, and BG, EH, and AF are the zero-flow boundaries. Observation surfaces were set at the top, middle, and toe of the slope, whereas observation points were installed at the middle part of the slope. As shown in Figure 3, the grid consists of 5,661 nodes and 11,524 elements. We simulated the rainfall intensity with reference to the data from the Alishan Weather Station where the greatest rainfall was recorded during the 2009 Typhoon Morakot. The recorded 48 h cumulative rainfall was 2,361 mm. The simulation duration was set to 48 h and the rainfall intensity was set to 49.18 mm/h.

We have considered loam and silt as examples in this study. The soil hydraulic properties and mechanical parameters are listed in Tables 1 and 2. Using the empirical formula developed by van Genuchten [70], we estimated the SWRC

TABLE 1: Hydraulic properties of soil (Carsel and Parrish, 1988).

Soil type	θ_s	θ_r	$\alpha(kPa^{-1})$	$n(-)$	K_s (m/sec)
Loam	0.43	0.078	0.36	1.56	3.0×10^{-6}
Silt	0.46	0.034	0.16	1.37	7.0×10^{-7}

TABLE 2: Mechanical properties of soil (MnDOT Pavement Design Manual, 2007).

Soil type	G_s (-)	c (kPa)	φ (°)	E (kPa)	v (-)
Loam	2.65	10	35	15,000	0.30
Silt	2.70	15	30	10,000	0.35

and the HCF. The hydraulic characteristics of loam and silt are shown in Figure 4.

The variables in this study include cohesion and the angle of internal friction. The values from Table 2 were considered as the mean. The equations for triangular fuzzy numbers are as follows:

$$x_c = \mathrm{TFN}[m_c - 2\sigma_c, m_c, m_c + 2\sigma_c]$$
$$= \mathrm{TFN}[m_c - 2(m_c \times \mathrm{cov}_c), m_c, m_c$$
$$+ 2(m_c \times \mathrm{cov}_c)],$$
$$x_\varphi = \mathrm{TFN}[m_\varphi - 2\sigma_\varphi, m_\varphi, m_\varphi + 2\sigma_\varphi]$$
$$= \mathrm{TFN}[m_\varphi - 2(m_\varphi \times \mathrm{cov}_\varphi), m_\varphi, m_\varphi$$
$$+ 2(m_\varphi \times \mathrm{cov}_\varphi)]. \quad (18)$$

The degree of variation of parameters is described by the coefficient of variation ($\mathrm{cov} = \sigma/\mu$). The larger the cov, the greater is the degree of variation. The cov value of cohesion is approximately 25–30%, and that of the angle of internal friction is approximately 10–20% [33, 78, 79]. We have selected the maximum values for cov, which are 30% for cohesion and 20% for the angle of internal friction, to construct the triangular fuzzy numbers. The triangular fuzzy numbers for loam and silt are presented in Figures 5 and 6, respectively. The α-cut values are listed in Table 3.

3.1. Comparison of Probability of Failure for Different Types of Soil. In this study, the correlation between cohesion and angle of internal friction ($\rho = 0$) was not considered. With the use of α-cut sets, combinations with different degrees of membership were computed for modeling. We calculated the factor of safety and reliability index of loam and silt using data from the observation points at the middle of the slope under the same rainfall condition. Their relationship with the degree of membership is shown in Figure 7. The factor of safety of loam fluctuated within (1.2435, 1.3135) whereas that of silt fluctuated within (1.5588, 1.6225). For loam, the fuzzy reliability is determined to be 1.3357, and the probability of failure is 0.0908. For silt, the fuzzy reliability is determined to be 2.2299, and the probability of failure is 0.0129.
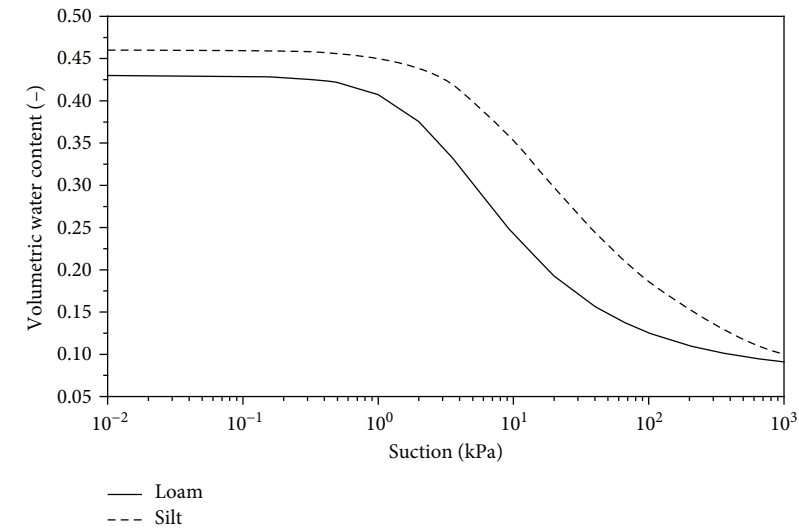
(a)
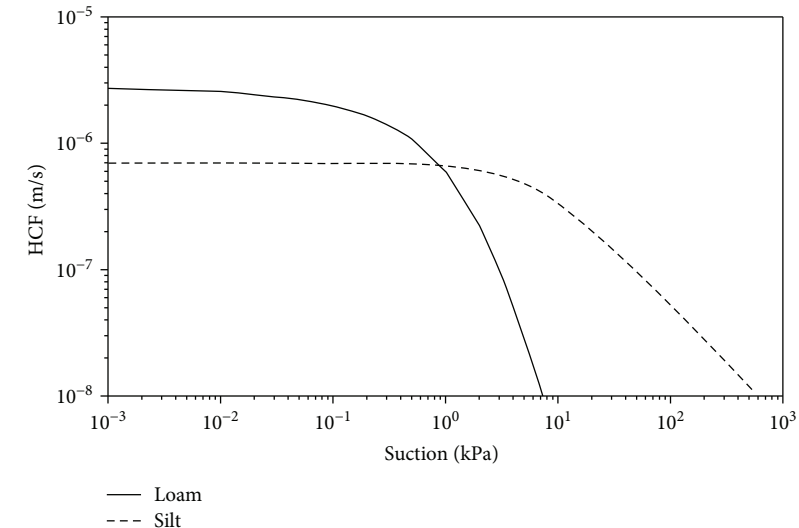
(b)
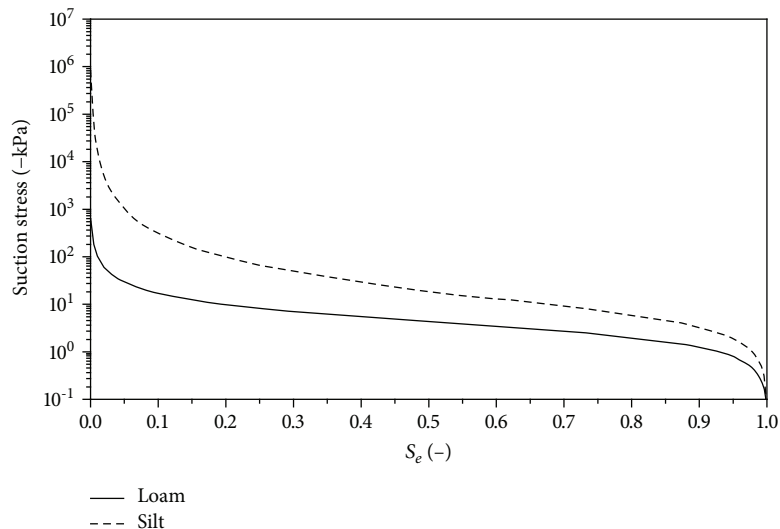
(c)

FIGURE 4: Hydraulic properties of loam soil and silt soil: (a) SWRC; (b) HCF; (c) SSCC.
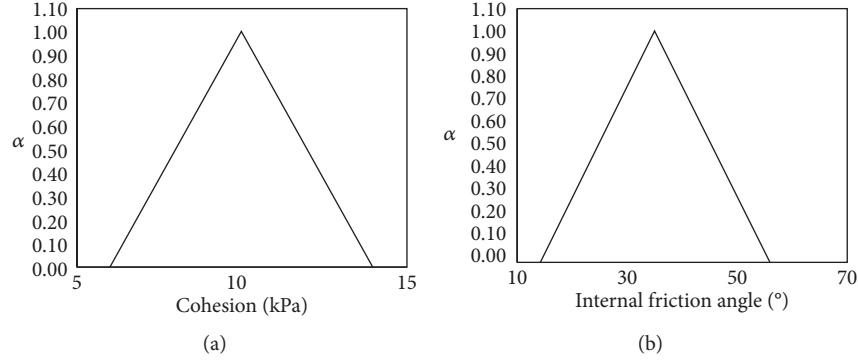
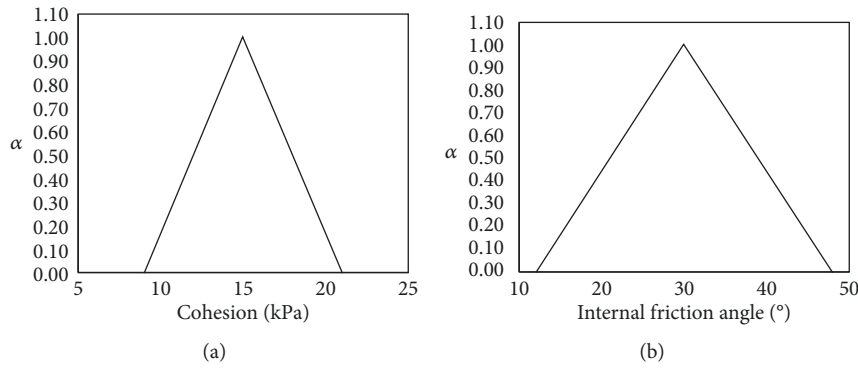Figure 5: Fuzzy number of (a) cohesion and (b) friction angle of loam soil.

Figure 6: Fuzzy number of (a) cohesion and (b) friction angle of silt soil.

Table 3: α-Cut value of loam soil and silt soil.

α-Cut	Loam soil				Silt soil			
	$c-$	$c+$	$\varphi-$	$\varphi+$	$c-$	$c+$	$\varphi-$	$\varphi+$
0.1	6.40	13.60	16.10	53.90	9.60	20.40	13.80	46.20
0.2	6.80	13.20	18.20	51.80	10.20	19.80	15.60	44.40
0.3	7.20	12.80	20.30	49.70	10.80	19.20	17.40	42.60
0.4	7.60	12.40	22.40	47.60	11.40	18.60	19.20	40.80
0.5	8.00	12.00	24.50	45.50	12.00	18.00	21.00	39.00
0.6	8.40	11.60	26.60	43.40	12.60	17.40	22.80	37.20
0.7	8.80	11.20	28.70	41.30	13.20	16.80	24.60	35.40
0.8	9.20	10.80	30.80	39.20	13.80	16.20	26.40	33.60
0.9	9.60	10.40	32.90	37.10	14.40	15.60	28.20	31.80

Figure 7: Average LFS, reliability index, and membership at observation points in the loam and silt soil slopes.

As the coefficient of permeability for loam was greater than that for silt in this study, the rainfall was likely to infiltrate into the interior of the slope, increasing the suction stress while decreasing the effective stress on the interior of the slope. Consequently, after 48 h of sustained rainfall, the factor of safety of loam was lower than that of silt at the observation points. The reliability index analysis reveals that, as the degree of membership increases, the reliability index increases. The results obtained from the observation points on the slope indicate that the probability of failure of a loam slope is 7.79% higher than that of a silt slope.

3.2. Comparison of Probability of Failure at Different Times. We investigated the change in suction stress owing to the change in soil water content in the slope at different times, as well as the change in the probability of failure after a sustained infiltration of rainfall into the interior of the soil. Observations were obtained at the 12th, 24th, and 48th hours. The variations in water content, suction stress, and

(a)

(b)

(c)

FIGURE 8: Results of water content, suction stress, and failure probability in the loam slope at 0, 12, 24, and 48 hours under rainfall conditions (a) at the top of the slope, (b) middle of the slope, and (c) toe of the slope.
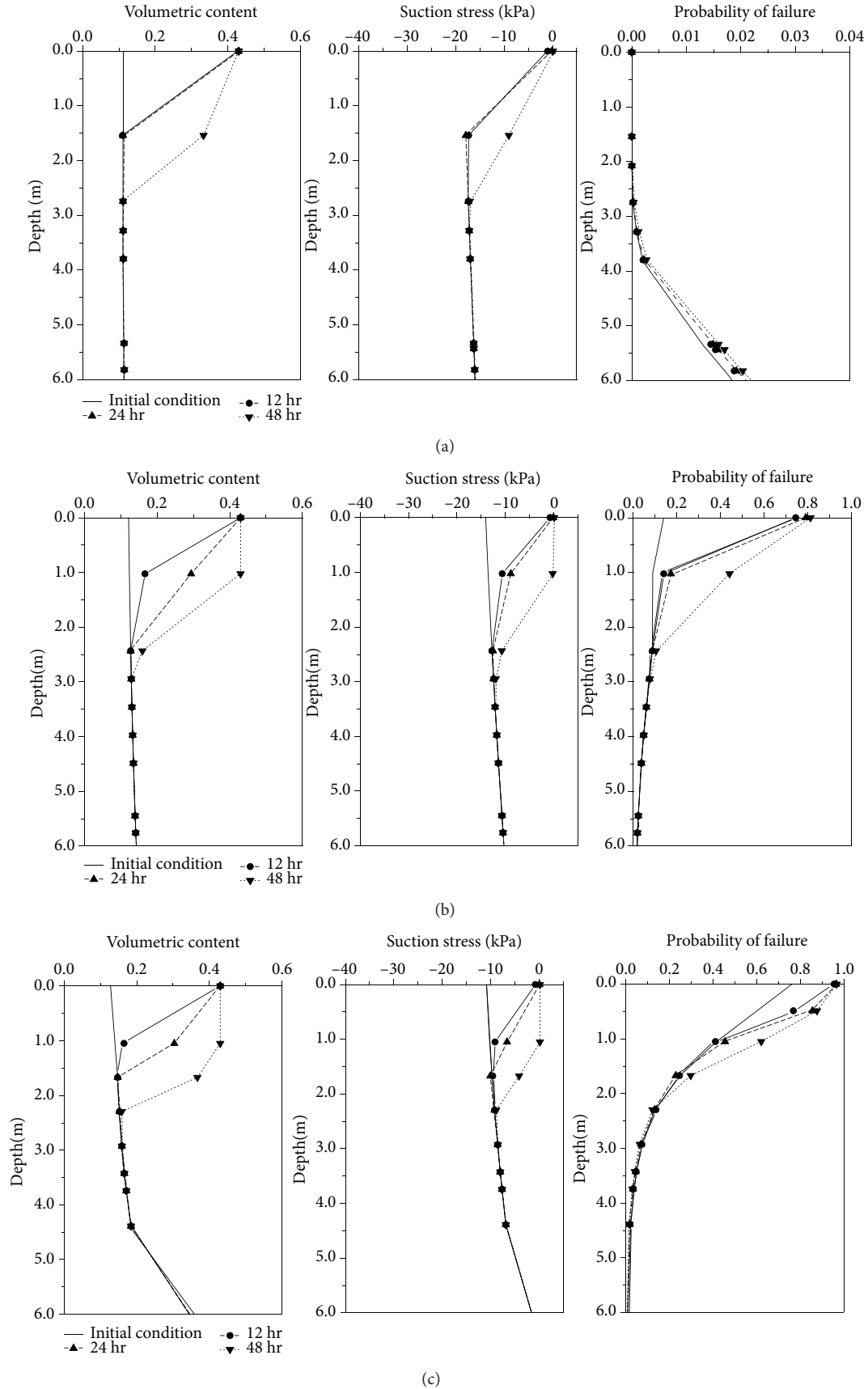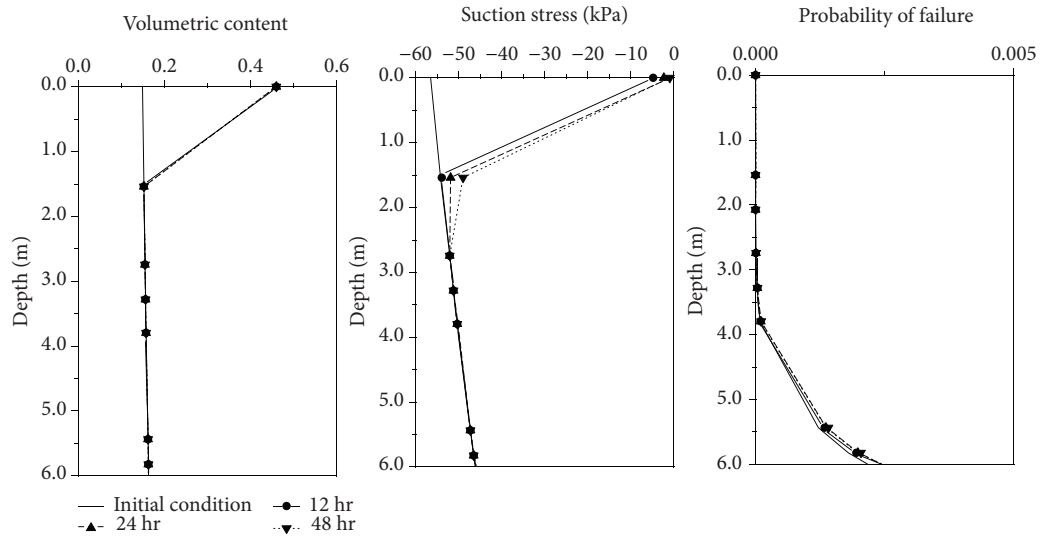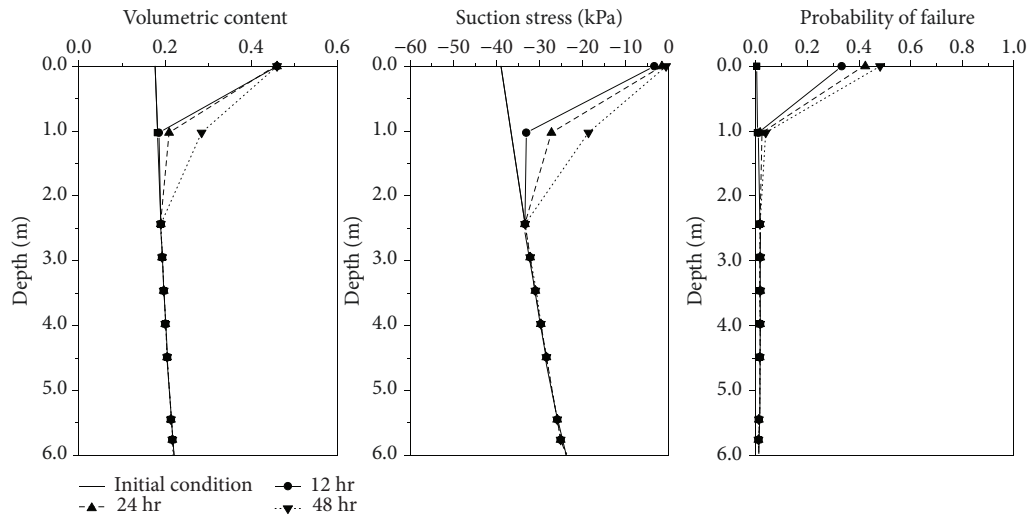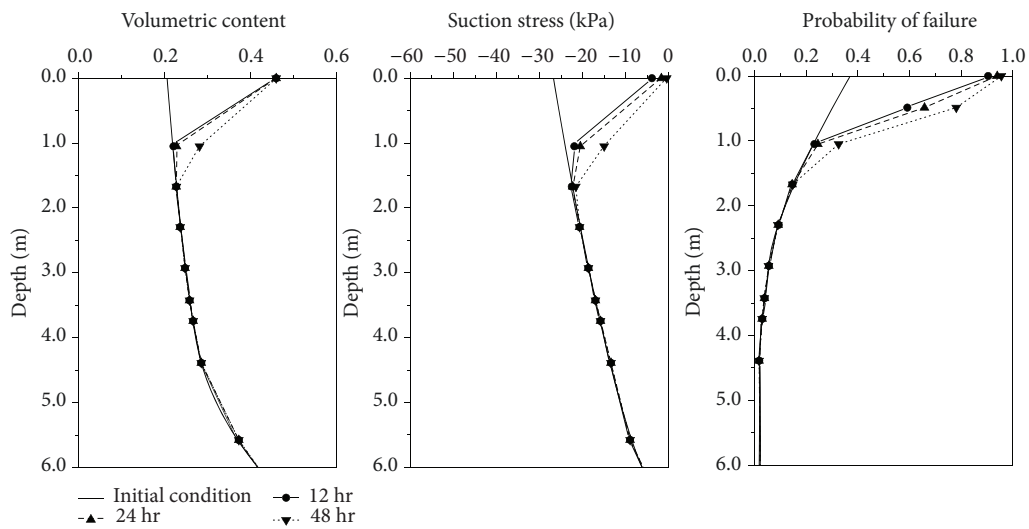
FIGURE 9: Results of water content, suction stress, and failure probability in the silt slope at 0, 12, 24, and 48 hours under rainfall conditions (a) at the top of the slope, (b) middle of the slope, and (c) toe of the slope.

■ < 0.1	■ 0.3 − 0.4
■ 0.1 − 0.2	■ 0.4 − 0.43
■ 0.2 − 0.3	

(a)

Unit: kPa

■ −21- −15	■ −5- −1
■ −15- −10	■ −1- −0
■ −10- −5	

(b)

■ < 0.1	■ 0.3 − 0.4
■ 0.1 − 0.2	■ 0.4 − 0.46
■ 0.2 − 0.3	

(c)

Unit: kPa

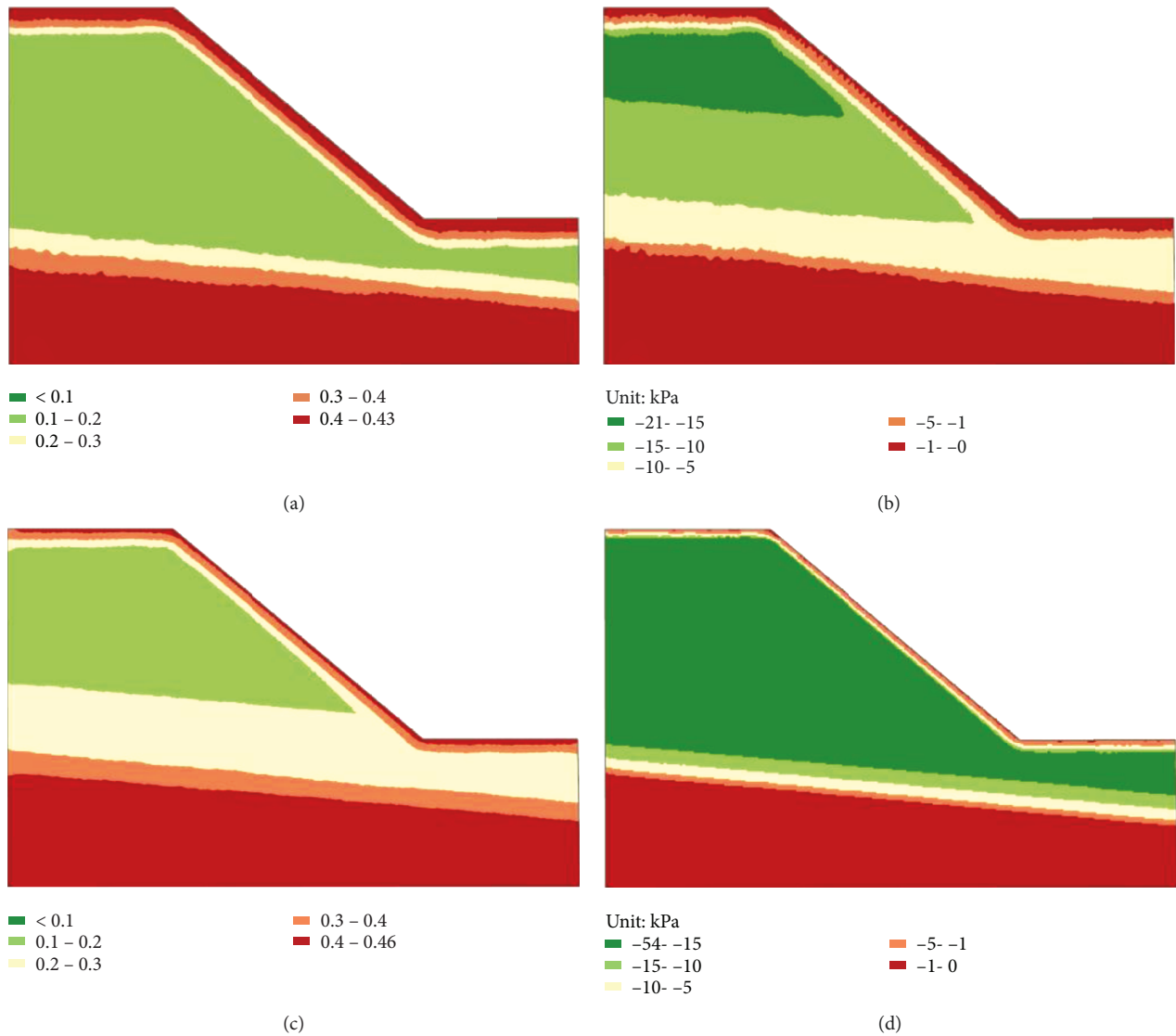| ■ −54- −15 | ■ −5- −1 |
| ■ −15- −10 | ■ −1- 0 |
| ■ −10- −5 | |

(d)

FIGURE 10: Results of water content and suction stress in different soil slopes at 48 hours under rainfall conditions: (a) water content distribution in the loam slope; (b) suction stress distribution in the loam slope; (c) water content distribution in the silt slope; (d) suction stress distribution in the silt slope.

the probability of failure of loam and silt at the top, middle, and toe of the slope are presented as follows:

In the loam soil slope, under the effect of sustained rainfall infiltration, the rainfall intensity exceeded the coefficient of permeability. Consequently, at the 12th hour, the surface layer of loam approached saturation with a water content of 0.43. As shown in Figure 8, the thickness of the soil moisture belt at the 48th hour was 2.74 m at the top, 2.95 m at the middle, and 2.29 m at the toe of the slope. As the soil water content increased, the soil suction stress increased. At the 48th hour, the increase in suction stress was 18.40 kPa at the top, 14.08 kPa at the middle, and 10.88 kPa at the toe of the slope. Analysis of probability of failure reveals that there was a low probability of failure at the top of the slope. At the middle and toe of the slope, the greatest change in the probability of failure was observed to be on the soil surface. Such changes decreased with depth. The probability of failure of the loam slope varied with time. At the middle of the slope, it increased

by 60.56% at the 12th hour, by 65.13% at the 24th hour, and by 67.34% at the 48th hour. At the toe of the slope, it increased by 20.97% at the 12th hour, by 21.93% at the 24th hour, and by 22.09% at the 48th hour.

In the silt soil slope, under the effect of sustained rainfall infiltration, the rainfall intensity exceeded the coefficient of permeability. Therefore, the surface layer of silt approached saturation, with a water content of 0.46 at the 12th hour. Figure 9 illustrates that the thickness of the soil moisture belt was 1.54 m at the top, 2.44 m at the middle, and 1.67 m at the toe of the slope. Changes in suction stress were determined to be 55.53 kPa at the top, 38.00 kPa at the middle, and 26.46 kPa at the toe of the slope. Analysis of probability of failure showed that there was a low probability of failure at the top of the slope. At the middle and toe of the slope, the greatest change in the probability of failure was observed to be on the soil surface. Such changes decreased with depth.
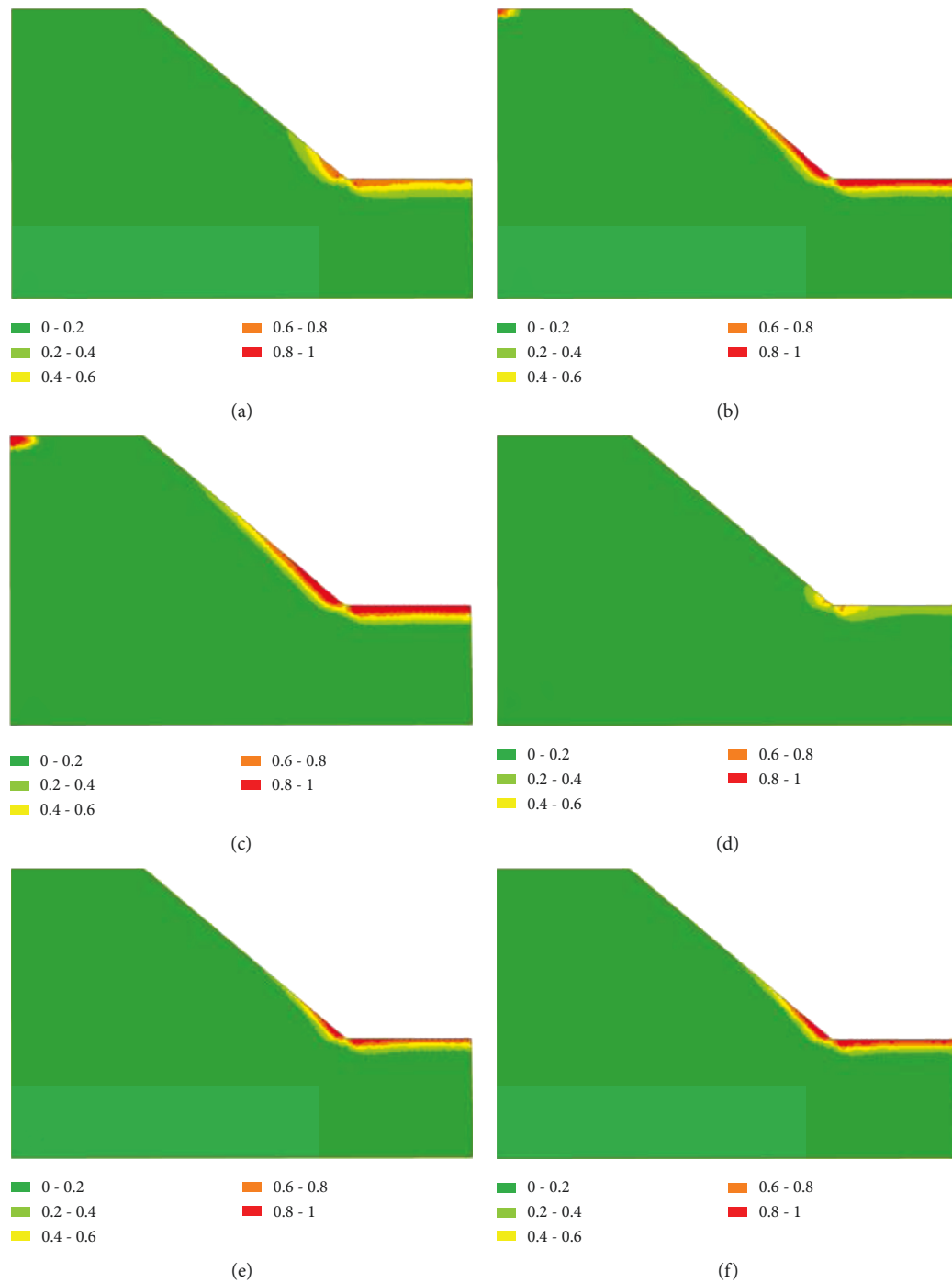
FIGURE 11: Results of slope failure probability in different soil slopes at 0, 24, and 48 hours under rainfall conditions: (a) 0 hours in the loam slope; (b) 24 hours in the loam slope; (c) 48 hours in the loam slope; (d) 0 hours in the silt slope; (e) 24 hours in the silt slope; (f) 48 hours in the silt slope.

The probability of failure of the silt slope varied with time. It increased by 32.86% at the 12th hour, by 42.07% at the 24th hour, and by 47.72% at the 48th hour. At the toe of the slope, it increased by 56.51% at the 12th hour, by 60.00% at the 24th hour, and by 61.63% at the 48th hour.

We observed that a greater change in probability of failure is associated with the infiltration depth and variation in suction stress. The variation of suction stress on the surface layer of silt was greater than that of loam. Nevertheless, the coefficient of permeability was lower for silt, limiting the rainfall infiltration depth. Consequently, under the same rainfall condition, the depth of the moisture band in silt was shallower than that of loam, as shown in Figures 10(a) and 10(c). Therefore, surface runoff owing to rainfall is likely to be formed in silt. As the suction stress of a slope is influenced by the depth of the moisture band, the effect of suction stress extended deeper in loam (Figure 10(b)) than in silt (Figure 10(d)). As the duration of rainfall increased, the
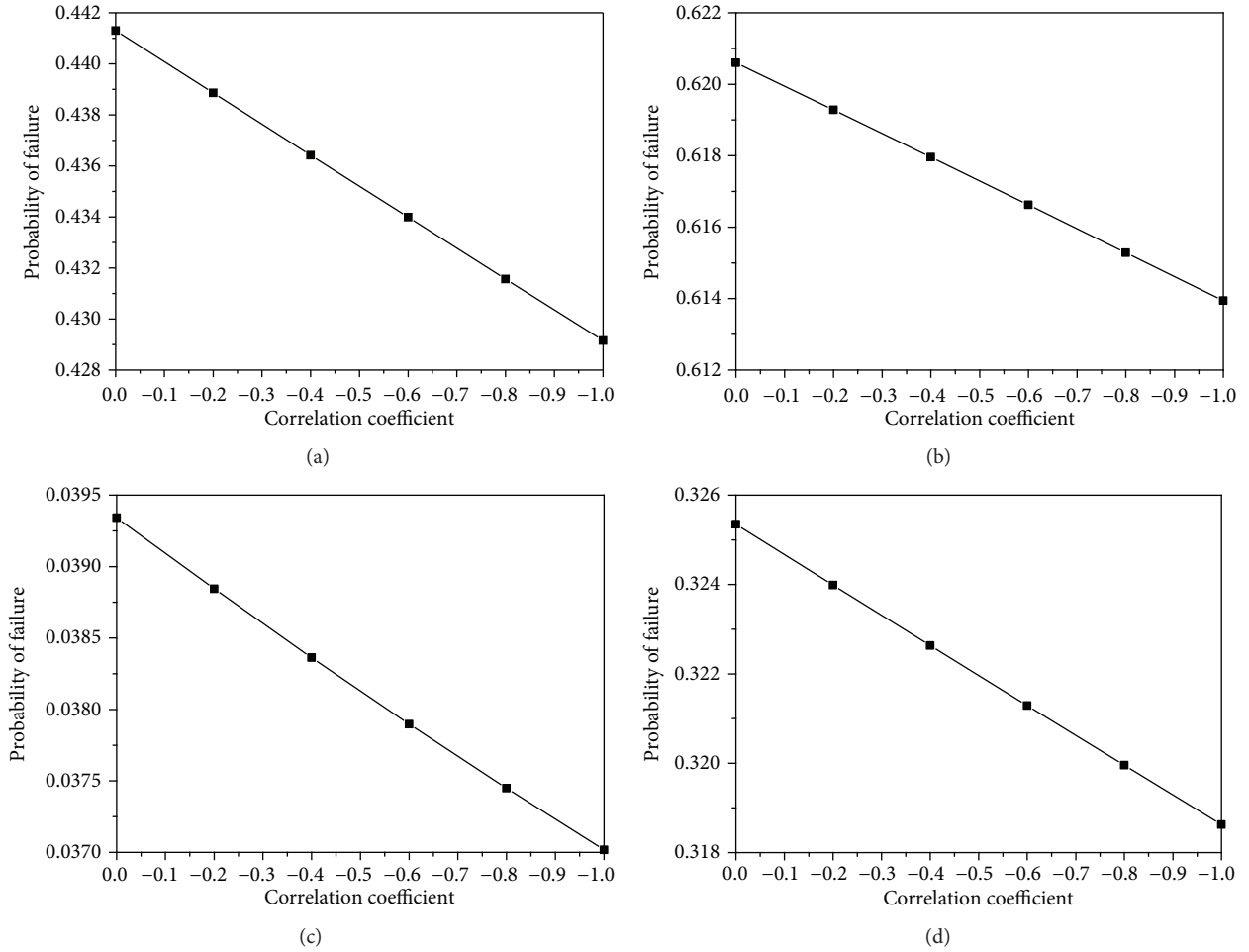
(a)

(b)

(c)

(d)

FIGURE 12: Effect of parameter correlation on slope failure probability at the following observation points (at 48 hours): (a) observation point at the middle in the loam slope; (b) observation point at the toe in the loam slope; (c) observation point at the middle in the silt slope; (d) observation point at the toe in the silt slope.

probability of failure of the slope increased from the toe toward the middle of the slope. Figure 11 shows that the middle of the slope was affected by rainfall infiltration and recharge from the top of the slope simultaneously. Therefore, the probability of failure increased with time. Overall, after 48 h of rainfall, the area of the loam slope in which the probability of failure was greater than 50% was approximately twice as large as that of the silt slope.

3.3. Effect of Parameter Correlation on the Probability of Failure. We assessed the effect of the coefficient of correlation of the parameters on the probability of failure. The top of the slope was not investigated because of its low probability of failure. Only the middle and toe of the slope were discussed. Previous studies have reported a correlation between cohesion and the angle of internal friction and that the correlation is mostly negative [64–66, 80]. In this study, the analysis of loam and silt slope stability reveals that (at the 48th hour) the stronger the negative correlation between the mechanical parameters the lower is the probability of failure. Observation points situated one meter below the surface at the middle and toe of the slope suggest a linear relationship between the

probability of failure and correlation coefficient. Figure 12 illustrates the differences in the computed probability of failure when considering a negative coefficient of −0.8 (compared to that without considering the correlation). In the loam slope, the probability of failure decreases by 0.9% at the middle and by 0.7% at the toe of the slope. In the silt slope, the probability of failure decreases by 0.2% at the middle and by 0.5% at the toe of the slope. This is consistent with the observation of Aladejare and Wang [68] that when the correlation between mechanical parameters is ignored, the probability of failure obtained from the reliability analysis might be overestimated.

4. Conclusion

In this study, we have examined the uncertainty in parameters. Fuzzy transform was performed on the cohesion and the angle of internal friction. Fuzzy point estimation was used in combination with the hydromechanical coupling model on HYDRUS 2D and the Slope Cube Module to examine the slope stability. The result shows that the fuzzy theory can effectively evaluate the fluctuation interval, mean, and

standard deviation of the factor of safety and the reliability index. The probability of failure in the interior of the slope was computed through reliability analysis. At our observation points on the loam slope, the fuzzy reliability of loam was determined to be 1.3357, and the probability of failure was 0.0908. For silt, the fuzzy reliability was observed to be 2.2299, and the probability of failure was 0.0129. The results of the slope failure mechanism investigation is that, after rainfall infiltrates into the soil, the change in water content causes an increase in suction stress (a decrease in its absolute value). The resulting decrease in soil effective stress leads to slope instability. It has been determined in this study that the change in the probability of failure is spatially related to the depth of the moisture band caused by the soil hydraulic conductivity and to the suction stress change controlled by the water content. After 48 hr of rainfall, the infiltration depth into the loam slope was deeper than that into the silt slope. The area of the loam slope in which the probability of failure exceeded 50% was approximately twice as large as that of the silt slope. It suggests that, as the rainfall infiltrates deeper, the area of instability in the slope increases. This study was also aimed at determining the effect of correlation between the parameters on the probability of failure. It was shown that a stronger negative correlation between the mechanical parameters yields a lower calculated probability of failure when performing slope stability analysis. When the correlation was considered, the computed probability of failure at observed points decreased by <1%. It suggests that the correlation between parameters may be ignored when a conservative estimate of slope stability is required.

Data Availability

The data used to support the findings of this study are available from the corresponding author upon request.

Conflicts of Interest

The authors declare that they have no conflicts of interest.

Acknowledgments

References

[1] L. L. Zhang, J. Zhang, L. M. Zhang, and W. H. Tang, "Stability analysis of rainfall-induced slope failure: a review," *Proceedings of the Institution of Civil Engineers - Geotechnical Engineering*, vol. 164, no. 5, pp. 299–316, 2011.

[2] M. Raj and A. Sengupta, "Rain-triggered slope failure of the railway embankment at Malda, India," *Acta Geotechnica*, vol. 9, no. 5, pp. 789–798, 2014.

[3] X. B. Tu, A. K. L. Kwong, F. C. Dai, L. G. Tham, and H. Min, "Field monitoring of rainfall infiltration in a loess slope and analysis of failure mechanism of rainfall-induced landslides," *Engineering Geology*, vol. 105, no. 1-2, pp. 134–150, 2009.

[4] N. Caine, "The rainfall intensity—duration control of shallow landslides and debris flows," *Geografiska Annaler: Series A, Physical Geography*, vol. 62, no. 1-2, pp. 23–27, 1980.

[5] R. M. Iverson, "Landslide triggering by rain infiltration," *Water Resources Research*, vol. 36, no. 7, pp. 1897–1910, 2000.

[6] T.-L. Tsai and J.-C. Yang, "Modeling of rainfall-triggered shallow landslide," *Environmental Geology*, vol. 50, no. 4, pp. 525–534, 2006.

[7] L. Zhang, J. Li, X. Li, J. Zhang, and H. Zhu, *Rainfall-Induced Soil Slope Failure: Stability Analysis and Probabilistic Assessment*, CRC Press, 2016.

[8] J. Zhang, J. Li, and H. Lin, "Models and influencing factors of the delay phenomenon for rainfall on slope stability," *European Journal of Environmental and Civil Engineering*, vol. 22, no. 1, pp. 122–136, 2018.

[9] F. C. Dai, C. F. Lee, and S. J. Wang, "Characterization of rainfall-induced landslides," *International Journal of Remote Sensing*, vol. 24, no. 23, pp. 4817–4834, 2003.

[10] N. Lu and J. Godt, "Infinite slope stability under steady unsaturated seepage conditions," *Water Resources Research*, vol. 44, no. 11, 2008.

[11] P. Aleotti, "A warning system for rainfall-induced shallow failures," *Engineering Geology*, vol. 73, no. 3-4, pp. 247–265, 2004.

[12] G. F. Wieczorek and T. Glade, "Climatic factors influencing occurrence of debris flows," in *Debris-flow Hazards and Related Phenomena*, pp. 325–362, Springer, 2005.

[13] F. Guzzetti, S. Peruccacci, M. Rossi, and C. P. Stark, "The rainfall intensity–duration control of shallow landslides and debris flows: an update," *Landslides*, vol. 5, no. 1, pp. 3–17, 2008.

[14] B. Postance, J. Hillier, T. Dijkstra, and N. Dixon, "Comparing threshold definition techniques for rainfall-induced landslides: a national assessment using radar rainfall," *Earth Surface Processes and Landforms*, vol. 43, no. 2, pp. 553–560, 2018.

[15] S. L. Gariano, M. T. Brunetti, G. Iovine et al., "Calibration and validation of rainfall thresholds for shallow landslide forecasting in Sicily, southern Italy," *Geomorphology*, vol. 228, pp. 653–665, 2015.

[16] G. Martelloni, S. Segoni, R. Fanti, and F. Catani, "Rainfall thresholds for the forecasting of landslide occurrence at regional scale," *Landslides*, vol. 9, no. 4, pp. 485–495, 2012.

[17] F. Guzzetti, S. Peruccacci, M. Rossi, and C. P. Stark, "Rainfall thresholds for the initiation of landslides in central and southern Europe," *Meteorology and Atmospheric Physics*, vol. 98, no. 3-4, pp. 239–267, 2007.

[18] T. Glade, M. Crozier, and P. Smith, "Applying probability determination to refine landslide-triggering rainfall thresholds using an empirical "Antecedent Daily Rainfall Model"," *Pure and Applied Geophysics*, vol. 157, no. 6-8, pp. 1059–1079, 2000.

[19] M. Melillo, M. T. Brunetti, S. Peruccacci, S. L. Gariano, and F. Guzzetti, "Rainfall thresholds for the possible landslide occurrence in Sicily (Southern Italy) based on the automatic reconstruction of rainfall events," *Landslides*, vol. 13, no. 1, pp. 165–172, 2016.

[20] F. C. Dai and C. F. Lee, "A spatiotemporal probabilistic modelling of storm-induced shallow landsliding using aerial photographs and logistic regression," *Earth Surface Processes and Landforms*, vol. 28, no. 5, pp. 527–545, 2003.

[21] K. T. Chang, S. H. Chiang, and F. Lei, "Analysing the relationship between typhoon-triggered landslides and critical rainfall conditions," *Earth Surface Processes and Landforms*, vol. 33, no. 8, pp. 1261–1271, 2008.

[22] W. Chen, H. R. Pourghasemi, M. Panahi et al., "Spatial prediction of landslide susceptibility using an adaptive neuro-fuzzy inference system combined with frequency ratio, generalized additive model, and support vector machine techniques," *Geomorphology*, vol. 297, pp. 69–85, 2017.

[23] E. A. C. Abella and C. J. van Westen, "Generation of a landslide risk index map for Cuba using spatial multi-criteria evaluation," *Landslides*, vol. 4, no. 4, pp. 311–325, 2007.

[24] M. Kouli, C. Loupasakis, P. Soupios, D. Rozos, and F. Vallianatos, "Landslide susceptibility mapping by comparing the WLC and WofE multi-criteria methods in the West Crete Island, Greece," *Environmental Earth Sciences*, vol. 72, no. 12, pp. 5197–5219, 2014.

[25] D. R. Montgomery and W. E. Dietrich, "A physically based model for the topographic control on shallow landsliding," *Water Resources Research*, vol. 30, no. 4, pp. 1153–1171, 1994.

[26] W. Wu and R. C. Sidle, "A distributed slope stability model for steep forested basins," *Water Resources Research*, vol. 31, no. 8, pp. 2097–2110, 1995.

[27] P. L. Wilkinson, M. G. Anderson, and D. M. Lloyd, "An integrated hydrological model for rain-induced landslide prediction," *Earth Surface Processes and Landforms*, vol. 27, no. 12, pp. 1285–1297, 2002.

[28] G. B. Crosta and P. Frattini, "Distributed modelling of shallow landslides triggered by intense rainfall," *Natural Hazards and Earth System Science*, vol. 3, no. 1/2, pp. 81–93, 2003.

[29] D. Salciarini, J. W. Godt, W. Z. Savage, P. Conversini, R. L. Baum, and J. A. Michael, "Modeling regional initiation of rainfall-induced shallow landslides in the eastern Umbria Region of central Italy," *Landslides*, vol. 3, no. 3, pp. 181–194, 2006.

[30] H.-J. Park, J.-Y. Jang, and J.-H. Lee, "Physically based susceptibility assessment of rainfall-induced shallow landslides using a fuzzy point estimate method," *Remote Sensing*, vol. 9, no. 5, p. 487, 2017.

[31] S. Zhang, L. Zhao, R. Delgado-Tellez, and H. Bao, "A physics-based probabilistic forecasting model for rainfall-induced shallow landslides at regional scale," *Natural Hazards and Earth System Sciences*, vol. 18, no. 3, pp. 969–982, 2018.

[32] J. Corominas, C. van Westen, P. Frattini et al., "Recommendations for the quantitative analysis of landslide risk," *Bulletin of Engineering Geology and the Environment*, vol. 73, no. 2, pp. 209–263, 2013.

[33] K.-K. Phoon and F. H. Kulhawy, "Characterization of geotechnical variability," *Canadian Geotechnical Journal*, vol. 36, no. 4, pp. 612–624, 1999.

[34] A. Burton, T. J. Arkell, and J. C. Bathurst, "Field variability of landslide model parameters," *Environmental Geology*, vol. 35, no. 2-3, pp. 100–114, 1998.

[35] K. S. Li and P. Lumb, "Probabilistic design of slopes," *Canadian Geotechnical Journal*, vol. 24, no. 4, pp. 520–535, 1987.

[36] D. V. Griffiths and G. A. Fenton, "Probabilistic slope stability analysis by finite elements," *Journal of Geotechnical and Geoenvironmental Engineering*, vol. 130, no. 5, pp. 507–518, 2004.

[37] H. El-Ramly, N. R. Morgenstern, and D. M. Cruden, "Probabilistic slope stability analysis for practice," *Canadian Geotechnical Journal*, vol. 39, no. 3, pp. 665–683, 2002.

[38] J. T. Christian, C. C. Ladd, and G. B. Baecher, "Reliability applied to slope stability analysis," *Journal of Geotechnical Engineering*, vol. 120, no. 12, pp. 2180–2207, 1994.

[39] T. Xiao, D.-Q. Li, Z.-J. Cao, and X.-S. Tang, "Full probabilistic design of slopes in spatially variable soils using simplified reliability analysis method," *Georisk: Assessment and Management of Risk for Engineered Systems and Geohazards*, vol. 11, no. 1, pp. 146–159, 2017.

[40] N. O. Nawari and R. Liang, "Fuzzy-based approach for determination of characteristic values of measured geotechnical parameters," *Canadian Geotechnical Journal*, vol. 37, no. 5, pp. 1131–1140, 2000.

[41] C. I. Giasi, P. Masi, and C. Cherubini, "Probabilistic and fuzzy reliability analysis of a sample slope near Aliano," *Engineering Geology*, vol. 67, no. 3-4, pp. 391–402, 2003.

[42] J. P. Harrison and J. A. Hudson, "Incorporating parameter variability in rock mechanics analyses: fuzzy mathematics applied to underground rock spalling," *Rock Mechanics and Rock Engineering*, vol. 43, no. 2, pp. 219–224, 2010.

[43] Z. Luo, S. Atamturktur, C. H. Juang, H. Huang, and P.-S. Lin, "Probability of serviceability failure in a braced excavation in a spatially random field: fuzzy finite element approach," *Computers and Geotechnics*, vol. 38, no. 8, pp. 1031–1040, 2011.

[44] M. Beer, Y. Zhang, S. T. Quek, and K. K. Phoon, "Reliability analysis with scarce information: comparing alternative approaches in a geotechnical engineering context," *Structural Safety*, vol. 41, pp. 1–10, 2013.

[45] G. R. Dodagoudar and G. Venkatachalam, "Reliability analysis of slopes using fuzzy sets theory," *Computers and Geotechnics*, vol. 27, no. 2, pp. 101–115, 2000.

[46] H. J. Park, J.-G. Um, I. Woo, and J. W. Kim, "Application of fuzzy set theory to evaluate the probability of failure in rock slopes," *Engineering Geology*, vol. 125, pp. 92–101, 2012.

[47] C. Xu, L. Wang, Y. M. Tien, J.-M. Chen, and C. H. Juang, "Robust design of rock slopes with multiple failure modes: modeling uncertainty of estimated parameter statistics with fuzzy number," *Environmental Earth Sciences*, vol. 72, no. 8, pp. 2957–2969, 2014.

[48] W. Gong, L. Wang, S. Khoshnevisan, C. H. Juang, H. Huang, and J. Zhang, "Robust geotechnical design of earth slopes using fuzzy sets," *Journal of Geotechnical and Geoenvironmental Engineering*, vol. 141, no. 1, article 04014084, 2015.

[49] W. Fellenius, "Calculation of stability of earth dam," in *Transactions of 2nd Congress Large Dams*, pp. 445–462, Washington, DC, USA, 1936.

[50] A. W. Bishop, "The use of the slip circle in the stability analysis of slopes," *Géotechnique*, vol. 5, no. 1, pp. 7–17, 1955.

[51] N. Janbu, "Application of composite slip surface for stability analysis," in *Proceedings of European Conference on Stability of Earth Slopes*, pp. 43–49, Stockholm, Sweden, 1954.

[52] N. R. Morgenstern and V. E. Price, "The analysis of the stability of general slip surfaces," *Géotechnique*, vol. 15, no. 1, pp. 79–93, 1965.

[53] B. Jeremić, "Finite element methods for 3D slope stability analysis," in *Slope Stability 2000*, pp. 224–238, Denver, CO, USA, 2000.

[54] H. Zheng, D. F. Liu, and C. G. Li, "Slope stability analysis based on elasto-plastic finite element method," *International Journal for Numerical Methods in Engineering*, vol. 64, no. 14, pp. 1871–1888, 2005.

[55] H. Zheng, G. Sun, and D. Liu, "A practical procedure for searching critical slip surfaces of slopes based on the strength reduction technique," *Computers and Geotechnics*, vol. 36, no. 1-2, pp. 1–5, 2009.

[56] S. Y. Liu, L. T. Shao, and H. J. Li, "Slope stability analysis using the limit equilibrium method and two finite element methods," *Computers and Geotechnics*, vol. 63, pp. 291–298, 2015.

[57] V. B. Maji, "An insight into slope stability using strength reduction technique," *Journal of the Geological Society of India*, vol. 89, no. 1, pp. 77–81, 2017.

[58] Y. M. Cheng, T. Lansivaara, and W. B. Wei, "Two-dimensional slope stability analysis by limit equilibrium and strength reduction methods," *Computers and Geotechnics*, vol. 34, no. 3, pp. 137–150, 2007.

[59] S. Liu and L. Shao, "Limit equilibrium conditions and stability analysis for soils," in *GeoShanghai International Conference*, pp. 92–100, Shanghai, China, 2018, Springer.

[60] N. Lu, B. Şener-Kaya, A. Wayllace, and J. W. Godt, "Analysis of rainfall-induced slope instability using a field of local factor of safety," *Water Resources Research*, vol. 48, no. 9, 2012.

[61] C. Cherubini, "Reliability evaluation of shallow foundation bearing capacity on $c'\phi'$ soils," *Canadian Geotechnical Journal*, vol. 37, no. 1, pp. 264–269, 2000.

[62] X.-S. Tang, D.-Q. Li, G. Rong, K.-K. Phoon, and C.-B. Zhou, "Impact of copula selection on geotechnical reliability under incomplete probability information," *Computers and Geotechnics*, vol. 49, pp. 264–278, 2013.

[63] S.-H. Jiang, D.-Q. Li, L.-M. Zhang, and C.-B. Zhou, "Slope reliability analysis considering spatially variable shear strength parameters using a non-intrusive stochastic finite element method," *Engineering Geology*, vol. 168, pp. 120–128, 2014.

[64] P. Lumb, "Safety factors and the probability distribution of soil strength," *Canadian Geotechnical Journal*, vol. 7, no. 3, pp. 225–242, 1970.

[65] H. Rahardjo, A. Satyanaga, E.-C. Leong, Y. S. Ng, and H. T. C. Pang, "Variability of residual soil properties," *Engineering Geology*, vol. 141-142, pp. 124–140, 2012.

[66] L. Di Matteo, D. Valigi, and R. Ricco, "Laboratory shear strength parameters of cohesive soils: variability and potential effects on slope stability," *Bulletin of Engineering Geology and the Environment*, vol. 72, no. 1, pp. 101–106, 2013.

[67] Y. Wang and O. V. Akeju, "Quantifying the cross-correlation between effective cohesion and friction angle of soil from limited site-specific data," *Soils and Foundations*, vol. 56, no. 6, pp. 1055–1070, 2016.

[68] A. E. Aladejare and Y. Wang, "Influence of rock property correlation on reliability analysis of rock slope stability: from property characterization to reliability analysis," *Geoscience Frontiers*, vol. 9, no. 6, pp. 1639–1648, 2018.

[69] J. Šimůnek, M. T. van Genuchten, and M. Šejna, "Development and applications of the HYDRUS and STANMOD software packages and related codes," *Vadose Zone Journal*, vol. 7, no. 2, p. 587, 2008.

[70] M. T. van Genuchten, "A closed-form equation for predicting the hydraulic conductivity of unsaturated soils 1," *Soil Science Society of America Journal*, vol. 44, no. 5, p. 892, 1980.

[71] Y. Mualem, "A new model for predicting the hydraulic conductivity of unsaturated porous media," *Water Resources Research*, vol. 12, no. 3, pp. 513–522, 1976.

[72] N. Lu and W. J. Likos, *Unsaturated Soil Mechanics*, Wiley, 2004.

[73] N. Lu and W. J. Likos, "Suction stress characteristic curve for unsaturated soil," *Journal of Geotechnical and Geoenvironmental Engineering*, vol. 132, no. 2, pp. 131–142, 2006.

[74] N. Lu, J. W. Godt, and D. T. Wu, "A closed-form equation for effective stress in unsaturated soil," *Water Resources Research*, vol. 46, no. 5, 2010.

[75] W. Dong and H. C. Shah, "Vertex method for computing functions of fuzzy variables," *Fuzzy Sets and Systems*, vol. 24, no. 1, pp. 65–78, 1987.

[76] E. Rosenblueth, "Point estimates for probability moments," *Proceedings of the National Academy of Sciences*, vol. 72, no. 10, pp. 3812–3814, 1975.

[77] G. B. Baecher and J. T. Christian, *Reliability and Statistics in Geotechnical Engineering*, John Wiley & Sons, 2005.

[78] H. J. Park, J. H. Lee, and I. Woo, "Assessment of rainfall-induced shallow landslide susceptibility using a GIS-based probabilistic approach," *Engineering Geology*, vol. 161, pp. 1–15, 2013.

[79] E. C. Hsiao, M. Schuster, C. H. Juang, and G. T. Kung, "Reliability analysis and updating of excavation-induced ground settlement for building serviceability assessment," *Journal of Geotechnical and Geoenvironmental Engineering*, vol. 134, no. 10, pp. 1448–1458, 2008.

[80] Y. Wang and A. E. Aladejare, "Bayesian characterization of correlation between uniaxial compressive strength and Young's modulus of rock," *International Journal of Rock Mechanics and Mining Sciences*, vol. 85, pp. 10–19, 2016.

WILEY | Hindawi

Research Article

The Impact of Reservoir Fluctuations on Reactivated Large Landslides: A Case Study

Javed Iqbal [iD],[1,2] **Xinbin Tu**,[2,3] **and Wei Gao** [iD] [2]

[1]*Key Laboratory for Mountain Hazards and Earth Surface Process, Institute of Mountain Hazards & Environment, Chinese Academy of Sciences, Chengdu, China*
[2]*Institute of Geology and Geophysics, Chinese Academy of Sciences, Beijing 100029, China*
[3]*State Grid Corporation of China, Beijing 100031, China*

Correspondence should be addressed to Javed Iqbal; javediqbalgeo@gmail.com and Wei Gao; gaowei@mail.iggcas.ac.cn

Filling of Xiangjiaba Reservoir Lake in the Southwest China triggered and reactivated numerous landslides due to water fluctuation. In order to understand the relationship between reservoirs and slope instability, a typical reservoir landslide (Dasha landslide) at the right bank of Jinsha River was selected as a case study for in-depth investigations. The detailed field investigations were carried out to identify the landslide with respect to its surroundings and to find out the slip surface. Boreholes were drilled to find out the subsurface lithology and the depth of failure of Dasha landslide. The in situ geotechnical tests were performed, and the soil samples from exposed slip surface were retrieved for geotechnical laboratory analysis. Finally, stability analysis was done using the 3D strength reduction method under different conditions of reservoir water level fluctuations and rainfall conditions. The in-depth investigations show that the Dasha landslide is a bedding rockslide which was once activated in 1986. The topography of Dasha landslide is relatively flat, while the back scarp and local terrain is relatively steep. The total volume of landslides is about 580×10^4 m^3 with an average thickness of 20 m. Bedrock in the landslide area is composed of Suining Formation of the Jurassic age. The main rock type is silty mudstone with sandstone, and the bedding orientation is 300~310° ∠ 7~22°. The factor of safety (FOS) of Dasha landslide obtained by 3D strength reduction cannot meet the minimum safety requirement under the working condition of reservoir level fluctuation as designed, with effect of rainfall and rapid drawdown.

1. Introduction

Landslides are common natural hazards which include a wide range of ground movement, such as rockfalls, deep failure of slopes, and shallow debris flows, which can occur in offshore, coastal, and onshore environments. Although gravity is the primary driving force for a landslide to occur, there are other contributing factors affecting the original slope stability.

Various studies have been done on reservoir slopes; however, there are two common factors which are always taken into consideration which include the effect of reservoir water on the slope and the corresponding effect of landslide on reservoir if slope fails. Particular considerations include the following: (i) reservoir slopes are subjected to load changes as a

result of inundation when the reservoir is filled and subsequently as a result of variations in lake level during operations, (ii) the reservoir impounding affects the slope material properties and generates more adverse groundwater conditions than previously existed within the slope, creating reservoir-specific changes that can lead to instability, and (iii) the reservoir can increase the probability and consequences of failure, which may include total or partial blockage of the reservoir, the possibility of damaging impulse waves which may have effects that extend beyond the reservoir [1].

Until 1963, the reservoir landslides were not studied in depth, and the first detailed studied landslide (Vaiont landslides in Italy) became the benchmark for reservoir slopes studies. It is found that maximum large reservoir landslides are the old reactivated landslides [1]. Maximum landslides
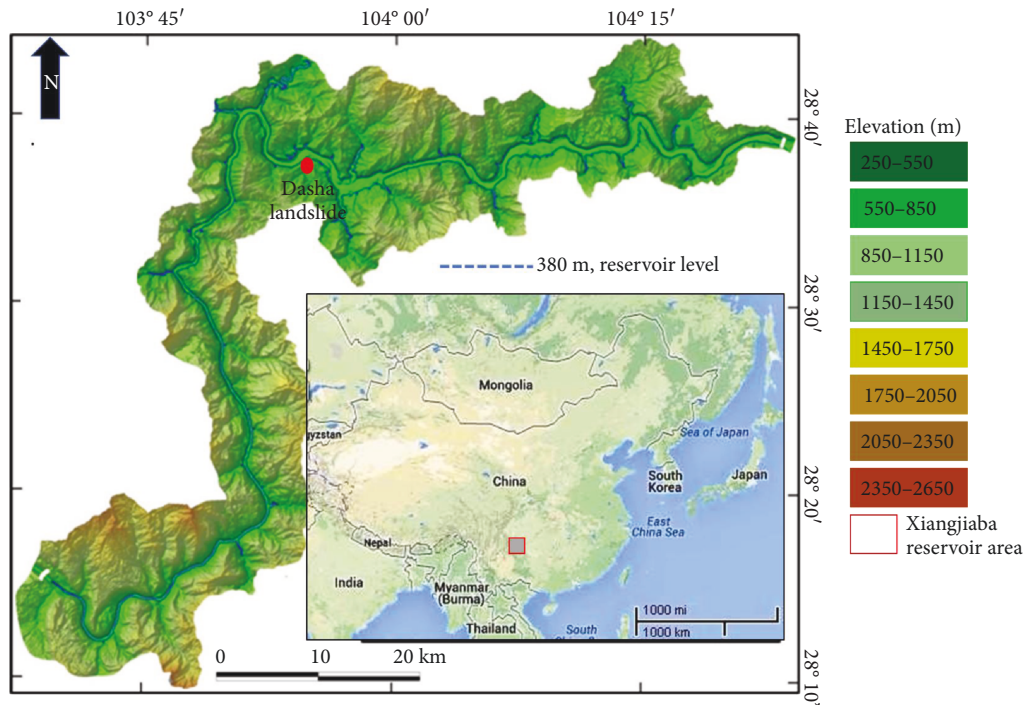
FIGURE 1: Topography of the reservoir area.

reactivate during the reservoir impoundment period or just after completion of the reservoir construction [2].

There are several studies found on Chinese reservoir landslides with different sets of objectives and outcomes (e.g., [3–13]). Various studies have been carried out in the Xiangjiaba reservoir area [14–16] and other reservoirs [17–20].

The impoundment of the Xiangjiaba reservoir is planned up to 380 m elevation in three stages. In the first stage, the reservoir filled to 354 m (October 12-16, 2012). In the second stage, the reservoir level increased to 370 m (June 26 to July 5, 2013). In the last stage, the reservoir reached to its maximum planned level of 380 m (September 7-12, 2013). Due to multiple episodes of reservoir rise and fall, the slopes were subjected to different conditions of alternate wetting and drying which may affect the stability of the slope. In addition, rainfall could also elevate the groundwater level which may create adverse effects on the stability of the slope. The current study is aimed at analyzing these impacts on the old reactivated large landslides.

2. Field Investigation and Landslide Descriptions

Dasha landslide is located at Dasha town, Suijiang County, at the right bank of Jinsha River about 60 km upstream of the Xiangjiaba damsite (Figures 1–3). In the northeast of the landslide near the Jinsha River, there is a about 260~370 m terrace, while in the southeast of the landslide there is also a flat terrace widely covered with alluvial deposits, between them there is a gully. Two bank slopes of the gully are quite different. The inclination of the bank slope with landside is low, while the river alluvial sediments terrace is very steep. In the north of the landslide, the red-bed hills are distributed along with alluvial sediments having gentle slope. In the west of landslide, a steep slope adjoins Gaofengshi Mountains, whose height is 687 m. Bedrock in the landslide area is composed of Suining Formation of the Jurassic age, which is composed of reddish brown or purple silty mudstone with sandstone interlayer; rock orientation is 300°~310° ∠ 7°~22°. These rocks are distributed in the steep slope area in the west (back edge) of the landslide and along the Jinsha River bank slope (along highway) in the north and gully bottom in the east.

It is revealed through drilling that the landslide slope is composed of clay, silt with some rock fragments, and the underlying bedrock orientation is 310°∠15°. This landslide was reactivated during the rainy season in 1986, resulting in structural damages to homes and the ground surface. There is mainly a paddy field on the landslide slope; on the edge of landslide, water permeates into the gulley; on the back margin of the landslide, obvious cracks can be observed in house walls (Figure 4). So, the rise of the ground water level as a result of rain in the landslide should be the main cause of the landslide deformation. Eliminating local terrain effect, the strike of tensional cracks is 315 to 340°, with inclination of 60 to 70°. According to the drilling data, bedrock orientation and the relationship with landslide directions of movement, landslide should be the creep deformation of the overlying loose deposits along the underlying bedrock. In the past decade, paddy field became upland dry land. During the current investigations, no groundwater infiltrated on the edge of landslide, and creep deformation of the landslide mass is not very obvious; so, the groundwater level change is the controlling factors of landslide deformation.

The overall topographic slope angle of the terrain is less than 15°; however, the head scarp and local terrain is
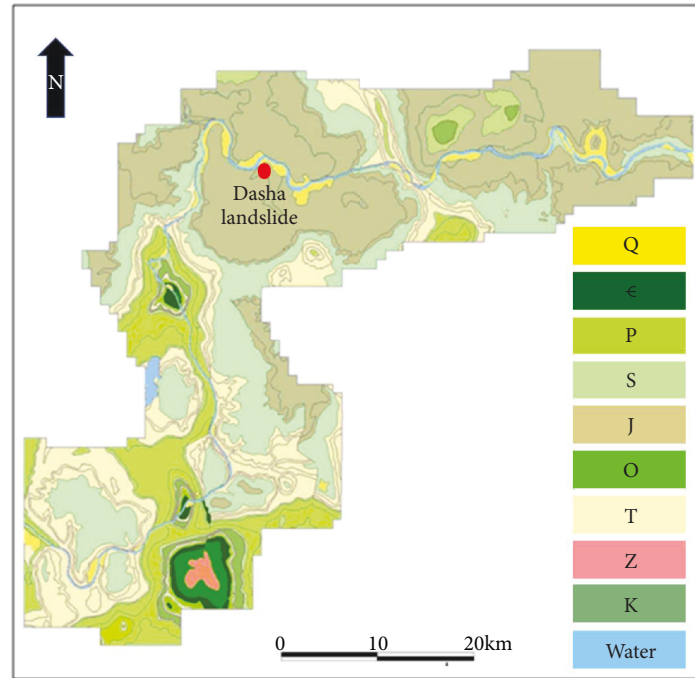
FIGURE 2: Generalized geological map of the Xiangjiaba reservoir area. Where Sinian system = Z; Cambrian system = Є; Ordovician system = O; Silurian system = S; Permian system = P; Triassic system = T; Jurassic system = J; Cretaceous system = K; Quaternary system = Q.
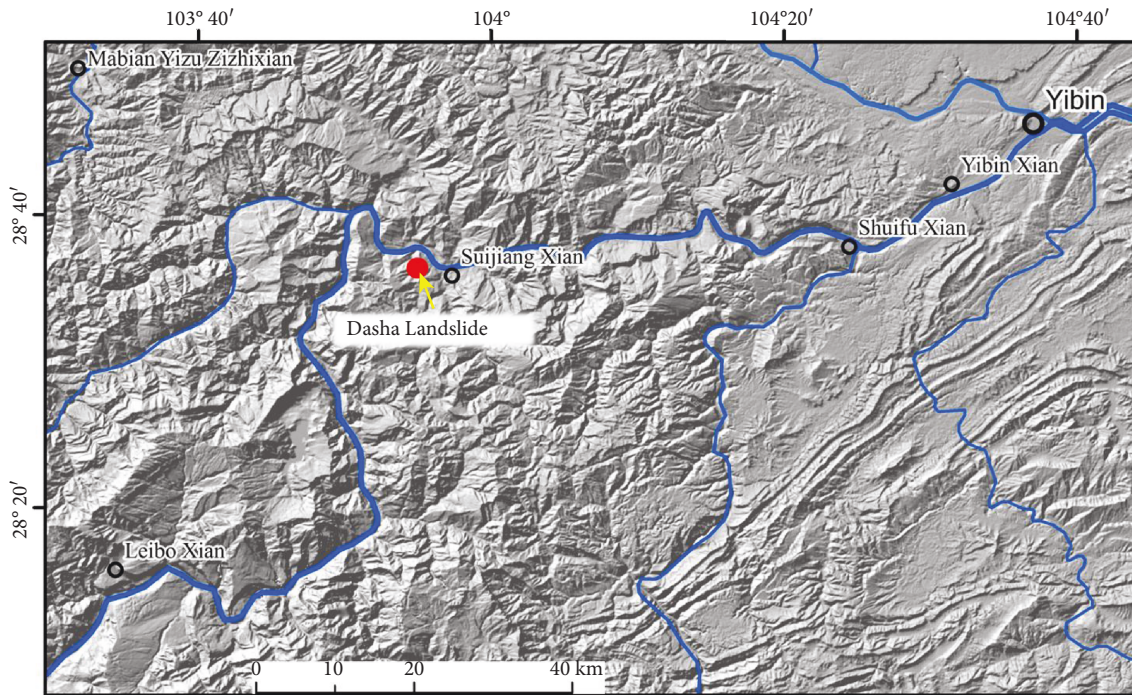

FIGURE 3: Location map of Dasha landslide.

relatively steep. The landslide area is about 29×10^4 m^2; the thickness of the landslide revealed by drilling is about 40 m, with the average thickness being about 20 m. The volume of the landslide is estimated to be about 580×10^4 m^3. From the landform conditions and air photo interpretation, a secondary landslide developed on the frontal margin of the landslide with clear chair-shaped landform is about 2.7×10^4 m^2 in area and about 16×10^4 m^3 in volume with the average thickness of about 6 m (Figures 5 and 6).

In the last decade, the paddy field was transformed into dry land, the groundwater levels lowered in the landslide, and the deformation of the landslide is not very obvious,
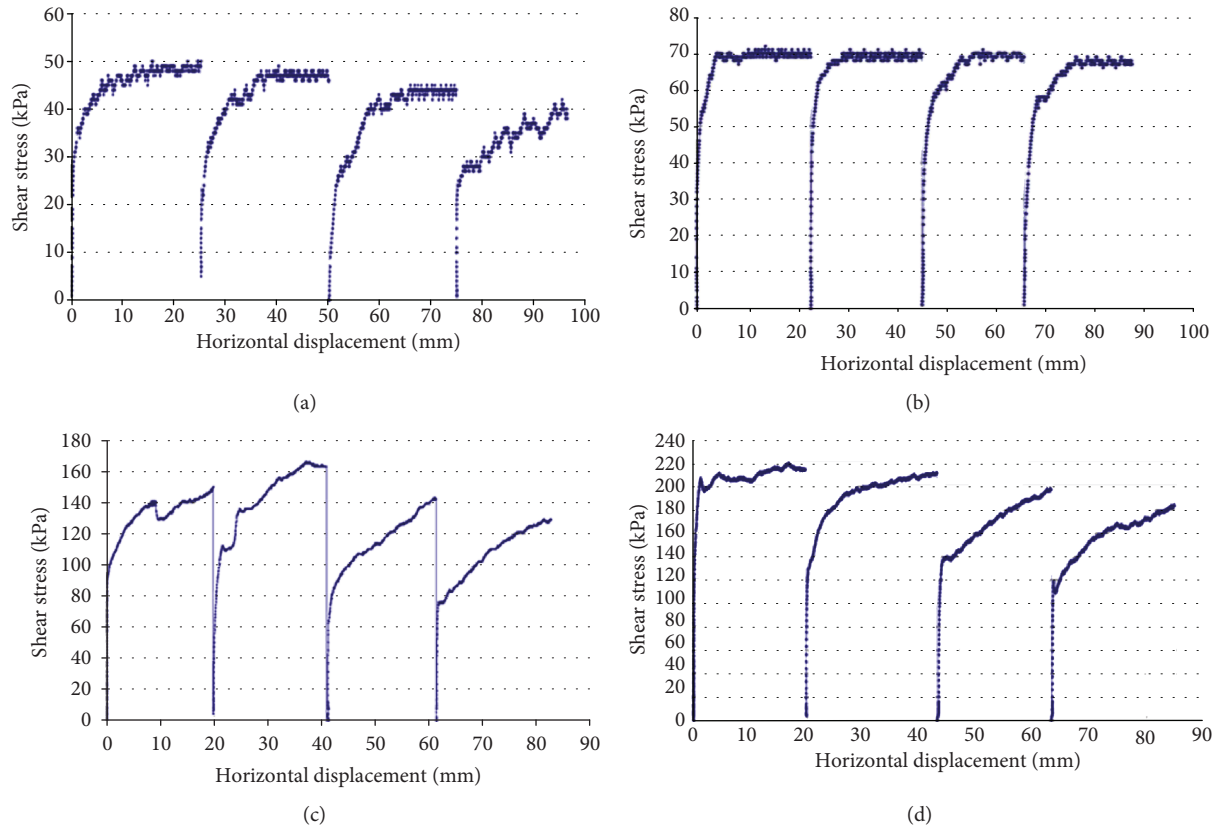
(a)

(b)

(c)

(d)

FIGURE 4: The shear stress-displacement curve of repeated direct shear at different normal stresses. (a) 60 kPa, (b) 110 kPa, (c) 260 kPa, and (d) 410 kPa.
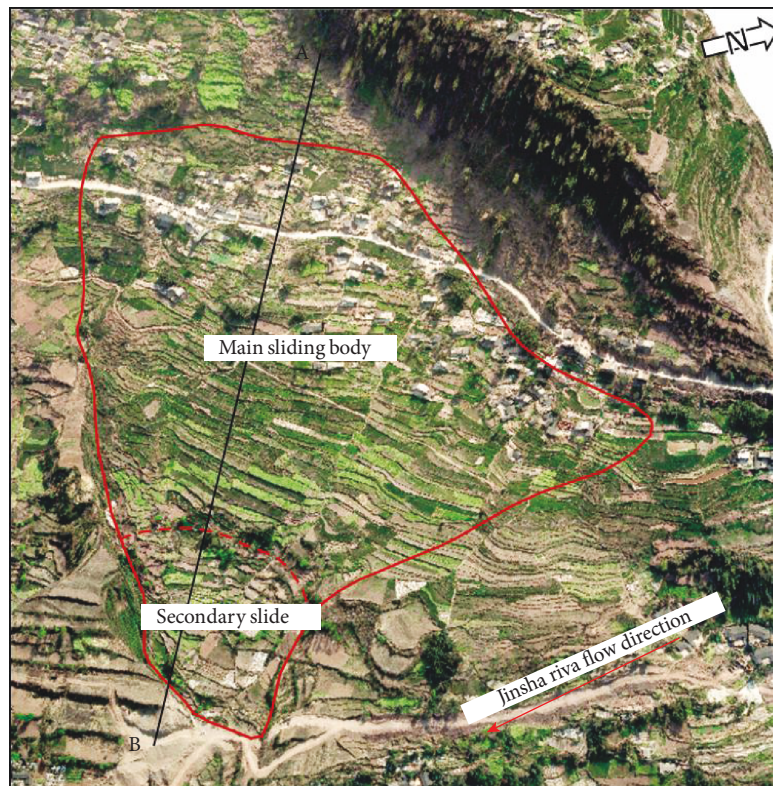

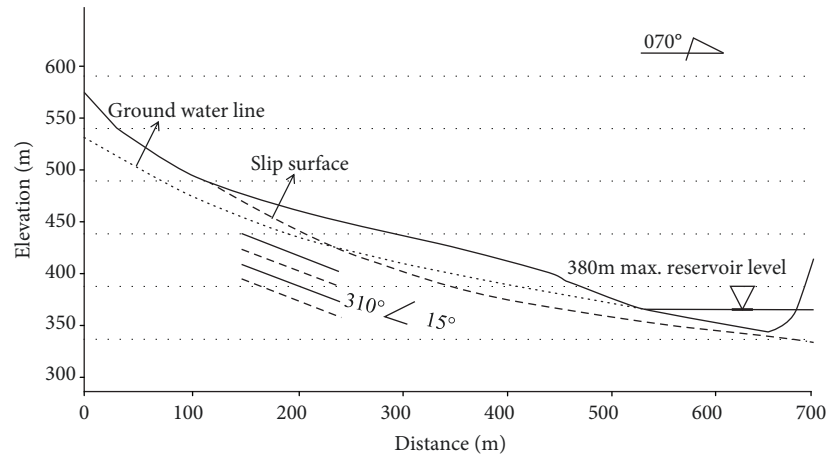FIGURE 5: Remote-sensing image of Dasha landslide.

FIGURE 6: Cross-section of Dasha landslide (A-B).

(a)

(b)

FIGURE 7: (a) A view of Dasha landslides; (b) tensional cracks in house wall.

but local visible cracks in the house wall can be found (Figure 7). This means that the landslide is still in the state of potential instability under the condition of the groundwater level rising or heavy rain. According to aerial photographs, houses are dense in the middle and back part of the landslide; hence, once the landslide moves perceptibly, it would create a huge loss in terms of human and property.

3. Geotechnical Laboratory Tests

Undisturbed soil samples taken near the slip surface were tested in the laboratory. Basic properties such as specific gravity, grain sizes, liquid limit, and plasticity index were measured. The natural density, dry density, and degree of saturation were found to be 2.233 g/cm^3, 1.975 g/cm^3, and 89%, respectively. The specific gravity was found to be 2.78 g/cm^3. The liquid limit, plastic limit, and plasticity index were found to be 25.8%, 19.7%, and 6.1, respectively. These basic properties were used in preparing the remolded samples for laboratory testing as well as in numerical simulation process to set the parameters. The laboratory direct shear tests are discussed below.

3.1. Medium-Sized Saturated Reversal Direct Shear Tests on Undisturbed Samples. The undisturbed samples were soaked for more than 24 hours. The size of the samples is $20 \times 20 \times 15$ cm. The horizontal shear rate of direct shear apparatus that was used for the tests can be controlled by regulating the motor speed, and the shear rate was 2.2 mm/min (fast shear); it could be stopped when the maximum shear displacement reaches 20 mm. The vertical loading system of direct shear apparatus was hydraulic pressure, and the pressure sensor of the apparatus has low accuracy, so the values of normal stress were acquired by vertical pressure sensor during tests.

The actual values of normal stress are 61, 110, 260, and 410 kPa, and the shear strength after the forth cycles of shearing is considered the residual strength. The displacement of one-way shear is more than 20 mm, and the cumulative displacement would be more than 80 mm after four cycles of shearing. During the first shear, all of the four samples reached the peak quickly and kept the shear stress stable. However, it was different after the two or three times of shearing, and the shear stress tends to increase. The shear stress-displacement curves at different normal stresses are shown in Figure 4, and the first peak value of shear stress is peak strength. According to the first shear strength and the
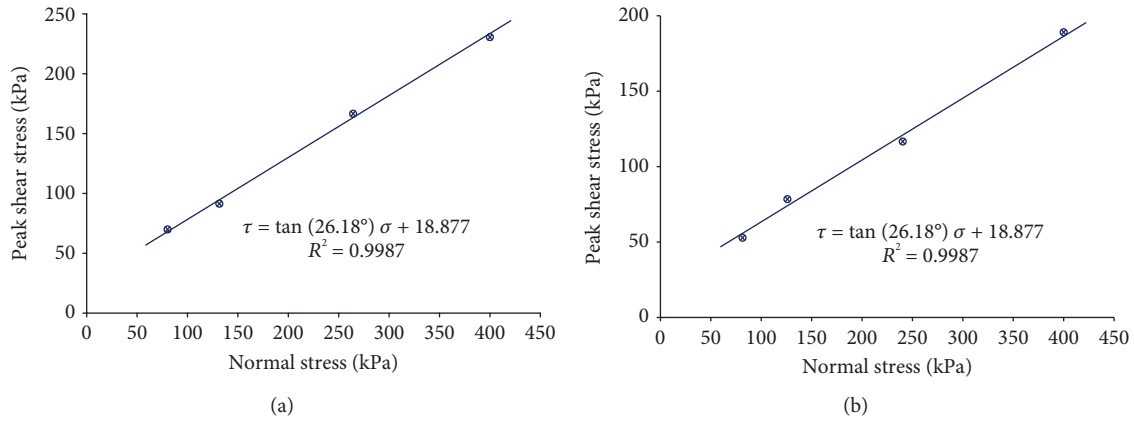
(a)

(b)

FIGURE 8: Graph showing the peak and residual strength parameters.
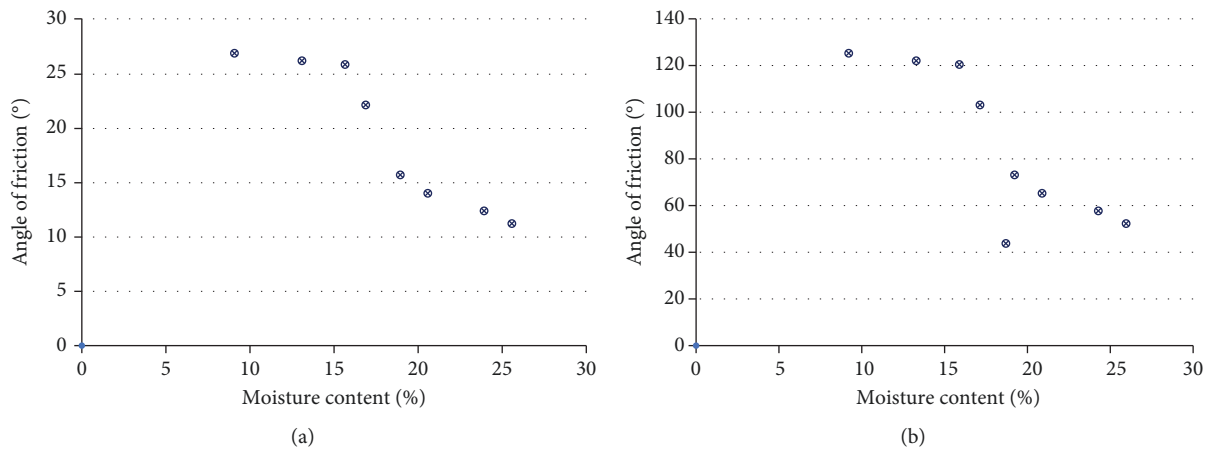

(a)

(b)

FIGURE 9: Effect of moisture on strength parameters.

last stable strength, the relationship between shear strength and normal stress can be drawn. As shown in Figure 8, the peak shear strength and the residual shear strength in the form of frictional angle and cohesion are 26.18°, 18.88 kPa and 21.38°, 17.95 kPa, respectively. The average moisture content of the soil samples measured from shear surface after opening of the shear box is 17.0%.

3.2. Medium-Size Direct Shear Test on Remolded Samples. Dasha landslide is a typical bedding landslide of red beds, and the particle size decreases with increase in depth. The soil samples consisting of high proportion of gravel-sized particles were taken near the toe of landslide at a depth of 1.5 m. The soil samples were remolded and prepared with different moisture content in order to explore the relationship between soil strength of the slope and water content. The size of samples is $20 \times 20 \times 15$ cm, and the shear rate is 1.0 mm/min. Under the consolidated and drained conditions, seven groups (each group with three samples) were tested in this series, and the moisture content of each group was determined after each test (Figures 9 and 10). As shown in Table 1, the direct shear tests for the soil with less than 2 mm particle size, the strength parameters are greatly influenced by the moisture content, and with a decrease in moisture content, the angle of friction and cohesion increases.

3.3. The Triaxial Consolidation Undrained Shear Tests. Three triaxial shear tests for Dasha landslide were performed in consolidated-undrained condition. The results of shear tests are shown in Figure 11. The effective cohesion and angle of friction for groups A, B, and C are 11.4 kPa and 22.5°, 21.6 kPa and 24.1°, and 23.4 kPa and 25.2°, respectively (Figure 11 and Table 2). It is observed that the shear strength parameters including cohesion and angle of internal friction of all three groups (A, B, and C) are in very small range, showing the reliability of the results which were later used in the simulation process.

4. Geotechnical In Situ Tests

The test was done on soil samples located near the toe of the landslide (fine sand and clay). The direct shear models were built on bedrock, which were perpendicular to the surface of bedrock, and specimens were pushed to shear along the bedrock. Two groups of large-sized direct shear tests (sample size of $50 \times 50 \times 40$ cm) were carried out at this test site to compare and better understand the results of in situ tests. The predefined values of normal stress were 50 kPa, 100 kPa, 150 kPa, and 200 kPa, and there was some deviation between the measured values and the predefined values of normal stress. Therefore, for the fitting of strength parameter
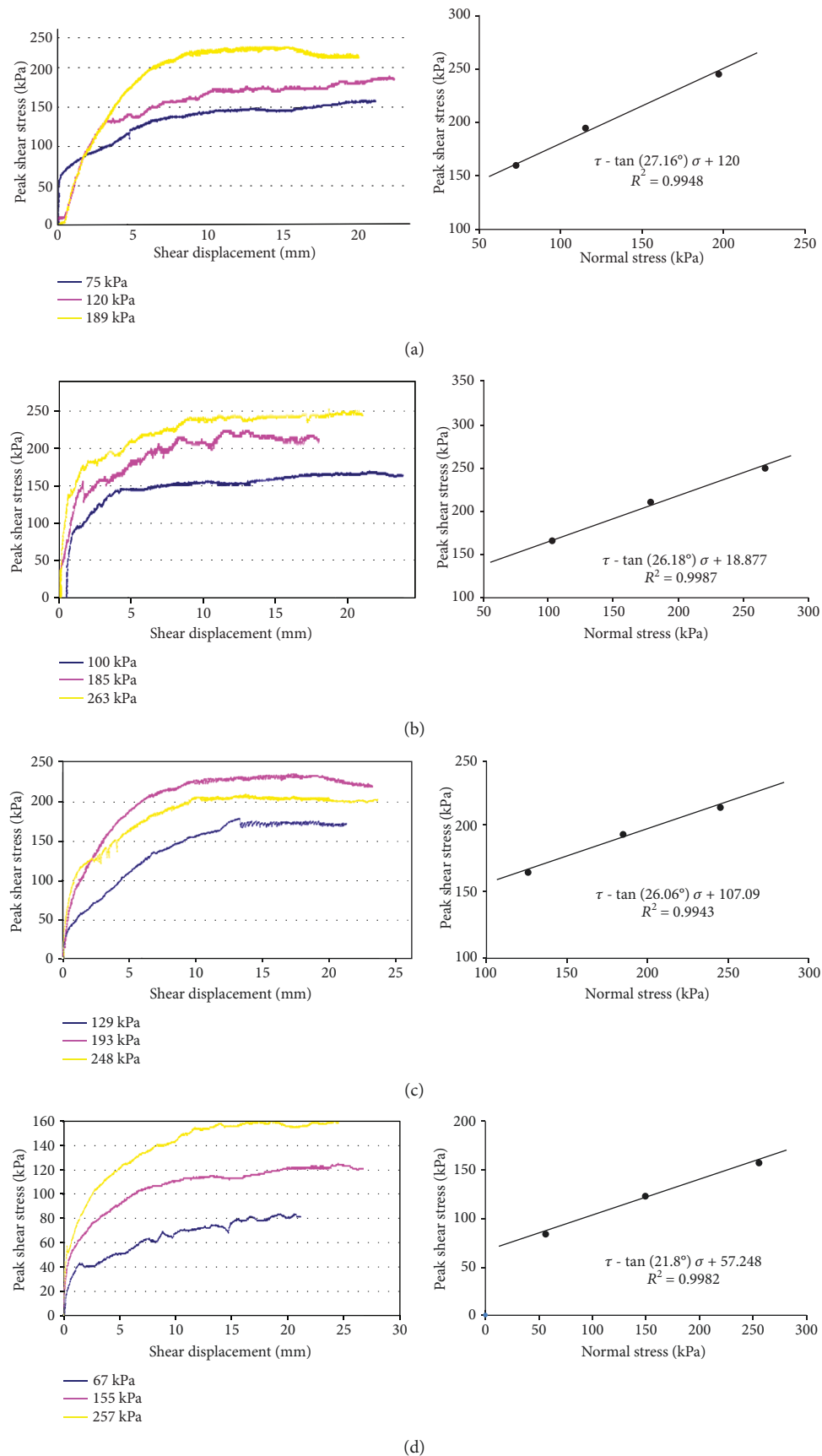
(a)

(b)
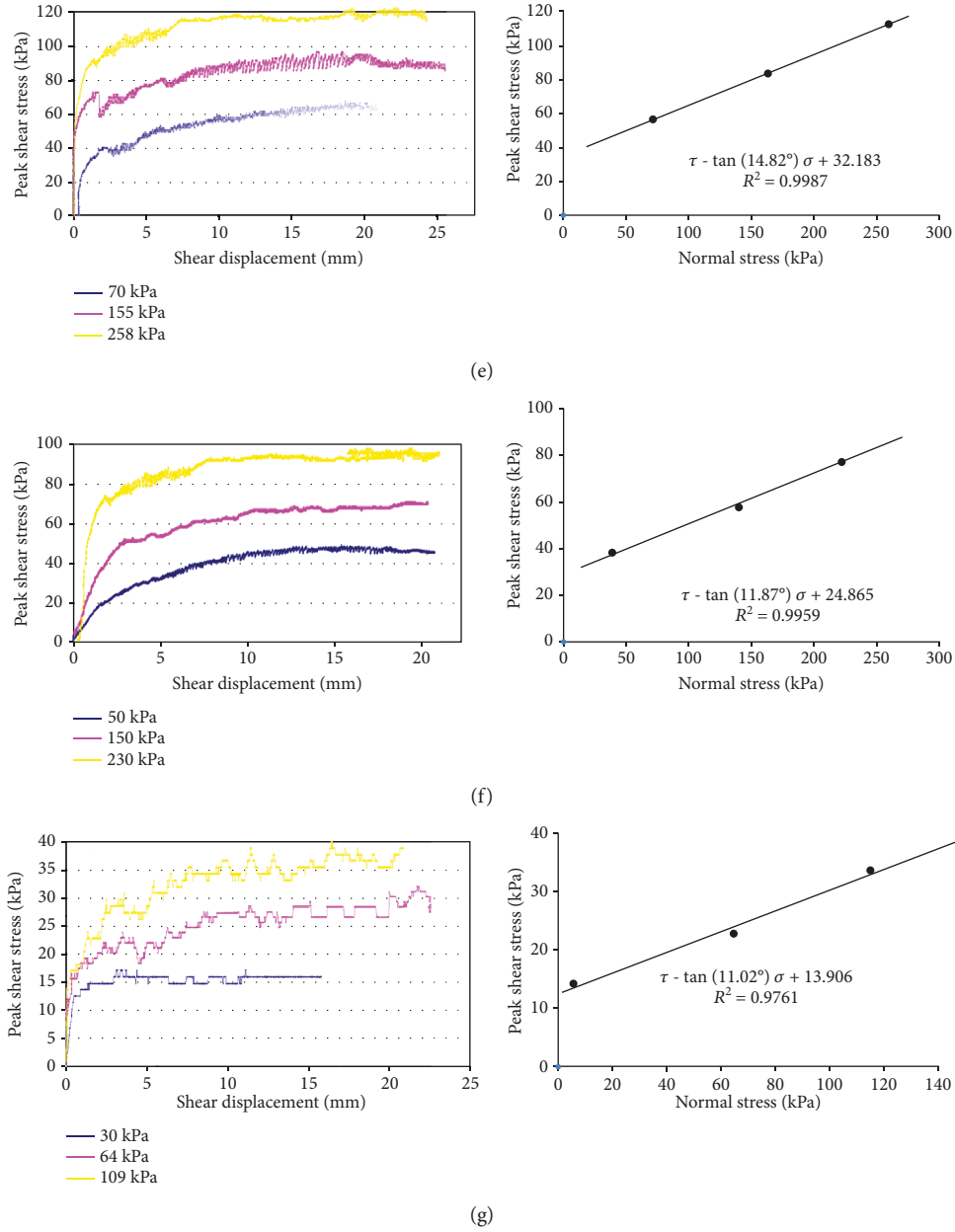

(c)

(d)

Figure 10: Continued.

(e)

(f)

(g)

FIGURE 10: Medium-size direct shear test on remolded samples; shear stress-displacement curves and strength parameters of all seven groups.

TABLE 1: Direct shear tests parameters of soil with particle size less than 2 mm.

Group	Cohesion (kPa)	Angle of friction (°)	Average moisture content (%)
1	120	27.16	8.2
2	114.74	26.46	12
3	107.09	26.06	14.3
4	57.25	21.8	15.8
5	32.18	14.82	18.1
6	24.86	11.87	20
7	12.3	10.01	25

curves, the measured normal stress values were applied. There were six samples in the first group of tests; however, only four samples were remained effective. Four samples were used in the second group, and only three were proved to be effective. The normal stress of the tests was adjusted by manual pump control jack, and the horizontal shear force was applied through the electric pump drive jack with an average shear rate of 0.9 mm/min. The sample preparation process in the field is shown in Figure 12.

4.1. The First Group of Direct Shear Test. For the predefined 50 kPa normal stress test, the measured value of normal stress is 49 kPa and the maximum shear displacement is 56 mm. For the predefined 100 kPa normal stress test, the measured normal stress is 100 kPa, the maximum shear displacement
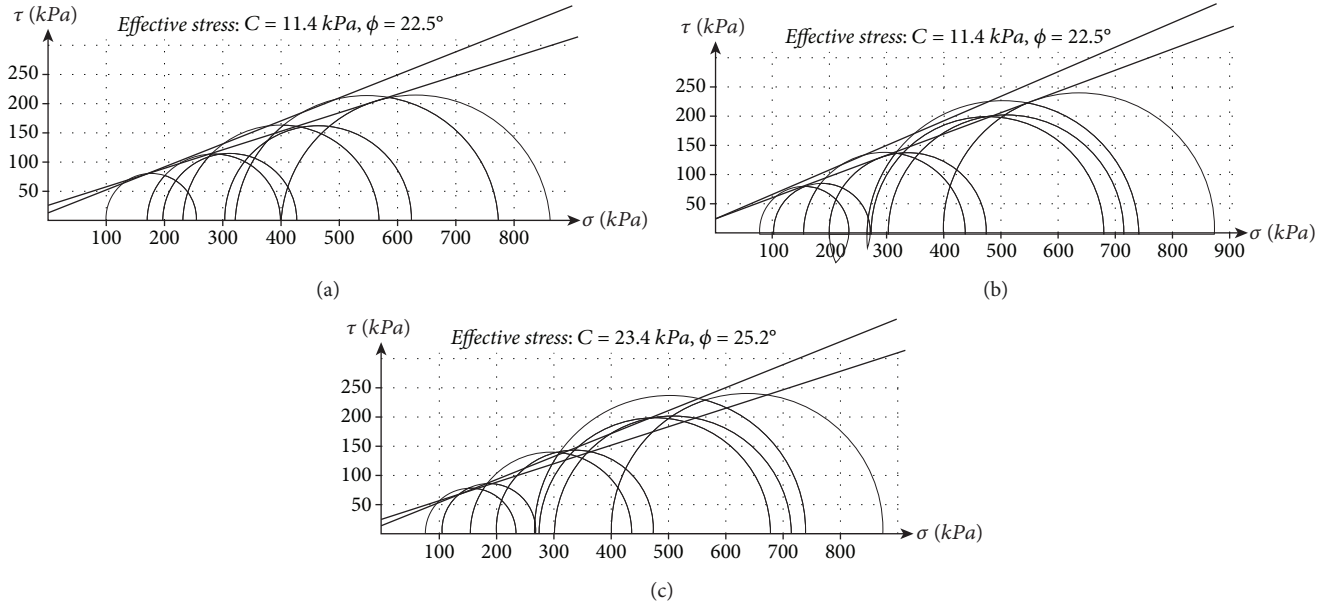
(a)

(b)

(c)

FIGURE 11: Tests fitting curve of soil samples for triaxial shear test (group a, b, and c).

TABLE 2: Results of triaxial consolidation undrained shear tests of soil samples.

$\sigma 3$	$\sigma 3'$	$\sigma 1$	$\sigma 1'$	$\dfrac{\sigma 1 + \sigma 3}{2}$	$\dfrac{\sigma 1' + \sigma 3'}{2}$	$\dfrac{\sigma 1' - \sigma 3'}{2}$
Group A						
100	96.0	269.0	265.0	184.5	180.5	84.5
200	174.0	430.0	404.0	315.0	289.0	115.0
300	242.0	625.0	567.0	462.5	404.5	162.5
400	326.0	847.0	773.0	623.5	549.5	223.5
Group B						
100	68.5	271.0	239.5	185.5	154.0	85.5
200	159.5	474.0	433.5	337.0	296.5	137.0
300	173.5	708.0	681.5	501.0	477.5	204.0
400	266.0	872.0	738.0	636.0	502.0	236.0
Group C						
100	98.0	305.0	303.0	202.5	200.5	102.5
200	153.0	520.0	473.0	360.0	313.0	160.0
300	238.5	722.0	660.5	511.0	449.5	211.0
400	318.0	941.0	889.0	670.5	588.5	270.5

is 79 mm, and the average shear rate is 0.59 mm/min. For the 150 kPa normal stress test, the actual normal stress is 147 kPa, the maximum shear displacement is 85 mm, and the average shear speed is 1.3 mm/min; during the horizontal displacement of 0 mm to 1.32 mm, it failed to get the data due to the fault in the cable of horizontal shear stress sensor, but it did not make a great difference. For the predefined 200 kPa normal stress test, the measured value of normal stress is also 200 kPa and the maximum shear displacement is 85 mm. The results of the first group are good, and the shapes of the shear stress displacement curves are similar. After the peak, stress values keep steady. For the normal stress values of 49, 79,

174, and 200 kPa, the peak shear stress values are 50, 78, 110, and 137 kPa, respectively. The shear strength parameters in the form of cohesion and angle of friction are 21.17 kPa and 30.3°, respectively (Figure 13 and Table 3).

4.2. The Second Group of Direct Shear Test. During the test, it rained a lot which greatly influenced the results. There are only three effective samples in the second group of the test, and the measured values of normal stress are 98 kPa, 145 kPa, and 197 kPa. When the normal stress is 98 kPa, the maximum shear displacement is 86 mm and the average shear speed is 1.95 mm/min. When the normal stress is 145 kPa, the maximum shear displacement is 81 mm and the average shear speed is 1.75 mm/min. When the normal stress is 197 kPa, the maximum shear displacement is 83 mm and the average shear speed is 1.7 mm/min. The average shear speed of three samples is similar. When the displacement is about 40 mm, it reaches its peak, and then the value of stress keeps steady. For the normal stress values of 98, 145, and 197 kPa, the corresponding peak shear stress values are 82, 102, and 127 kPa, respectively. The results of the fitting curves are good, and the strength parameters in the form of cohesion and angle of friction are 37 kPa and 24.4°, respectively (Figure 14 and Table 3).

4.3. The In Situ Permeability Tests. Sixteen permeability tests were carried out in the Dasha landslide using the double-ring infiltration method using ASTM [21] D3385-09 (Figure 15(b)). During the test site preparation, the inner ring diameter of the infiltrometer was 25 cm while the outer ring diameter was 50 cm, and the height of the ring was 30 cm. During the experiment, the infiltrometer was dug into the soil at a depth of 10 cm keeping both rings concentric. Usually the bottom edge of the ring is not in well contact with the soils which lead to the leakage of water, resulting in a high permeability coefficient value. In order to reduce this error,
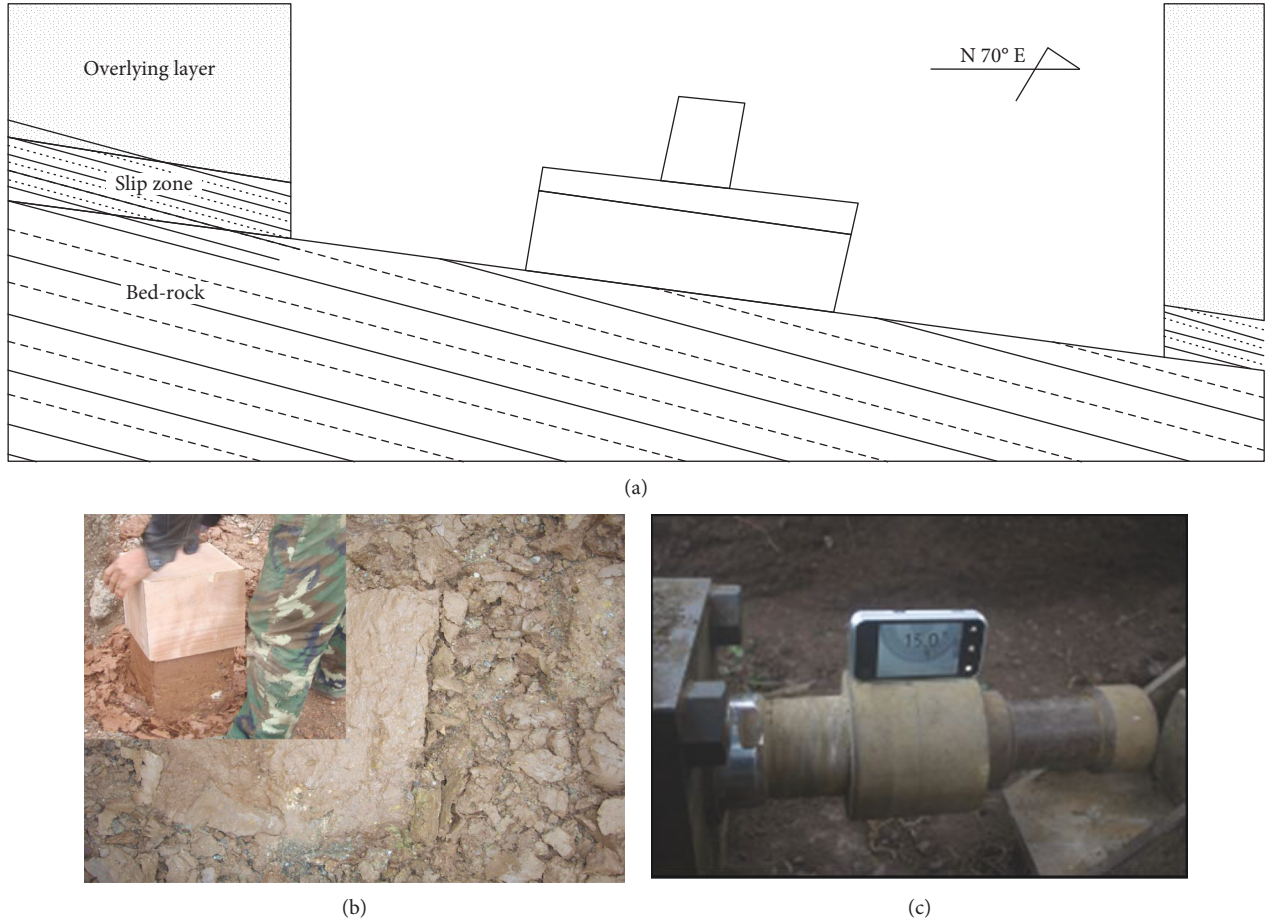
(a)

(b)

(c)

Figure 12: Sample preparation for test in field. (a) Schematic diagram of pruning samples, (b) inclined pruning samples, and (c) inclined push shear.
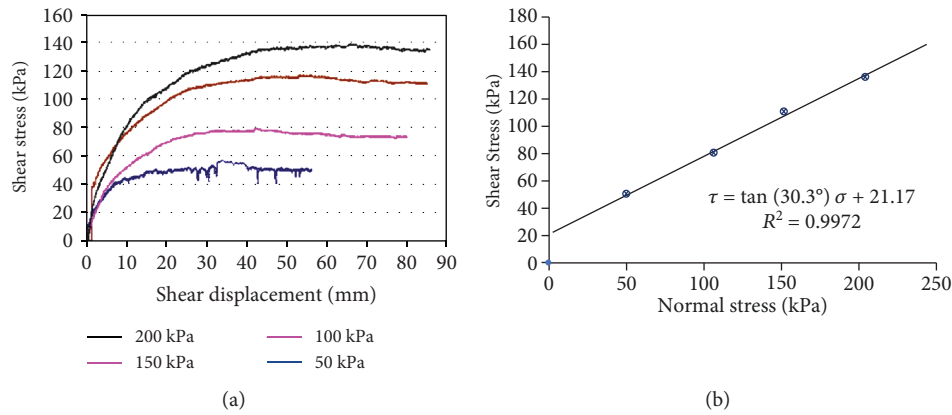

(a)

(b)

Figure 13: Shear stress-displacement curve and strength parameters of the first group.

firstly, the small trench was dug from top to bottom along the outer walls of both of the rings and then the bottom edge of the rings was sealed with bentonite, while the outer ring was filled with 10 cm thick compacted soil. The landslide has a gentle slope and is developed as farmland, so it is convenient while choosing test sites and water intake for in-site testing. Out of total sixteen permeability tests, the first four tests were carried within the area from where in situ direct shear tests were performed, while the rest of the test points were evenly distributed within the landslide body (Figure 15(a) and Table 3).

5. Stability Analysis

5.1. Three-Dimensional Stability Analysis Based on Strength Reduction Method. FLAC 3D software is used for stability analysis. The model area is 880 m × 900 m. X-axis which is parallel with the cross-section 1-1'of the landslide with the

TABLE 3: The test results of different parameters on site.

(a)

					Strength parameters	
First group of direct shear test of Dasha						
Normal stress (kPa)	49	100	147	200	Cohesion (kPa)	21.17
The peak shear stress (kPa)	50	78	110	137	Angle of friction (˚)	30.3
Average moisture content of tests (%)	8.2	7.1	5.0	9.0		
Second group of direct shear test of Dasha						
Normal stress (kPa)	98	145	197	—	Cohesion (kPa)	37
The peak shear stress (kPa)	82	102	127	—	Angle of friction (˚)	24.4
Average moisture content of tests (%)	6.9	7.1	7.5	—		

(b)

The permeability test in Dasha and in situ density		
The range of permeability (m/s)	The average permeability (m/s)	In situ density (g/cm^3)
4.530E-06…4.530E-05	2.11274E-05	2.233

$$\tau = \tan(24.4°)\,\sigma + 37.036$$
$$R = 0.9989$$

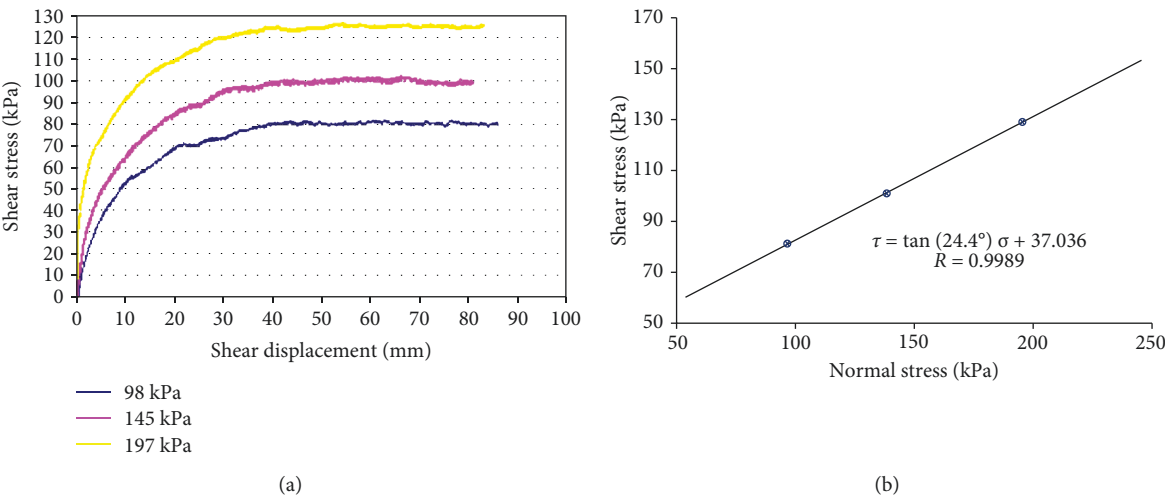(a)   (b)

FIGURE 14: Shear stress - displacement curve and strength parameters of second group.

(a)   (b)
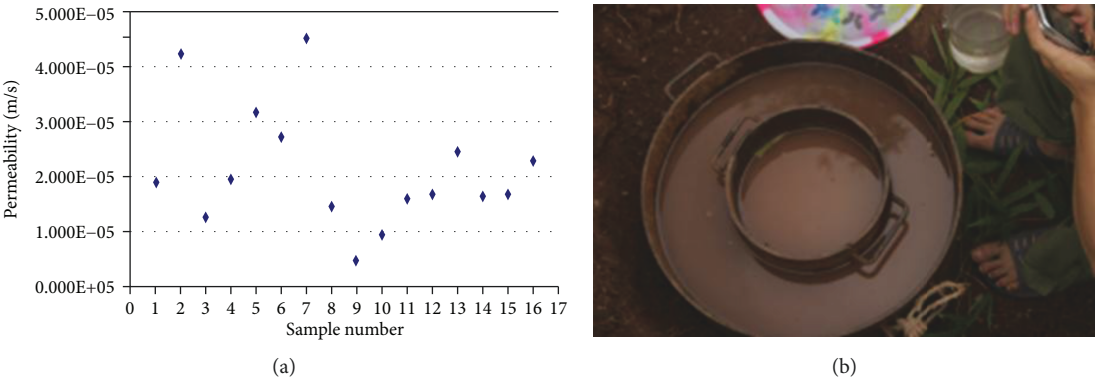
FIGURE 15: (a) Distribution of in situ permeability tests; (b) permeability test in the field using the double-ring infiltrometer method.
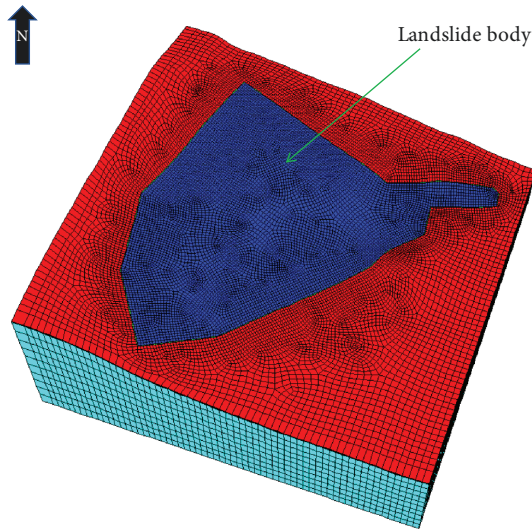
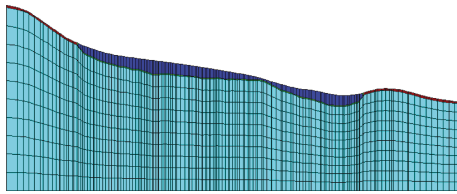FIGURE 16: 3D numerical model of Dasha landslide.

FIGURE 17: Sectional view of the model of Dasha landslide.

direction towards Jinsha River. Y-axis is vertical with respect to the cross-section 1-1' and the Z-axis with positive upward direction. The range of X-axis is 0~880 m, Y axis is 0~900 m, and Z-axis is from the elevation of 200 m up to the ground surface. Computational mesh is shown in Figures 16 and 17, and the model is divided into 182416 nodes and 166836 elements. In numerical analysis, the fixed constraints at the bottom of the model and normal constraints around the perimeter of the model were applied. X-axis is bounded by 0 m and 880 m, Y-axis is bounded by 0 m and 900 m, and Z-axis is bounded by 200 m. The slope materials were assumed to be perfectly elastoplastic and satisfy the Mohr-Coulomb failure criteria. Based on the actual geological and geomorphological conditions of the Dasha landslide, the numerical model was built which include the slip zone, the landslide, and the underlying bedrock. Three material layers were built including the slip zone, the landslide, and the bedrock. In order to obtain the geotechnical parameters of Dasha landslide, the in situ tests, as well as laboratory tests, were carried out. The parameters used in numerical modeling are shown in Table 4; bulk modulus (K) and shear modulus (E) were converted from Young's modulus (E) and Poisson' ratio (v). The initial stress under the gravity and hydrostatic pressure were calculated under natural conditions.

The calculation is performed in two steps, while performing the calculations in natural condition (without considering water effect), the first step is to calculate elastic deformation and stress of bedrock, landslide body, and slip zone under the effect of gravity and as the initial state. The

second step is to simulate the deformation development process by eliminating the initial elastic displacement and setting the slip zone as elastic-plastic. The slip zone was assumed as a perfect elastic-plastic constitutive model with yield criteria of Mohr-Coulomb, while the landslide body and the underlying bedrock were assumed as the linear elastic model. When considering the reservoir water level, the steady flow analysis is applied in this condition by assuming that the reservoir water level does not change and there is no raining. Analysis of transient flow is applied in other conditions. Water pressure change is measured by Abaqus software, and it can carry out coupled fluid-solid analysis in different conditions of rainfall and reservoir level and also export data of hydraulic condition and stress condition from analysis results as an initial state and finally import to the FLAC^{3D} landslide model for three-dimensional strength reduction analysis in the natural conditions (without considering the reservoir water level) to get the FOS of the landslide.

5.2. Three-Dimensional Strength Reduction Analysis without Consideration of Groundwater. Every strength reduction calculation is carried out by using the test of transfixion of slip plastic zone. Under the natural conditions without considering groundwater, the maximum principal stress distribution is shown in Figure 18 and the development process of slip plastic zone is shown in Figure 19. When the strength reduction factor (RF) reaches 1.212, it indicates that the continuous yield area has basically formed in the slip zone, with only a small range of area not reaching the yield limit, i.e., the factor of safety of the landslide is 1.212. The distribution and development of the slip plastic zone at the left side and the middle upper side enter the plastic phase earlier than the right side. The maximum principal stress of Dasha landslide within the range of the numerical simulation is about 8.0 MPa; the maximum principal stress of the slope is about 0.1 MPa. The principal stress values of the landslide range approximately from 0.4 MPa to 0.8 MPa. The maximum principal stress whose direction is nearly vertical is almost equal to the vertical stress.

5.3. Three-Dimensional Strength Reduction Analysis with Effect of Rainfall and Reservoir Filling. This condition is after the final phase of reservoir filling, which reflects the global stability of Dasha landslide with the consideration of the groundwater, reservoir level of 380 m, and rainfall conditions. For numerical simulation under the condition of heavy rainfall, the transient flow analysis is used. Under the condition of heavy rainfall, the changes of water pressures of Dasha landslide are shown in Figure 20. The figure shows that during heavy rainfall, the water pressures keep increasing gradually with the increase in rainfall, and the saturation line gradually increases as well. After the rain water pressure decreases, the saturation line gradually reduces to a particular reservoir level. The change of water pressures is not very significant after the rainfall. Under the condition of heavy rainfall of 94.7 mm in 2 hours, the factor of safety obtained by strength reduction method is 0.991, which does not meet the standards of safety requirements (Table 5).

TABLE 4: Calculation parameters of Dasha landslide taken from field and lab experiments.

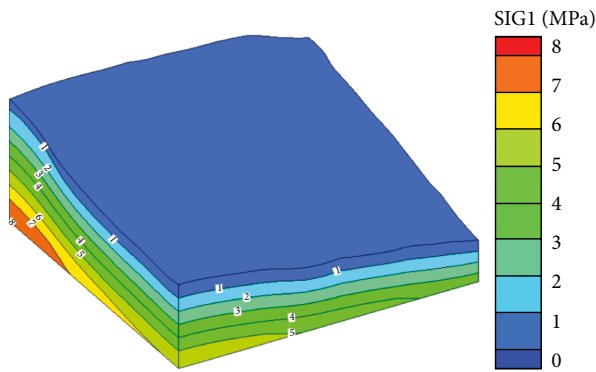| Material	Unit weight (KN/m^3)		Elastic modulus (MPa)	Poisson's ratio	Natural		Saturated	
	Natural	Saturated			Cohesion (kPa)	Angle of friction (°)	Cohesion (kPa)	Angle of friction (°)
Landslide deposits	19	22	500	0.32	17	20	14	17
Slip zone	18	21	15	0.40	13	18	8	14
Bedrock	25	26	1000	0.28	1000	35	800	30

FIGURE 18: Maximum principal stress of Dasha landslide under the gravity.

6. Discussion

The Dasha landslide located at the right bank of the Jinsha River in the Xiangjiaba reservoir area has been studied from various aspects using diverse field, lab, and simulation techniques to better understand the slope stability in natural conditions as well as the effects of reservoir fluctuations on the slope stability. The stability, even the movement (e.g., [22]), of reactivated landslides has been successfully evaluated and interpreted using the assumption that shear strength mobilized on the slip surface of a landslide is equal to the residual shear strength on the basis of laboratory drained multiple reversal direct shear, or ring shear tests, independent of the time after reaching the residual condition. The landslides with a slip surface at residual condition rarely remain stationary for a long time and may move at the rate of approximately 2–50 mm/year (e.g., [22, 23]). The stability analysis and laboratory tests cannot be expected to yield results with accuracy better than approximately ±10% [24].

Skempton [24, 25] had done the benchmark studies on residual shear strength measured by laboratory tests, and it has been successfully used for stability analyses of reactivated landslides (e.g., [26, 27]; James 1970; [28–35]). The reversal direct shear tests or ring shear tests, using either undisturbed or reconstituted specimens, have become the most common methods for determining residual shear strength of stiff clays, shales, and mudstones (e.g., [29, 31, 36, 37]). For direct shear tests, the best procedure is to start with precut specimens, sometimes cut from intact undisturbed samples, but more often prepared from reconstituted samples [38].

Although each test has been discussed and explained with its results within the same section for better understanding of the readers, however, as there were numerous tests and their subgroups, so we tried to summarize the tests and compared with the previous studies as concluding section of the shear strength tests. As shown in Figure 8, the drained undisturbed sample test results for the peak shear strength and the residual shear strength in the form of frictional angle and cohesion are 26.18°, 18.88 kPa and 21.38°, 17.95 kPa, respectively. The average moisture content of the soil samples measured from shear surface after opening of the shear box is 17.0%. In the remolded direct shear tests, it was noted that the cohesion as well as the angle of internal friction decreases in all cases with a decrease in water content which shows the reliability of the tests (Figures 9 and 10). Both groups of the triaxial consolidation undrained shear tests show similar results; however, they show slight variations in strength parameters from the direct shear tests which is acceptable due to difference in the rest of the methods. For the in situ tests, two shear rates of 1.3 mm/minute and 1.75 mm/minute were applied in this study and the results show that the cohesion increases with shear rate while the angle of internal friction decreases [39].

The direct shear test results indicate that the residual strength of both in situ soils and disturbed soils from the slip zones of the Dasha landslide is influenced by their index properties, for example, the direct shear tests for the soil with less than 2 mm particle size; the strength parameters are greatly influenced by the moisture content, and with a decrease in moisture content, the values of the angle of friction and cohesion increases. However, influences of these index properties on residual strength are quite different for the in situ and disturbed soils. After the fourth cycle of shearing of the medium-sized reversal direct shear tests, the samples had basically reached the residual shear state. It was noted that the residual shear strength obtained by shear box tests has a nonzero cohesion component. Similar results were also reported by other researchers (e.g., [37, 40–43]). The simulation results show that the landslide is stable in the natural situation; however, the water fluctuation will lead to decrease the stability of the slope making it unstable.

7. Conclusions

The Dasha landslide was investigated in detail using field, land, and simulation methods to better understand the effects of reservoir water on the slopes along the banks of the Jinsha River in the Xiangjiaba reservoir. Based on our results and analysis, the following conclusions and recommendations can be drawn:
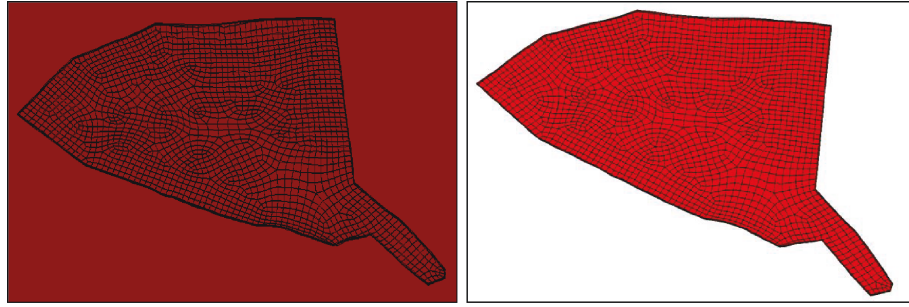
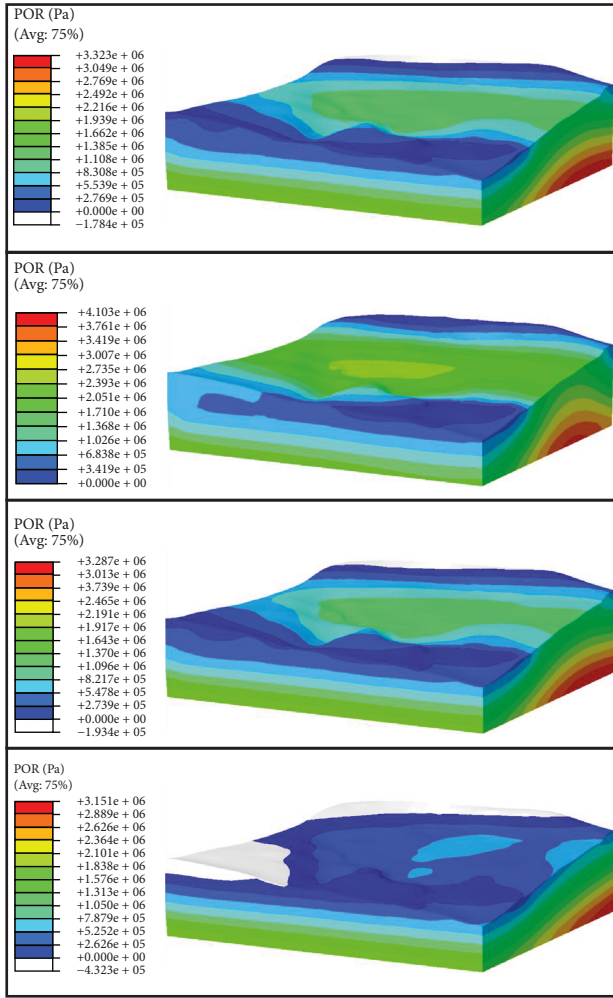FIGURE 19: Plastic zone of Dasha landslide slip surface under the gravity.

FIGURE 20: Distribution of water pressure of Dasha bank slope (rainfall in 2 hours is 94.7 mm).

TABLE 5: Factor of safety of Dasha landslide under different working conditions in different periods.

Period	Working condition	FOS using FLAC^{3D}
Construction	Natural	1.212
Operational	Fluctuation as designed, with effect of rainfall and rapid drawdown	0.991

(1) The underlying bedrock in the landslide area is composed of Suining Formation (silty mudstone interbedded with sandstone) of the Jurassic age. This landslide was reactivated during the rainy season in 1986, resulting in opening and cracking on the wall of houses and the ground surface

(2) The overall topography of Dasha landslide is relatively flat with an average slope angle of 15°; however, the back scarp and local terrain are relatively steep. The area of the landslide is about 29×10^4 m^2, and the maximum thickness of the landslide deposits revealed by drilling is about 40 m with the average thickness of about 20 m, and the volume is thus estimated being about 580×10^4 m^3

(3) A secondary landslide was also identified near the toe with an area of about 2.7×10^4 m^2, with an average thickness of about 6 m and an estimated volume of about 16×10^4 m^3

(4) The factor of safety (FOS) of Dasha landslide obtained by 3D strength reduction cannot meet the minimum safety requirement under the working condition of reservoir level fluctuation as designed, due to the effect of rainfall and rapid drawdown. For the safety of local residents, it is recommended that surface monitoring should be carried out so that early warning can be issued prior to failure

(5) The bedding landslides of red stratum in the Xiangjiaba reservoir area (for example, Dasha landslide) are characterized by slow moving. The shear rate effect of the slip surface should be carried out using ring shear apparatus where possible. This would be useful to predict the deformation of active landslides

(6) Comprehensive monitoring, including rainfall, reservoir level fluctuation, groundwater level, surface displacement, and horizontal displacements at different depths, should be conducted on active landslides so that early warning can be issued and local residents can be evacuated prior to failure. In addition, these monitoring data can be very useful for quantitative evaluation of effect of rainfall as well as the reservoir level fluctuation in landslide activation and reactivation in the reservoir areas

Data Availability

The data used to support the findings of this study are available from the corresponding author upon request.

Disclosure

The earlier version of the abstract was published in a conference of the World Academy of Science, Engineering and Technology International Journal of Geological and Environmental Engineering Vol: 12, No: 6, 2018.

Conflicts of Interest

The authors declare that they have no conflicts of interest.

Acknowledgments

References

[1] ICOLD (International Commission of Large Dams), *Reservoir Landslides: Investigation and Management—Guidelines and Case Histories*, International Commission of Large Dams Publications, 124, Paris, 2002.

[2] W. Riemer, "Landslides and reservoirs (keynote paper)," in *Proceedings of the 6th International Symposium on Landslides*, pp. 1373–2004, Christchurch, 1992.

[3] J. H. Deng, S. S. Ma, and C. F. Lee, "Reactivation of a reservoir landslide," in *Proceedings of the 1st International Conference on Slope Engineering*, pp. 930–935, Hong Kong, December 2003.

[4] X. Z. Guo, *Geological Hazards of China and their Prevention and Control*, Geological Publication House, Beijing, 1991.

[5] X. M. Hu, "The study on the slope stability near the dam of Chenchun Reservoir," *Acta Scientiarum Naturalium Universitatis Pekinensis*, vol. 35, no. 6, pp. 809–815, 1999.

[6] G. Y. Li, *The research on stability of Jinlongshan landslide after the reservoir storing water, [M.S. thesis]*, Chengdu University of Technology, 2002.

[7] H. Liu, R. G. Deng, and Z. Y. Zhang, "Characteristics and genetic analysis of the landslides along Baozhusi reservoir bank in Sichuan," *The Chinese Journal of Geological Hazard and Control*, vol. 12, no. 4, pp. 48–52, 2001.

[8] H. Peng, S. F. Chen, and S. H. Chen, "Analysis on unsaturated seepage and optimization of seepage control for Dayantang landslide in Shuibuya project," *Chinese Journal of Rock Mechanics and Engineering*, vol. 21, no. 7, pp. 1027–1033, 2002.

[9] Y. H. Wei, *The research on the stability of the reservoir bank in Fengjie section of the Three Gorges Reservoir, the Yangtze River, [M.S. thesis]*, Chengdu University of Technology, 2002.

[10] Q. W. Wu and C. H. Wang, "The largest landslide of half-rock and half-soil in China," *Typical slopes in China*, pp. 225–230, Science Press, Beijing, 1988.

[11] L. Xu, *A study on genetic mechanism and stability of Jinjiang landslide at the Baihetan hydropower station in the Jinsha River, [M.S. thesis]*, Chengdu University of Technology, 2004.

[12] R. F. Yu, "Studies on landslide induced waves and landslide warning system near Longyangxia hydroelectric power station in Yellow River," *Water Power*, no. 3, pp. 14–17, 1995.

[13] L. X. Zhong, "Case study on significant geo-hazards in China," *The Chinese Journal of Geological Hazard and Control*, vol. 10, no. 3, pp. 1–10, 1999.

[14] J. Iqbal, D. Fuchu, and X. Tu, "Landslide hazards in reservoir areas: case study of Xiangjiaba reservoir, Southwest China," *Natural Hazards Review*, vol. 18, no. 4, 2017.

[15] J. Iqbal, F. Dai, M. Hong, and X. Tu, "Failure mechanism and stability analysis of an active landslide in the Xiangjiaba reservoir area, Southwest China," *Journal of Earth Science*, vol. 29, no. 3, pp. 646–661, 2018.

[16] L. Xu, F. C. Dai, J. Chen, J. Iqbal, and Y. Qu, "Analysis of a progressive slope failure in the Xiangjiaba reservoir area, Southwest China," *Landslides*, vol. 11, no. 1, pp. 55–66, 2014.

[17] B. Huang, Y. Yin, S. Wang, G. Liu, and J. Tan, "Tangjiaxi landslide and impulse wave analysis in Zhexi reservoir of China by granular flow coupling model," *Natural Hazards and Earth System Sciences Discussions*, vol. 17, pp. 657–670, 2017.

[18] A. Panizzo, P. De Girolamo, M. Di Risio, A. Maistri, and A. Petaccia, "Great landslide events in Italian artificial reservoirs," *Natural Hazards and Earth System Sciences*, vol. 5, no. 5, pp. 733–740, 2005.

[19] M. Yamao, R. C. Sidle, T. Gomi, and F. Imaizumi, "Characteristics of landslides in unwelded pyroclastic flow deposits, southern Kyushu, Japan," *Natural Hazards and Earth System Sciences*, vol. 16, no. 2, pp. 617–627, 2016.

[20] Y. Yonghui, Z. Baiping, M. Xiaoding, and M. Peng, "Large-scale hydroelectric projects and mountain development on the upper Yangtze River," *Mountain Research and Development*, vol. 26, no. 2, pp. 109–114, 2006.

[21] ASTM, *D3385-09, Standard Test Method for Infiltration Rate of Soils in Field Using Double-Ring Infiltrometer*, ASTM International, West Conshohocken, PA, USA, 2009.

[22] A. W. Skempton, A. D. Leadbeater, and R. J. Chandler, "The Mam Tor landslide North Derbyshire," *Philosophical Transactions of the Royal Society A: Mathematical, Physical and Engineering Sciences*, vol. 329, no. 1607, pp. 503–547, 1989.

[23] A. W. Skempton and J. N. Hutchinson, "Stability of natural slopes and embankment foundations," in *Proceedings of the 7th International Conference on Soil Mechanics and Foundation Engineering, 3(State of the Art), Sociedad Mexicana de Mecanica de Suelos*, pp. 291–340, Mexico City, Mexico, 1969.

[24] A. W. Skempton, "Residual strength of clays in landslides, folded strata and the laboratory," *Geotechnique*, vol. 35, no. 1, pp. 3–18, 1985.

[25] A. W. Skempton, "Long-term stability of clay slopes," *Geotechnique*, vol. 14, no. 2, pp. 77–102, 1964.

[26] J. N. Hutchinson, "A reconsideration of the coastal landslides at Folkestone Warren, Kent," *Géotechnique*, vol. 19, no. 1, pp. 6–38, 1969.

[27] A. W. Skempton and D. J. Petley, "The strength along structural discontinuities in stiff clays," in *Proceedings of the Geotechnology Conference on Shear Strength Properties of Natural Soils and Rocks, NGI, Norwegian Geotechnical Institute*, vol. 2, pp. 29–47, Oslo, Norway, 1967.

[28] F. Blondeau and H. Josseaume, "Mesure de la resistance au asaillement rediduelle en laboratoire," *Bulletin de liaison des laboratoires des ponts et chaussées*, pp. 90–106, 1976, Numero Special II.

[29] E. N. Bromhead and N. Dixon, "The field residual strength of London Clay and its correlation with loboratory measurements, especially ring shear tests," *Géotechnique*, vol. 36, no. 3, pp. 449–452, 1986.

[30] R. J. Chandler, "A Discussion on valley slopes and cliffs in southern England: morphology, mechanics and Quaternary history - The history and stability of two Lias clay slopes in the upper Gwash valley, Rutland," *Philosophical Transactions of the Royal Society of London, Series A*, vol. 283, no. 1315, pp. 463–491, 1976.

[31] R. J. Chandler, "Back analysis techniques for slope stabilization works: a case record," *Géotechnique*, vol. 27, no. 4, pp. 479–495, 1977.

[32] R. J. Chandler, "Recent European experience of landslides in overconsolidated clays and soft rocks," in *Proceedings of the 4th International Symposium on Landslides, Canadian Geotechnical Society*, vol. 1, pp. 61–81, Richmond, BC, Canada, 1984.

[33] N. R. Morgenstern, "Slopes and excavations," in *9th International Conference on Soil Mechanics and Foundation Engineering, 12 (State of the Art)*, pp. 567–581, 1977.

[34] D. J. Palladino and R. B. Peck, "Slope failures in an overconsolidated clay, Seattle, Washington," *Géotechnique*, vol. 22, no. 4, pp. 563–595, 1972.

[35] K. Terzaghi, R. B. Peck, and G. Mesri, *Soil Mechanics in Engineering Practice*, Wiley, New York, 3rd Ed edition, 1996.

[36] A. W. Bishop, G. E. Green, V. K. Garga, A. Andresen, and J. D. Brown, "A new ring shear apparatus and its application to the measurement of residual strength," *Géotechnique*, vol. 21, no. 4, pp. 273–328, 1971.

[37] T. D. Stark and H. T. Eid, "Drained residual strength of cohesive of soils," *Journal of Geotechnical Engineering*, vol. 120, no. 5, pp. 856–871, 1994.

[38] G. Mesri and F. Cepeda-Diaz, "Residual shear strength of clays and shales," *Géotechnique*, vol. 36, no. 2, pp. 269–274, 1986.

[39] R. Saito, H. Fukuoka, and K. Sassa, "Experimental study on the rate effect on the shear strength," in *Disaster Mitigation of Debris Flows, Slope Failures and Landslides*, pp. 421–427, Universal Academy Press, Inc., Tokyo Japan, 2006.

[40] H. Rahardjo, K. K. Aung, E. C. Leong, and R. B. Rezaur, "Characteristics of residual soils in Singapore as formed by weathering," *Engineering Geology*, vol. 73, no. 1-2, pp. 157–169, 2004.

[41] A. Rouaiguia, "Residual shear strength of clay-structure interfaces," *International Journal of Civil& Environmental Engineering*, vol. 10, pp. 6–18, 2010.

[42] B. P. Wen, A. Aydin, N. S. Duzgoren-Aydin, Y. R. Li, H. Y. Chen, and S. D. Xiao, "Residual strength of slip zones of large landslides in the Three Gorges area, China," *Engineering Geology*, vol. 93, no. 3-4, pp. 82–98, 2007.

[43] C. Xu, X. Xu, F. Dai, and A. Saraf, "Comparison of different models for susceptibility mapping of earthquake triggered landslides related with the 2008 Wenchuan earthquake in China," *Computers & Geosciences*, vol. 46, pp. 317–329, 2012.